

Dottorato di Ricerca in Ingegneria Civile

Graduate School in Civil Engineering

Sede: Facoltà di Ingegneria - Università di Pavia - via Ferrata 1 – 27100 Pavia – Italy

Dottorato di Ricerca in Ingegneria Civile IX Nuova serie (XXIII Ciclo)

**Verification of Wind Pressure and Wind
Induced Response of a Supertall Structure using
a Long Term Structural Health Monitoring
System**

Ph.D Thesis

Raed AlSaleh

Advisor:

Prof. Yi Qing Ni

Reviser:

Prof. Fabio Casciati

Pavia, October 2010

To My Beloved Homeland Palestine
To My Father

Acknowledgment

The author wishes to express his sincere gratitude and appreciation to Professor Fabio Casciati for constantly providing his enthusiastic support, scientific knowledge, patient guidance, and human experience during the whole PhD study period as a coordinator of the PhD school in Civil Engineering, and for his useful and valuable suggestions and encouraging preparing this thesis, as a reviser.

The author would like to sincerely thank Professor Ni from The Polytechnic University of Hong Kong for giving the access to the database and software utilized to develop this research in the Civil and Structural Engineering department, and for his appreciated guidance and advising in this thesis.

The collaboration with Dr. Clemente Fuggini in researches accomplished during the PhD study and the valuable exchange of views are also gratefully acknowledged by the author.

Dottorato di Ricerca in Ingegneria Civile

Settore:	Ingegneria
Field:	Engineering
Sede Amministrativa non consortile:	Università degli Studi di Pavia
Administrative location:	University of Pavia
Durata del dottorato in anni:	3 anni
Duration:	3 years
Periodo formativo estero:	Come previsto dal regolamento del Dottorato di Ricerca
Period in external organization:	As required by the school's law
Numero minimo di corsi:	6 corsi
Minimum number of courses:	6 courses

Recapiti



Dipartimento di Meccanica Strutturale
via Ferrata 1 - 27100 Pavia - Italy
Tel. 0382 / 505450 Fax 0382 / 528422



Dipartimento di Ingegneria Idraulica e Ambientale
via Ferrata 1 - 27100 Pavia - Italy
Tel. 0382 / 505300 Fax 0382 / 505589

Coordinatore

CASCIATI Fabio - Professore Ordinario di Scienza delle Costruzioni (ICAR08)

Dipartimento di Meccanica Strutturale
via Ferrata 1 - 27100 Pavia – Italy Tel. 0382 / 505458 Fax 0382 / 528422
e-mail: fabio@dipmec.unipv.it

Collegio dei Docenti

CIAPONI Carlo	-	Professore Straordinario (ICAR02)
DEL GROSSO Andrea	-	Professore Ordinario UniGe (ICAR08)
FARAVELLI Lucia	-	Professore Ordinario (ICAR08)
GALLATI Mario	-	Professore Ordinario (ICAR01)
GOBETTI Armando	-	Professore Associato (ICAR08)
MOISELLO Ugo	-	Professore Ordinario (ICAR02)
PAPIRI Sergio	-	Professore Associato (ICAR02)
SALA Roberto	-	Professore Associato (ING-IND08)
MARCELLINI Alberto	-	Dirigente di ricerca CNR- Milano

Organizzazione del corso

Il dottorato di ricerca in *Ingegneria Civile* presso la Scuola di Dottorato in Scienze dell'Ingegneria dell'Università degli Studi di Pavia è stato istituito nell'anno accademico 1994/95 (X ciclo).

Il corso consente al dottorando di scegliere tra quattro curricula: idraulico, sanitario, sismico e strutturale. Il dottorando svolge la propria attività di ricerca presso il Dipartimento di Ingegneria Idraulica e Ambientale per i primi due curricula o quello di Meccanica Strutturale per gli ultimi due.

Durante i primi due anni sono previsti almeno sei corsi, seguiti da rispettivi esami, che il dottorando è tenuto a sostenere. Il Collegio dei Docenti, composto da professori dei due Dipartimenti e da alcuni esterni all'Università di Pavia, organizza i corsi con lo scopo di fornire allo studente di dottorato opportunità di approfondimento su alcune delle discipline di base per le varie componenti. Corsi e seminari vengono tenuti da docenti di Università nazionali ed estere.

Il Collegio dei Docenti, cui spetta la pianificazione della didattica, si è orientate ad attivare ad anni alterni corsi sui seguenti temi:

- Meccanica dei solidi e dei fluidi
- Metodi numerici per la meccanica dei solidi e dei fluidi
- Rischio strutturale e ambientale
- Metodi sperimentali per la meccanica dei solidi e dei fluidi
- Intelligenza artificiale

più corsi specifici di indirizzo.

Al termine dei corsi del primo anno il Collegio dei Docenti assegna al dottorando un tema di ricerca da sviluppare sotto forma di tesina entro la fine del secondo anno; il tema, non necessariamente legato all'argomento della tesi finale, è di norma coerente con il curriculum, scelto dal dottorando.

All'inizio del secondo anno il dottorando discute con il Coordinatore l'argomento della tesi di dottorato, la cui assegnazione definitiva viene deliberata dal Collegio dei Docenti.

Alla fine di ogni anno i dottorandi devono presentare una relazione particolareggiata (scritta e orale) sull'attività svolta. Sulla base di tale relazione il Collegio dei Docenti, "previa valutazione della assiduità e dell'operosità dimostrata dall'iscritto", ne propone al Rettore l'esclusione dal corso o il passaggio all'anno successivo.

Il dottorando può svolgere attività di ricerca sia di tipo teorico che sperimentale, grazie ai laboratori di cui entrambi i Dipartimenti dispongono, nonché al Laboratorio Numerico di Ingegneria delle Infrastrutture.

Il “Laboratorio didattico sperimentale” del Dipartimento di Meccanica Strutturale dispone di:

1. una tavola vibrante che consente di effettuare prove dinamiche su prototipi strutturali;
2. opportuni sensori e un sistema di acquisizione dati per la misura della risposta strutturale;
3. strumentazione per la progettazione di sistemi di controllo attivo e loro verifica sperimentale;
4. strumentazione per la caratterizzazione dei materiali, attraverso prove statiche e dinamiche.

Il laboratorio del Dipartimento di Ingegneria Idraulica e Ambientale dispone di:

1. un circuito in pressione che consente di effettuare simulazioni di moto vario;
2. un tunnel idrodinamico per lo studio di problemi di cavitazione;
3. canalette per lo studio delle correnti a pelo libero.

Course Organization

The Graduate School of Civil Engineering, a branch of the Doctorate School in Engineering Science, was established at the University of Pavia in the academic year of 1994/95 (X cycle). The School allows the student to select one of the four offered curricula: Hydraulics, Environment, Seismic Engineering and Structural Mechanics. Each student develops his research activity either at the Department of Hydraulics and Environmental Engineering or at the Department of Structural Mechanics. During the first two years, a minimum of six courses must be selected and their examinations successfully passed. The Faculty, made by Professors of the two Departments and by internationally recognized external scientists, organizes courses and provides the students with opportunities to enlarge their basic knowledge. Courses and seminars are held by University Professors from all over the country and abroad. The Faculty starts up, in alternate years, common courses on the following subjects:

- solid and fluid mechanics,
- numerical methods for solid and fluid mechanics,
- structural and environmental risk,
- experimental methods for solid and fluid mechanics,
- artificial intelligence.

More specific courses are devoted to students of the single curricula.

At the end of each course, for the first year the Faculty assigns the student a research argument to develop, in the form of report, by the end of the second year; the topic, not necessarily part of the final doctorate thesis, should be consistent with the curriculum selected by the student. At the beginning of the second year the student discusses with his Coordinator the subject of the thesis and, eventually, the Faculty assigns it to the student. At the end of every year, the student has to present a complete report on his research activity, on the basis of which the Faculty proposes to the Rector his admission to the next academic year or to the final examination. The student is supposed to develop either

theoretical or experimental research activities, and therefore has access to the Department Experimental Laboratories, even to the Numerical Laboratory of Infrastructure Engineering. The Experimental Teaching Laboratory of the Department of Structural Mechanics offers:

1. a shaking table which permits one to conduct dynamic tests on structural prototypes;
2. sensors and acquisition data system for the structural response measurements;
3. instrumentation for the design of active control system and their experimental checks;
4. an universal testing machine for material characterization through static and dynamic tests.

The Department of Hydraulics and Environmental Engineering offers:

1. a pressure circuit simulating various movements;
2. a hydrodynamic tunnel studying cavitations problems;
3. a micro-channels studying free currents.

Elenco delle tesi – Previous Ph.D Theses

Battaini Marco (X Ciclo)	Sistemi strutturali controllati: progettazione ed affidabilità.
Mariani Claudia (X Ciclo)	Problemi di ottimizzazione per strutture bidimensionali anisotrope
Negri Antonella (X Ciclo)	Stima delle perdite idrologiche nei bacini di drenaggio urbani
Pisano Aurora Angela (XI Ciclo)	Structural System Identification: Advanced Approaches and Applications
Saltalippi Carla (XI Ciclo)	Preannuncio delle piene in tempo reale nei corsi d'acqua naturali
Barbieri Eugenio (XI Ciclo)	Thermofluid Dynamics and Topology: Optimization of an Active Thermal Insulation Structure
Barbolini Massimiliano (XII Ciclo)	Dense Snow Avalanches: Computational Models, Hazard Mapping and Related Uncertainties
Espa Paolo (XII Ciclo)	Moti atmosferici generati da forze di galleggiamento: simulazioni numeriche e studio su modello fisico
Petrini Lorenza (XII Ciclo)	Shape Memory Alloys: Modelling the Martensitic Phase Behaviour for Structural Engineering Exploitation
Podestà Stefano (XIII Ciclo)	Risposta sismica di antichi edifici religiosi: una nuova proposta per un modello di vulnerabilità
Sturla Daniele (XIII Ciclo)	Simulazioni lagrangiane di flussi rapidamente variati nell'approssimazione di acque poco profonde
Marazzi Francesco (XV Ciclo)	Semi-active Control of Civil Structures: Implementation Aspects
Nascimbene Roberto (XV Ciclo)	Sail Modelling for Maximal Speed Optimum Design
Giudici Massimo (XVI Ciclo)	Progettazione in regime non lineare di strutture in CAP a cavi aderenti e non aderenti

Mutti Matteo (XVI Ciclo)	Stability Analysis of Stratified Three--phase Flows in Pipes
Petaccia Gabriella (XVI Ciclo)	Propagazione di onde a fronte ripido per rottura di sbarramenti in alvei naturali
Casciati Sara (XVII Ciclo)	Damage Detection and Localization in the Space of the Observed Variables
D'Amico Tiziana (XVI Ciclo)	Ricerca e sviluppo di metodologie diagnostiche per il recupero di edifici monumentali: prove vibroacustiche sul tufo
Barco Olga Janet (XVII Ciclo)	Modeling the Quantity and Quality of Storm Water Runoff Using SWMM
Boguniewicz Joanna (XVIII Ciclo)	Integration of Monitoring and Modelling in the Surface Water State Evaluation Process of a Sub-Alpine Lake Watershed
Bornatici Laura (XVIII Ciclo)	L'impiego degli algoritmi generici per la risoluzione dei problemi di progetto di reti di distribuzione idrica
Collivignarelli Maria Cristina (XVIII Ciclo)	Trattamento di rifiuti liquidi mediante processi biologici aerobici termofili e mesofili e processi avanzati di ossidazione chimica in diversa
Domaneschi Marco (XVIII Ciclo)	Structural Control of Cable-stayed and Suspended Bridges
Ráduly Botond (XVIII Ciclo)	Artificial Neural Network applications in Urban Water Quality Modeling
Antoci Carla (XVIII Ciclo)	Simulazione numerica dell'interazione fluido-struttura con la tecnica SPH
Cappabianca Federica (XVIII Ciclo)	La valutazione del rischio valanghivo attraverso la modellazione dinamica
Callegari Arianna (XVIII Ciclo)	Applicazione di tecnologie di monitoraggio on-line per la gestione dei processi di trattamento reflui
Gazzola Elisa (XVIII Ciclo)	Applicazione di processi biologici anaerobici al trattamento di acque reflue e fanghi di depurazione: aspetti tecnici ed energetici
Giuliano Fabio (XIX Ciclo)	Performance Based Design and Structural Control for Cable Suspension Bridges

Maranca Federica (XVIII ciclo)	Valutazione del ciclo di vita (LCA): confronto tra sistemi di trasporto gas via gasdotto
Falappi Stefano (XIX Ciclo)	Simulazioni numeriche di flussi di fluidi viscosi e materiali granulari con la tecnica SPH
Zanaboni Sabrina (XIX Ciclo)	Pre-trattamento di rifiuti liquidi industriali mediante ossidazione ad umido
Bruggi Matteo (XX Ciclo)	Topology optimization using mixed finite elements
Cimellaro Gian Paolo (XX Ciclo)	Passive Control of Industrial Structures for Natural Hazard Mitigation: Analytical Studies and Applications
Abba Alessandro (XXI Ciclo)	Il recupero dei rifiuti speciali nel settore delle costruzioni: studio delle possibilità di recupero e valutazione dei meccanismi di lisciviazione.
Hamdaoui Karim (XXI Ciclo)	Experimental Application on Cu-based Shape Memory Alloys: Retrofitting of Historical Monuments and Base Isolation.
Messervey Thomas (XXI Ciclo)	Integration of Structural Health Monitoring into the Design, Assessment, and Management of Civil Infrastructures.
Ubertini Filippo (XXI Ciclo)	Wind Effects on Bridges: Response, Stability, and Control.
Fuggini Clemente (XXII Ciclo)	Using Satellites Systems for Structural Monitoring: Accuracy, Uncertainty, and Reliability
Raboni Massimo (XXII Ciclo)	Impiego di tecniche numeriche e sperimentali per l'analisi di fenomeni multiphysics

Table of Contents

	Page no.
Introduction and Main Motivation	1
<i>Abstract</i>	5
 Chapter 1	
Structural Health Monitoring of Towers	
1.1 Introduction	7
1.2 Guangzhou New TV Tower	7
1.2.1 GTVT configuration	9
1.2.2 SHM of GTVT	10
1.3 Wind Effect and Typhoons	13
1.3.1 Typhoons	23
1.3.1.1 Types of Typhoons	24
1.3.1.2 Typhoon Formation	25
1.3.1.3 Damage from Typhoons	25
1.3.2 Typhoons in China	26
1.3.2.1 Kammuri Typhoon	27
1.3.2.2 Nuri Typhoon	28
1.3.2.3 Hagupit Typhoon	29
1.3.2.4 Molave Typhoon	30
1.3.2.4 Koppu Typhoon	31

Chapter 2

Fundamental Theories of Signal Processing	33
2.1 Introduction	33
2.2 Frequency Domain Decomposition	34
2.3 Hilbert-Huang Transform	38
2.3.1 Improved HHT by filtering approach	43
2.4 Damage Detection and Assessment	44
2.4.1 Modal Assurance Criterion	46
2.4.2 Coordinate Modal Assurance Criterion	48
2.4.3 Modal Correlation Coefficient	49

Chapter 3

Analysis of GTVT Response to Wind Pressure by FDD Method	53
3.1 Introduction	53
3.2 Typhoon Kammuri	55
3.2.1 Wind properties	55
3.2.2 Response analysis and processing	56
3.3 Typhoon Nuri	60
3.3.1 Wind properties	60
3.3.2 Response analysis and processing	61
3.4 Typhoon Hagupit	63
3.4.1 Wind properties	63
3.4.2 Response analysis and processing	65

3.5 Typhoon Molave	67
3.5.1 Wind properties	67
3.5.2 Response analysis and processing	68
3.6 Typhoon Koppu	70
3.6.1 Wind properties	70
3.6.2 Response analysis and processing	71
3.7 Results Discussion	73
3.8 Conclusions	76
Chapter 4	
Damage Assessment of GTVT	77
Based on FDD Analysis	
4.1 Introduction	77
4.2 Damage Assessment	78
4.2.1 Assessment after Nuri typhoon	79
4.2.2 Assessment after Hagupit typhoon	83
4.2.3 Assessment after Molave typhoon	85
4.2.4 Assessment after ST and HT earthquakes.	87
4.3 Conclusions	92
Chapter 5	
Signal Processing by	93
Improved HHT Method	
5.1 Introduction	93

5.2 Response of GTVT to Typhoons	93
5.3 Response of GTVT to Earthquakes	103
5.3.1 Southern Taiwan Earthquake	103
5.3.2 Taiwan Hualien Earthquake	103
5.2.3 Response analysis	104
5.3 Results Discussion	107
5.4 Conclusion	110
 Chapter 6	
Damage Assessment of GTVT	113
Based on HHT Analysis	
6.1 Introduction	103
6.2 Instantaneous Frequency and Phase Angle	114
6.2.1 Calculation procedure	117
6.2.2 GTVT assessment during typhoon event	118
6.3 Fundamental Modes Consistency	121
6.3.1 Mode shapes by HHT	121
6.3.2 GTVT assessment after extreme events	124
6.4 EMD Based Damage Assessment	129
6.5 Conclusion	133
 Conclusions	135
References	139

Appendix A	
GTVT Response Signals during Extreme Events	145
Appendix B	
Spectral Density of GTVT Response Signals during Extreme Events by FDD Method	167
Appendix C	
Hilbert Huang Spectra of GTVT Response Signals during Extreme Events	179

Introduction and Main Motivation

Wind effects are the major concern in designing supertall structures, particularly those located in the coastal cities. However, the wind-resistant design parameters obtained from the specifications are usually unable to provide an accurate description of fluctuating wind loads acting on these structures. Wind tunnel tests have benefited the wind-resistant design significantly; but because of the artificial nature of the wind tunnel environment and the scale issues, wind tunnel tests can only provide a limited answer to the problem. The real answer lies in full scale testing and monitoring of the real structures during actual events.

This dissertation presents long term investigation on verifying the wind characteristics and wind-induced responses of supertall structures by taking the instrumented Guangzhou Television and sightseeing Tower (GTVT) of 610 m high as a test bed. The GTVT was instrumented with a long-term structural health monitoring (SHM) system comprising over 700 sensors of sixteen types. In this research, the wind-relevant properties and structural responses obtained from this SHM system under extreme event periods caused by strong wind or ground motions are investigated. The achieved signals are then operated to extract the modal parameters of the tower by several implemented algorithms. The structure is then assessed by performing some damage assessment coefficients to detect any possible sign for damages that could be caused by the considered extreme events.

The performed research work presented in this thesis is organized in five chapters as follows:

Chapter 1 is reserved mainly; in its first part to the configuration of the supertall building GTVT that is the case of study in this thesis. The long term SHM system, that the supertall structure is equipped with, is also described in this chapter. And the second part of the chapter focuses on some strong wind events (i.e typhoons) occurred in the tower region, and the definition of the typhoons in general is also explained.

In Chapter 2; two methods of operational modal analysis are presented, which are adopted in the signal analysis procedure. The first is the Frequency domain decomposition method, and the second is the Hilbert-Huang Transform method. In addition, an implemented technique to improve the second method by filtering approach is discussed also in detail. At the end of the chapter, various criteria of damage assessment of structures based on the parameters obtained from operational modal analysis methods are also discussed.

Chapter 3 studies the behavior of the GTVT when exposed to extreme wind events, through investigating the dynamic response of the tower to five different typhoons occurred at different times and various stages of the tower construction. The Frequency domain decomposition method is utilized in signal analysis. Then wind properties of the considered typhoons are illustrated, and the modal parameters of the structure are calculated. Then the variations of these parameters during the various typhoons are presented.

Chapter 4 is devoted mainly to the damage assessment of the tower after being exposed to several typhoons as well as two events of ground motion. The damage assessment of the structure is performed, based on the operational modal analysis results obtained by Frequency domain decomposition method, which is applied on the ambient vibration response signals of the tower obtained before and after the exposure to the severe event. The damage identification algorithms adopted in achieving this assessment are MAC, COMAC, and MCC.

In Chapter 5; the response signal of the tower upon seven different extreme events is analyzed by the aid of the improved Hilbert-Huang Transform by filtering approach. The calculation procedure of this method is explained in detail, and the response of the tower is illustrated in the frequency and time domain. The results are then discussed in detail and the benefits of this method are demonstrated.

Chapter 6; further evaluates the condition of the tower body structure after the considered extreme events by some criteria based on the results obtained by Hilbert-Huang Transform, and a proposed damage index based on the Empirical Mode Decomposition method in decomposing the signals is discussed and verified.

The resulted conclusions of this research work and proposed recommendations for the future work are mentioned at the end of this thesis.

Abstract

Structural health monitoring has become the highlight of researches in structural engineering and its application is the main concern of many researchers all over the world. This dissertation presents long term investigation on verifying the wind characteristics and wind-induced responses of supertall structures considering the instrumented Guangzhou Television and sightseeing Tower (GTVT) of 610 m high as the case study. It is a part of a bigger campaign to monitor the tower held by the Polytechnic University of Hong Kong. The scope is monitoring the tower dynamical behavior in various weather conditions and under exposure to extreme events, and to analyze this response by the aid of several algorithms to reach for a full performance assessment in real time. The response data were obtained through the long-term SHM system the tower is equipped with.

The response of the tower under five typhoons and two earthquakes is studied. Firstly, signals measured during typhoons are analyzed by FDD method to identify the modal parameters of the structure, and correlating them with the wind properties for the several typhoons. The mode shapes of the tower extracted by this method were used later in the damage assessment process of tower, based on performing three main coefficients; MAC, COMAC, MCC.

The obtained signals during the considered typhoons and earthquakes are analyzed again by HHT method improved by an implemented filtering approach, and the produced modal parameters are verified. Then damage assessment based on this method is conducted by two suggested approaches, and a damage index mainly based on EMD method is proposed and validated at the end of the thesis and the results obtained by the this index are verified.

The tower showed perfect condition upon being assessed after extreme events by every criterion adopted in this dissertation. However, the differentiation between all of these criteria is clarified.

Chapter 1

Structural Health Monitoring of Towers

1.1 Introduction

After several years of development, structural health monitoring has currently become the highlight of researches and applications in civil structures all over the world. Structural Health Monitoring (SHM) is referred to the process used for implementation of damage detection and characterization strategy in engineering structures. The damage is detected by the induced changes of material and/or geometric properties of a structural system. The SHM process involves; the observation of a system over time using periodically sampled dynamic response measurements from an array of sensors, the extraction of damage-sensitive features from these measurements, and the statistical analysis of these features to determine the current state of the system health.

The objectives for implementing a SHM system are numerous, and could be summarized as following; (i) validating design assumptions and parameters and improving design specifications for future similar structures; (ii) detecting any possible damage or deterioration at an early stage; (iii) providing real-time data for the assessment of a structure after extreme events; (iv) In planning process

of inspection and rehabilitation, by providing essential instruction and prioritizing (v) monitoring the effectiveness of repairs and reconstruction; and (vi) providing massive amounts of data for research works in structural dynamics engineering (Farrar and Worden 2007)..

However, the achievement of the above mentioned objectives and benefits is a challenge. It needs well coordinated interdisciplinary research for full adaptation of innovative technologies. Actually, structural health monitoring has been a subject of major international research in recent years. It requires collaboration between civil, mechanical, electrical and computer engineering among others.

In long term SHM, the output of this process is periodically updated information regarding the ability of the structure to perform its intended function in light of the inevitable aging and degradation resulting from operational environments. After extreme events, such as earthquakes or typhoons, SHM is used for condition screening to provide, in near real time, reliable information regarding the integrity of the structure

The development of structural health monitoring technology for surveillance, evaluation, and assessment of existing structures has attained some degree of maturity. Long-term monitoring systems have been implemented on structures in many countries around the world.

For bridges; many successful implementation and operation of SHM systems have been reported worldwide (Casciati 2003), while the applications of SHM to building structures are not as widespread. One sophisticated example of SHM applications on bridges is the Wind and Structural Health Monitoring System (WASHMS) in Hong Kong, implemented by the Hong Kong Highways Department to ensure road user comfort and safety of three bridges, namely; Tsing Ma, Ting Kau, and Kap Shui Mun bridges that run between Hong Kong and the Hong Kong Airport, with total cost of US\$1.3 million (Ko and Ni 2005)

However, many researches have been performed recently based on long-term monitoring implementation for building structures. The work accomplished by Brownjohn and his co-investigators is one of these researches. The program was held on a 280m high 65-story office tower, to monitor the

structural dynamic responses and to track any variations in the structural performance [Brownjohn et al. 1998].

Li and his co-investigator have made full-scale measurements on a number of high-rise structures under strong wind conditions (Li and Wu 2007), with the intention to identify wind-induced structural response characteristics.

A monitoring program was initiated by the University of Notre Dame In U.S.A. in collaboration with design and consultancy firms to monitor the full-scale responses of three tall buildings in Chicago and compare them with the predicated responses from wind tunnel test and finite element analysis (Kijewski-Correa 2006).

Reports show that more than 150 buildings in California, U.S.A., more than 100 buildings in Japan, and more than 40 buildings in Taiwan have been instrumented with health monitoring systems for seismic measurement and post earthquake damage assessment (Ni et al 2009).

In this chapter; the supertall building of Guangzhou city in China is configured, as it has been being the case of interest for many research works and it is the case of study in this dissertation. The supertall structure gained this interest due to the long term SHM system it is equipped with, which is also explained in details in this chapter.

The region in which the tower stands is likely to be exposed to extreme wind events like typhoons, therefore in this research; most of the attention is focused on the behavior of the tower upon these extreme events, and a brief definition of the typhoons in general and the typhoons which are under consideration in this study is explained at the end of this chapter.

1.2 Guangzhou New TV Tower

Several supertall structures were built and are being constructed in the coastal cities of south-east China, such as: the International Finance Center of 416 m high in Hong Kong, the Shanghai World Financial Center of 492 m high, the Shanghai Center of 580 m high, and the Television and Sightseeing Tower of 610 m high in Guangzhou (GTVT); which is the tower of interest for the

author in this research work, as it was in several previously performed researches by the author (AlSaleh et. al 2009, and Casciati et. al 2009).

1.2.1 GTVT configuration

Guangzhou New TV Tower was constructed to broadcast the 16th Asian Games, which will be held in Guangzhou-China from November 12 to November 27, 2010. Later on, it is supposed to serve as offices, entertainment, catering, tourism, and transmission of television and radio programs. On the top level of the tower at height of 454 m an antennary mast is mounted with 164 m height (Figure 1.1.a).

The tower is a tube-in-tube structure; the outer tube is made of steel (Figure 1.1.b) and inner one is reinforced concrete tube (Figure 1.1.c). The two tubes are linked together by 36 floors and 4 levels of connection girders. The underground part of the tower is 10 m height and consists of 2 floors with plan dimensions of 167 m \times 176 m. Figure 1.2 shows also the plan of the inner tube (Figure 1.2.a), and the plan of a floor (Figure 1.2.b).

The outer tube is shaped by concrete-filled-tube (CFT) columns, spaced in an oval shape, inclined vertically, and connected by hollow steel rings and braces. The oval shape dimensions varies from 60 m \times 80 m at the underground level (altitude of -10 m) to their minimum values of 20.65 m \times 27.5 m at the altitude of 280 m, and then they increase again to 40.5 m \times 54 m at the top level of the tube (altitude of 450m). The oval shape of the top level is rotated 45 degrees horizontally relative to that of the bottom level. The top level plan is also inclined 15.5 degrees to the horizontal plane.

The inner tube shape is an oval with constant dimensions along its height (14 m \times 17 m), and its centroid is not that of the outer tube. The thickness of the tube varies from 1 m at the bottom to 0.4 m at the top. The cross section variations of both inner and outer tube are illustrated in Figure 1.3 (Xia et al. 2008, and Xia et al. 2009).



a) Aerial view

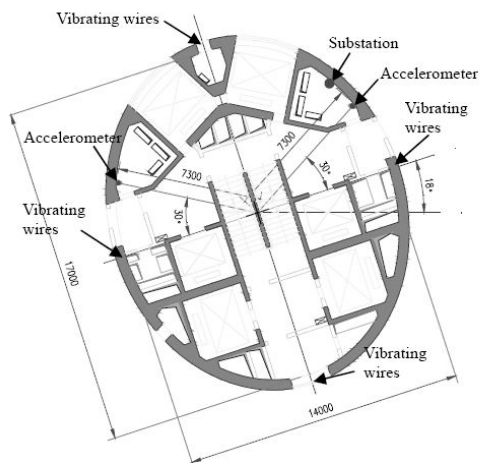


b) Outer tube

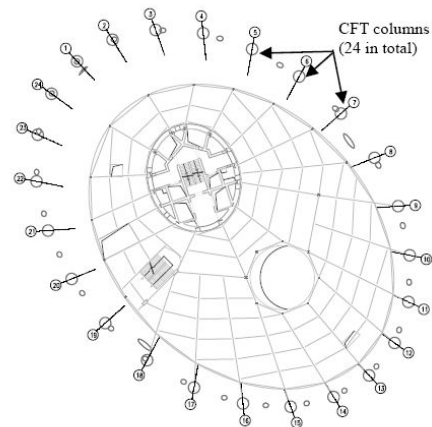


c) Inner tube

Figure 1.1. Guangzhou New TV Tower (GTVT)



a)



b)

Figure 1.2. a) Plan of the inner tube (unit: mm) b) Plan of a floor.

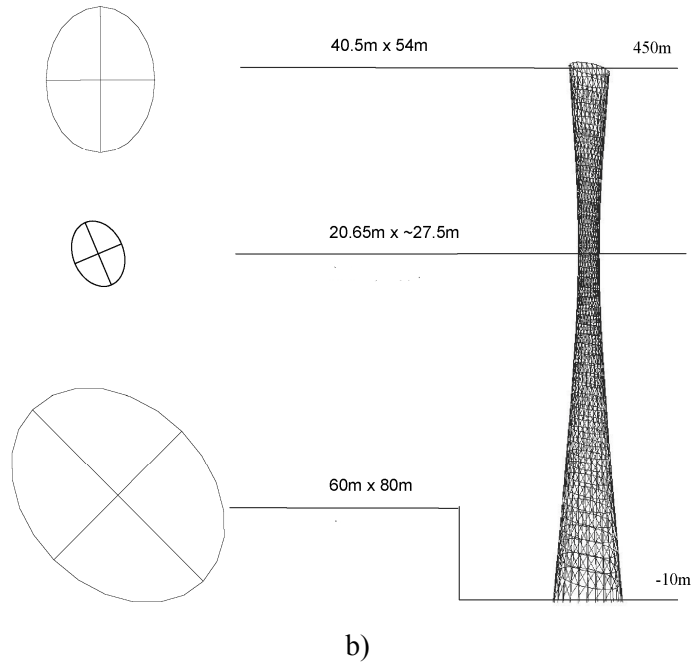
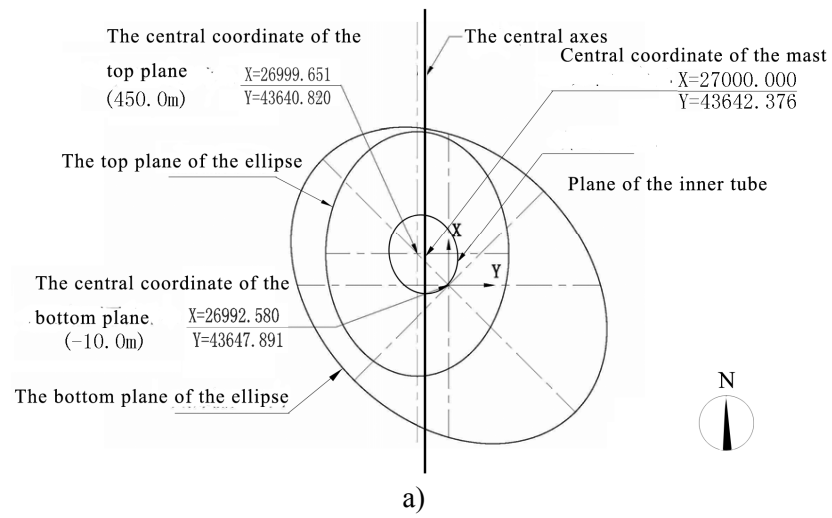


Figure 1.3. Variation of sections along the tower.

1.2.2 SHM of GTVT

Aiming at monitoring the supertall structure in both construction and service stages; a sophisticated SHM system has been designed and is being implemented by the Consortium of Hong Kong Polytechnic University and Sun Yat-Sen University. It consists of 16 different types of more than 700 sensors distributed along the height of the structure (Benchmark 2008).

The SHM system for GNTVT has been devised on the basis of a modular design concept, which consists of six modules, namely, Module 1: Sensory System, Module 2: Data Acquisition and Transmission System, Module 3: Data Processing and Control System, Module 4: Data Management System, Module 5: Structural Health Evaluation System, and Module 6: Inspection and Maintenance System. Figure 1.4 shows the integration of these models (Ni et al. 2008, and Ni et al. 2009).

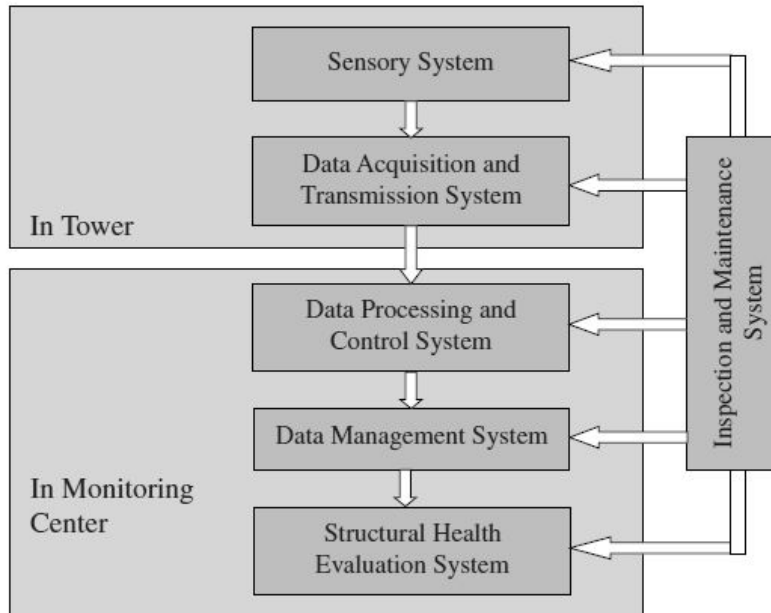


Figure 1.4. Modules of the SHM system for GNTVT

Table 1.1 lists the types of sensors forming the sensory system in both in-construction and in-service monitoring stages of GTVT. These sensors are deployed for monitoring three main categories of parameters:

- (i) loading sources (wind, seismic, and thermal loading).
- (ii) structural responses (strain, displacement, inclination, acceleration, and geometric configuration).
- (iii) environmental effects (temperature, humidity, rain, air pressure, and corrosion).

The data transmission and acquisition system consists of 19 stand-alone Data Acquisition Units (DAU); 13 are for in-construction monitoring, and the other 6 are for in-service monitoring to ensure the quality and fidelity of the acquired data.

The data processing and control system comprises high-performance servers and data-processing software, to control the on-structure DAUs regarding data acquisition and pre-processing, data transmission and filing, and the display of the data.

The data management system is an Oracle-driven database system for non-spatial temporal data management with a Geographic Information System (GIS) for spatial data management.

The subsequent developments in this chapter were ordered following a working document elaborated within the Marie Curie program SMARTEN. The first issue is formulated as:

- Combined Monitoring and Inspection Systems: WSN can provide a wide spatial and temporal coverage of the system with a relatively lower level of reliability, accuracy and cost as compared to direct inspection. On the other hand, the WSN will act as a warning system flagging the areas/locations where more expensive and accurate NDT inspections are required.

and the tower designers took the following decisions:

The structural health and evaluation system is composed of an on-line structural condition evaluation system and an off-line structural health and safety assessment system. The on-line structural condition evaluation system is mainly used to compare the static and dynamic measurement data with the design values, finite element analysis results, and pre-determined thresholds and patterns to provide a prompt evaluation on the structural condition. The off-line structural health and safety assessment system incorporates varieties of model-based and data-driven damage diagnostic and prognostic algorithms, which mostly require both historical and current monitoring data.

Moreover, a wireless system, as shown in Figure 1.5, is being operated for synchronous acquisition of strain and temperature data and real-time data transmission from the sub-stations to the site office during the construction monitoring. It consists of three parts: WiFi router, wireless bridge, and antenna.

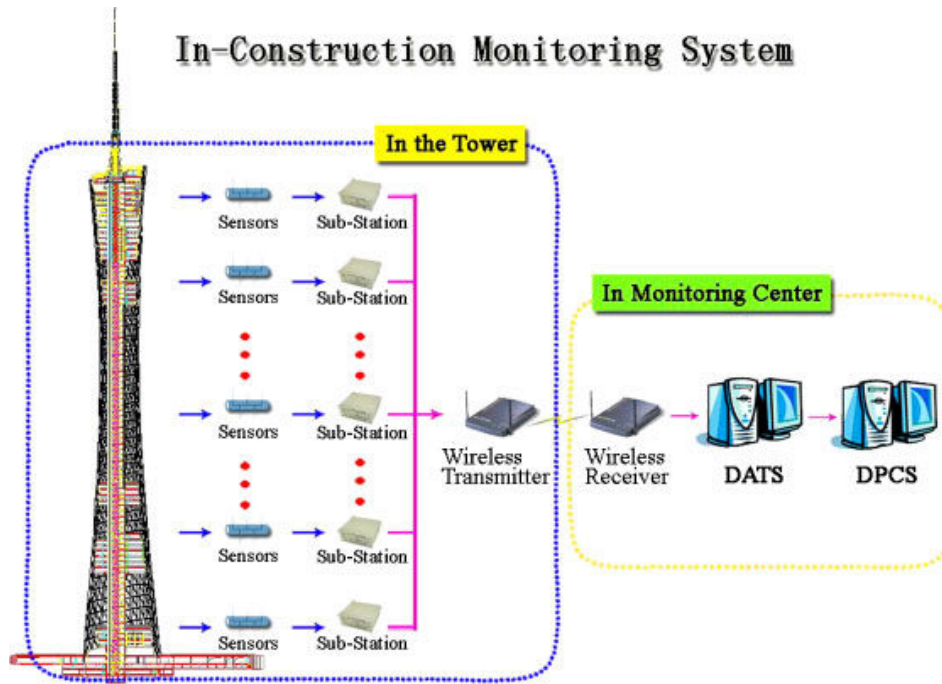


Figure 1.5. Wireless system of strain and temperature (Ni et al. 2009).

Another issue was highlighted in the SMARTEN program is as follows

- Optimum Sensor Locations and Requirements for NDE: study of the deployment plan (sensor placement, antenna option).

The quality of monitoring data is essential to evaluate the structural condition and detect the structural damage reliably, which relies to a great extent on the appropriate selection and placement of sensors. In developing the SHM system for GTVT, the sensors were selected according to the following criteria: (i) the Sensory System should have the ability to capture all important information about the structural static and dynamic properties; (ii) It should have the function to combine multiple types of sensors, as to achieve an accurate measurement for specific structural response/parameter; and (iii) different types of sensors should be collocated at crucial locations for cross-calibration. An example of illustrating criterion 1 is the selection of accelerometers. As the tallest TV tower structure in the world, GTVT has the fundamental modal frequency of 0.11 Hz predicted by finite element analysis. The experience in similar buildings shows that the vibration amplitude under normal ambient excitation is in the order of cm/s^2 (Ni et al. 2009).

Figure 1.6 shows the measured waveforms by an accelerometer during the controlled shaking table testing in the presence of environmental noise. It has a frequency range of DC to 50 Hz, a scale range of $\pm 20 \text{ m/s}^2$, a sensitivity of 125 mV/m/s^2 , and an operating temperature of -20 to $+70^\circ\text{C}$. This type of uniaxial servo accelerometers was finally selected to be installed on GTVT (Xia et al. 2009).

Moreover, global positioning system (GPS) and digital video cameras are deployed for the measurement of horizontal deflection at various construction stages as shown in Figure 1.7, while a combination of GPS, accelerometers, and digital video cameras is adopted at long-term service stage. Total station and zenithal telescope are adopted for in-construction monitoring of inclination, and both strain gauges and fiber optic sensors are installed for in-service monitoring of strain. Sensors locations are determined according to the finite element analysis results.

Figures 1.8 and 1.9 show the deployment of sensors and DAUs for in-construction monitoring and in-service monitoring of GTVT, respectively. The in-construction monitoring system includes 527 sensors, while the in-service monitoring system involves 280 sensors. A total of 12 cross-sections have been selected for in-construction monitoring and a total of 5 cross-sections for in-service monitoring (each cross-section is allocated one DAU and one additional DAU is located at the ground floor). These critical cross-sections which are suffering large stresses under construction were determined through finite element analysis.

Accelerometers are positioned at more cross-sections to capture complete modal shapes. The distribution of accelerometers along the tower height is demonstrated in Figure 1.10, while their locations in the horizontal plan is shown in Figure 1.11.a. Figure 1.11.b depicts the type of accelerometer used.

All the sensors for in-service monitoring and their cabling networks are deployed in synchronism with construction progress. As shown in Table 1.1, a considerable number of sensors are shared by in-construction monitoring and in-service monitoring (Ni et al. 2009).

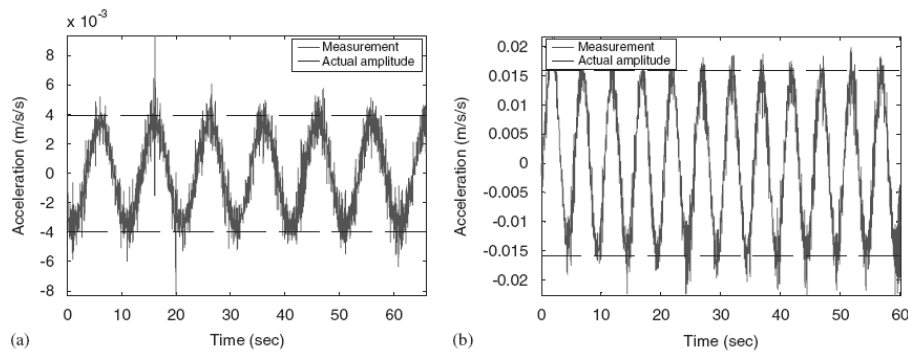


Figure 1.6. Calibration of accelerometers on shaking table: (a) frequency 0.1 Hz and amplitude 1 cm and (b) frequency 0.2 Hz and amplitude 1 cm (Ni et al. 2009).

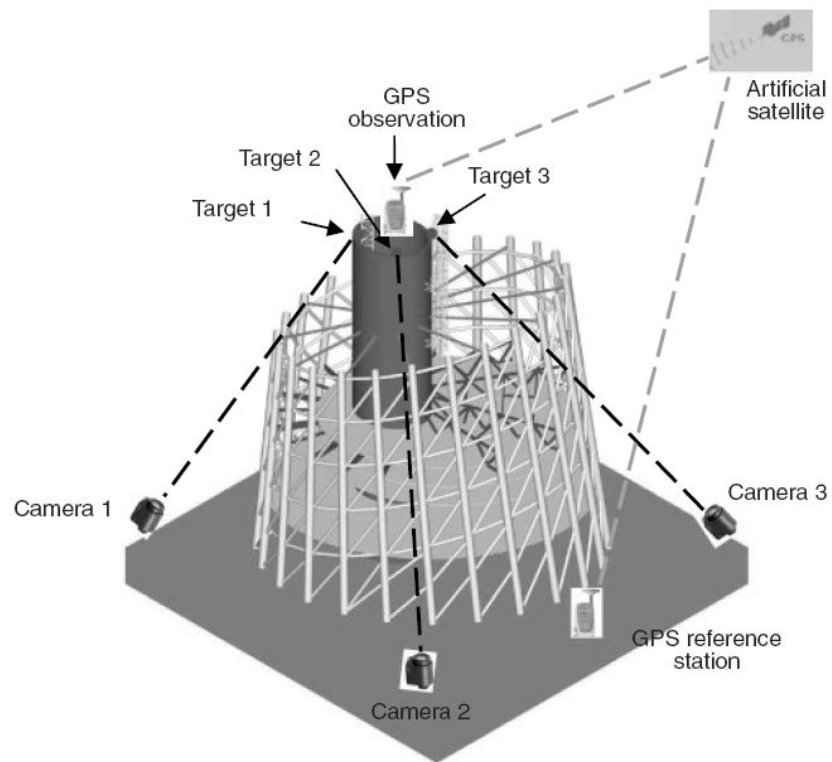


Figure 1.7. Combination of GPS and digital video camera for deflection measurement.

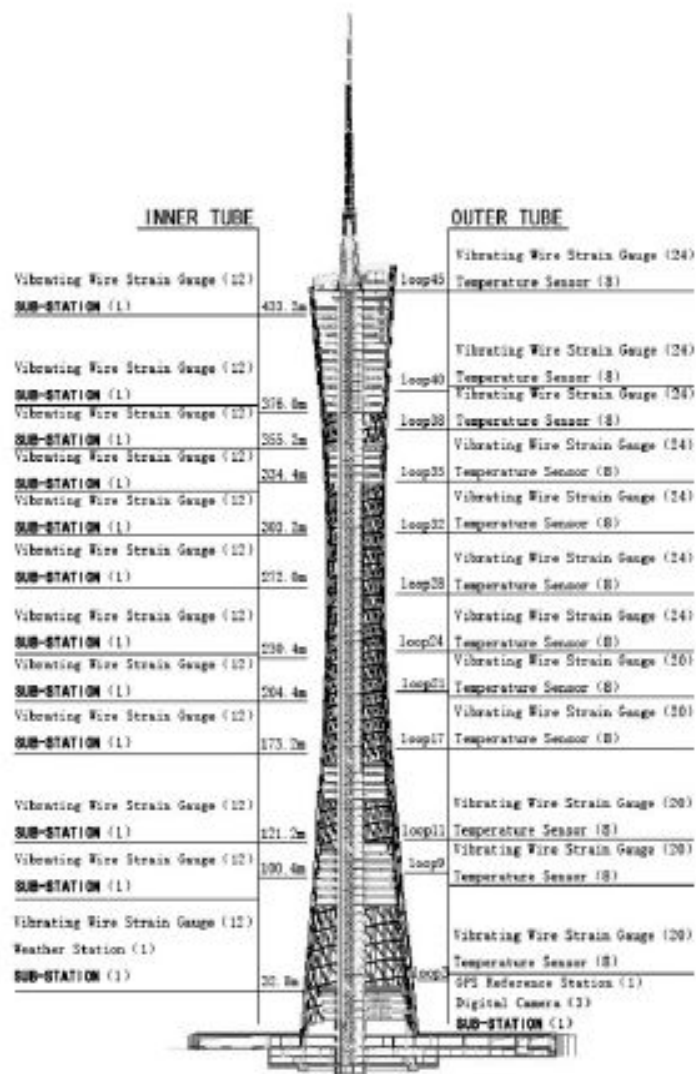


Figure 1.8. Deployment of sensors and DAUs for in-construction monitoring

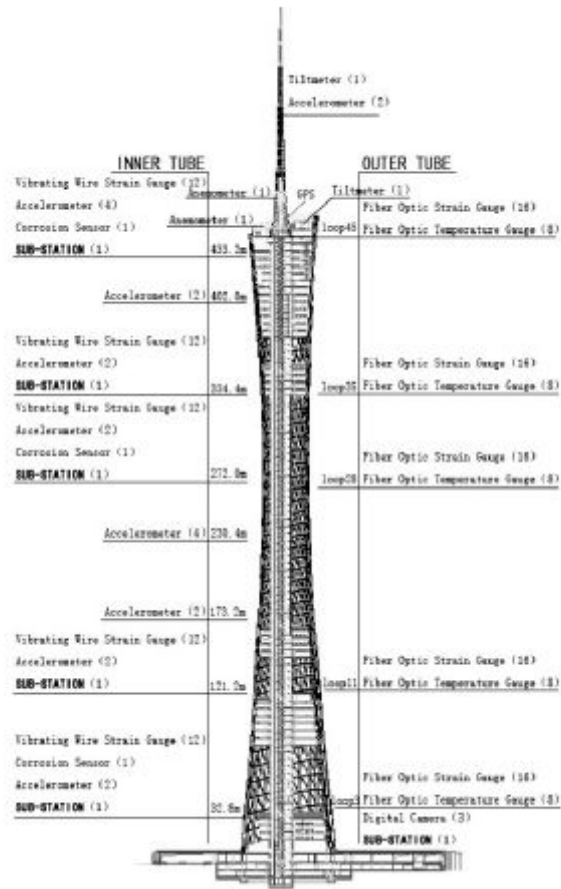


Figure 1.9. Deployment of sensors and DAUs for in-service monitoring.

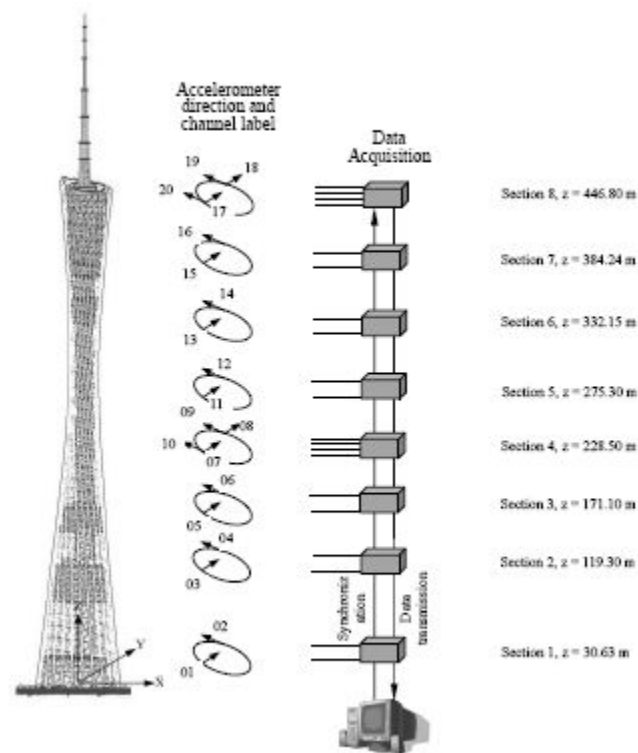


Figure 1.10. Position of accelerometers and data acquisition system

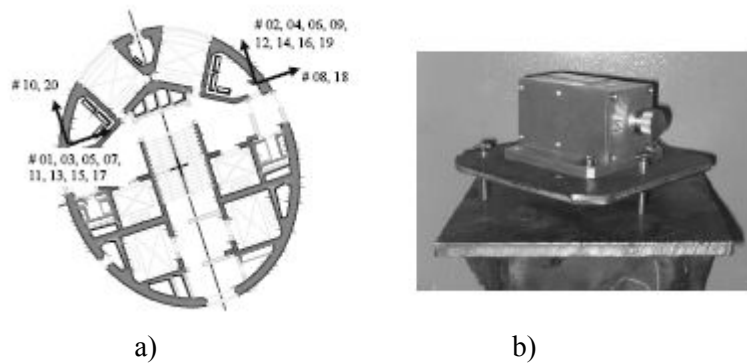


Figure 1.11. a) Plan position of accelerometers and channel labels, b) An installed accelerometer.

Table 1.1. Sensors deployed for SHM of the tower.

No.	Sensor type	Monitoring Items	Number of sensors	
			In-construction monitoring	In-service monitoring
1	Weather station	Temperature, humidity, rain, air pressure	1	1
2	Anemometer	Wind speed and direction	2	2
3	Wind pressure sensor	Wind pressure	0	4
4	Total station	Inclination, leveling, elevation	1	0
5	Zenithal telescope	Inclination of tower	2	0
6	Tiltmeter	Inclination of tower	0	2
7	Level sensor	Leveling of floors	2	0
8	Theodolite	Elevation	2	0
9	GPS	Displacement	2	2
10	Vibrating wire gauge	Strain, shrinkage, and creep	416	60
11	Thermometer	Temperature of Structure	96	60
12	video camera	Displacement	3	3
13	Seismograph	Earthquake motion	0	1
14	Corrosion sensor	Corrosion of reinforcement	0	3
15	Accelerometer	Acceleration	0	22
16	Fiber optic sensor	Strain and temperature	0	120
Total			527	280

An SHM benchmark problem for high-rise structures is currently being developed by taking the instrumented GTVT as a test bed. The first stage of the SHM benchmark problem consists of the following four tasks:

- 1) Output-only modal identification and finite element model updating.
- 2) Damage detection using model-based simulation data.
- 3) Performance-based optimal sensor placement for SHM.
- 4) Damage detection using field measurement data.

This benchmark problem is considered as an appropriate tool that would provide elaborated answers to other two issues SMARTEN program is concerning; as follows:

- Low Complexity Adaptive Algorithms for Event Identification and Tracking and Damage identification and Classification: Emphasis will be given on Distributed Algorithms.
- Performance Model Updating Based on Sensor Information: new methods for incorporating information from diverse sources of different type, spatial and temporal coverage, quality and reliability which may also require the combination of both quantitative and qualitative information.

1.3 Wind Effect and Typhoons

Wind is a phenomenon of great complexity because of the many flow situations arising from the interaction of wind with structures. It is composed of a multitude of eddies of varying sizes and rotational characteristics carried along in a general stream of air moving relative to the earth's surface. These eddies give wind its gusty or turbulent character. The gustiness of strong winds in the lower levels of the atmosphere largely arises from interaction with surface features. The average wind speed over a time period of the order of ten minutes or more tends to increase with height, while the gustiness tends to decrease with height.

In general, structures, particularly, those that are tall or slender, respond dynamically to the effects of wind. The most known structural collapse due to wind was the Tacoma Narrows Bridge which occurred in 1940 at a wind speed of only about 19 m/s. It failed after it had developed a coupled torsional and flexural mode of oscillation (Mendis et al. 2007).

There are several different phenomena giving rise to dynamic response of structures in wind. These include buffeting, vortex shedding, galloping and flutter. Slender structures are likely to be sensitive to dynamic response in line with the wind direction as a consequence of turbulence buffeting

An important problem associated with wind induced motion of buildings is concerned with human response to vibration and perception of motion. At this point it will suffice to note that humans are sensitive to vibration to the extent that motions may feel uncomfortable even if they correspond to relatively low levels of stress and strain. Therefore, for most tall buildings serviceability considerations govern the design and not strength issues.

1.3.1 Typhoons

A typhoon is defined as a tropical cyclone in the western Pacific. They generally track in a westward or northern direction, and occur most frequently in a region of the western Pacific and East Asia.

A typhoon is essentially the same as a hurricane, which is defined as a strong tropical storm with winds over 75 miles per hour, occurring in the west Atlantic and the eastern Pacific, particularly in southeastern North Americas and the Caribbean. Similar storms in the Indian Ocean are called tropical cyclones which describe all low pressure systems over tropical waters and include typhoons and hurricanes. All these storms feature super heavy rain as well as high winds.

The word "typhoon" comes from the Cantonese word "tai feng." The approach of a typhoon is heralded by large waves, a storm surge, and falling barometric pressure. As it gets nearer, mountains of cumulus clouds appear and

wind squalls intensify, climaxing with a sweeping wall of dense clouds with furious winds and torrential rain.

The typhoon season lasts from the early summer to early autumn, often coinciding with the monsoon season in Southeast Asia and the wet season in eastern Japan. The main typhoon and hurricane season is from June to November. Sometimes they appear as early as May and as late as December. Usually more damage is caused by the heavy rain than by the winds (Facts and Details).

1.3.1.1 Types of Typhoons

Super-typhoons are very destructive. They are defined as typhoons with winds over 150 miles per hour. Such storms produce horizontal rain and can measure several hundred miles across, cover thousands of square miles and reach an altitude of almost ten miles. The largest storm on record, the 1979 typhoon Tip, produced gale force across a 650 mile area. The power generated by a major hurricane or typhoon is said to be equal to half a million nuclear bombs. The power of an average storm is said to be equal to 1.5 trillion watts, the equivalent to about half the world's entire electrical generating capacity.

Atlantic storms and hurricanes are defined as: 1) a tropical depression; 2) a tropical storm (less than 74 miles per hour); 3) Category One (between 74 and 95 miles per hour); 4) Category Two (between 95 and 110 miles per hour); 5) Category Three (between 111 and 130 miles per hour); 6) Category Four (between 131 and 155 miles per hour); and 7) Category Five (more than 155 miles per hour).

In Asia, different countries have different systems for identifying typhoons. Some countries such as Japan use numbers. Others use names (Facts and Details).

1.3.1.2 Typhoon Formation

Typhoons develop in an area of the tropical Pacific at latitude between 10 and 20 degrees north. They usually begin as westward-drifting waves of clouds

drawn into an area of low pressure around the Caroline Islands of Micronesia (between Hawaii and the Philippines in the Pacific) and grow into westward-moving tropical depressions.

As the clouds advance across the warm water they pick up energy as the water evaporates. At a critical point the clouds develop into a vortex of air that rotates in a counter-clockwise direction because of the Coriolis Effect. The water temperatures generally have to be above 80°F for all this to occur. The warmer the sea surface temperatures are, and the warmer, moist air there is, the stronger the storm will be.

A number of things have to come together for a typhoon to form. Among them are the presence of an initial low-pressure system that pulls the air to a particular spot in the ocean; the Coriolis effect spinning the air in a vortex; differences in wind speed in the upper and lower parts of the atmosphere that create horizontal shear forces; and the presence of cold air at 10 miles up in the atmosphere (Facts and Details).

1.3.1.3 Damage from Typhoons

Typhoons can cause millions or even billions of dollars in damage. Destruction levels can be particularly high when a storm stalls and strong, driving rains persist for hours or even days, or when the storm slams into mountains, producing particularly large amounts of rain. Some typhoons are so powerful they blow plankton and small sea creatures into the sky, where they float around on clouds.

1.3.2 Typhoons in China

Devastating typhoons strike southern and eastern provinces of China such as Guangdong, Fujian, Zhejiang, and south of Shanghai, uprooting trees, knocking down power lines, destroying houses, producing flash floods.

It is common for typhoons to hit Taiwan and then devastate the Fujian coast of China. Most typhoons track east and north and first strike places like Guam,

Saipan, Taiwan and Okinawa and then either move northward into Japan or Korea or move westward into the Philippines, Vietnam, or China.

Damages are more often the result of heavy rains than high winds. Typhoons tend to hit hardest in coastal areas that have elaborate dike networks and extensive practice in evacuating flood-prone areas.

In August 1956, a typhoon killed 4,900 people in Zhejiang Province. In 1997 Typhoon Winnie, a very powerful typhoon, struck the east coast of China, killing 250 people and causing \$2.2 billion worth of damage, in July 2001, a powerful typhoon called Utor killed 121 people in the Philippines and 46 in China. Therefore, the need to spend all the possible efforts in overcoming as much as possible the damages caused by typhoons is highly arisen, and many research works have been being adopted to perform safer places against these severe events (Facts and Details).

In this research work, 5 different typhoons are considered and studied in detail; which were affecting disparately the GTVT in Guangzhou city. These typhoons in chronological sequence are: Kammuri, Nuri, Hagupit, Molave, and Koppu. Three of these typhoons occurred before the total completion of the tower construction (namely: Kammuri, Nuri, and Hagupit), while the last two typhoons (Molave and Koppu) occurred after the construction of the tower has reached the top level.

1.3.2.1 Kammuri Typhoon

It occurred on 6th of August 2008, making landfall on south China, and having a maximum wind speed of 50 knots, and it was the ninth tropical cyclone to occur in the Western North Pacific in 2008.

Kammuri developed as a tropical depression on August 4 to the north of the island of Luzon with the depression then intensifying into a tropical storm. The following day it reached its peak wind speeds of 50 Knots which made it a weak severe tropical storm. It then made landfall on China in the western Guangdong province. This landfall made Kammuri weaken first into a tropical Storm that evening.

Heavy rains from Kammuri in Vietnam led to the loss of at least 100 lives and destroyed over 300 homes while damaging over 3,500 others. Figure 1.12 illustrates the path of Kammuri typhoon (Wikipedia).

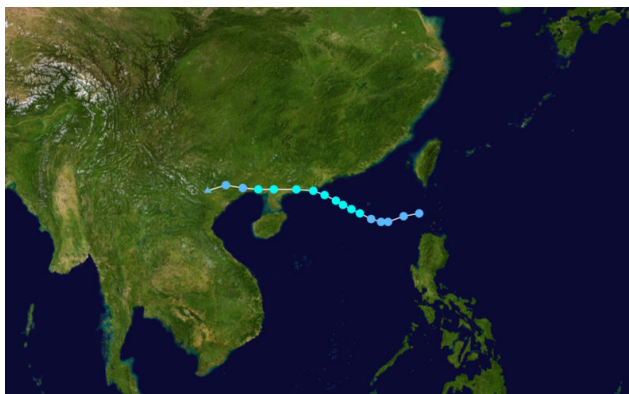


Figure 1.12. Kammuri typhoon path.

1.3.2.2 Nuri Typhoon

Typhoon Nuri formed as a tropical depression on August 17 then designating it as tropical storm Nuri the next day. It reached typhoon status later that day. Nuri then made landfall in the Philippines as a typhoon on August 20 leaving at least 10 people dead and 11 injured. Then it emerged into the South China Sea the next day and started moving towards Southern China, and then it moved closer towards Hong Kong and made a direct hit on Hong Kong as a typhoon.

On August 20 as Typhoon Nuri moved away from the Philippines towards southern China, The Hong Kong Observatory (HKO) issued the Standby Signal No. 1 as Typhoon Nuri was centered within 800 kilometers of Hong Kong. Late the next day the HKO issued the Strong Wind Signal No. 3 as Typhoon Nuri had tracked closer towards Hong Kong. On August 22, the HKO issued the Northwest Gale or Storm Signal No. 8. Later that day the HKO hoisted the Increasing Storm Signal No. 9 at 13:40 (HKT). The HKO then warned that they

would be forced to hoist the Hurricane Signal No. 10. Figure 1.13 illustrates the path of Nuri typhoon (Wikipedia).

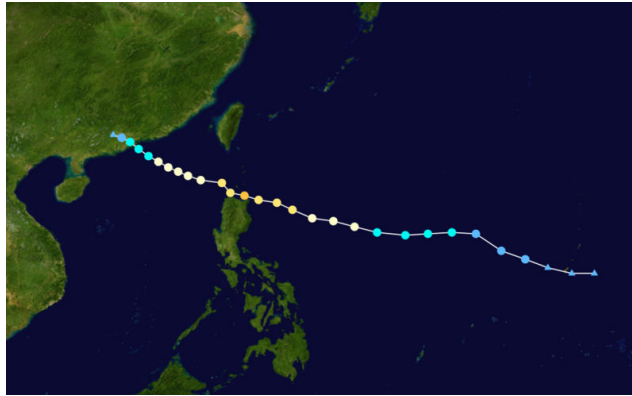


Figure 1.13. Nuri typhoon path.

1.3.2.3 Hagupit Typhoon

On the 14th of September 2008, a tropical disturbance formed to the northeast of Guam, and over the next few days it slowly developed as it moved westwards towards the Philippines. On later September 19, the depression was upgraded to a tropical storm. On September 20 the Hagupit had intensified into a severe tropical storm. On later September 22 Hagupit intensified into a Category 4 typhoon as Hagupit was approaching southern China. Hagupit struck Guangdong Province with this intensity, becoming the first known typhoon to hit Guangdong province as a category 4. Figure 1.14 illustrates the path of Hagupit typhoon (Wikipedia).

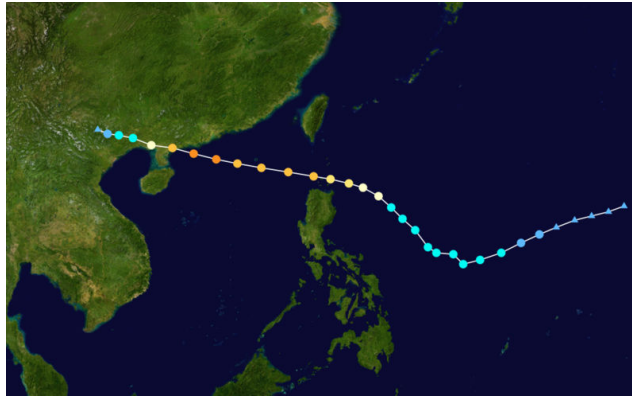


Figure 1.14. Hagupit typhoon path.

1.3.2.4 Molave Typhoon

On the 10th of July 2009, an area of disturbed weather persisted about 280 km, to the southeast of Yap. (Yap is an island in the Caroline Island of the western Pacific Ocean). Then the disturbance had dissipated, but late on July 13, it redeveloped rapidly and early. The next day the disturbance was designated as a Tropical Depression. The Depression continued to develop and on morning of July 18, Molave was updated as a Typhoon. Later that day, Molave quickly moved into the South China Sea. On the 19th of July Molave made its first landfall on Shenzhen city. In the afternoon, as Molave moved through China, final warning was issued since Molave weakened into a Tropical depression. Figure 1.15 illustrates the path of Molave typhoon (Wikipedia).

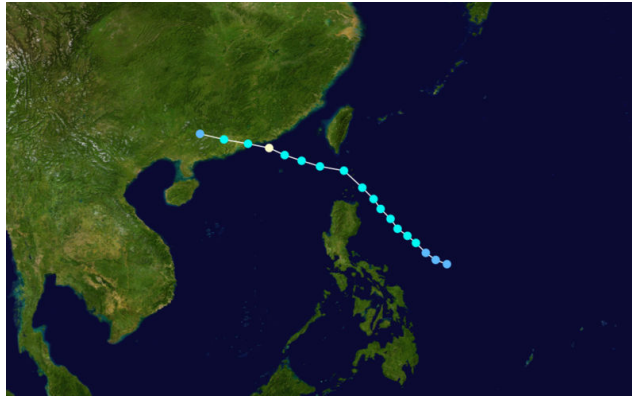


Figure 1.15. Molave typhoon path.

1.3.2.4 Koppu Typhoon

On the 9th of September 2009, an area of convectional cloudiness associated with the monsoon trough formed 370 km to the northwest of Palau. Early of September 13, it was upgraded into a tropical storm and assigned its international name Koppu. On the 14th, it was reported that Koppu had intensified to a minimal typhoon.

In Luzon, a 48 hour rainfall was experienced. In and Mindanao, a 24 hour rainfall was also experienced due to Nando's enhancing southwest monsoon. About 10 provinces were raised in signal warning no.1 from September 12 to September 13. The storm then caused major flood in Luoding-China. The path of the typhoon is illustrated in Figure 1.16 (Wikipedia).

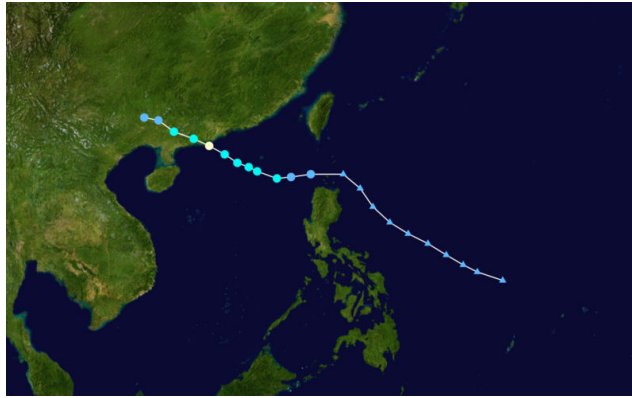


Figure 1.16. Koppu typhoon path.

Figure 1.17 presents the legend for the Figures 1.12 to 1.16 based on Saffir-Simpson Hurricane scale; which provides classification criteria of the typhoons based on the accompanied wind velocity (Wikipedia).












Saffir-Simpson Hurricane Scale					
 Tropical depression	0–39 mph	0–62 km/h	 Category 3	111–130 mph	178–209 km/h
 Tropical storm	39–73 mph	63–117 km/h	 Category 4	131–155 mph	210–249 km/h
 Category 1	74–95 mph	119–153 km/h	 Category 5	≥156 mph	≥250 km/h
 Category 2	96–110 mph	154–177 km/h	 Unknown		
Storm type					
 Tropical cyclone					
 Subtropical cyclone					
 Extratropical cyclone / Remnant low / Tropical disturbance					

Figure 1.17. Saffir-Simpson Hurricane scale.

Chapter 2

Fundamental Theories of Signal Processing

2.1 Introduction

In civil engineering applications, many practical and robust non-destructive techniques for evaluating the structures were developed aiming at assessing the structural performance after being exposed to severe dynamic excitations. These techniques involve two main components; data acquisition, and signal processing and interpretation. When field measurements are performed on modern tall buildings to measure their dynamic characteristics and responses, signal processing is an indispensable step for extraction of important information from raw signals.

One of the most recently used simple techniques is the so called Modal Analysis; which studies the dynamic properties or “structural characteristics” of a mechanical structure under dynamic excitation (namely: natural frequency, mode shapes, and damping).

The natural frequency is the frequency at which any excitation produces an exaggerated response. This is important to know since excitation close to a structure’s natural (resonant) frequency will often produce adverse effects. These generally involve excessive vibration leading to potential fatigue failures,

damage to the more delicate parts of the structure or, in extreme cases, complete structural failure.

Modal analysis refers to a complete process including both an acquisition phase and an analysis phase. The structure is excited by external forces such as an impact hammer or shaker. In this case, the talk is about experimental modal analysis. While, operational modal analysis complements traditional modal analysis methods. It only measures the response of test structures under actual operating conditions. It is used to test cars, airplanes, wind turbines and any other applications that are difficult or even impossible to excite by external force, owing to boundary conditions or sheer physical size. Modal testing results can also be used to correlate simulation analysis and create a ‘real-life’ simulation model.

In this chapter; two methods of operational modal analysis are presented. The first is the Frequency domain decomposition method, and the second is the Hilbert-Huang Transform method. A technique to improve the second method by filtering approach is discussed in detail. At the end of the chapter some various criteria of damage assessment for structures based on the parameters obtained from operational modal analysis methods are also discussed.

2.2 Frequency Domain Decomposition

Frequency domain decomposition (FDD) is an operational modal analysis method which is used for the modal identification of systems considering the output data only. In such methods it is assumed that the input forces are stochastic in nature, which is usually the case for civil engineering structures like buildings, towers, bridges and offshore structures. These structures are mainly loaded by ambient forces like wind, waves, traffic or seismic loads and as the input forces to the structure are not measured, special attention is paid to identify the modal parameters of structures; such as natural frequencies, damping ratios, and mode shapes by performing special algorithms that deals only with the output data; which are simply the measured response of the structure upon exciting to one or more of the aforementioned loads by well

established SHM system (Brincker et al. 2000, Brincker et al. 2001, and Brincker et al. 2001).

The FDD technique is an extension of the classical frequency domain approach, which is referred to as Basic Frequency Domain (BFD) or the peak picking technique (Le and Tamura 2009). The classical approach is based on the simple signal processing taking in consideration that well separated modes can be estimated directly from the power spectral density matrix at the peak. The classical technique gives reasonable estimates for natural frequencies and mode shapes if the modes are quit separated. However, in the case of close modes it would be difficult to detect close modes, and if they are detected the estimates becomes heavily biased. Furthermore, damping estimates is uncertain in all cases. The FDD technique is able to overcome all of the disadvantages of the classical approach.

In FDD the relation between the unknown inputs and the measured response is expressed as:

$$G_{yy}(j\omega) = \overline{H}(j\omega)G_{xx}(j\omega)H(j\omega)^T \quad (2.2.1)$$

Where; $G_{xx}(j\omega)$ is the $r \times r$ Power Spectral Density (PSD) matrix of the input, r is the number of inputs, $G_{yy}(j\omega)$ is the $m \times m$ PSD matrix of the responses, m is the number of responses, $\overline{H}(j\omega)$ is the complex conjugate of $H(j\omega)$, which is the $m \times r$ Frequency Response Function (FRF) matrix, and can be written as:

$$H(j\omega) = \sum_{k=1}^n \frac{R_k}{j\omega - \lambda_k} + \frac{\overline{R_k}}{j\omega - \overline{\lambda_k}} \quad (2.2.2)$$

Where n is the number of modes, λ_k is the pole, and R_k is the residue $= \phi_k \gamma_k^T$; where, ϕ_k, γ_k^T are the mode shape and modal participation vectors respectively.

Assuming white noise input then its PSD is a constant matrix $= C$. Then equation 1 becomes:

$$G_{yy}(j\omega) = \sum_{k=1}^n \sum_{s=1}^n \left[\frac{R_k}{j\omega - \lambda_k} + \frac{\overline{R_k}}{j\omega - \overline{\lambda_k}} \right] C \left[\frac{R_s}{j\omega - \lambda_s} + \frac{\overline{R_s}}{j\omega - \overline{\lambda_s}} \right]^H \quad (2.2.3)$$

Where; the superscript H denotes complex conjugate and transpose. Multiplying the two partial fractions and mathematically rearranging the formula, the output PSD could be written as:

$$G_{yy}(j\omega) = \sum_{k=1}^n \frac{A_k}{j\omega - \lambda_k} + \frac{\overline{A_k}}{j\omega - \overline{\lambda_k}} + \frac{B_k}{-j\omega - \lambda_k} + \frac{\overline{B_k}}{-j\omega - \overline{\lambda_k}} \quad (2.2.4)$$

Where A_k is the k^{th} residue matrix of the output PSD. At certain frequency ω only a limited number of modes will contribute significantly, then for the case of lightly damped structure the response spectral density can be written as:

$$G_{xy}(j\omega) = \sum_{k \in Sub(\omega)} \frac{d_k \phi_k \phi_k^T}{j\omega - \lambda_k} + \frac{\overline{d_k \phi_k \phi_k^T}}{j\omega - \overline{\lambda_k}} \quad (2.2.5)$$

Where d_k is a scalar constant

The estimate of the output PSD $\hat{G}_{yy}(j\omega_i)$ known at discrete frequencies $\omega = \omega_i$ is then decomposed by taking the Singular Value Decomposition (SVD) of the matrix:

$$\hat{G}_{yy}(j\omega_i) = U_i S_i U_i^H \quad (2.2.6)$$

Where the matrix $U_i = [u_{i1}, u_{i2}, \dots, u_{im}]$ is a unitary matrix for the singular vector u_{ij} , and S_i is a diagonal matrix holding the scalar singular values s_{ij} . Points near the peak of the k^{th} mode will be dominated to the mode or the close mode in the spectrum.

If only the k^{th} mode is dominated, the mode shape will be estimated as the first singular vector u_{ij} in the matrix U_i . The PSD function of response around the peak will then be determined by the estimated mode shape. If a singular vector has a relatively high modal assurance criterion value, the singular value u_{ij} of the vector will be involved in the SDOF density function. When the SDOF density functions around the peaks of the PSD are determined, the natural frequency and damping ratio would be obtained by analyzing the function. On the contrast, if two modes are dominating, the singular vector can also make a good estimation to the mode shape. The natural frequency and the damping ratio can be obtained from the SDOF functions around the peaks of the PSD by one of the following two formulae:

$$\partial = \left[\ln \frac{y_i}{y_{i+k}} \right] / k \quad (2.2.7)$$

$$\partial = \left[\ln \frac{y''_i}{y''_{i+k}} \right] / k \quad (2.2.8)$$

Where ∂ is the logarithmic decrement, k is the number of cycles chosen to consider the peak value, y_i and y_{i+k} are the peak values of displacement of the i^{th} and $i+k^{th}$ cycle respectively, y''_i and y''_{i+k} are the peak values of acceleration of the i^{th} and $i+k^{th}$ cycle respectively. The damping ratio (ζ) can be represented as the following in terms of logarithmic decrement.

$$\xi = \frac{\delta}{\sqrt{\delta^2 + 4\pi^2}} \quad (2.2.9)$$

Then the undamped natural frequency f of the system can be calculated from the damped natural frequency f_d as follows:

$$f = \frac{f_d}{\sqrt{1 - \xi^2}} \quad (2.2.9)$$

2.3 Hilbert-Huang Transform

For tall structures, the most critical loads that should be considered in the design process are the wind loads. This fact raises the need for identifying the modal parameters of the structure such as natural frequencies and modal damping ratios; which are the most important parameters to be determined when designing against strong winds.

Knowledge of these properties is essential to understand and interpret with confidence the response of a high raised building to strong wind. Therefore, field measurements are always desirable to be carried out for providing such information; to check the modal parameters used in the design, to understand the actual dynamic performance of the structure under strong winds, and to develop better design theories for future tall structures.

The ambient vibration measurements in the field processed by the fast Fourier transform (FFT) based method are probably the most popular way for identifying natural frequencies and modal damping ratios. However, this approach can identify building natural frequencies quite accurately but often overestimates building modal damping ratios because of bias errors involved in the spectral analysis (Xui et al. 2003). Moreover when processing the field measurements obtained for a tall building under different wind speeds it then becomes more questionable to use the FFT based method to identify the modal

damping ratios, especially when the building response to strong winds is non-stationary.

In 1998 The Hilbert–Huang transform (HHT) method was proposed (Huang et al. 1998). This method combines the empirical mode decomposition method with the Hilbert transform (HT). The most powerful feature of the HHT method is the capability of analyzing nonlinear and non-stationary time histories in the frequency-time domain.

The Hilbert transform $y(t)$ for an arbitrary time series $x(t)$ is defined as:

$$y(t) = \frac{1}{\pi} P \int_{-\infty}^{\infty} \frac{x(\tau)}{t - \tau} d\tau \quad (2.3.1)$$

Where; P is the Cauchy principal value. Given; $y(t)$ is the complex conjugate of the time series $x(t)$; then the analytical signal associated with $y(t)$ is defined as:

$$z(t) = x(t) + iy(t) = a(t)e^{i\theta(t)} \quad (2.3.2)$$

Where $a(t)$ and $\theta(t)$ are the instantaneous amplitude, and the phase angle respectively and are defined in the following two formulae:

$$a(t) = \sqrt{(x(t))^2 + y(t)^2} \quad (2.3.3)$$

$$\theta(t) = \tan^{-1} \frac{y(t)}{x(t)} \quad (2.3.4)$$

Then the instantaneous frequency $\omega(t)$ could be defined as:

$$\omega(t) = \frac{d\theta(t)}{dt} \quad (2.3.5)$$

The previous definition is only applicable on the mono-component signals in which a single dominant harmonic component is processed. Therefore a straightforward application of the Hilbert transform to the multi-frequency signal will give some negative values for the instantaneous frequencies. The Empirical Mode Decomposition (EMD) method has been then proposed by (Huang et al. 1998) to overcome this limitation.

The EMD data processing method is generally based on decomposing the set of data into several intrinsic mode functions (IMF's) by a procedure called the sifting process. This procedure has two main purposes; eliminating riding waves and making the profile of the signal more symmetric about the local zero-mean line (Lei et al. 2009, and Cheng et al. 2008).

The steps for conducting the sifting process procedure on a signal $y(t)$ can be summarized as following; first, constructing the upper and lower envelope of $y(t)$ by connecting its local maxima and local minima through a cubic spline, then; the mean of the two envelopes is computed and subtracted from the original time history. The difference between the original time history and the mean value is called the first IMF if it satisfies two main conditions:

(1) within the data range, the number of extrema and the number of zero-crossings are equal or differ by one only.

(2) the envelope defined by the local maxima and the envelope defined by the local minima are symmetric with respect to the mean.

The difference $d(t)$ between the original signal $y(t)$ and the mean of the upper envelop $e_{\max}(t)$ and lower envelop $e_{\min}(t)$ is calculated as in the following equation:

$$d(t) = y(t) - \frac{e_{\max}(t) + e_{\min}(t)}{2} \quad (2.3.6)$$

Next iteration then started by setting $d(t)$ as the new signal $y(t)$, and applying the same procedure again until $d(t)$ becomes a zero mean process, or by using a stopping criterion based on the computed standard deviation of two consecutive sifting results as follows:

$$SD = \sum_{t=0}^T \left[\frac{|d_{k-1}(t) - d_k(t)|^2}{d_{k-1}^2(t)} \right] \quad (2.3.7)$$

Where $d_{k-1}(t)$ and $d_k(t)$ are the two computed consecutive sifting results $k-1$ times and k times, respectively (Wu and Huang 2009, and Wu and Chung 2009).

The final $d(t)$ then treated as a new time history and subjected to the same sifting process, to give the second IMF. The EMD procedure continues until the residue becomes less than a predetermined value of consequence, or the residue becomes a monotonic function. The original time history $y(t)$ is finally expressed as the sum of the IMF components (c_i) plus the final residue (r_n) as follows:

$$y(t) = \sum_{i=1}^n c_i + r_n \quad (2.3.8)$$

Hilbert transform then can be applied on the obtained IMF components aiming at computing the corresponding instantaneous frequency according to Equation (2.3.5). Then the original time history can be expressed as the real part (RP) of the summation of Hilbert transforms for all the IMF components:

$$y(t) = RP \sum_{j=1}^N a_j(t) \exp\left(i \int \omega_j(t) dt\right) \quad (2.3.9)$$

Where $a_j(t)$ and $\omega_j(t)$ are respectively the instantaneous amplitude and frequency of the i^{th} IMF. It is shown in the last equation that the amplitude is a function of both time and frequency, from which the frequency-time distribution of the amplitude is designated in the Hilbert transform, and the

inherent characteristics of a nonlinear or non-stationary time history can be identified.

It worth's noting that the final residue is neglected in Equation (2.2.2), because it is either a monotonic function or a constant, and the energy involved in the residual trend could be over powering. Therefore, considering the uncertainty of longer trend and the information contained in the other low energy and higher frequency components, the final non IMF component should be omitted (Tan 2010).

The advantages provided by HHT method in signal processing are various and can be summarized as follows: energy leakage problem does not occur in the process of the HHT, which means the HHT is able to provide a more accurate description of the signal. In addition, the HHT allows a direct algorithmic analysis of the signal. Its computation is more efficient than that of other methods. This merit of the HHT enables it to process large-scale data that the other methods are not able to deal with efficiently. All these advantages of the HHT make it more ideal for analyzing the non-linear and non-stationary signals.

Consequently, some successful applications of the HHT have been achieved recently. For example, Yang and Lei (Yang and Lei 2000) applied the HHT to the structural health condition monitoring of a benchmark structure. Yang and Suh (Yang and Suh 2004) used the HHT to analyze the non-linear response of a cracked rotor. Liu et al. (Liu et al, 2006) diagnosed a gearbox with the aid of the HHT. However, the HHT also shows deficiencies in practice (Peng et al. 2005). For example, as the EMD cannot decompose the narrowband multi-harmonic signals, the IMF sometimes covers a too wide frequency range and even generates unidentified information occasionally. These deficiencies significantly limit the further application of the HHT are mainly originated from the EMD. The purpose of the EMD is to decompose a signal into a number of simple intrinsic oscillatory modes, rather than decomposing the signal into a series of monocomponent functions like what Fourier transform does. Moreover, it has been proved that the EMD cannot decompose the narrowband multi-harmonic signal (Yang 2008). So, the derived IMFs often comprise

multiple frequency components; which means that the monocomponents in the signal are not completely isolated from each other by the EMD (Kerschen et al. 2008).

2.3.1 Improved HHT by filtering approach

In order to overcome the deficiencies related to HHT method an improvement to the method was proposed by (Yang 2008) based on employing an adaptive band-pass filter to extract the monocomponents from the signal. In this technique the principal frequency components are detected from the PSD spectrum of the signal by using the peak detection method. After that an adaptive band-pass filter with frequency bandwidth of f_b is designed to extract the monocomponent functions from the signal. The central frequency f_0 of the filter is adaptively equal to the frequency of the principal frequency component being considered. The upper cut-off frequency (f_{upper}) and lower cut-off frequencies (f_{lower}) of the filter are:

$$f_{upper} = f_0 + \frac{f_b}{2} \quad (2.3.1.1)$$

$$f_{lower} = f_0 - \frac{f_b}{2} \quad (2.3.1.2)$$

To avoid morbid solutions the following two boundary conditions are applied:

- a) If $f_{upper} = 0.5f_s$ then $f_{upper} = 0.5f_s$
- b) And if $f_{lower} < 0$ then $f_{lower} = 0$

Where; f_s represents the sampling frequency of the signal. The filter coefficients can be readily derived by using a MATLAB (Matlab 2004) program (namely 'firls.m'), which is available in the MATLAB toolbox of signal processing.

The monocomponent functions (1, 2,...,k) then extracted using this filter. But in order to keep the energy reserved, the power of the derived monocomponent functions is then calibrated by the following equation:

$$y_j = \hat{y}_j \sqrt{\frac{\hat{A}_j}{A_j}} \quad (j=1,2,\dots,k) \quad (2.3.1.3)$$

Where; y_j is the calibrated function, \hat{A}_j is the power spectral density of the monocomponent function \hat{y}_j , and A_j is the j^{th} principal frequency component.

The EMD is then employed to extract the new IMF from y_j . The first IMF will be almost a true monocomponent function. Then it is considered as a new IMF and the other IMFs as part of the residue of the whole EMD.

Having obtained all new IMFs corresponding to the selected principal frequency components, the instantaneous time-frequency features of the signal can be extracted by the HHT (Guo et al. 2009, and Tan 2010).

2.4 Damage Detection and Assessment

Various damage identification algorithms have been developed based on operational modal analysis for structural assessment and identification purposes. These algorithms are dealing mainly with three key problems; detection of the presence of damages, detection of the structural damage locations and estimation of the damage extents. For the last two stated problems, most of the existing methods are two-stage algorithm; in which damage locations are detected at first, and then damage extents are estimated. Generally, the first step may be more important, but probably more difficult (Lin et al. 2005).

For the damage detection problem, Chen and Garba calculated the residual force vectors; by picking out the degrees of freedom (DOFs) with non-zero components in the residual force vectors (Chen and Garba 1998), the damage

locations can then be identified. Ricles and Kosmatka employed the same methodology by further considering the variation of the mass matrix due to damages (Ricles and Komatka 1992). By employing control-based Eigen structure assignment techniques, a subspace rotation algorithm was proposed; in which the damage vector and relative rotation angle are used to identify the DOFs affected by damage.

Another method was proposed by Casciati; which uses response surface models for the solution of SHM problems. It is based on detecting a change in the statistical distribution of the error associated to the function that approximates the relationship among measurements taken at different sensors locations across the structure by a formulated damage index. The method was applied to a masonry wall affected by distributed cracks, and the results from the ambient vibration tests showed that the method is able to resemble the correct damage scenario, before the retrofitting operation. It also identifies the parts of the structure where the retrofit restored a monolithic behaviour, thus enabling an evaluation of the efficiency of the retrofitting operation (Casciati 2005, and Casciati 2010).

More methods in concept using best achievable eigenvectors were put, however, to identify the damaged structural members directly. Another important and interesting category uses the characteristics of the flexibility matrix. Unlike the stiffness matrix, the flexibility matrix can be formed more accurately through the usage of first several order experimental modal data. The flexibility matrix was used to multiply the pre-damaged finite element method stiffness matrix to determine the damage locations, and the damage locations were detected through the variation of the flexibility matrices before and after damage. An important advantage in this category is that the usage of the analytical model can be avoided (Hu et al. 2001).

Although there has been much development in this area, as to practical applications, many difficulties should be overcome, such as the measurement uncertainty and inadequate test data, etc. Also, another important difficulty stems from the difference between the analytical models and real structures. Generally, the error in analytical model may be classified into the following

several aspects: (1) approximation in boundary conditions of analytical models may make the analytical stiffness matrix deviate from the practical one, (2) connectivity conditions of elements in analytical models cannot reflect the real connective state of structural members, (3) some important material parameters in analytical models, e.g. Young's modulus, may not represent the real ones, (4) there are many stiffness sources in practical structures, which are ignored in analytical models due to computational capacity and (5) the coarse mesh or unsuitable element types can cause the errors in analytical models.

Most of the approaches mentioned previously, except for those using the flexibility matrix, however, employ the analytical models. For the practical applications, it may be more attractive to avoid employing too much information of the analytical models. Hence, the kinds of algorithms presented in this section are not dependent on analytical models; they are rather dependent on the modal parameters i.e. natural frequency, damping ratios, and mode vectors, which are obtained by the operational modal analysis that deals only with the output measurements of a structure subjected to external forces. It is sufficiently used instead of classical mobility-based modal analysis for accurate modal identification under actual operating conditions, and in the situations where it is difficult or even impossible to artificially excite the structure.

2.4.1 Modal Assurance Criterion

The historical development of the modal assurance criterion originated from the need for a quality assurance indicator for experimental modal vectors that are estimated from measured frequency response functions. The standard of the late 1970s, when the modal assurance criterion was developed, was the orthogonality check. The orthogonality check, however, coupled errors in the analytical model development, the reduction of the analytical model and the estimated modal vectors into a single indicator, and it was not always the best approach.

The original development of the modal assurance criterion was modeled after the development of the ordinary coherence calculation associated with

computation of the frequency response function. It is important to recognize that this least squares based form of linear regression analysis yields an indicator that is most sensitive to the largest difference between comparative values (minimizing the squared error) and results in a modal assurance criterion that is insensitive to small changes. In the original thought process, this was considered an advantage since small modal coefficient values are often seriously biased by frequency response function measurements or modal parameter estimation errors.

In the internal development of the modal assurance criterion at the University of Cincinnati, Structural Dynamics Research Lab (UCSDRL), a little modal assurance criterion (Little MAC), a big modal assurance criterion (Big MAC) and a multiple modal assurance criterion (Multi-MAC) were formulated as part of the original development. Little MAC and Multi-MAC were primarily testing methods and are not discussed further here. The modal assurance criterion that survives today is what was originally identified as Big MAC. Since the “Big Mac” acronym was already in use at that time, MAC is the designation that has persisted (Allemang 2003).

The MAC is defined as a scalar constant relating the degree of consistency (linearity) between one modal and another reference modal vector as follows:

$$MAC(x, p) = \frac{\left[\sum_{j=1}^N (\phi_x)_j \cdot (\phi_p)_j \right]^2}{\left[\sum_{j=1}^N (\phi_x)_j^2 \right] \left[\sum_{j=1}^N (\phi_p)_j^2 \right]} \quad (2.4.1.1)$$

This procedure results in a matrix $m_x \times m_p$. When considering two modes: one as the damaged mode and the other as the undamaged mode; m_x will be the number of undamaged modes and m_p is the number of damaged modes, $(\phi_x)_j$ and $(\phi_p)_j$ are, respectively, the j^{th} mode shape of the undamaged (x) and damaged structure (p), and N is the number of included coordinates.

The MAC takes on values from zero which represents no consistent correspondence, to one which represents a consistent correspondence. In this manner, if the modal vectors under consideration truly exhibit a consistent linear relationship, the MAC should approach unity and the value of the modal scale factor can be considered reasonable.

2.4.2 Coordinate Modal Assurance Criterion

An extension of the MAC is the Coordinate Modal Assurance Criterion (COMAC). The COMAC attempts to identify which measurement degrees of freedom contribute negatively to a low value of MAC. The COMAC is calculated over a set of mode pairs, damaged modes versus undamaged modes, or they could be experimental modes versus analytical modes. The two modal vectors in each mode pair represent the same modal vector, but the set of mode pairs represents all modes of interest in a given frequency range. For two sets of modes that are to be compared, there will be a value of COMAC computed for each (measurement) degree of freedom (Roitman and Viero 1997). The (COMAC) is calculated using the following approach, once the mode pairs have been identified with MAC:

$$COMAC(j) = \frac{\left[\sum_{L=1}^{L \max} ({}_j\phi_{x,L})({}_j\phi_{p,L}) \right]^2}{\left[\sum_{L=1}^{L \max} ({}_j\phi_{x,L})^2 \right] \left[\sum_{L=1}^{L \max} ({}_j\phi_{p,L})^2 \right]} \quad (2.4.2.1)$$

Where ${}_j\phi_{x,L}$ and ${}_j\phi_{p,L}$ are, respectively, the j^{th} component of the undamaged structure mode shape ϕ_x and the damaged structure mode shape ϕ_p , corresponding to the mode shape L .

This complete procedure results in a list of COMAC values of magnitude between zero and unity; the unity indicates full similitude between the two

considered mode shapes, while if they suffer some differences the value will be less than unity down to zero indicating the level of consistency.

2.4.3 Modal Correlation Coefficient

Since the MAC is a magnitude based coefficient, it has one shortcoming; that it is not suited for detecting shape differences in mode shapes if the corresponding mode shapes are minimal. This deficiency creates a problem in many damage detection applications where the objective is to detect the kinks in mode shapes.

The formation of a severe crack in the middle of a simply supported beam can change its first mode shape from a smooth curve to another one with a kink formulated in the middle and relatively straight sides as shown in Figure 2.1. This change can be indicative of a catastrophic defect. Nevertheless, the corresponding MAC for the two mode shapes shown in the figure is almost unity, which indicates relatively identical mode shapes. Therefore, in this case, the severity of the difference is not well expressed by MAC (Roitman and Viero 1997).

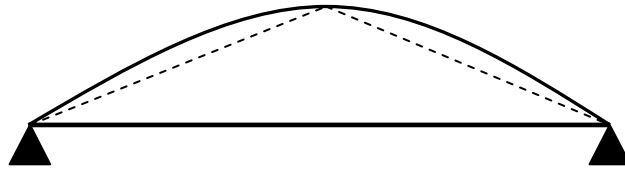


Figure 2.1. Two single span modes.

The need for a measure that accounts for kink formations is evident, and this new measure should satisfy the following minimal conditions:

- a. It should be sensitive to slope discontinuities even if magnitude changes are negligible.
- b. It should maintain its sensitivity to kink formations even if they exist in a small part of a relatively large structure.

- c. It should maintain the orthogonality property of MAC.
- d. It should be as sensitive as MAC to magnitude changes that are not accompanied by kinks.

Kinks are points at which slope discontinuities exist, and to detect a kink, the value of the incidental change of slope can be used as an indicator. If a single kink exist in a mode shape, the slope changes at the location of the kink is expected to be much larger in magnitude than at any other location on the structure. Therefore, the Modal Correlation Coefficient (MCC) for x and p mode shapes is defined as:

$$MCC(x, p) = MAC(x, p) \cdot k(x, p) \quad (2.4.3.1)$$

In which $k(x, p)$ is the kink factor which is a real coefficient that compares the existence of kinks in x and p , and it is defined using the following equations:

$$k(x, p) = \frac{\min(C^x, C^p)}{\max(C^x, C^p)} \quad (2.4.3.2)$$

In which;

$$C^x = \max[|c_2^x|, |c_3^x|, \dots, |c_{n-2}^x|, |c_{n-1}^x|] \quad (2.4.3.3)$$

$$C^p = \max[|c_2^p|, |c_3^p|, \dots, |c_{n-2}^p|, |c_{n-1}^p|] \quad (2.4.3.4)$$

$$c_i^x = \frac{x_{i+1} - x_i}{d_i} - \frac{x_i - x_{i-1}}{d_{i-1}} \quad (2.4.3.5)$$

$$c_i^p = \frac{p_{i+1} - p_i}{d_i} - \frac{p_i - p_{i-1}}{d_{i-1}} \quad (2.4.3.6)$$

Where n is the number of measurement points, d_i is the incremental distance between the points at which measurements i and $i+1$ are obtained such that the

summation of all distances in the vector is equal to the total span length of the structure of interest.

The previous equations prove that MAC is a special case of MCC to which it reduces when the smoothness of the two mode shapes are identical ($k=1$).

The effectiveness of MCC is dependent on the smoothness of mode shapes. Since experimental mode shapes are obtained using vibration measurements at discrete points, the smoothness of mode shapes is a function of a spatial distance between these points. As measurement points get closer, mode shapes look smoother. Therefore, MCC is more sensitive to kinks when measurement points are closely spaced.

Chapter 3

Analysis of GTVT Response to Wind Pressure by FDD Method

3.1 Introduction

In this chapter; the behavior of the GTVT when exposed to extreme wind events is studied, through investigating the dynamic response of the tower to five different typhoons occurred at different times and various levels of the tower construction. Three of the five typhoons occurred when the total height of the tower had not been reached (namely: Kammuri, Nuri, and Hagupit typhoons), and the response to these typhoons were recorded by the SHM system applied to the structure in the in-construction stage. The other two typhoons (namely: Molave and Koppu typhoons) occurred when the construction of the tower was completed and the final level was reached.

Figure 3.1 depicts the tower state of construction at various times, and Table 3.1 lists the five studied typhoons with the corresponding date of occurrence for each, and the achieved height of construction at that date for both the inner tube and outer tube of the tower.

The wind prosperities of each typhoon are then presented; aiming at correlating them with modal prosperities (i.e. natural frequencies and damping ratios) of the tower resulted upon the exposure to these extreme wind events.

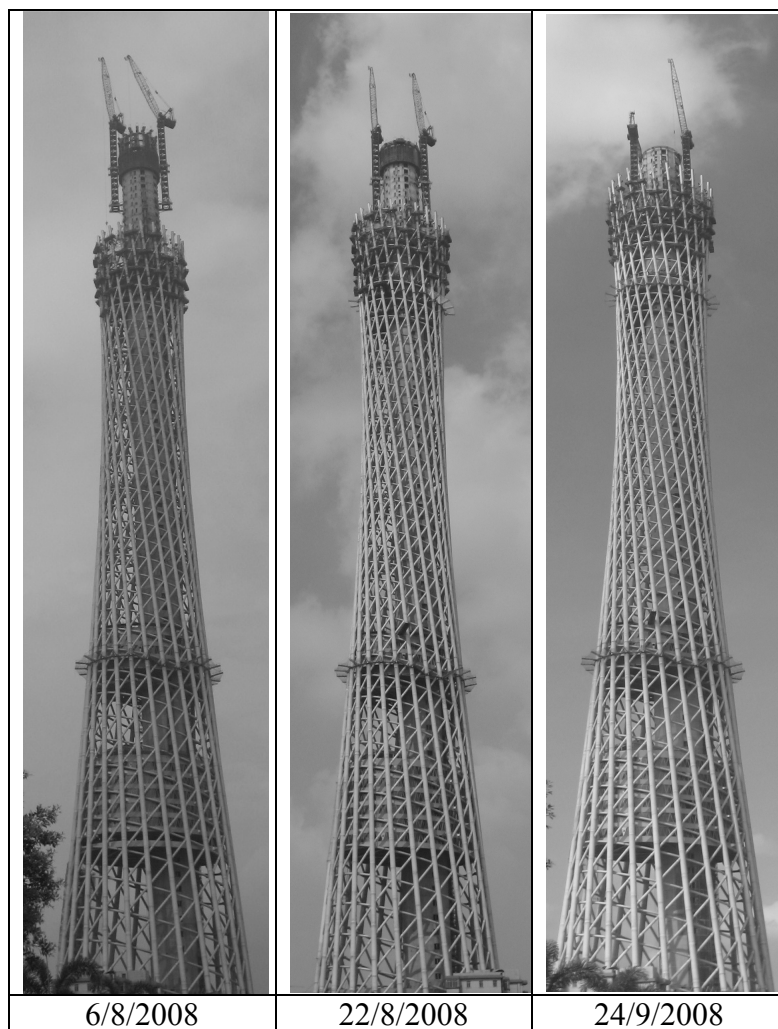


Figure 3.1. The GTVT construction level progress.

Table 3.1. Tower construction heights at each typhoon

Typhoon	Date of occurrence	Height of inner tube (m)	Height of outer tube (m)
Kammuri	6/8/2008	433.2	376.0
Nuri	22/8/2008	443.6	386.4
Hagupit	24/9/2008	448.8	402
Molave	18/7/2009	454	450
Koppu	15/9/2009	454	450

3.2 Typhoon Kammuri

3.2.1 Wind properties

On the 6th of August 2008; the day in which Kammuri typhoon occurred, the time histories of wind velocity and direction recorded by the anemometer placed on the top level of the tower were registered. These data are considered and analyzed in this subsection.

Figure 3.2 shows the one hour mean wind velocities measured at the top of the tower for the whole 24 hours of that day. It can be seen that the maximum one hour mean wind velocity was 26.8 m/s, which was calculated for the period of time between 5:00 and 6:00 pm, while the maximum calculated 3-second gust wind speed at the tower top was 31.8 m/s for the period of time between 4:00 and 5:00 pm.

The corresponding wind rose diagram obtained using the directions measured by the same anemometer is shown in Figure 3.3. It is illustrated that the primary wind direction of kammuri typhoon was around the 90° which denotes east, as in the figure 0° denotes the north direction 180° south direction and 270° the west direction.

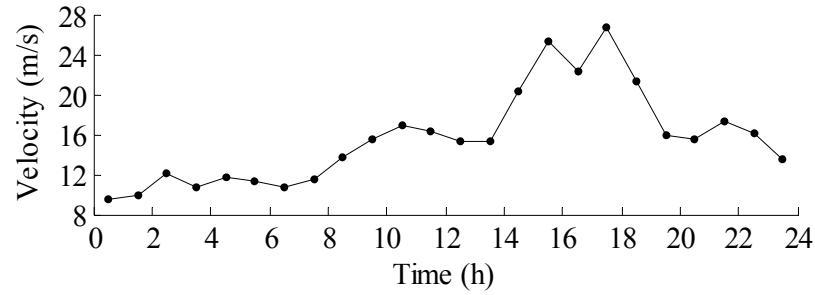


Figure 3.2. Wind mean velocity measured on 6/8/2008

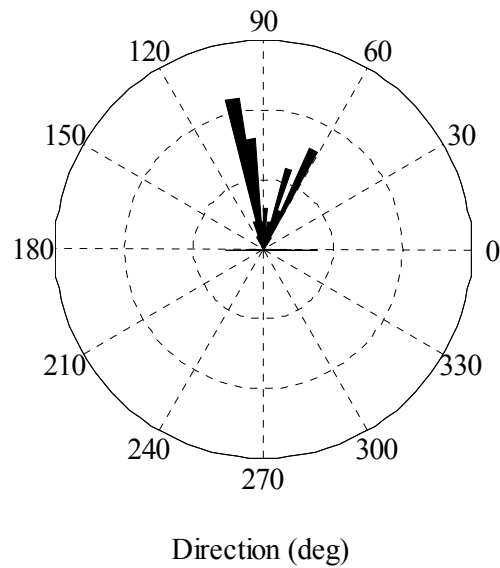


Figure 3.3. Wind rose diagram of Kammuri typhoon.

3.2.2 Response analysis and processing

The response of the tower was recorded by means of unidirectional accelerometers mounted on different heights of the inner tube. The heights of these monitoring points and sensors' numbering are listed in Table 3.2. The X

and Y directions in the table denote, respectively, the major and minor axis of the oval cross section shape of the tube.

In the case of Kammuri typhoon the data from the sensors 17-20 are not available, because at that time these sensors were not mounted; because the tower maximum height had not been reached.

The recorded time histories by sensors labeled from 1 to 16 for one sample hour (6:00 - 7:00 pm) of the same day are drawn in Figure 3.4. The sampling frequency of these data is 50 Hz. It could be clearly seen in the figure that the response is increasing when the elevation of the sensor increases, because the wind loading increases with the increase in altitude. Also the responses in the minor axis direction (left hand side of the figure) are slightly higher than those of the major axis (right hand side of the figure); this is caused by the higher stiffness imparted by the larger dimension of the cross section at the major axis direction. In addition, the main wind direction of the typhoon at the tower was closer to coincide with the minor axis than major axis, which made the wind pressure on the tower more effective in that direction.

Other available data during this typhoon is figured in Appendix A.

Table 3.2. Sensors labels, directions and heights.

Sensor's No.	Measuring direction	Height (m)	Sensor's No.	Measuring direction	Height (m)
1	Y	27.6	11	Y	272.0
2	X	27.6	12	X	272.0
3	Y	121.2	13	Y	334.4
4	X	121.2	14	X	334.4
5	Y	173.2	15	Y	386.4
6	X	173.2	16	X	386.4
7	Y	230.4	17	Y	443.2
8	Y	230.4	18	Y	443.2
9	X	230.4	19	X	443.2
10	X	230.4	20	X	443.2

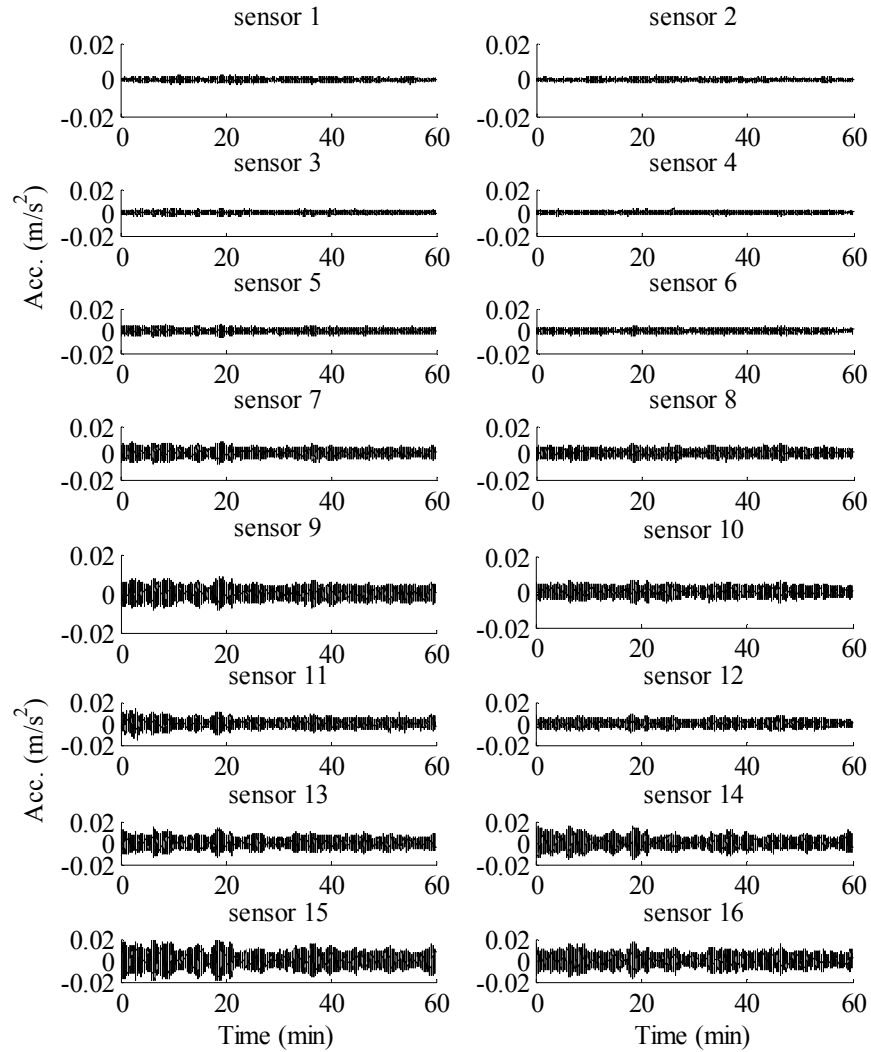


Figure 3.4. Time Histories of recorded response to Kammuri typhoon

The entire recorded time histories were processed by the FDD method aiming at detecting the modal properties of the tower and their variation with wind properties of different typhoons.

The ARTeMIS software for signal processing was utilized for data processing purposes by FDD method (ARTeMIS 1999), and calculating the natural frequencies and damping ratios for the entire obtained signal in this chapter.

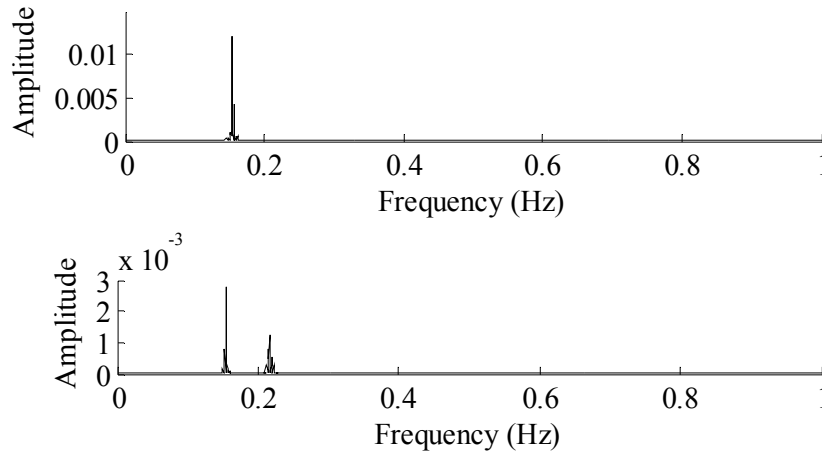


Figure 3.5. PSD for signals obtained by sensors 15 (upper) and 16 (lower) during Kammuri typhoon.

Table 3.3. Frequencies of tower during Kammuri typhoon

Hour	Frequency (Hz)					
	Mode 1	Mode 2	Mode 3	Mode 4	Mode 5	Mode 6
17:32-18:32	0.1545	0.2171	0.4655	0.5714	0.8126	0.9879
18:32-19:32	0.1546	0.2167	0.4647	0.5701	0.8125	0.9903
19:32-20:32	0.1542	0.2163	0.4642	0.5699	0.8128	0.9909

In Figure 3.5 the Power Spectrum Density (PSD) diagram obtained by Fourier Transform (FT) for the signals obtained by sensors 15 and 16 are demonstrated. The first two fundamental frequencies could be clearly detected from these figures (i.e. 0.154 and 0.217 Hz) However, the signals of three-hour data (from 17:32 to 20:32) are processed and investigated in detail, and the

resulted frequencies and damping ratios for these signals are listed in Table 3.3 and 3.4 respectively.

PSDs obtained by ARTeMIS for the entire available data registered during Kammuri typhoon as well as the other considered extreme events are figured in Appendix B

Table 3.4. Damping ratios of tower during Kammuri typhoon

Hour	Damping ratios					
	Mode 1	Mode 2	Mode 3	Mode 4	Mode 5	Mode 6
17:32-18:32	1.062	1.052	0.6375	0.5513	0.3605	0.7542
18:32-19:32	1.134	0.9607	0.6073	0.6737	0.3985	0.6615
19:32-20:32	1.051	1.031	0.635	0.5112	0.4574	0.6173

3.3 Typhoon Nuri

3.3.1 Wind properties

On the 22nd of August 2008 when Nuri typhoon occurred, the time histories of wind velocity and direction were recorded. Systematically, Figure 3.6 shows the one hour mean wind velocities measured at the top of the tower for the whole 24 hours of that day. It can be seen that the maximum one hour mean wind velocity was 16.8 m/s, measured between 9:00 and 10:00 pm, while the maximum calculated 3-second gust wind speed at the tower top was 25.5 m/s for the period of time between 2:00 and 3:00 pm.

The wind rose diagram for Nuri typhoon is shown in Figure 3.7, in which it is illustrated that the primary wind direction of Nuri typhoon was around the 30° which denotes northeast direction.

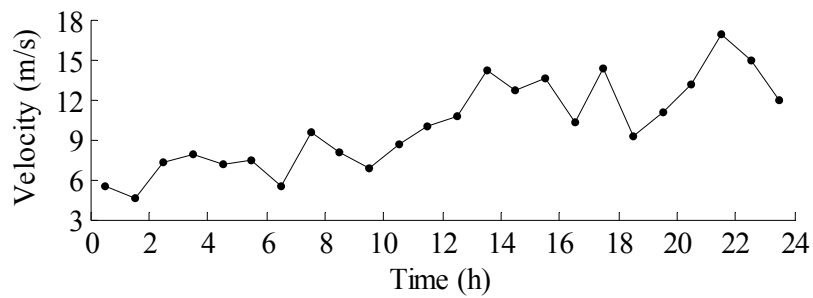


Figure 3.6. Wind mean velocity measured on 22/8/2008

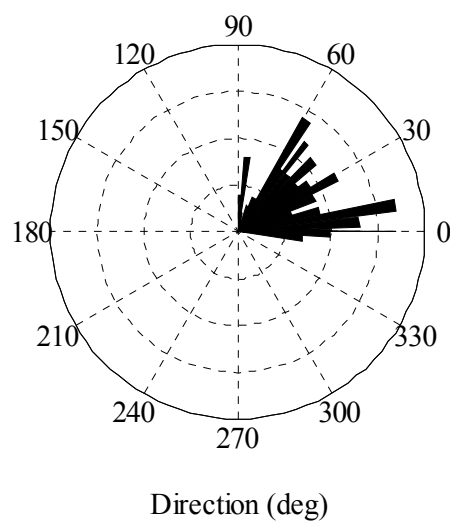


Figure 3.7. Wind rose diagram of Nuri typhoon.

3.3.2 Response analysis and processing

Similarly, the response of the tower was recorded by sensors labeled 1-16. Figure 3.8 shows the recorded two time histories by sensors labeled 15 and 16 for one sample hour (3:00 - 4:00 pm) chosen from the available data to be

considered. The sampling frequency of these data is 50 Hz. All the other available records from the sensors of different levels registered during Nuri typhoon are shown in Appendix A at the end of this thesis.

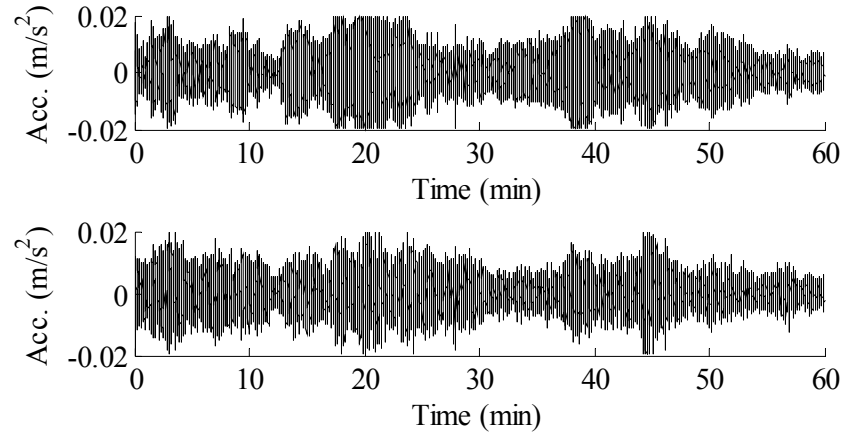


Figure 3.8. Time Histories of recorded response to Nuri typhoon by sensors labeled 15 (upper) and 16 (lower).

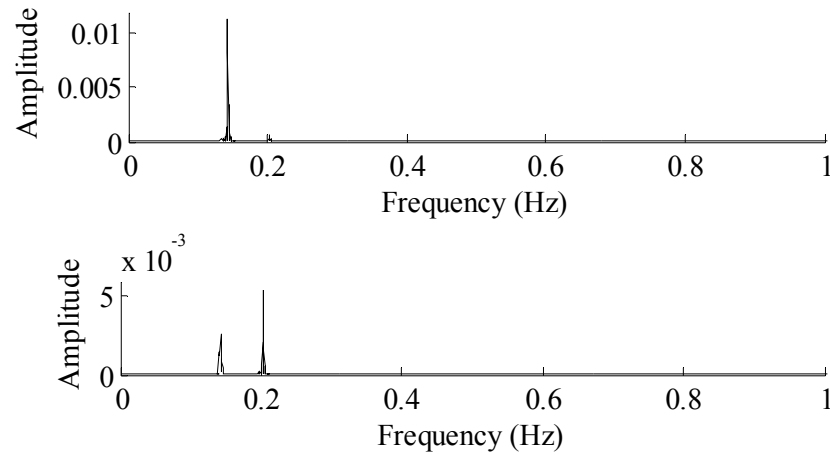


Figure 3.9. PSD for signals obtained by sensors 15 (upper) and 16 (lower) during Nuri typhoon.

The corresponding PSD diagrams for the same signal are shown in Figure 3.9, and the results of three hour data (from 14:00 to 17:00) for the natural frequencies and damping ratios are listed in Table 3.5 and 3.6 respectively.

Table 3.5. Frequencies of tower during Nuri typhoon

Hour	Frequency (Hz)					
	Mode 1	Mode 2	Mode 3	Mode 4	Mode 5	Mode 6
14:00-15:00	0.142	0.203	0.4531	0.5624	0.8337	0.9964
15:00-16:00	0.1428	0.203	0.4539	0.5637	0.8334	0.9958
16:00-17:00	0.1431	0.2037	0.454	0.5693	0.8355	0.9946

Table 3.6. Damping ratios of tower during Nuri typhoon

Hour	Damping ratios					
	Mode 1	Mode 2	Mode 3	Mode 4	Mode 5	Mode 6
14:00-15:00	1.263	0.9381	0.7259	1.394	0.6553	0.6425
15:00-16:00	1.135	0.7933	0.7501	1.527	0.5786	0.4737
16:00-17:00	1.166	1.116	0.8351	1.449	0.5115	0.5561

3.4 Typhoon Hagupit

3.4.1 Wind properties

The time histories of wind velocity and direction were recorded for the 24 hours of the day 24th of September 2008. Figure 3.10 shows the one hour mean wind velocities measured at the top of the tower. The maximum one hour mean wind velocity was 27.6 m/s, measured between 2:00 and 3:00 am, and the maximum calculated 3-second gust wind speed was 34.6 m/s measured at the same period of time.

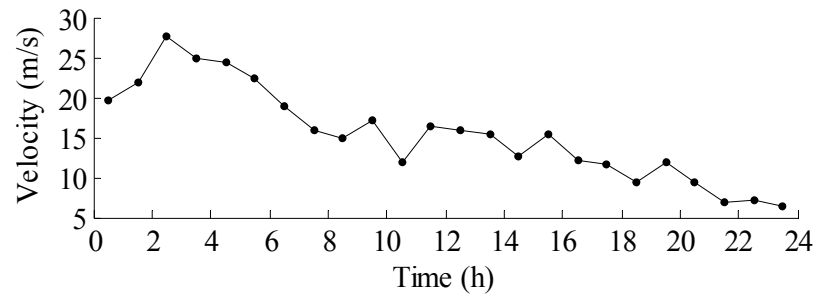


Figure 3.10. Wind mean velocity measured on 24/9/2008

Figure 3.11 illustrates the wind rose diagram for Hagupit typhoon from which it is clear that the primary wind direction of the typhoon was around the 130° i.e. southeast direction.

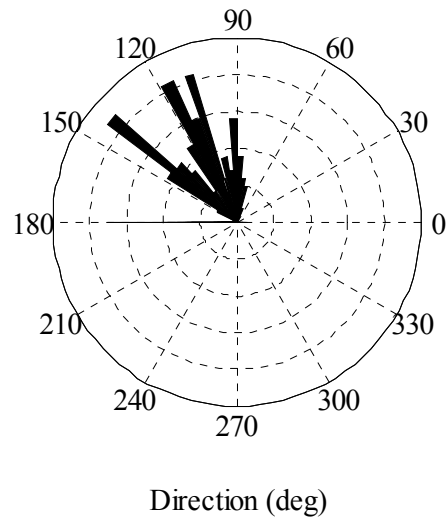


Figure 3.11. Wind rose diagram of Hagupit typhoon.

3.4.2 Response analysis and processing

For Hagupit typhoon the response of the tower was recorded by 14 sensors from the total sensors 1-16, where data from sensors 3 and 4 are not available, due to the problems of site operations and power supply. Figure 3.12 shows the recorded two time histories by highest level sensors (15 and 16) for an hour sample (4:00 - 5:00 am) chosen from the available data to be considered. The sampling frequency of these data is 50 Hz. The other available records obtained by the other 12 sensors during Hagupit typhoon are included in Appendix A, and PSD diagrams for the two time histories are shown in Figure 3.13, and the results of three hour data (from 3:00 to 6:00) for the natural frequencies and damping ratios are listed in Table 3.7 and 3.8 respectively.

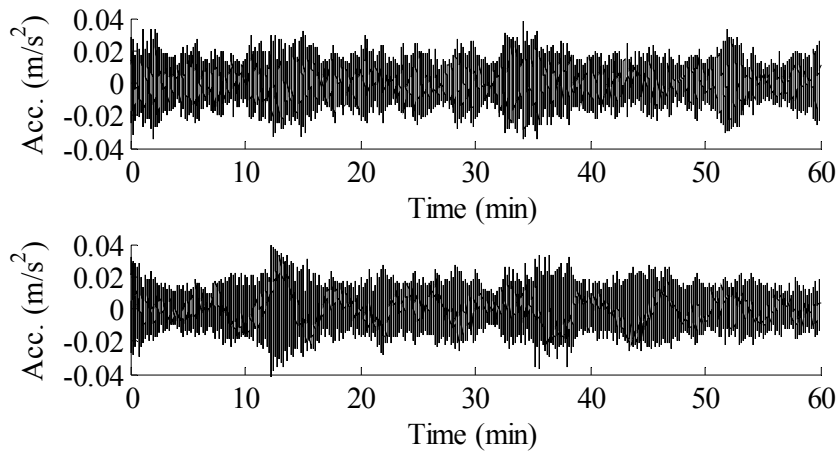


Figure 3.12. Time Histories of recorded response to Hagupit typhoon by sensors 15 (upper) and 16 (lower).

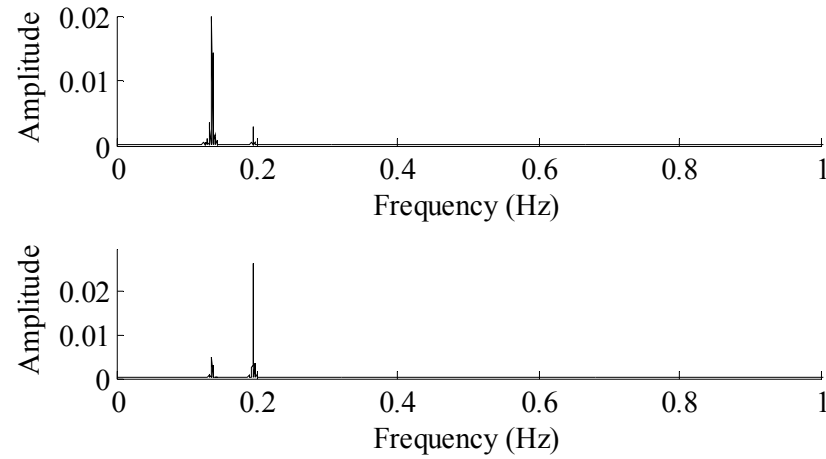


Figure 3.13. PSD for signals obtained by sensors 15 (upper) and 16 (lower) during Hagupit typhoon.

Table 3.7. Frequencies of tower during Hagupit typhoon

Hour	Frequency (Hz)					
	Mode 1	Mode 2	Mode 3	Mode 4	Mode 5	Mode 6
3:00-4:00	0.1363	0.1945	0.4486	0.5646	0.853	1.051
4:00-5:00	0.136	0.1945	0.4498	0.5636	0.8579	1.05
5:00-6:00	0.1361	0.1946	0.4492	0.5636	0.8559	1.051

Table 3.8. Damping ratios of tower during Hagupit typhoon

Hour	Damping ratios					
	Mode 1	Mode 2	Mode 3	Mode 4	Mode 5	Mode 6
3:00-4:00	1.46	0.9304	0.5558	0.707	0.7256	0.5856
4:00-5:00	1.369	0.8095	0.7087	0.7152	1.358	0.5495
5:00-6:00	1.145	1.012	0.7316	0.558	0.8624	0.5284

3.5 Typhoon Molave

3.5.1 Wind properties

On the 18th of July 2009 when the typhoon Molave started to affect the GTVT, The time histories of wind velocity and direction were recorded for 16 hours; starting from 5:32 pm to 7:32 am of the next day.

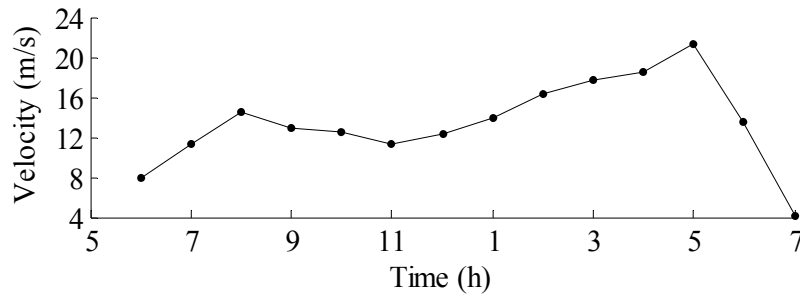


Figure 3.14. Wind mean velocity measured on 18-19/7/2009

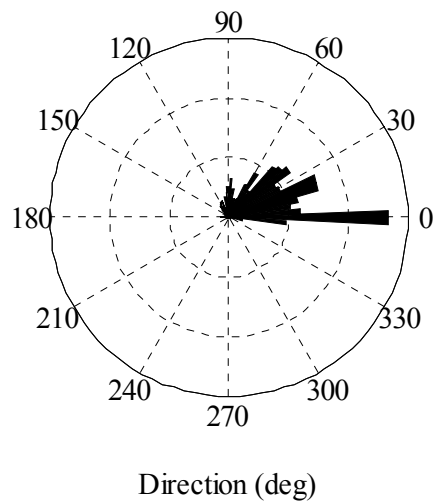


Figure 3.15. Wind rose diagram of Molave typhoon.

Figure 3.14 shows the one hour mean wind velocities measured at the top of the tower level at that time. The maximum one hour mean wind velocity was 21.4 m/s, measured around 5:00 am, and 3-second gust wind speed 31.2 m/s.

In Figure 3.15 the wind rose diagram for Molave typhoon is drawn by the data obtained for 14 hours. The figure shows that the wind direction of the typhoon was between 0 and 30° which means from north to northeast.

3.5.2 Response analysis and processing

At the time when Molave typhoon started to hit the tower, the maximum level of the tower was reached for both the inner and outer tube, therefore the responses of the tower was recorded by 16 sensors labeled from 1 to 20 excluding sensors 1,2,15, and 16; where the data from these sensors are not available due to the problems of site operations and power supply.

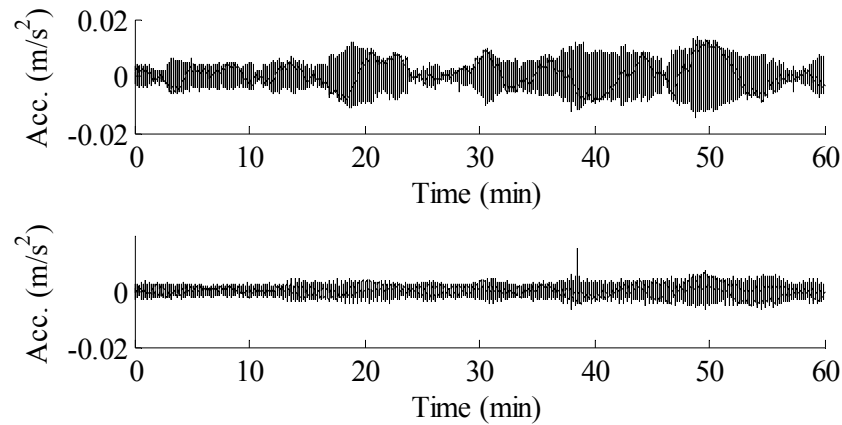


Figure 3.16. Time Histories of recorded response to Molave typhoon by sensors 18 (upper) and 20 (lower).

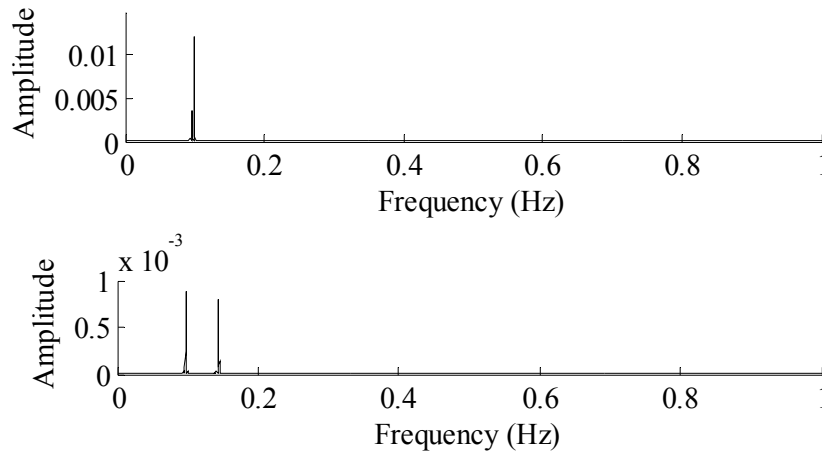


Figure 3.17. PSD for signals obtained by sensors 18 (upper) and 20 (lower) during Molave typhoon.

Figure 3.16 shows the recorded two time histories by the highest level sensors (18 and 20) for a sample of one selected hour starting from 23:32 pm. The sampling frequency of these data is 50 Hz. The other available records obtained during Molave typhoon are included in Appendix A. PSD diagrams for time histories of Figure 3.16 are shown in Figure 3.17, and the results of 3 hour data, for the natural frequencies and damping ratios are listed and Table 3.9 and 3.10 respectively.

Table 3.9. Frequencies of tower during Molave typhoon

Hour	Frequency (Hz)					
	Mode 1	Mode 2	Mode 3	Mode 4	Mode 5	Mode 6
21.32-22.32	0.0981	0.1442	0.3661	0.4208	0.4765	0.5257
22.32-23.32	0.0979	0.1442	0.3663	0.4206	0.4761	0.5275
23.32-0:32	0.0979	0.1443	0.3671	0.4211	0.4759	0.5278

Table 3.10. Damping ratios of tower during Molave typhoon

Hour	Damping ratios					
	Mode 1	Mode 2	Mode 3	Mode 4	Mode 5	Mode 6
21.32-22.32	1.464	1.089	1.094	0.575	0.4131	0.6576
22.32-23.32	1.906	1.01	0.4823	0.4143	0.3413	0.7316
23.32-0:32	1.654	0.9598	0.5689	0.4009	0.4046	0.7778

3.6 Typhoon Koppu

3.6.1 Wind properties

The last typhoon considered in this study is Koppu which occurred on 15th of September 2009.

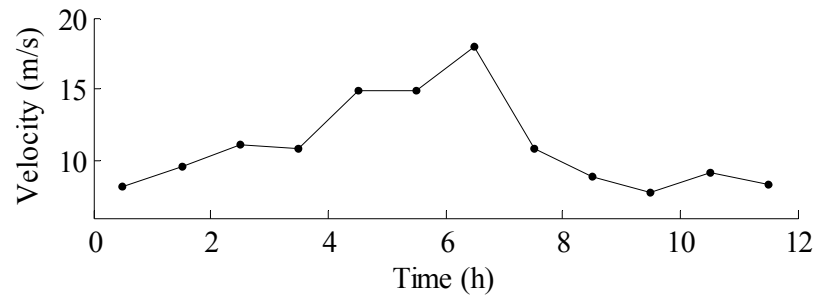


Figure 3.18. Wind mean velocity measured on 15/9/2009

The time histories of wind velocity and direction were recorded at the top level of the tower for the first 12 hours of that day, and the one hour mean velocities are calculated and drawn in Figure 3.18. The maximum one hour mean wind velocity was 18 m/s, measured between 6:00 and 7:00 am.

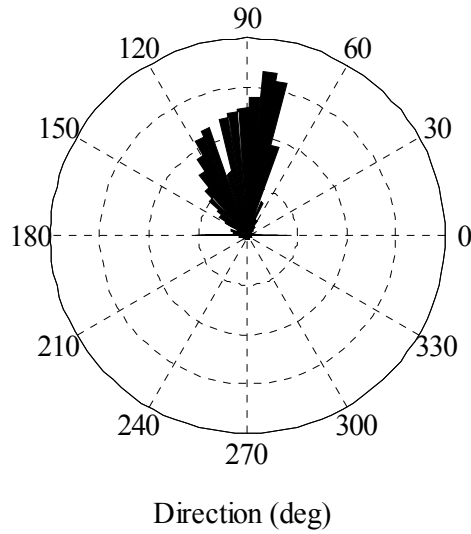


Figure 3.19. Wind rose diagram of Koppu typhoon.

The wind rose diagram for Koppu typhoon is drawn in Figure 3.19, using the measurements of the 12 hours. The figure shows that the wind direction of the typhoon was mainly around 90° denoting east direction.

3.6.2 Response analysis and processing

The maximum level of the tower was reached when Koppu typhoon happened, and the responses of the tower was recorded by 12 sensors labeled from 1 to 20 excluding sensors 1,2,3,4,8,10,18, and 20; due to the problems of site operations and power supply.

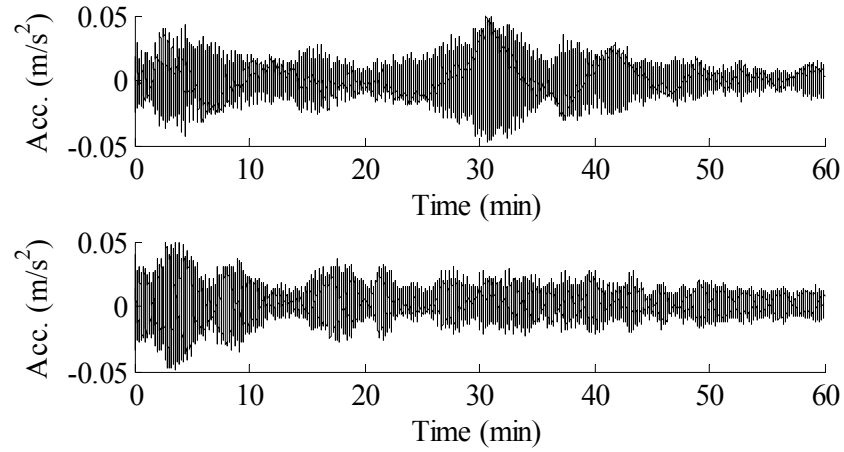


Figure 3.20. Time Histories of recorded response to Koppu typhoon by sensors 17 (upper) and 19 (lower).

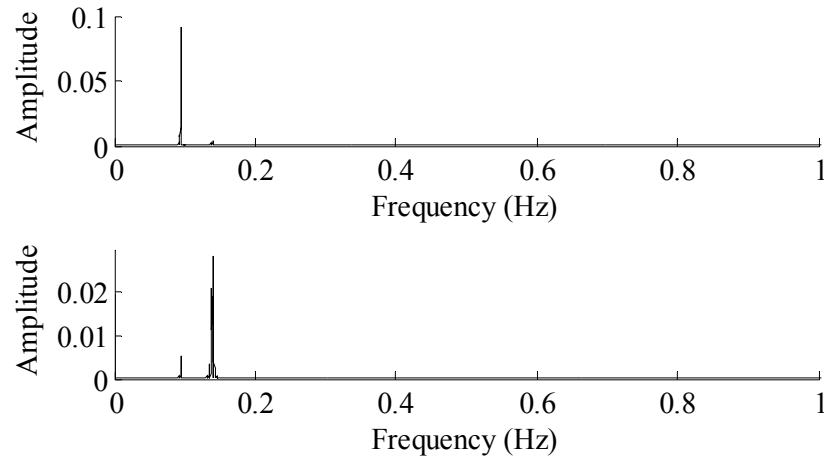


Figure 3.21. PSD for signals obtained by sensors 17 (upper) and 19 (lower) during Koppu typhoon.

Figure 3.20 shows the recorded two time histories by highest level sensors (17 and 19) for the one-hour available data from 6:00 – 7:00 am. The sampling frequency of these data is 50 Hz. The other available records obtained by the

other 10 sensors at the same hour are included in Appendix A. PSD diagrams for the data obtained from sensor 17 and 19 are shown in Figure 3.21. Whereas Table 3.11 and 3.12 list, respectively, the values of frequencies and damping ratios for the same hour calculated for the first six modes.

Table 3.11. Frequencies of tower during Koppu typhoon

Hour	Frequency (Hz)					
	Mode 1	Mode 2	Mode 3	Mode 4	Mode 5	Mode 6
6:00-7:00	0.0946	0.1398	0.3634	0.4208	0.4743	0.5234

Table 3.12. Damping ratios of tower during Koppu typhoon

Hour	Damping ratios					
	Mode 1	Mode 2	Mode 3	Mode 4	Mode 5	Mode 6
6:00-7:00	1.603	1.182	0.7348	0.5352	0.283	0.338

3.7 Results Discussion

In order to simplifying the detection of mean wind speed effect on the modal parameters of the structures in this section Figures 3.22-24 are drawn. In Figure 3.22 the changes of the natural frequency of the first mode with the hourly mean wind speed are drawn. Three hour-samples for each Kammuri, Nuri, and Hagupit typhoons are included. It is seen that the modal frequency for one typhoon is not significantly changed with mean wind speed, the frequencies are slightly fluctuating but they do not follow a particular trend. Therefore it could be confirmed that the modal frequency has not been affected with mean wind speed vibration during the mentioned typhoons. Nevertheless, the frequency was varying from one typhoon to another; because each typhoon occurred at different construction stage of the tower. The sequence of typhoons occurrence along with changes in frequencies indicate the decrease of first modal frequency of the tower with its height as was expected.

In Figure 3.23 the frequencies variation of the first six modes during Molave typhoon are drawn for the 14 hour available data. It could be seen from the

figure that frequencies remain nearly constant with wind speed variation, not only for the first mode but also for higher modes.

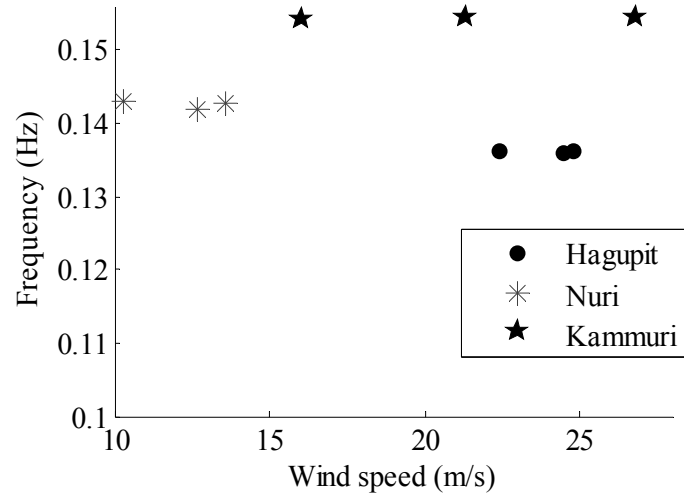


Figure 3.22. Frequency variation with wind speed during Hagupit, Nuri, and Kammuri typhoons.

Using the same data of Figure 3.23, the damping ratio's variation with wind speed is drawn in Figure 3.24 during Molave typhoon for the first two modes. The figure shows that damping ratio slightly increases with the mean wind speed; however, the rate of increase is higher in the second mode than it is for the first mode; which means that damping increase rate differs from one direction of the structure to the other depending on the geometry of the structure and the wind direction.

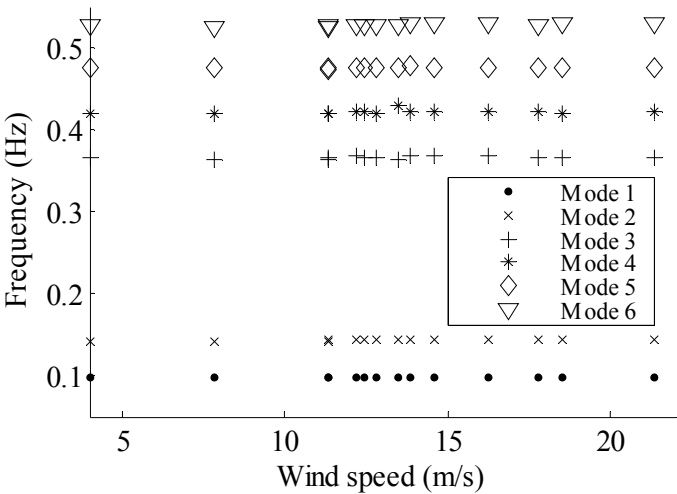


Figure 3.23. Frequency variation during Molave typhoon

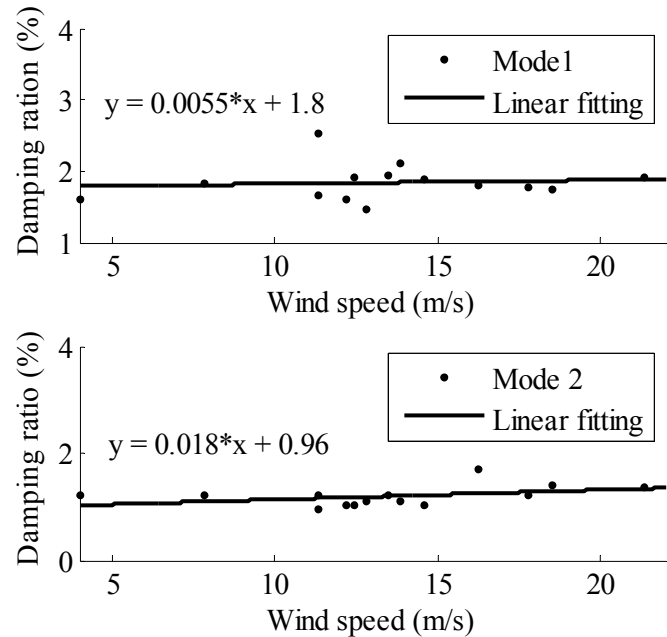


Figure 3.24. Damping ratio variation during Molave typhoon.

3.8 Conclusions

In this chapter the response of GTVT to wind effect is studied; by analyzing the acceleration response time histories obtained by the sensors mounted at different elevations of the tower to five different typhoons occurred at different times; during the tower construction and after the completion of the total height of the tower.

The data are analyzed by the FDD method in order to identify the modal parameters of the tower. And the properties of wind typhoons are also analyzed aiming at investigating the strong wind effect on the dynamic behavior of the tower; by correlating the wind properties with the modal parameters.

The five typhoons varied in the hourly mean wind speed as well as the main direction of blowing and the duration, which gave the possibility to study the tower behavior under different types of typhoons and at different stages of the tower construction.

The results proved that the fundamental frequencies of the tower was decreasing as the level of construction was increasing, while no sufficient change in the frequency was detected through different speeds of wind at the same level of construction; this could mean that the tower did not suffer any change in its properties during these typhoons proved by the constant fundamental frequencies which means no change occurred in the stiffness of the structure, however, the values of the frequency was slightly fluctuating around the real values due to the heavy rain accompanied by the typhoons which increases the mass of the tower. On the other hand the damping ratios were found to increase with the speed of the wind affecting the tower.

Chapter 4

Damage Assessment of GTVT Based on FDD Analysis

4.1 Introduction

The principal purpose of processing signals obtained by SHM system by various methods in this research work is to reach for realistic assessment of the GTVT condition after being exposed to several severe events.

In following sections; the damage assessment of the structure is performed, based on the operational modal analysis results obtained by FDD method for the ambient vibration response signal of the tower before and after being exposed to the following severe events: Nuri, Hagupit, and Molave typhoons, and Southern Taiwan (ST) and Taiwan Hualien (TH) earthquakes.

The damage identification algorithms explained in Chapter 2 (namely: MAC, COMAC, and MCC) are calculated for the aforementioned cases and the results are discussed in details

4.2 Damage Assessment

In order to assess a structure by any of MAC, COMAC, and MCC coefficients, it is essential to have the mode shapes of the structure calculated from a two response signals; the first is measured before an extreme event, and the second is after.

To achieve this purpose the Ambient Response Testing and Modal Identification Software (ARTEMIS) extractor is utilized, which is a software used for output-only modal identification. A model of the tower is created in the program with 9 levels shaped by 13 nodes at each level (Figure 4.1), giving 117 nodes in total for the tower body, and 4 more nodes for the foundation. The locations of accelerometers are simulated at the second to the ninth levels and the first level is considered as the ground level. The relationships governing the relative motions of nodes are then defined, and the function of Enhanced FDD Peak Picking is used for modal identification.

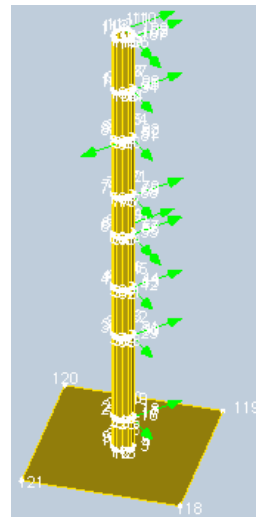


Figure 4.1. Model of the tower by ARTEMIS software.

Figure 4.2 shows the first six mode shapes of the tower, which present the case for all the analyzed ambient vibration signals in this chapter. The first two modes shown in the figure represent the first lateral bending modes of the tower around the short axis and long axis, the third and fourth are the second lateral bending around the two axes, the fifth is the third lateral bending around the short axis and the last is the first torsional mode of the tower.

4.2.1 Assessment after Nuri typhoon

As mentioned in Chapter 3, Nuri typhoon affected the tower on the 8th of August 2008; therefore, the two signals chosen from the available data to perform this assessment are obtained under normal ambient vibration for the following times:

- 1) 22:00 to 23:00 on the 18th of August 2008.
- 2) 21:00 to 22:00 on the 25th of August 2008.

Response of the tower during these times was measured by 16 sensors distributed along the height of the tower, and the time histories of six samples chosen from the total available signals for each hour are presented in Figures 4.3.a and 4.3.b. In the figures; the left hand side group of figures are measured along the minor axis and the right hand side figures are along the major axis of the elliptical cross section of the tower.

The resulted mode shapes obtained by ARTeMIS software from these signals are normalized and listed in Table 4.1 for both signals measured before and after the typhoon which are assumed to present the undamaged and damaged status of the tower, respectively.

The adopted coefficients are then calculated based on the corresponding formulae explained in Chapter 2. Calculating MAC values for the first six modes of vibration, a matrix of 6x6 dimensions is resulted and shown in Table 4.2. The values of the main diagonal of this matrix are the corresponding MAC values to each mode. While in Table 4.3 the values of COMAC are listed for the same group of signals, and systematically, the MCC values are calculated and listed in Table 4.4.

By investigating all the values of the three mentioned tables it could be clearly concluded that the dynamical behavior of the tower has not changed significantly during Nuri typhoon. Hence, no sign for any possible damage indicated by the calculated coefficients.

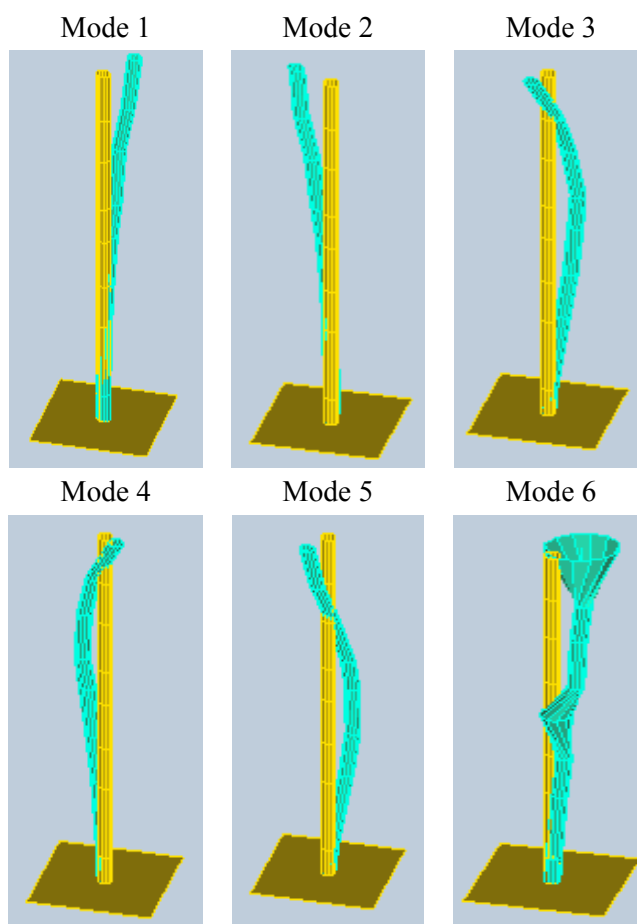


Figure 4.2. Mode shapes of GTVT.

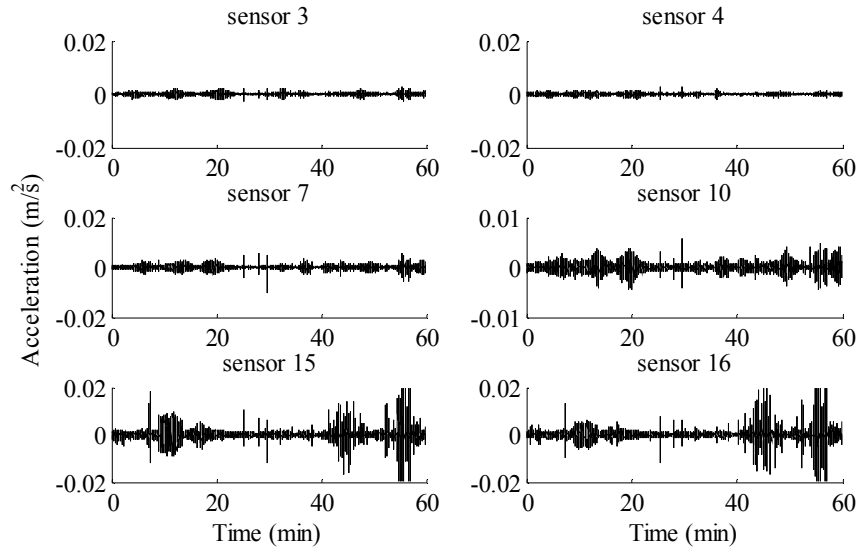


Figure 4.3.a. ambient vibration response before Nuri typhoon.

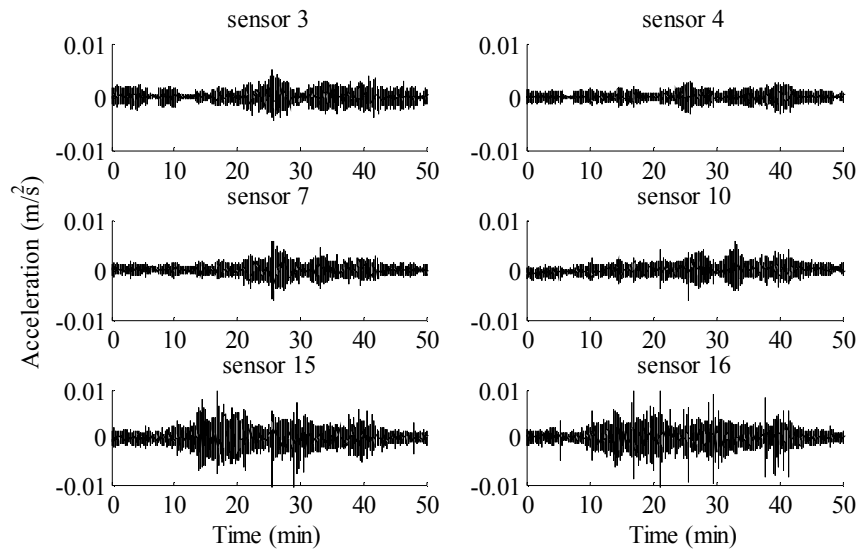


Figure 4.3.b. ambient vibration response after Nuri typhoon.

Table 4.1. Normalized mode shapes of the tower around Nuri typhoon period.

Sensor #	Undamaged			Damaged		
	Mode 1	Mode 2	Mode 3	Mode 1	Mode 2	Mode 3
1	0.01	0.02	0.06	0.00	0.02	0.05
2	0.01	-0.01	0.11	0.02	0.00	0.10
3	0.03	0.12	0.16	0.02	0.12	0.11
4	0.08	0.00	0.66	0.08	0.00	0.63
5	0.05	0.23	0.16	0.05	0.23	0.09
6	0.18	0.05	0.96	0.18	0.04	0.92
7	0.31	-0.09	0.99	0.31	-0.11	0.98
10	0.14	0.38	0.3	0.14	0.39	0.23
8	0.33	-0.05	1	0.33	-0.06	1
9	0.12	0.4	0.22	0.11	0.40	0.16
11	0.12	0.57	0.01	0.11	0.59	-0.05
12	0.43	-0.26	0.69	0.42	-0.27	0.75
13	0.49	0.67	-0.03	0.49	0.68	-0.05
14	0.71	-0.3	0.09	0.71	-0.32	0.13
15	0.49	1	-0.46	0.48	1	-0.39
16	1	-0.33	-0.93	1	-0.38	-0.79

Table 4.2. MAC values for signals around Nuri typhoon period.

Mode #	Mode 1	Mode 2	Mode 3	Mode 4	Mode 5	Mode 6
Mode 1	1.00	0.09	0.02	0.09	0.34	0.07
Mode 2	0.11	1.00	0.12	0.13	0.02	0.40
Mode 3	0.07	0.07	0.99	0.12	0.16	0.15
Mode 4	0.09	0.09	0.02	1.00	0.06	0.15
Mode 5	0.28	0.02	0.09	0.06	0.99	0.04
Mode 6	0.03	0.38	0.12	0.12	0.04	1.00

All the calculated values of three coefficients are almost equal to unity; which means; that the mode shapes of the assumed-damaged and the undamaged structure have a high consistency represented by unity MAC values, and no degree of freedom is suspected to contribute negatively to a low value of MAC, proved by COMAC unity values. Furthermore, there is no evident for kinks formation or a relatively high change in slope between any couple of nodes indicated by the values of MCC. Nevertheless, MCC values are not as close to unity as the other coefficient, showing more sensitivity in detecting damages in the structure.

Table 4.3. COMAC values for signals around Nuri typhoon period.

Sensor	1	2	3	4	5	6	7	8	9	10
COMAC	1.00	0.99	1.00	1.00	1.00	1.00	1.00	1.00	1.00	1.00
Sensor	11	12	13	14	15	16	17	18	19	20
COMAC	1.00	1.00	1.00	1.00	0.99	0.98	n.a	n.a	n.a	n.a

Table 4.4. MCC values for signals around Nuri typhoon period.

Mode	1	2	3	4	5	6
K	0.98	0.99	0.91	0.99	0.93	1.00
MCC	0.98	0.99	0.90	0.99	0.92	0.99

4.2.2 Assessment after Hagupit typhoon

Hagupit typhoon started to efficiently affecting the GTVT on the 24th of September 2008; therefore, aiming at assessing the tower condition after this extreme event the ambient vibration response at the following two time periods are considered:

- 1) 03:00 to 04:00 on the 13th of September 2008.
- 2) 05:00 to 06:00 on the 24th of September 2008.

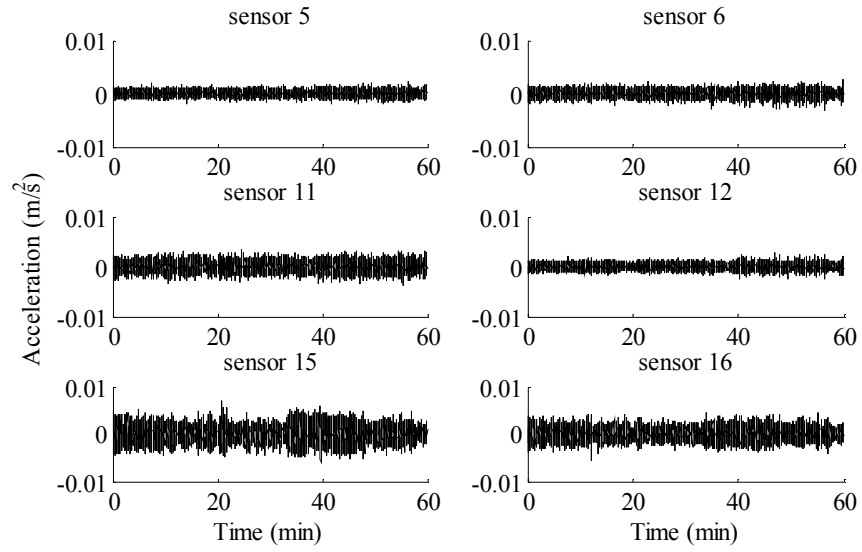


Figure 4.4.a. ambient vibration response before Hagupit typhoon.

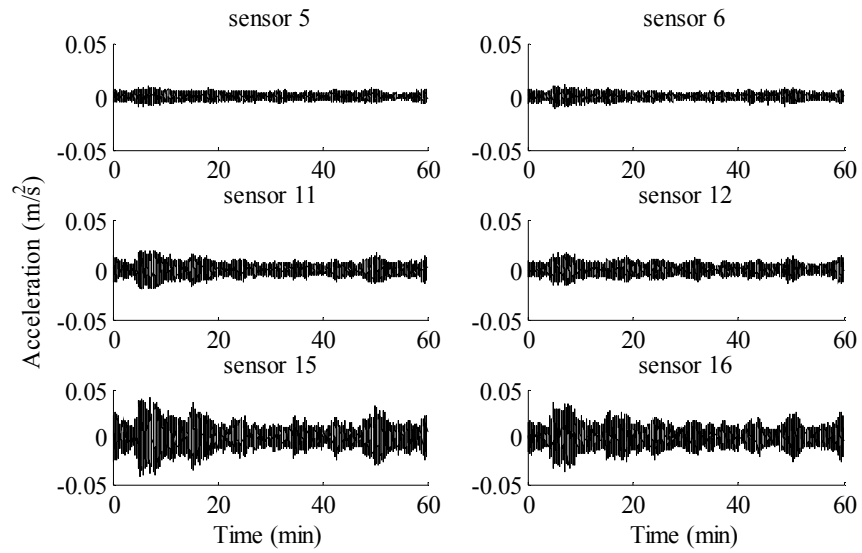


Figure 4.4.b. ambient vibration response after Hagupit typhoon.

12 sensors were in service to measure the response of the tower during these times, from which six samples of the resulted time histories are illustrated in Figure 4.4.

Consequently, MAC, COMAC, and MCC values are calculated and listed, respectively, in Tables 4.5-4.7, which concludes the same observed fact after Nuri typhoon of not having any sign for possible damage suffered by the tower after Hagupit typhoon.

Table 4.5. MAC values for signals around Hagupit typhoon period.

Mode	1	2	3	4	5	6
MAC	1.00	1.00	1.00	1.00	1.00	1.00

Table 4.6. COMAC values for signals around Hagupit typhoon period.

Sensor	1	2	3	4	5	6	7	8	9	10
COMAC	n.a	n.a	n.a	n.a	1.00	1.00	1.00	1.00	1.00	1.00
Sensor	11	12	13	14	15	16	17	18	19	20
COMAC	1.00	1.00	1.00	1.00	1.00	1.00	n.a	n.a	n.a	n.a

Table 4.7. MCC values for signals around Hagupit typhoon period.

Mode	1	2	3	4	5	6
K	0.99	0.99	0.98	0.98	0.94	0.96
MCC	0.99	0.99	0.98	0.98	0.94	0.96

4.2.3 Assessment after Molave typhoon

The assessment of GTVT after Molave typhoon is conducted by ambient vibration signals shown in Figure 4.5, which are measured at the following time periods of 15 minutes only; due to the lake of continues 1-hour data around this typhoon:

- 1) 17:32 to 17:47 on the 18th of July 2009.
- 2) 06:32 to 06:47 on the 19th of July 2009.

Tables 4.9-4.10 list the values of MAC, COMAC, and MCC calculated from the mode shapes obtained by the data measured by 12 sensors.

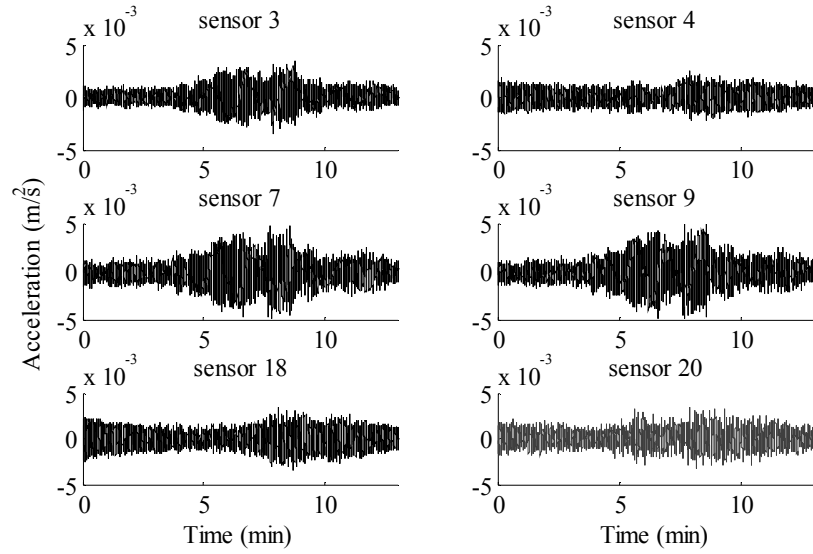


Figure 4.5.a. ambient vibration response before Molave typhoon.

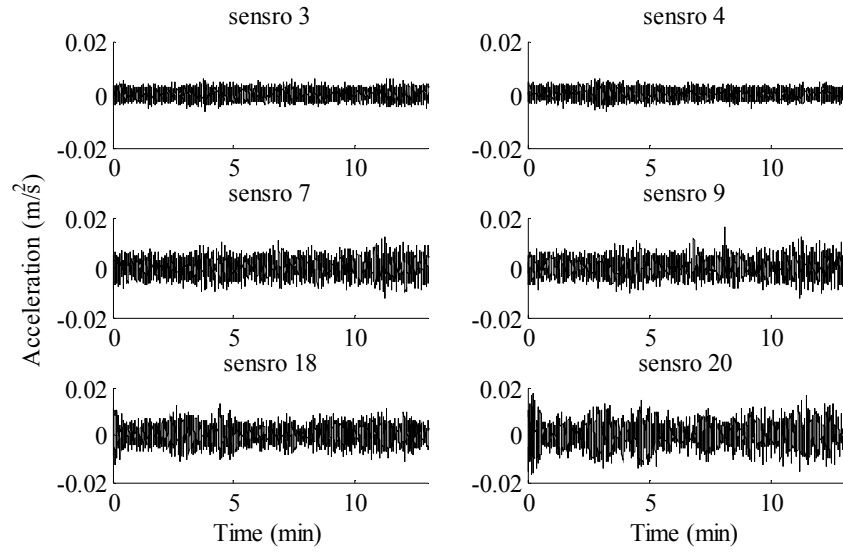


Figure 4.5.b. ambient vibration response after Molave typhoon.

Results found to be consistent with the previously calculated and the same conclusion applies also in this case, despite the relatively low values of MCC for the fifth and sixth modes of vibration which might be caused by the non sufficient data provided by 15-minute signal in detecting clearly these modes. Also the values of MAC and COMAC did not prove any sign for damage. Nevertheless, this could prove the higher sensitivity of MCC.

Table 4.8. MAC values for signals around Molave typhoon period.

Mode	1	2	3	4	5	6
MAC	1.00	0.99	1.00	0.99	1.00	0.96

Table 4.9. COMAC values for signals around Molave typhoon period.

Sensor	1	2	3	4	5	6	7	8	9	10
COMAC	n.a	n.a	0.90	0.99	1.00	0.99	0.98	n.a	1.00	n.a
Sensor	11	12	13	14	15	16	17	18	19	20
COMAC	1.00	0.97	0.92	0.99	n.a	n.a	n.a	n.a	1.00	1.00

Table 4.10. MCC values for signals around Molave typhoon period.

Mode	1	2	3	4	5	6
K	1.00	0.93	0.92	0.91	0.86	0.87
MCC	1.00	0.92	0.92	0.90	0.86	0.83

4.2.4 Assessment after ST and HT earthquakes.

The SHM system of the tower provided also data measured during two different earthquakes occurred in the region of the tower (namely; ST earthquake, and HT earthquake), and the ground motions could be felt there. These data are treated similarly, and the condition of the structure is assessed after being exposed to both of these earthquakes.

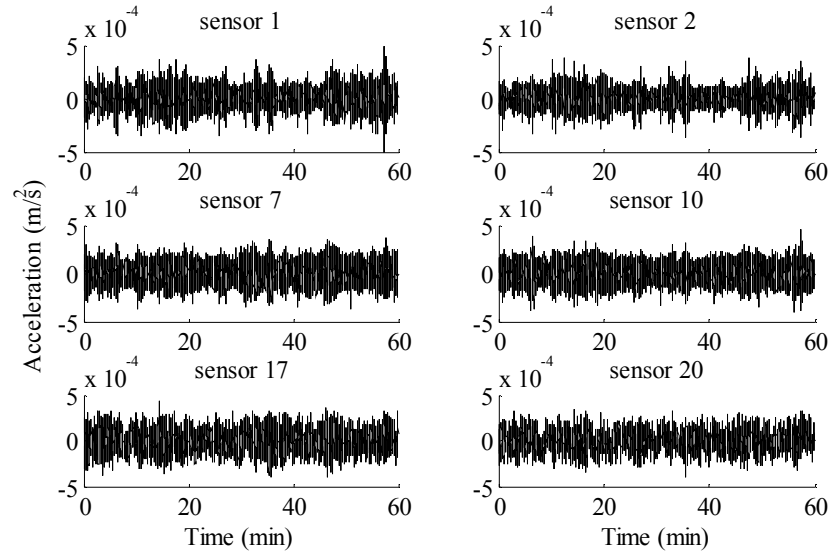


Figure 4.6.a. ambient vibration response before ST earthquake.

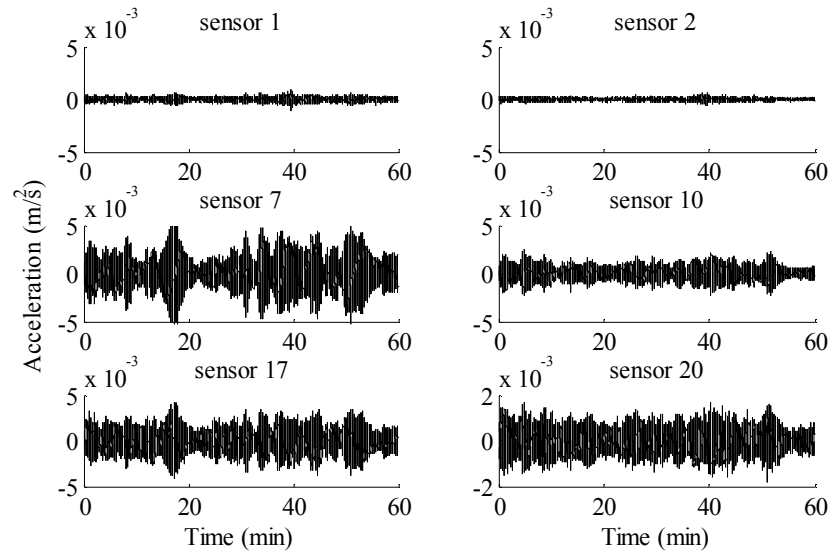


Figure 4.6.b. ambient vibration response after ST earthquake.

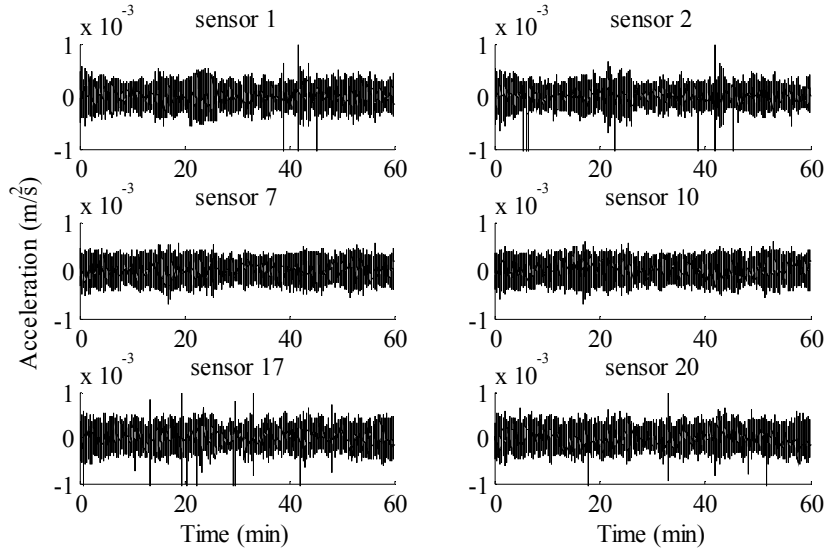


Figure 4.7.a. ambient vibration response before TH earthquake.

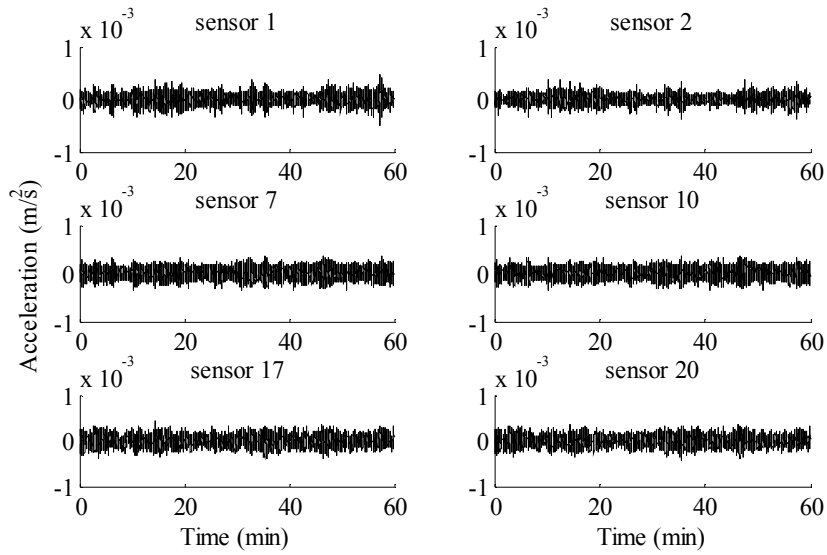


Figure 4.7.b. ambient vibration response after TH earthquake.

ST and TH earthquakes affected the tower on 4th of March 2010 and 19th of December 2009, respectively. Accordingly, the ambient vibration data used in this assessment are; 23:12 to 00:12 on 21st January 2010 and 00:45 to 01:45 on 7th of March 2010 for ST earthquake, while for TH earthquake the data were measured from 09:51 to 10:51 on 19th of December 2009 and from 23:12 to 00:12 on 21st January 2010. The corresponding samples of selected time histories to represent these data are shown in Figures 4.6 and 4.7.

Table 4.11. Normalized mode shapes of the tower around ST earthquake period.

Sensor #	Undamaged			Damaged		
	Mode 1	Mode 2	Mode 3	Mode 1	Mode 2	Mode 3
1	0.03	0.04	0.01	0.00	0.01	0.01
2	0.04	0.00	0.08	0.01	0.00	0.08
3	0.01	0.07	0.04	0.01	0.07	0.04
4	0.06	0.02	0.50	0.06	0.01	0.50
5	0.06	0.15	0.05	0.02	0.15	0.06
6	0.16	0.02	0.76	0.12	0.00	0.76
7	0.28	0.02	1	0.25	0.02	1
10	0.07	0.28	0.06	0.05	0.26	0.07
8	0.27	-0.01	0.98	0.24	-0.03	0.97
9	0.10	0.30	0.19	0.08	0.27	0.20
11	0.11	0.40	0.03	0.08	0.40	0.03
12	0.40	-0.07	0.97	0.36	-0.08	0.95
13	0.23	0.56	0.11	0.23	0.55	0.12
14	0.56	-0.14	0.70	0.56	-0.16	0.69
15	0.18	0.80	-0.10	0.16	0.79	-0.10
16	0.80	-0.26	0.19	0.77	-0.27	0.19
17	1	-0.34	-0.64	1	-0.34	-0.64
20	0.26	1	-0.15	0.28	0.97	-0.22
18	1	-0.30	-0.63	0.98	-0.30	-0.63
19	0.28	1	-0.22	0.25	1	-0.15

The mode shapes are calculated by ARTeMIS again for the four signals considered. Table 4.13 lists the normalized values for the first three modes of vibration extracted from the signals measured around ST earthquake period only as a sample, and from total calculated modes MAC, COMAC, and MCC values are obtained, and listed in Table 4.12-4.14 respectively.

Table 4.12. MAC values of signals around the two earthquakes period.

Mode	1	2	3	4	5	6
ST earthquake	1.00	1.00	1.00	0.99	1.00	0.99
TH earthquake	1.00	1.00	1.00	0.99	1.00	0.99

Table 4.13. COMAC values of signals around the two earthquakes period.

Sensor #	1	2	3	4	5	6	7	8	9	10
ST earthquake	0.84	0.89	1.00	1.00	1.00	0.99	1.00	0.99	1.00	1.00
TH earthquake	0.82	0.85	1.00	1.00	1.00	1.00	1.00	1.00	1.00	1.00
Sensor #	11	12	13	14	15	16	17	18	19	20
ST earthquake	1.00	0.99	1.00	1.00	1.00	1.00	1.00	0.99	1.00	0.99
TH earthquake	1.00	1.00	1.00	1.00	1.00	1.00	1.00	1.00	0.99	0.99

Table 4.14. MCC values of signals around the two earthquakes period.

Mode		1	2	3	4	5	6
ST earthquake	K	0.92	0.99	0.99	0.90	0.98	0.99
	MCC	0.91	0.99	0.99	0.89	0.98	0.99
TH earthquake	K	0.96	1.00	0.99	0.96	0.99	0.99
	MCC	0.96	1.00	0.99	0.95	0.99	0.98

From the previous tables it could be clearly seen that the tower has not been defected by any of the two earthquakes, represented by the almost unity values spread everywhere in the three previous tables. But in Table 5.13 lower values of COMAC is produced for both cases at the first two sensors (i.e. degrees of freedom). These sensors are located on first level of the tower above the ground

which is expected to be more sensitive to the ground motions. Therefore, it could be said that COMAC in this case showed more sensitivity to the effect caused by earthquakes.

4.3 Conclusions

The benefits of establishing a health monitoring system for structures are various, and one of the most valuable benefits that could be gained from such system is the ability to assess the structure after an occurrence of some extreme events, which would give an alarm about the structure condition to the responsible persons to be able to take a suitable decision to avoid any possible tragedy.

The tower under consideration in this research work experienced several extreme events during its construction period at various achieved levels. The condition of the structure after three typhoons and two earthquakes is assessed by calculating three coefficients (namely; MAC, COMAC, and MCC); that evaluates the structure based on the mode shape consistency before and after the extreme event.

Generally, the results of the conducted assessments for all the considered cases showed that the tower did not give any sign for a possible formation of damage in the tower. This was proved by the almost unity value produced for all results of the three coefficients in all cases, as for the calculated coefficients the possibility of damage is decreasing as the values are approaching the unity. However, the results are slightly varying from one coefficient to another for the different cases of dynamic loading; for example; in case of earthquakes COMAC values at lower sensor positions were not as high as those of MAC and MCC, and MCC in general was not giving a perfect condition of the assessed tower. This leads to declare that; generally, the more sensitive coefficient to modes inconsistency is MCC. Therefore, it is recommended in structure's assessment to choose the most sensitive index to the case of dynamic loading, and the more number of possible indexes of assessment are calculated is the better configuration of the tower condition given.

Chapter 5

Signal Processing by Improved HHT Method

5.1 Introduction

The improved Hilbert–Huang transform method explained previously in Chapter 2 is used to analyze the signals of GTVT response. The processed signals are obtained from the series of accelerometers utilized to monitor the tower behaviour in normal conditions and under extreme events as well. In this chapter, the response of the tower upon seven different extreme events is analyzed using the improved HHT by filtering approach. These events are the previously mentioned five typhoons (i.e. Kammuri, Hagupit, Nuri, Molave, and Koppu) and two earthquakes occurred in the near region of Guangzhou city namely; Southern Taiwan earthquake which occurred on the 4th of March 2010, and Taiwan Hua-Lien earthquake which occurred on the 19th of December 2009.

5.2 Response of GTVT to Typhoons

In this section; the response of the tower to the five typhoons discussed in details in Chapter 3 is analyzed. Therefore, wind properties will not be

mentioned again and will be referred to those previously explained. Also the signals that are processed here are extracted from those of chapter 3.

To facilitate the analysis procedure of the signals of response, a segment of 15 minutes is extracted from the response available data for each typhoon. Figure 5.1 shows the time history of 15-minute acceleration chosen from the 3-hour data available of Kammuri typhoon. This signal was measured by sensor number (11) which is at 272 m height.

The adopted improved HHT technique based on filtering approach is applied on the aforementioned signal to produce the Hilbert spectrum as follows:

At the beginning, the peak detection method is applied on the signal to detect the tower principal frequencies by performing Fast Fourier Transform (FFT) and producing the Power Spectrum Density (PSD) Figure 5.2 shows the PSD obtained and the peaks of the diagram (f_0) are detected and indicated by small circles in the frequency range of 0 to 1 Hz.

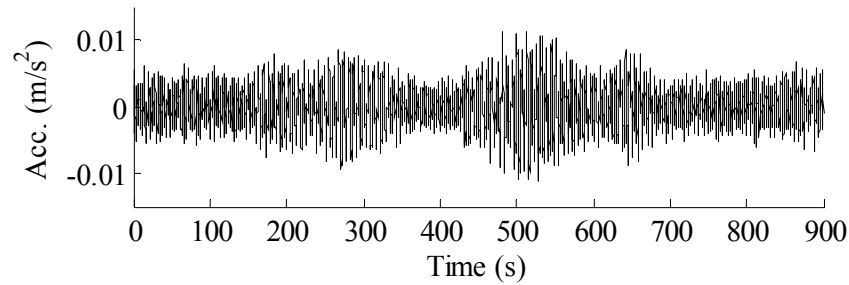


Figure 5.1. Response time history for 15 minutes during Kammuri typhoon.

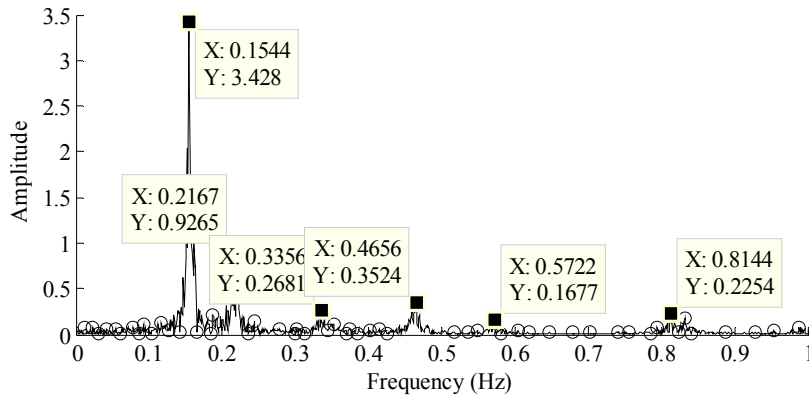


Figure 5.2. PSD spectrum by FFT of Kammuri typhoon response signal.

Subsequently, the band-pass filters with a similar frequency bandwidth of 0.001 Hz are designed to extract the monocomponents related to each detected peak in PSD. The filter coefficients are calculated by utilizing a ready program provided by Matlab toolbox of signal processing named 'firls.m'. The frequency response of the filter is illustrated in Figure 5.3. The monocomponent functions are then extracted by using the designed filter.

After that, it is essential to keep the energy reserved; the power of the derived monocomponent function is calibrated as explained previously in Chapter 2

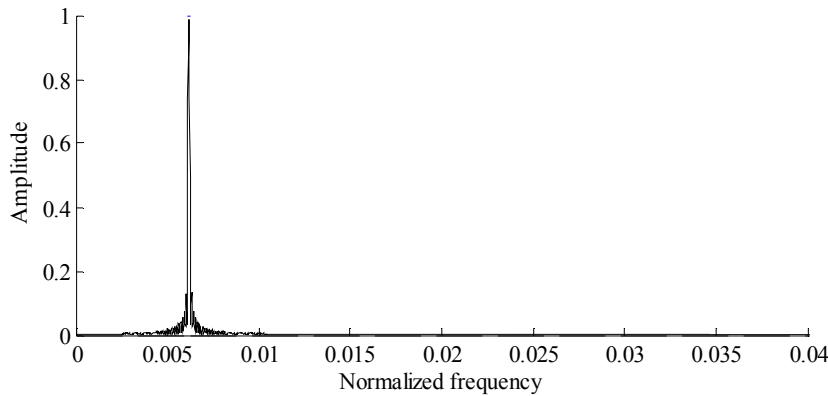


Figure 5.3. Frequency response of the designed filter.

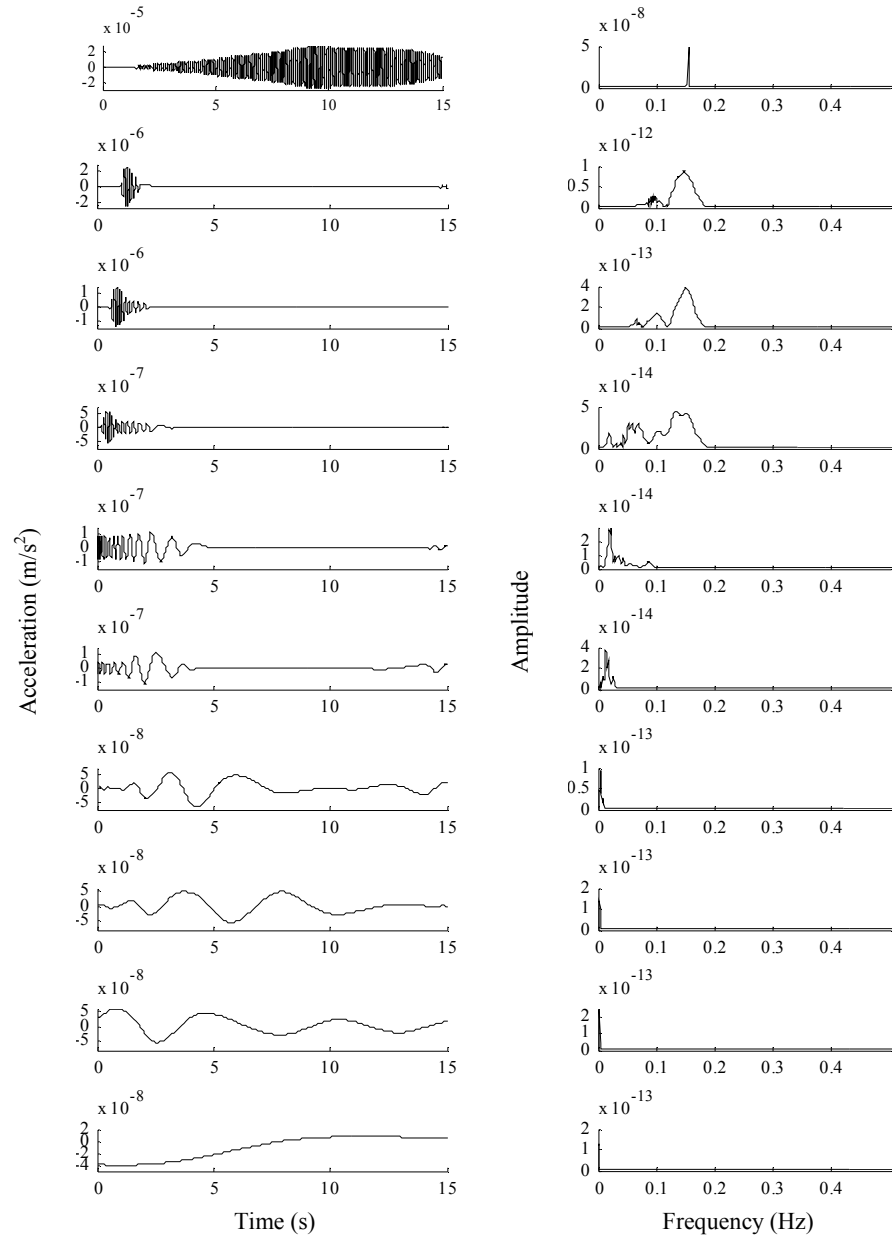


Figure 5.4. IMFs and their relevant PSD

The EMD is then employed to extract the IMFs from the calibrated function as shown in Figure 5.4, which shows also the relevant PSD for each IMF. From the figure it could be seen that the first IMF has almost become a true monocomponent function, so it is taken as a new IMF and the other IMFs will be regarded as part of the residue of the whole EMD.

After obtaining all new IMFs corresponding to the selected principal frequency components, the instantaneous time–frequency features of the signal are extracted by the Hilbert spectrum as shown in Figure 5.5.

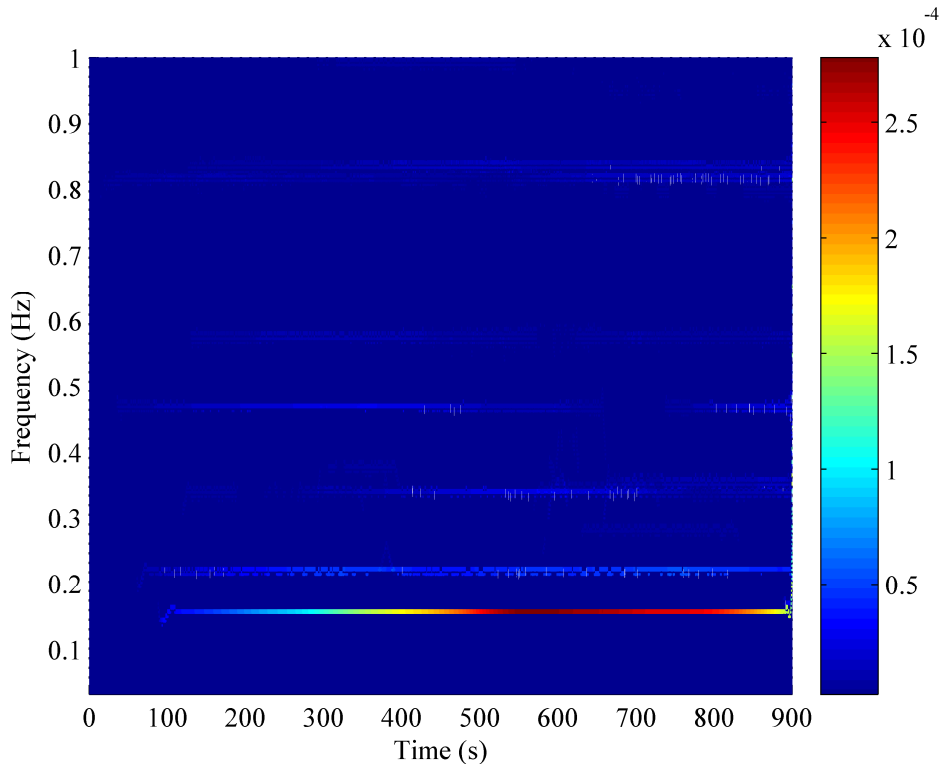


Figure 5.5. Improved Hilbert spectrum of Kammuri typhoon response signal.

The same procedure is applied to perform the Hilbert spectrum of the response signal recorded under the exposure to the other four typhoons. Figures 5.6 to 5.9 show the time histories and the corresponding Hilbert spectrum for

15-minute segment extracted from each relevant data of the typhoons (i.e. Nuri, Hagupit, Molave, and Koppu, respectively). Other spectrums for signals measured along the tower height during all extreme events are figured in Appendix C.

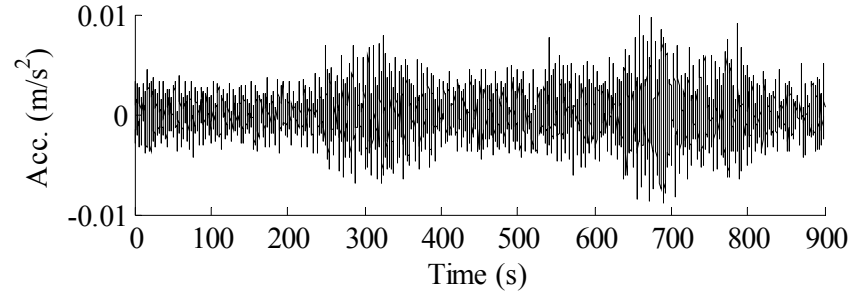


Figure 5.6.a. Response time history for 15 minutes during Nuri typhoon.

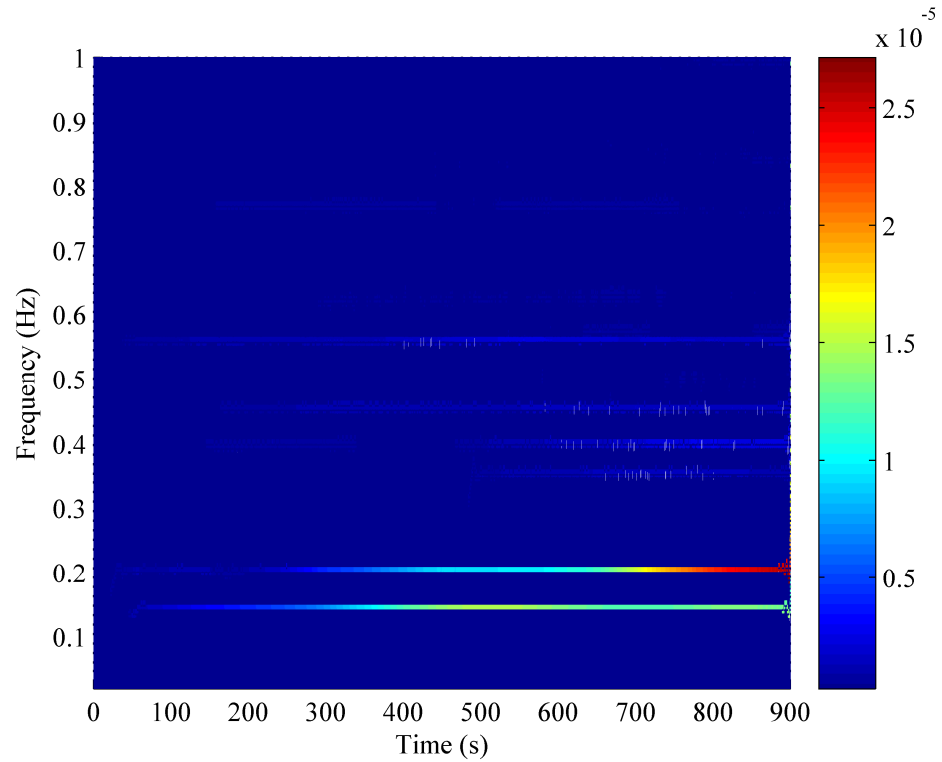


Figure 5.6.b. Improved Hilbert spectrum of Nuri typhoon response signal.

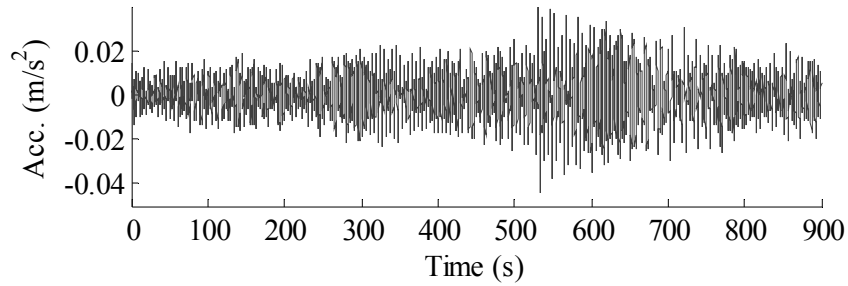


Figure 5.7.a. Response time history for 15 minutes during Hagupit typhoon.

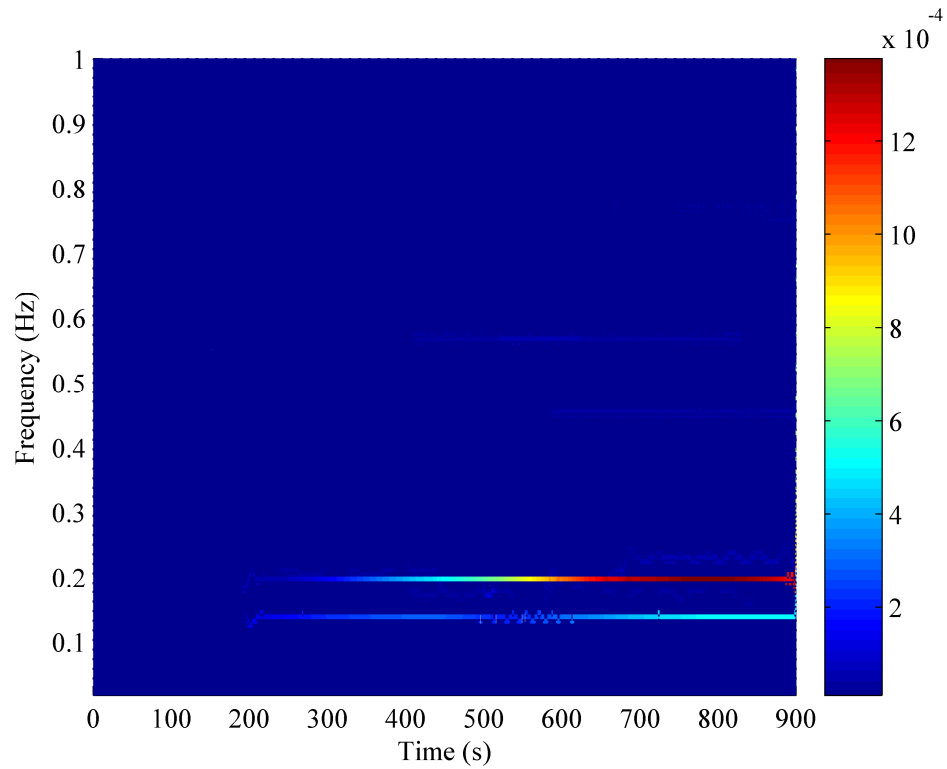


Figure 5.7.b. Improved Hilbert spectrum of Hagupit typhoon response signal.

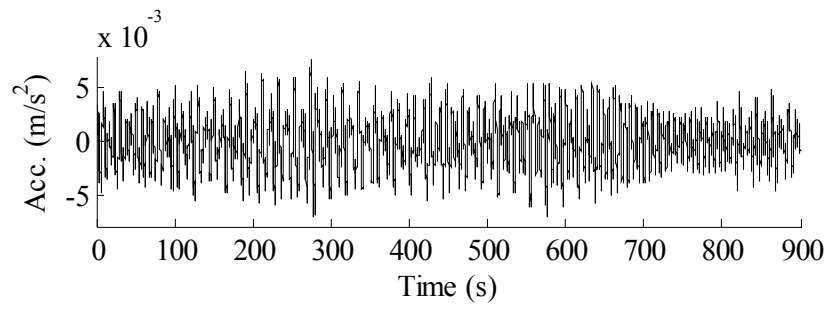


Figure 5.8.a. Response time history for 15 minutes during Molave typhoon.

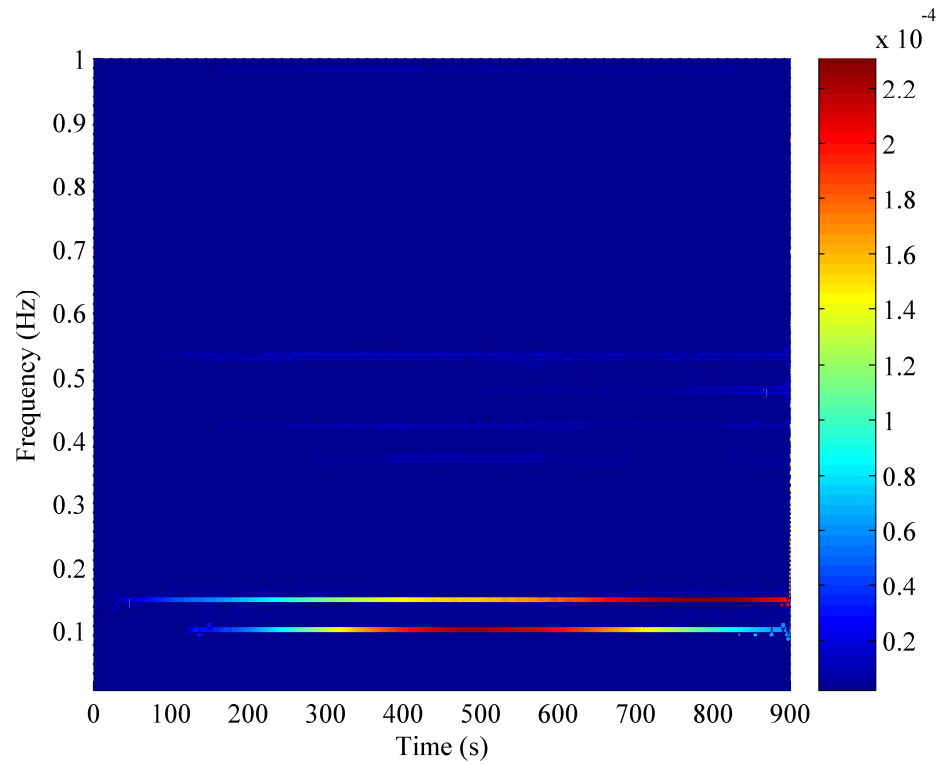


Figure 5.8.b. Improved Hilbert spectrum of Molave typhoon response signal.

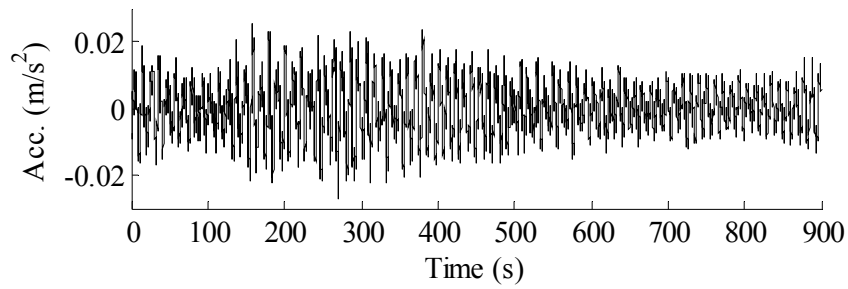


Figure 5.9.a. Response time history for 15 minutes during Koppu typhoon.

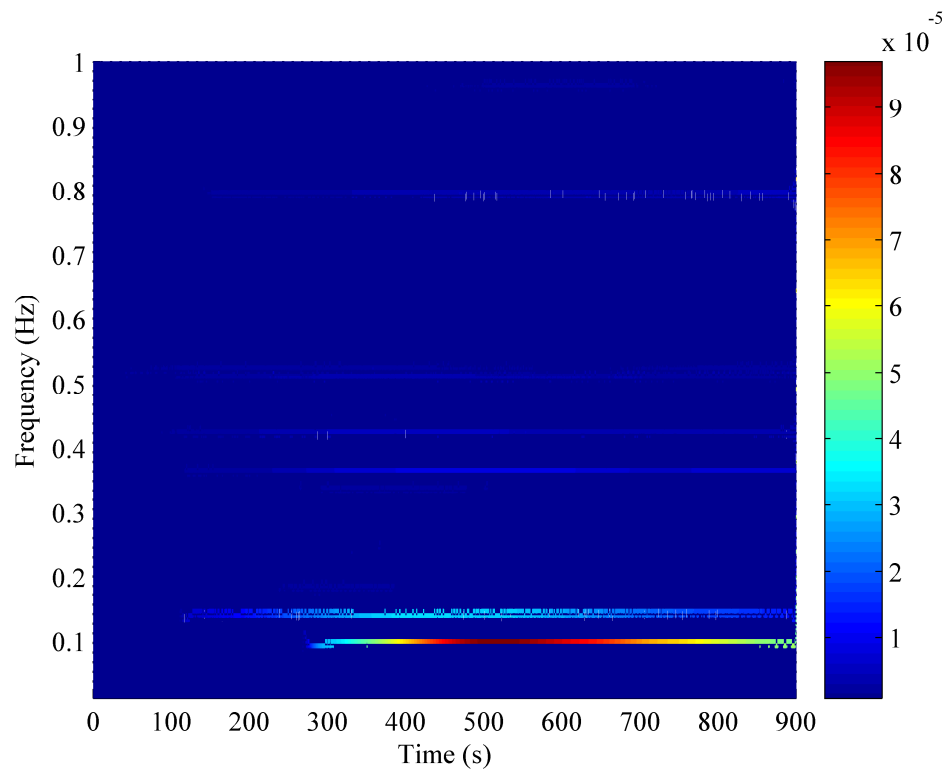


Figure 5.9.b. Improved Hilbert spectrum of Koppu typhoon response signal.

From the previous figures of Hilbert spectrum, the fundamental frequency variation of the tower could be detected during the various typhoons. It is clear from all the spectrums that the first two modes were dominant during all the typhoons, proven by the higher energy lines drawn for these modes.

The detected frequencies during Kammuri typhoon (Figure 5.4.b) were fluctuating slightly around the following values (in ascending order): 0.15, 0.21, 0.46, 0.57, and 0.81 Hz, while in case of Nuri event the first four frequencies that can be clearly detected were: 0.14, 0.2, 0.45, and 0.56 Hz (Figure 5.5.b). As expected the frequencies were decreased due to the increase of the tower height achieved when Nuri typhoon happened. However, relatively less decrease in frequency values was noticed during Hagupit typhoon due to the less mass added to the body of the tower. As presented in Figure 5.6.b the first four fundamental frequencies are: 0.135, 0.195, 0.445, 0.56 Hz.

The signals from typhoons occurred when the last level of tower the was constructed (namely; Molave, and Koppu) showed relatively high difference in the first fundamental frequencies; Figure 5.7.b proves that the highest energy during the Molave typhoon were at 0.098 and 0.144 Hz which are the frequencies of the first and second mode of vibration, while the energy at 0.42, 0.47, and 0.52 Hz, was high enough to indicate them as the other fundamental frequencies. However, from Figure 5.8.b it can be seen that the highest energy is at first mode (i.e. 0.094 Hz) and relatively less energy is detected for the other modes (i.e. 0.14, 0.36, 0.42, 0.79 Hz). It is noticeable also that the two typhoons are not stimulating similarly the higher modes of the tower; as no clear energy is noticed at 0.79Hz during Molave and at 0.47 Hz during Koppu.

The figures of the selected time history periods for all typhoons show a highest maximum acceleration induced in the tower in case of Hagupit typhoon which reached to 0.04 m/s^2 , consequently the highest energy was imparted to the second mode of the tower during that typhoon. However, when considering the completed tower, Molave typhoon imparted higher energy to first and second modes of vibration of the tower that that of Koppu despite the higher acceleration induced by Koppu typhoon.

5.3 Response of GTVT to Earthquakes

In this section, two earthquakes occurred in the region where the GTVT stands are briefly discussed, and the response of the tower to these ground motions was recorded by the SHM system and is analyzed by the improved HHT method.

5.3.1 Southern Taiwan Earthquake

On the 4th of March 2010, a strong earthquake of Richter magnitude 6.4 struck southern Taiwan at 8:18 a.m. The quake centered at 17 km southeast of Jiasian Township in Kaohsiung County. It was the most powerful earthquake in Kaohsiung County since 1900. The energy released was equal to two Hiroshima nuclear bombs (China post).

The earthquake was a shallow-focus earthquake with a depth of 5 km, and shallow earthquakes usually cause more damages than deeper earthquakes as they are released closer to the surface and there is less rock to absorb the shaking, and they tend to have a lot more aftershocks. 226 aftershocks were recorded, with the biggest one measured magnitude 5.7.

The earthquake could also be felt in various cities in Guangdong province and Fujian province (e.g. Guangzhou, Shenzhen, Shantou and Fuzhou).

5.3.2 Taiwan Hualien Earthquake

The 2009 Hualien earthquake of a 6.4 magnitude occurred on December 19, 2009 off the coast of Hualien-Taiwan. The Central Weather Bureau put the magnitude at 6.8. The earthquake could be felt in many places in the vicinity, just like Hong Kong and Xiamen, China, and on several islands between Yonagumi and Tarama, Japan (China post).

5.2.3 Response analysis

The two mentioned earthquakes caused ground motions at the city of Guangzhou which could be clearly felt, and the dynamical response of GTVT to these ground motions was recorded by 17 sensors in case of Southern Taiwan (ST) earthquake, and 19 sensors for Taiwan Hualien (TH) earthquake. The sensors were mounted at different elevations up to the last level of the tower as it was fully constructed at the time of these earthquakes occurrence. The acceleration time history obtained from sensor number 14 is illustrated in Figure 5.10 for six minutes of response under ST-earthquake,. Similarly, the response due to TH-earthquake for five minutes is shown in Figure 5.11 obtained by sensor number 17. The sampling frequency of both signals is 50 Hz.

Consequently, the improved HHT method is applied on both signals, following the same procedure explained in the previous section, and the corresponding Hilbert spectrums are drawn in Figure 5.12 and 5.13 for the signal obtained under ST earthquake and TH earthquake, respectively.

In general, the measured acceleration induced in the tower by HT earthquake is larger than that induced by ST earthquake (Figure 5.10 and 5.12), therefore, the resulted energy imparted to the modes of the structure are higher in case of HT earthquake.

The fundamental frequencies of the first modes of vibration can be clearly detected from both Figure 5.11 and 5.13. These frequencies are almost the same values in both cases which are (in ascending order): 0.093, 0.14, 0.36, 0.42, 0.47, 0.52, 0.79 and 0.96 Hz. Nevertheless, apart from the first mode, the modes of higher energy are not the same in both cases; for ST earthquake high energy appeared in the fifth, sixth and seventh mode of vibration, while the highest stimulated mode in case of TH earthquake was seventh, which means that the two different earthquakes did not have the same effect on the tower and higher modes should be taken in consideration in such cases of extreme events.

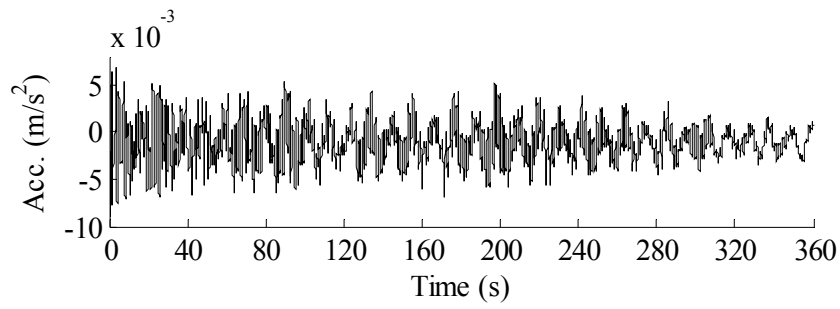


Figure 5.10. Time history response to ST earthquake.

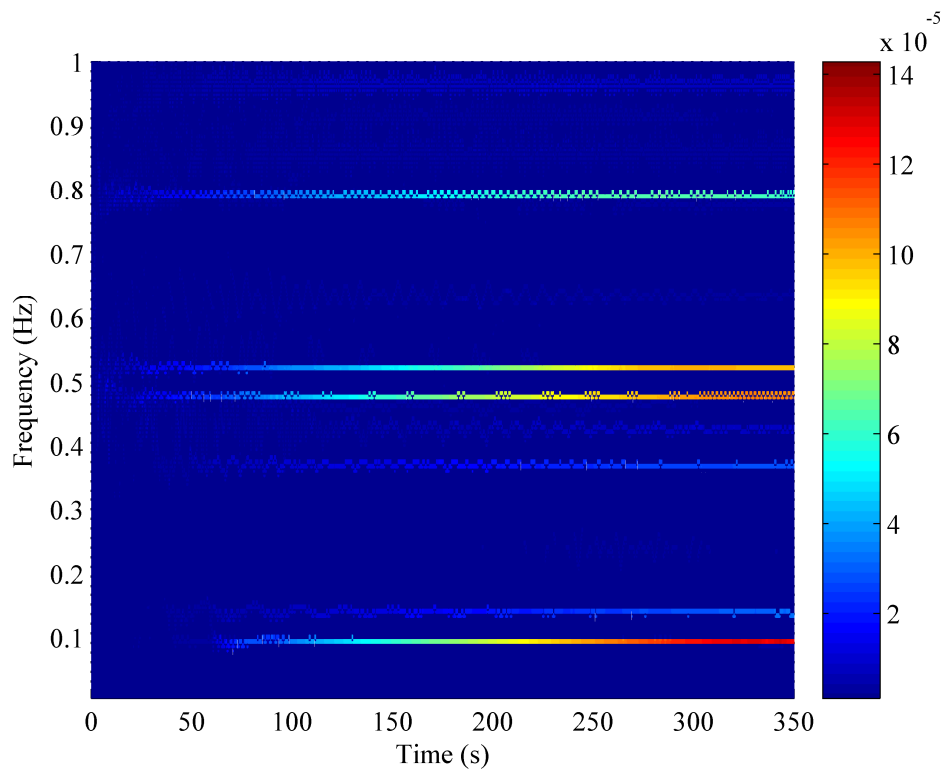


Figure 5.11. Improved Hilbert spectrum of ST earthquake response signal.

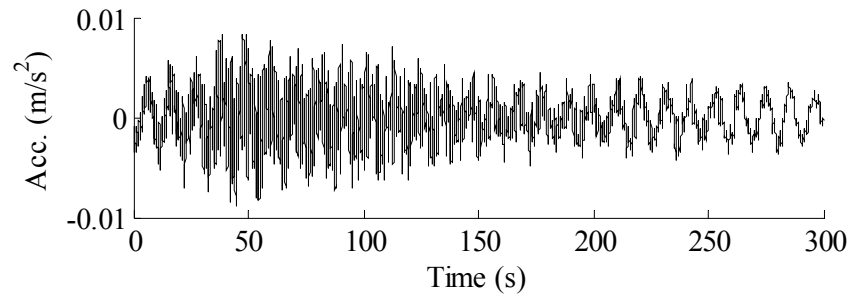


Figure 5.12. Time history response to TH earthquake.

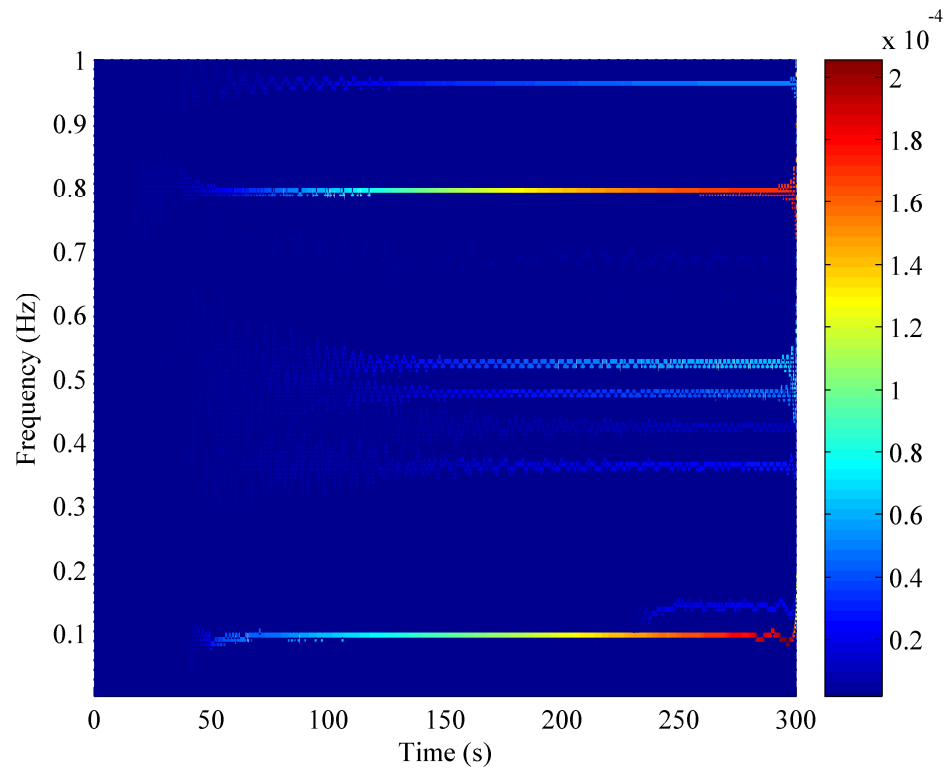


Figure 5.13. Improved Hilbert spectrum of TH earthquake response signal.

5.3 Results Discussion

In order to demonstrate the efficiency of the improvement adopted on HHT method Figure 5.14 is drawn; which illustrate the regular Hilbert spectrum without any improvement for the signal recorded during Kammuri typhoon.

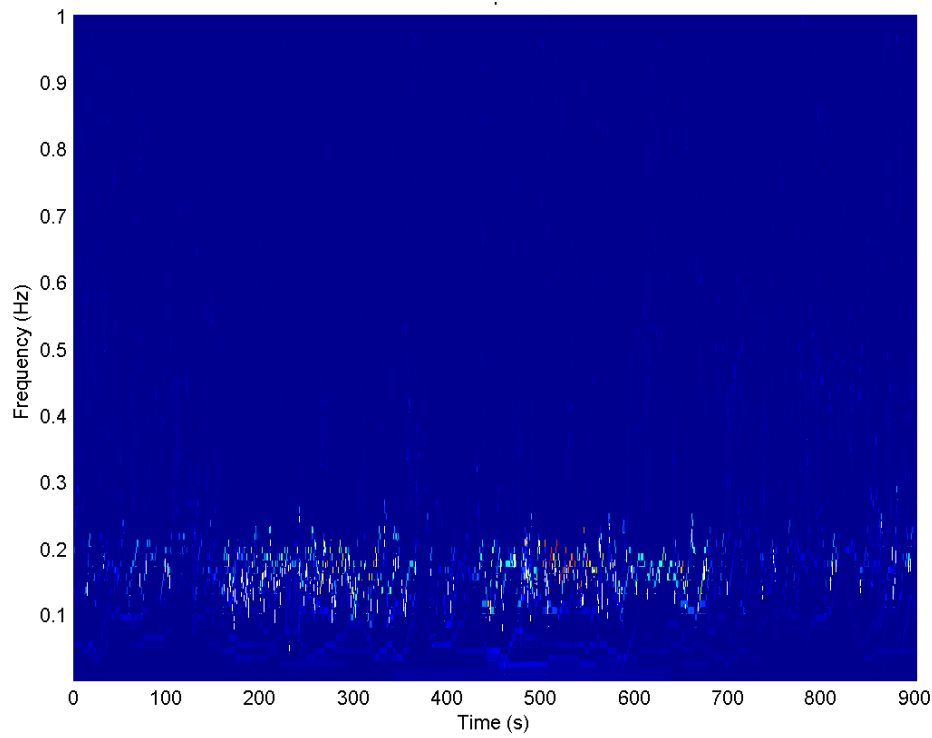


Figure 5.14. Regular Hilbert spectrum of Kammuri typhoon response signal.

The purpose of the EMD is to decompose a signal into a number of simple IMFs. However, it has been proved that, the EMD can not decompose the narrowband multi-harmonic signal, so the derived IMFs often comprise multiple frequency components. In other words, the monocomponents in the signal of acceleration response are not completely isolated from each other by

the EMD. Thus it is reasonable to believe that the confusing time-frequency information presented in Figure 5.14 is indeed generated by the IMFs with multiple frequency components creating mode mixing problem.

Comparing the resulted Figure 5.14 with Figure 5.5 produced by the improved approach the difference can be clearly seen. The interference is absent in Figure 5.5 in which the Hilbert spectrum shows the capacity, by adopting this improvement, to present the variation of each instantaneous frequency in the time and frequency domain.

Furthermore, when considering the FFT spectrum shown in Figure 5.2, it shows that the greatest energy components at 0.154 Hz and 0.217 Hz are exactly the first and second vibration modes of GTVT at the time when Kammuri typhoon occurred, however, it can not give any local time information except exhibiting an overall energy distribution in the frequency domain. On the other hand, the principle frequencies obtained by the improved HHT method can coincide quite well with those of FFT spectrum, and it could capture the energy variation in both the time and frequency domains.

It also could be found from Figure 5.5 that the frequencies of the modes beyond the first and second can be also easily detected. Furthermore, the frequencies of the third and fourth modes calculated in Chapter 3 by FDD method during Kammuri typhoon are 0.46 Hz to 0.57 Hz respectively, which coincide with the frequencies obtained from Figure 5.5. The same mentioned coincidence is also noticed and proved by the results of the other typhoons, which means that the improved HHT method based on filtering approach is able to present all principle vibration frequencies of GTVT when excited by typhoon wind loading rather than highlighting the largest energy one.

When considering the Hilbert spectra drawn for the period during the earthquakes excitation, one more advantage of the improved HHT can be gained. The variation of the frequency with time shown in Figure 5.13 (for example) can give an almost clear idea about when exactly the tower started to be in dynamical motion, when the energy has suddenly increased significantly in the whole concerned frequency range; which means that the spectrum can also indicate the time in which the earthquake started to affect the tower. This

indicates that the Hilbert spectrum has a fine time resolution and is capable of capturing the time information.

While in case of typhoons this could not be achieved as the wind starts gradually to affect the tower and mostly not with a significant starting shock, therefore, the energy was not increased sudden. This property of the improved HHT spectrum could be more useful and more sufficient in many other cases like; an earthquake or even a collision of some vehicle to a structure or a nearby explosion, because spectrums produced by other methods like FFT are unable to give any local time information except exhibiting an overall energy distribution in the frequency domain.

Aiming at detecting any commencement of structural damage (Pines and Salvino 2002), two essential phenomena must be investigated, that are imparted by the Hilbert spectrums improved by filtering approach:

- 1) The reduction in modal frequencies may indicate the loss of structural stiffness, hence a sign for structural deterioration.
- 2) Spreading of vibration energy between near modes as an energy intensity decrease suggests the presence of structural nonlinearity.

Inspecting all the results obtained by the improved HHT method based on filtering, during both typhoons and earthquakes, the instantaneous frequencies of individual vibration modes almost remain constant with small modulations during the selected time range of the signal processing. Nevertheless, some small modulations may be resulted from the relatively small frequencies distribution in these components and noise effect.

The generally constant instantaneous frequencies indicate the stiffness of GTVT is invariant during the considered typhoons and earthquakes periods. Also, in the frequency domain, the distribution energy intensity of each mode is within the narrowband, without any energy shift to other bands in every obtained Hilbert spectrum, which indicates that no nonlinearity appeared. From both the instantaneous frequency information and the energy distribution information, it could be concluded that the GTVT did not suffer from damage during all considered extreme events. However, damage assessment of is tower based on HHT analysis is elaborated in more details in the next chapter

5.4 Conclusion

The tower under consideration in this thesis is located in a region where several kinds of extreme events occur frequently. Typhoons and earthquakes effect on the tower are studied through analyzing the dynamical response of the tower during these events. The vibration of the tower is measured by the integrated SHM system and the obtained signal is processed.

The HHT method is adopted in this chapter in signal processing with an implemented improvement based on filtering approach, and the corresponding spectra are drawn for the signals obtained during five different typhoons (namely; Kammuri, Nuri, Hagupit, Molave, and Koppu typhoons), in addition to two earthquakes affected the region of the tower (namely; Southern Taiwan, and Hualien earthquakes).

The improved approach proved the ability to express the dynamical behavior of the structure in both the time and frequency domain. Nevertheless, the resulted fundamental frequencies presented by the improved HHT method are almost the same as the FDD method. And because the improved HHT method possesses a strong power against noise, the first two vibration modes of GTVT which were dominant during the typhoons are presented in the HHT spectrum clearly.

When investigating the response to earthquakes, improved HHT method figured clearly the high energy imparted to higher modes of the tower which were dominant. Furthermore, it was possible to detect the time at which the tower started to have a significant response to the ground motions; by tracking the point at which the energy started to have a sudden increase in the tower various vibration modes.

It could be concluded from improved Hilbert spectrums that the dynamical behaviour of the tower did not alarm for any damage during the considered extreme events. This conclusion is proven by the almost constant frequency in the studied time period for each signal, in addition to the distribution energy intensity of each mode which remained within the narrowband without any

energy shift to other bands in every obtained Hilbert spectrum, hence, no nonlinearity appeared in the body of the structure i.e. no commencement of structural damage is detected.

Chapter 6

Damage Assessment of GTVT Based on HHT Analysis

6.1 Introduction

In the previous chapter, the empirical mode decomposition associated with Hilbert spectral analysis has shown promising results in the analysis of time-series data. This great potential could be applied to help the diagnosis and the prognosis of structures, which has been the main concern of several researches (Bao et al. 2009, and Chen et al. 2007). A standard criterion is the key tool to infer if the damage occurred and, in case, the size of damage. From the measurement of a specific physical property of the structure (damping, stiffness, energy...), a metric will give the necessary information to alert for damage and to quantify the severity of the damage. This chapter is therefore dedicated to the investigation of the HHT and EMD features that could be used to obtain robust and efficient metrics for damage detection in structures.

The following sections; discuss the possibility to reach a dependable damage assessment for the GTVT; firstly, by investigating the instantaneous frequency and phase angle produced by HHT analysis, then, by the aid of the previously

presented coefficients in Chapter 3 (namely: MAC, COMAC, and MCC), but this time mode shapes produced by HHT analysis will be considered. Finally, a proposed damage index based on EMD approach is presented and discussed in detail.

6.2 Instantaneous Frequency and Phase Angle

To identify, locate and quantify structural damage is the main purpose of SHM system. Most of currently used structural damage detection methods are built on the idea that the measured modal parameters or the properties derived from these modal parameters are functions of the physical properties of the structure; and hence, changes in the physical properties will cause detectable changes in the modal parameters. Such methods start from available data for the undamaged structure to be compared with data recorded after the occurrence of an event that could cause structural damage. Therefore, if for any reason there is a sudden damage event occurring during the measurement period, these methods cannot be used to find when the damage event occurs.

In this connection, some researchers has recently suggested exploiting instantaneous phase features of the vibration signals combined with wave mechanics based concepts for damage detection (Zemmour A. 2006). Compared to the other time-frequency methods; the Hilbert instantaneous phase is a unique feature that describes the traveling structural wave propagation. Salvino and Pines (Salvino and Pines 2006) have proved the dependency of the phase on the structural parameters as stiffness, mass and damping. The Hilbert instantaneous phase turns therefore out to be an interesting feature to investigate for damage detection metrics.

This section studies the applicability of EMD followed by HHT analysis in extracting the instantaneous frequency and phase angle from data recorded during extreme events for GTVT; in order to reach for an online identification of structural damage that could be caused by a sudden change of the structural stiffness.

The tower under consideration in this research has been investigated and assessed in the previous chapters and the results have not shown any possible damage that could be caused by the various extreme events the tower was exposed to. Consequently, in this section the tower is expected to show the same results of no damage as the same data will be processed again but with different methods. Therefore, it worth's demonstrating how instantaneous phase angle and frequency were sufficient tools in detecting damage in previous researches before applying the concept to the tower available data.

Yang and his coauthors (Yang et al. 2004) used time-frequency relation in detecting the damage time instants. The study was conducted on a 4-story benchmark structure and damage patterns were achieved by removing the bracings from one floor of the structure at certain time instant during measuring the response of the structure, data were then processed. Figure 6.1 shows the time-frequency relation produced. It is clearly proven in this figure that the structure suffered a drop in its fundamental frequency, which means loss in its stiffness, and the moment at which this drop happened can be easily identified from the figure.

Whereas, Zemmour (Zemmour A. 2006) simulated the dynamic behavior of a rod in finite element analysis, and the assumed damage was performed by changing the material property of one element to be less at certain time instant. The obtained response is then processed and the phase angle with time relation is drawn; in which it was clear that the reflection from the damage is interpreted by a slope change in the Hilbert phase.

Physically, any damage in a structure alters the speed at which the energy traverses the structure, and once the wave passed through the damage, the energy speed is no more affected and the Hilbert phase behaves in the same manner. Furthermore, the slope change appears to be dependent on the size of the damage. The energy speed propagation would be therefore altered in a different way depending on the size of the damage. This implies that one can track increasing amount of damage as a function of phase. Thus, the Hilbert phase allows the size and location of damage to be determined.

In another study (Bernal and Gunes 2000), the concept of instantaneous frequency was examined as a potential candidate for damage detection purposes. This was achieved by developing a numerical model of a 4-story shear building, then subjecting it to El Centro ground motion, and after 10 seconds the first floor was assumed to suffer a sudden 80% loss in stiffness. The acceleration on the roof level through the experiment is then evaluated and the obtained signal is processed by EMD and HHT to reach for the time-phase and time-frequency plots shown in Figure 6.2 and 6.3, respectively. From the figure one can easily see the indication of damage in the change in slope of the phase angle and the drop of the instantaneous frequency around time=10 seconds.

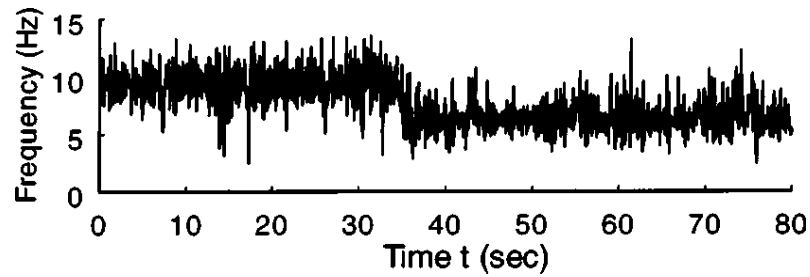


Figure 6.1 Frequency variations with time (Yang et al. 2004).

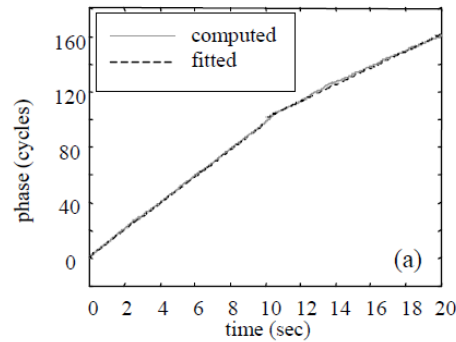


Figure 6.3. Instantaneous phase (Bernal and Gunes 2000).

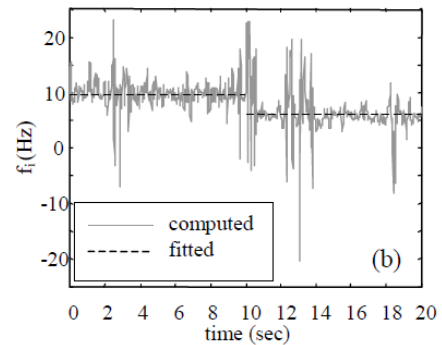


Figure 6.4. Instantaneous frequency (Bernal and Gunes 2000).

6.2.1 Calculation procedure

Recently, many definitions for instantaneous frequency have been developed. This search for alternative definitions has been motivated by the fact that in many cases the variability of the phase angle is large and, as a consequence, the frequency has large fluctuations about the mean value. In any case, there has been consensus on the fact that the concept of instantaneous frequency is physically meaningful only when applied to monocomponent signals (Bernal and Gunes 2000). Therefore; in order to extract physically meaningful information, it is necessary to first decompose the signal into a series of monocomponent contributions, which can be achieved by EMD technique explained previously in Chapter 2.

The isolation of modal responses using the EMD method has a significant advantage in that the frequency content of the signal at each time instant has been persevered. This is the reason why it is possible to determine the damage time instant very accurately as shown in Figures 6.1-6.3. However, the numerical computation based on this approach may be quite involved by high level of noises. Therefore the adopted filtering approach in the previous chapter is also proposed in this case prior to the decomposition.

The procedure can be summarized as follows: The EMD technique decomposes the signal into a series of monocomponent contributions designated as IMF's, and the procedure for identifying the natural frequencies of the system can be accomplished easily by the decomposition of the filtered signal (as described in Chapter 2), and then performing the HHT analysis on the first IMF resulted by the decomposition to produce the time-phase and time-frequency relations as defined by Equations 2.3.4 and 2.3.5 respectively. The instantaneous frequency ($f(t)$) in (Hz) units can then be calculated as follows:

$$f(t) = \frac{1}{2\pi} \frac{d\theta(t)}{dt} \quad (6.2.1.1)$$

6.2.2 GTVT assessment during typhoon event

The available response data of the case study in this dissertation permitted the application of this damage detection criterion on a real standing structure response to an extreme event. The obtained signal during Koppu typhoon is processed by the previously explained procedure. The response obtained by sensor 19 shown in Figure 6.4. is considered:

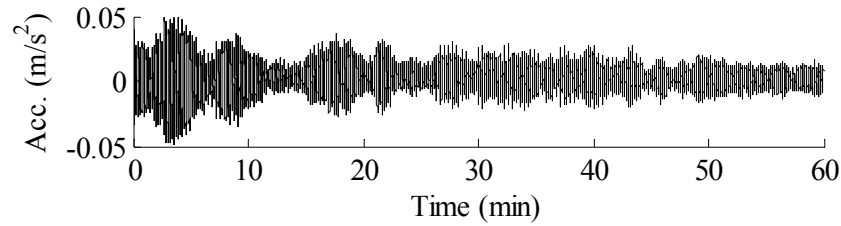


Figure 6.4. Time History response to Koppu typhoon measured by sensor 19.

The FFT is performed for the signal, and then the peak picking procedure. The adopted filtering approach in previous chapters is then applied by developing a band pass intervals containing the peaks corresponding to the fundamental frequencies of the tower. The resulted signals are then decomposed by the EMD to several IMFs, and finally the instantaneous phase and frequency are obtained for every first IMF produced from the decompositions.

The first IMF resulted from the decomposition of the signal filtered around the first fundamental frequency of the tower is shown in Figure 6.5, whereas, Figures 6.6 and 6.7 show the time-phase and time-frequency relations, respectively, for that IMF.

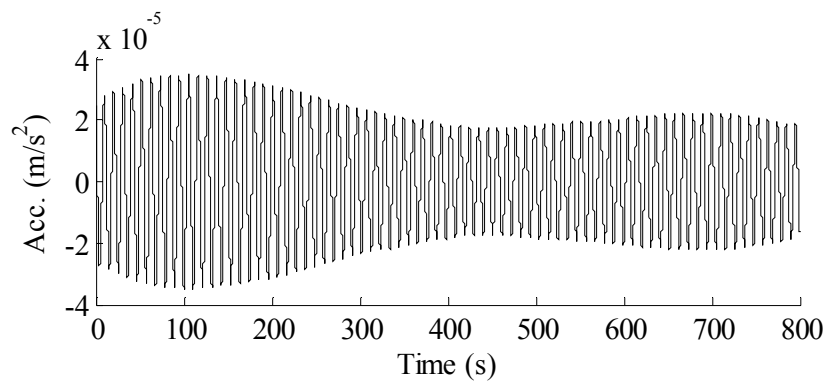


Figure 6.5. IMF 1 of the filtered signal at the first fundamental frequency.

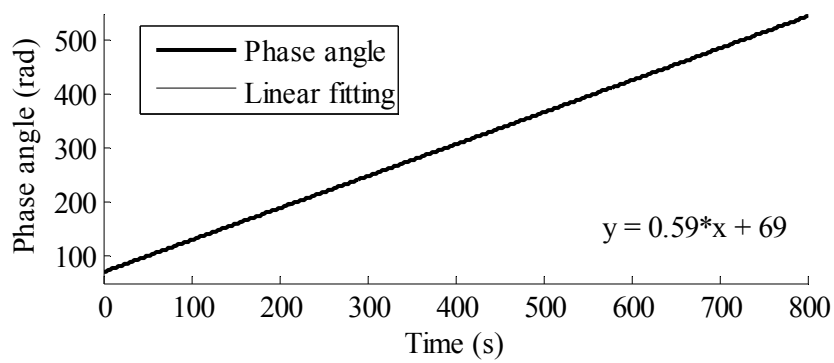


Figure 6.6 Instantaneous phase angle of IMF1

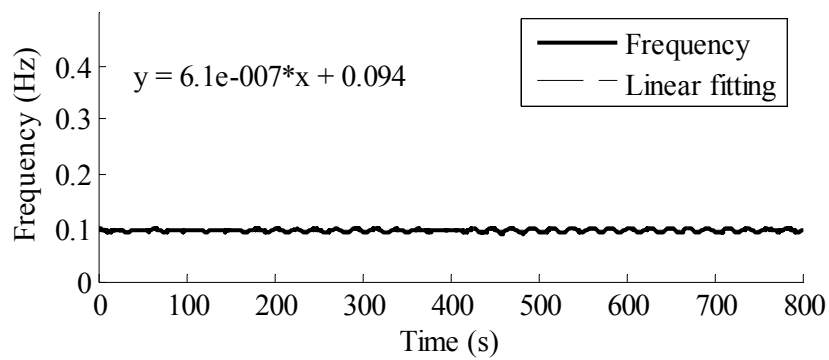


Figure 6.7. Instantaneous frequency of IMF1.

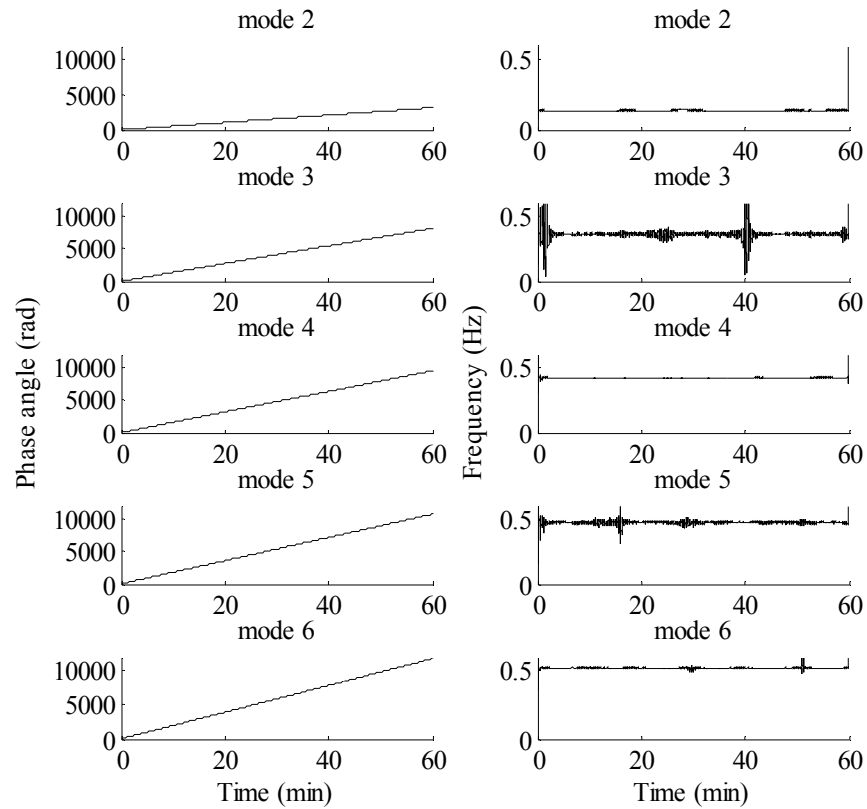


Figure 6.8. Instantaneous frequency (right) and phase (left) for first IMFs of the 2nd to 6th modes.

Figure 6.6 shows a constant slope for the phase angle with time. The slope is indicated on the figure equal to 0.59 and it is clearly seen that the linear fitting line of this slope is totally coinciding with phase angle curve. Furthermore, Figure 6.7 shows slight fluctuation of the frequency around the first fundamental frequency of the tower (0.094). Also a fitting line is drawn to ensure that the curve is not fluctuating around a decreasing value, and the slope of the fitting line is almost zero as indicated in the formula; which means that the frequency is constant.

The same results are obtained from the first IMFs of the signals filtered around the 2nd to the 6th fundamental frequencies of the tower as shown in Figure 6.8. Thus no damage alert in the structure of GTVT during Koppu typhoon is inferred from analyzing the first six fundamental modes. This result confirms the performed damage assessment of the tower in Chapter 4. However, the response obtained by only one sensor is analyzed in this section; therefore, processing the other available signals at other locations would give more confident assessment.

6.3 Fundamental Modes Consistency

Previously in this dissertation; a mode-consistency assessment of the GTVT structural condition is performed based on the operational modal analysis results obtained by FDD method, processing the ambient vibration response signal of the tower obtained before and after being exposed to severe events. Damage identification algorithms (namely: MAC, COMAC, and MCC) were calculated from the resulted mode shapes, and the damage assessment was achieved.

In this section, the same criteria of damage assessment by performing the aforementioned coefficients are repeated again but to assess the consistency of the mode shapes of the tower calculated by the aid of HHT improved by the adopted filtering approach.

6.3.1 Mode shapes by HHT

Recently, several researchers reached for convenient criterion to obtain mode shapes by HHT (Yang et al. 2003, and Chena et al. 2004). The process starts with the equation of motion of an n DOF structure, expressed as

$$M\ddot{X}(t) + C\dot{X}(t) + KX(t) = F(t) \quad (6.3.1.1)$$

Where; $X(t)$ is the n-displacement vector, $F(t)$ is the n-excitation vector, and M , C , and K are (n×n) mass, damping and stiffness matrices, respectively. Assuming normal modes, the displacement and acceleration responses can be decomposed into n real modes, as follows:

$$X(t) = \sum_{j=1}^n \Phi_j q_j(t) \quad ; \quad \ddot{X}(t) = \sum_{j=1}^n \Phi_j \ddot{q}_j(t) \quad (6.3.1.2)$$

In which Φ_j and $q_j(t)$ are the jth modal vector and coordinate, respectively. By substituting Equation (6.3.1.2) in (6.3.1.1) and decoupling of Equation (6.3.1.1) into n modes:

$$\ddot{q}_j(t) + 2\zeta_j \omega_j \dot{q}_j + \omega_j^2 q_j = \Phi_j^T F(t) / m_j^* \quad (6.3.1.3)$$

Where; ω_j , ζ_j , and m_j^* are the jth modal frequency, damping ratio, and mass, respectively. When the excitation $F(t)$ is a stationary white noise vector, the function of the floor responses, $(R_{rs}(\tau))$, can be obtained as:

$$R_{rs}(\tau) = \sum_{j=1}^n \phi_{rj} \alpha_{sj} e^{-\zeta_j \omega_j \tau} \sin(\omega_{dj} \tau + \theta_{sj}) \quad (6.3.1.4)$$

Where; $\omega_{dj} = \omega_j \sqrt{1 - \zeta_j^2}$ is the jth damped modal frequency, and θ_{sj} is the phase lag, and α_{sj} is a positive constant. Simplifying the equation in terms of t :

$$R_{rs}(t) = \sum_{j=1}^n R_{rs,j}(t) = \sum_{j=1}^n |\phi_{rj}| \alpha_{sj} e^{-\zeta_j \omega_j t} \cos(\omega_{dj} t + \varphi_{sj} + \frac{\pi}{2} + \varphi_{rs,j}) \quad (6.3.1.5)$$

If $B_{rs,j} = |\phi_{rj}| \alpha_{sj}$; then:

$$R_{rs,j}(t) = B_{rs,j}(t)e^{-\zeta_j \omega_j t} \cos(\omega_{dj}t + \varphi_{sj} + \frac{\pi}{2} + \varphi_{rs,j}) \quad (6.3.1.6)$$

Where; $\varphi_{rs,j}$ is the phase difference between the r th element and the s th element in the j th mode shape. With the existence of normal modes, all the mode shapes are real and hence $\varphi_{rs,j}$ is either $\pm 2m\pi$ or $\pm(2m+1)\pi$; m is an integer, i.e.

$$\begin{aligned} \phi_{rj}/\phi_{sj} > 0 & \quad \text{when} \quad \varphi_{rs,j} = \pm 2m\pi \\ \phi_{rj}/\phi_{sj} < 0 & \quad \text{when} \quad \varphi_{rs,j} = \pm(2m+1)\pi \end{aligned} \quad (6.3.1.7)$$

$R_{rs,j}(t)$ is the contribution from the j th mode. $R_{rs}(t)$ will be decomposed into modal contributions using the EMD method after being filtered by the adopted approach. Then, the HHT is applied to each modal contribution (i.e. IMF) to determine the mode shape vector (Φ_j).

Taking the HHT of $R_{rs,j}(t)$ to form the analytical function $Y_{rs,j}(t)$:

$$Y_{rs,j}(t) = R_{rs,j}(t) + iH(R_{rs,j}(t)) = A_{rs,j}(t)e^{-i\theta_{rs,j}(t)} \quad (6.3.1.8)$$

Then:

$$\ln A_{rs,j}(t) = \ln B_{rs,j}(t) - \zeta_j \omega_j t \quad (6.3.1.9)$$

In order to identify the mode shapes of the structure, the response time histories at all measuring points should be considered. From Equations (6.3.1.7) and (6.3.1.9); the ratio of the absolute value of the modal elements ϕ_{rj} and ϕ_{mj} ($r, m = 1, 2, \dots, n$) can be identified as:

$$\frac{|\phi_{rj}|}{|\phi_{mj}|} = \exp[A'_{rs,j}(t_0) - A'_{ms,j}(t_0)] \quad (6.3.1.10)$$

Where; $A'_{rs,j}(t_0)$ and $A'_{ms,j}(t_0)$ are, respectively, the magnitudes at the time ($t=t_0$) of the least-square straight lines for the decaying amplitudes $\ln A_{rs,j}(t)$ and $\ln A_{ms,j}(t)$ obtained previously. Then, the sign of ϕ_{rj} relative to ϕ_{mj} can be determined from Equation (6.3.1.7) substituting the differences between the phase angle $\phi_{rs,j}$ of the modal element ϕ_{rj} and that of ϕ_{mj} as follows:

$$\Delta\phi_{rm,j} = \phi_{rs,j} - \phi_{ms,j} = \theta'_{rs,j}(t_0) - \theta'_{ms,j}(t_0) \quad (6.3.1.11)$$

In which $\theta'_{rs,j}(t_0)$ and $\theta'_{ms,j}(t_0)$ are, respectively, the magnitudes of the least-square straight lines for the phase angles $\theta_{rs,j}(t)$ and $\theta_{ms,j}(t)$ at the time ($t=t_0$). Repeating the same procedures for all modal contributions the modal matrix Φ can be identified.

6.3.2 GTVT assessment after extreme events

The ambient vibration response of the tower before and after typhoon Hagupit is considered in this subsection aiming at identifying the mode shapes of the tower before and after the typhoon by the HHT, and then to perform the damage coefficients MAC, COMAC, and MCC. The signals are the same considered in Chapter 4 and demonstrated in Figure 4.4.

Signal obtained by sensor 16 is presented as an example hereafter. The response signals of all sensors are processed according to the following procedure:

- FFT is performed and the peaks of the spectrum are picked.
- Having known previously the approximate values of the frequencies of the fundamental modes of the tower, the corresponding peaks are considered.
- The adopted filtering approach is applied according to the frequency of the each considered peak.
- EMD is then applied on the resulted signals to obtain the first IMF from each signal. Figures 6.9a shows the first IMF corresponding to the first

fundamental frequency for the response measured before Hagupit typhoon.

- HHT is applied on the IMFs and the instantaneous phase angle and amplitude are then calculated by Equation (2.3.4) and (2.3.3). Figures 6.9b and 6.9c show the obtained phase angle and amplitude (in semi-logarithmic scale) as a function of time. And the fitting lines are drawn.
- At certain time instant ($t_0=b$) the phase angle and amplitude is obtained for the first two consecutive signals, and applied in Equations (6.3.1.10) and (6.3.1.11) to get the percentage and sign difference between them.
- The first value in the first normalized modal vector is set equal to 1, and then the second is calculated as a fraction with the appropriate sign.
- The procedure continues till the signal of last degree of freedom (i.e. measuring point), to obtain the first modal vector, and then the whole procedure is applied again on the signals of the next considered peaks to have the complete required modal matrix.

The resulted first three mode vectors of the tower obtained from the response before and after Hagupit typhoon are listed in Table 6.1. Consequently, MAC values are calculated and listed in Table 6.2. While, COMAC and MCC values are listed in Tables 6.3 and 6.4 respectively.

The results of all calculated coefficients confirm the previously obtained results of no damage appeared in the structure after being exposed to Hagupit typhoon, represented by the approaching unity value of all the calculated coefficients.

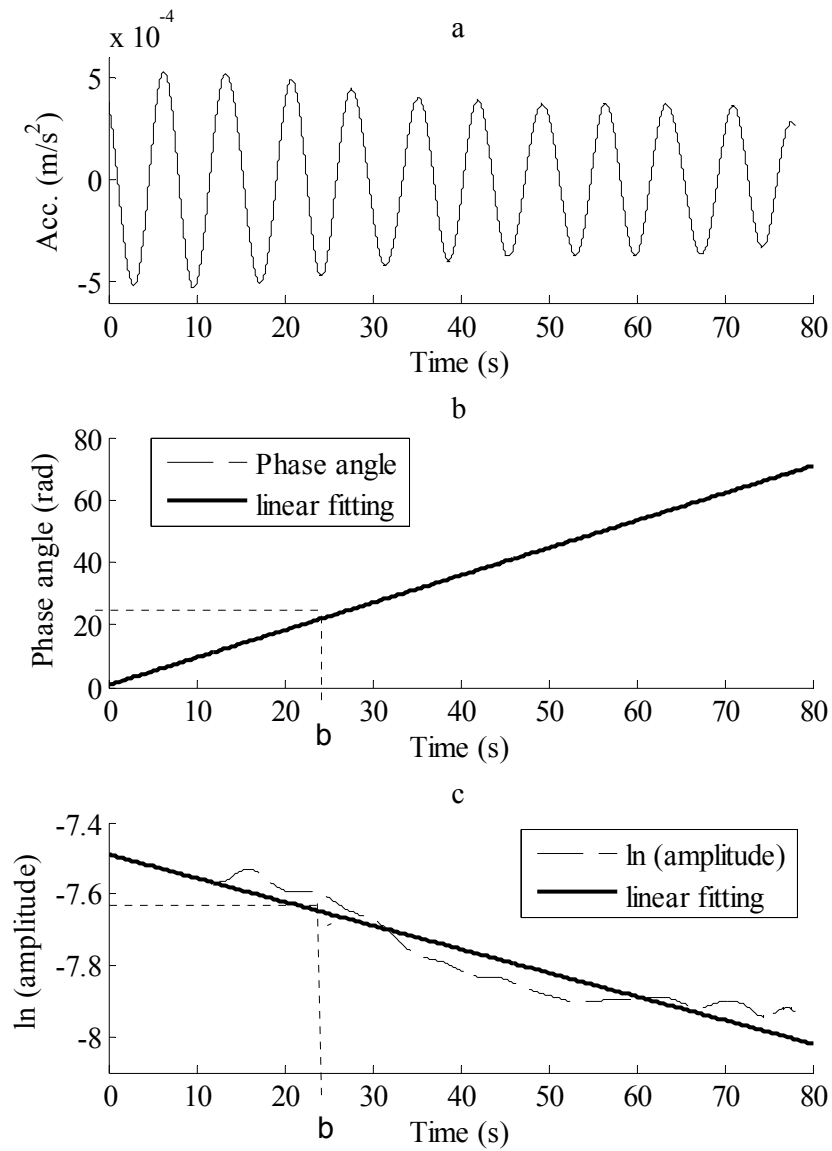


Figure 6.9. a) First IMF of the filtered signal b) Instantaneous phase angle
c) Instantaneous amplitude.

In order to validate this procedure, the tower is subjected to the same assessment after being exposed to an earth motion event (namely; Southern Taiwan earthquake). The calculated mode shapes are listed in Table 6.5. Resulted MAC, COMAC, and MCC values are listed in Tables 6.6, 6.7, and 6.8 respectively; which are all approach the value of unity, hence, no alert for damage is inferred also after this earthquake, as expected.

It worth's noting that the procedure of calculating these coefficients by this method, is based on mode shapes obtained at certain time instant from two functions of time (i.e. instantaneous phase angle and frequency). This means that it could be possible to obtain these mode shapes as function of time also, and hence, MAC, COMAC, MCC variation with time could be easily identified.

Table 6.1. Normalized mode shapes of GTVT around Hagupit typhoon period.

Sensor #	Before			After		
	Mode 1	Mode 2	Mode 3	Mode 1	Mode 2	Mode 3
6	0.37	0.33	2.38	0.34	0.27	2.64
10	0.19	0.24	0.80	0.25	0.32	0.53
9	0.33	0.32	0.67	0.29	0.31	0.68
12	0.23	0.36	0.18	0.26	0.35	-0.18
14	0.97	0.91	0.14	0.98	0.85	0.25
16	1.00	1.00	1.00	1.00	1.00	1.00

Table 6.2. MAC values for signals around Hagupit typhoon period.

Mode	1	2	3	4
MAC	1.00	0.99	0.97	0.98

Table 6.3. COMAC values for signals around Hagupit typhoon period.

Sensor	6	10	9	12	14	16
COMAC	0.99	0.94	0.99	0.89	0.98	1.0

Table 6.4. MCC values for signals around Hagupit typhoon period.

Mode	1	2	3	4
K	0.99	0.95	0.89	0.92
MCC	0.99	0.95	0.86	0.90

Table 6.5. Normalized mode shapes of GTVT around ST earthquake period.

Sensor #	Before			After		
	Mode 1	Mode 2	Mode 3	Mode 1	Mode 2	Mode 3
1	0.07	0.15	0.10	0.02	0.12	0.13
3	0.11	0.78	0.87	0.06	0.78	0.77
5	0.20	1.28	1.15	0.12	1.19	1.06
7	0.35	1.67	1.69	0.24	1.53	1.09
8	0.40	1.59	1.37	0.25	1.56	1.13
11	0.50	1.64	0.90	0.36	1.49	0.80
13	0.62	1.06	-0.11	0.56	1.09	-0.17
15	0.76	-0.35	0.48	0.77	-0.31	0.50
17	1.00	1.17	1.05	0.98	0.98	0.98
18	1.00	1.00	1.00	1.00	1.00	1.00

Table 6.6. MAC values for signals around ST earthquake period.

Mode	1	2	3	4	5
MAC	0.98	1.00	1.00	0.97	0.98

Table 6.7. COMAC values for signals around ST earthquake period.

Sensor	1	2	3	4	5	6	7	8	9	10
COMAC	0.88	1.00	1.00	0.98	1.00	1.00	0.97	0.99	1.00	1.00
Sensor	11	12	13	14	15	16	17	18	19	20
COMAC	1.00	1.00	0.99	1.00	1.00	0.98	1.00	1.00	1.00	0.98

Table 6.8. MCC values for signals around ST earthquake period.

Mode	1	2	3	4	5
K	0.91	0.91	0.98	0.99	0.93
MCC	0.89	0.91	0.98	0.96	0.92

6.4 EMD-Based Damage Assessment

In this dissertation, the EMD has been always associated with the HHT in signal analysis and processing for various purposes. In this section, the space is preserved for the EMD and its capability in performing further criterion for damage assessment of structures.

EMD is based on the assumption that each signal is composed of some different simple intrinsic modes of oscillations, so it decomposes a real signal into a collection of simpler modes (IMFs). These IMFs are associated with energy at different timescales and contain important characteristics of the signal. This fact led some researchers to conduct more investigations on the ability of these IMF's to provide useful information regarding the structural condition (Chen 2009, Rezaei and Taheri 2009, and Cheraghi et al.2005).

In a study by Chen (Chen 2009); EMD was applied to determining time varying mean wind speed for wind data and to extract multipath effect from GPS data, then experimental investigation was carried out to study the applicability of EMD for identifying structural damage caused by a sudden change of the structural stiffness. The study concluded that EMD is a promising tool for structural health monitoring of large civil structures. And the experimental investigation showed that EMD approach with intermittency check can accurately identify the damage time instant by observing the occurrence time of damage spike appearing in the first IMF component of the acceleration response.

In another study; a novel damage index was introduced (Cheraghi et al.2005) and it was used to identify and locate damages in a cantilever pipe by (Rezaei and Taheri 2009). This damage index is based on the energy of the first IMF of the vibration signals, which is obtained by EMD approach. According to this

method free vibration of the structure at its healthy state is captured through an array of sensors attached to the structure. The output signals of these sensors are passed through a band-pass filter to ensure they contain the first natural frequency of the structure and then decomposed by EMD to extract the first IMF of each sensor. The energy of the first IMF for each sensor is then established by:

$$E = \int_0^{t_0} (IMF)^2 dt. \quad (6.4.1)$$

The result of this equation is a scalar value representing the energy of the respected IMF. The procedure is then repeated for the same structure at its damaged state to derive the energy of the first IMF of each sensor. Finally, an EMD-energy damage index for each sensor is defined as:

$$DI = \left| \frac{E_{Healthy} - E_{Damaged}}{E_{Healthy}} \right| \times 100 \quad (6.4.2)$$

The equation provides a scalar value, which is the percentage difference in the structure's energies at its healthy and damaged states, as evaluated by equation (6.4.1) (Rezaei and Taheri 2009).

The above damage index was performed on steel pipes to examine the energy quantity in the IMF's of two signals which are exposed to the same excitation. At each case the pipe was impacted by a hummer three times and the acquired signals were normalized based on the input force; hence, equal energy is expected for undamaged case, and any error would indicate changes in the structure's stiffness. However, in a case of building structures, it is impossible to expose the structure to the same excitation twice; it could be excited by an extreme event or normally by ambient dynamic forces for example, but it is very difficult to perform the same dynamic forces again to examine the energy difference between the two responses. Nevertheless, the energy distribution

among the different degrees of freedom of the structure should be consistent with any other distribution measured at any later time if the structure did not experience any change in its properties

Therefore, another formulation of the index is proposed based on the energy of the first IMF's of the signals. It is defined as a scalar constant relating the degree of consistency between one IMF's energy vector and another reference one; as follows:

$$DI = \frac{\left[\sum_{j=1}^N (E_{jx})(E_{jy}) \right]^2}{\left[\sum_{j=1}^N (E_{jx})^2 \right] \left[\sum_{j=1}^N (E_{jy})^2 \right]} \quad (6.4.3)$$

Where; E_{jx} and E_{jy} are the energy, by Equation (6.4.1), of the first IMFs resulted from the decomposition of two signals at certain degree of freedom (j) for damaged and undamaged cases, respectively, and N is the number of considered degrees of freedom (i.e. measuring points). The index has a scale of values from zero representing no consistent correspondence, to one representing a consistent correspondence.

Systemically; any signal before being decomposed to its IMFs is applied to the adopted filtering approach at the frequencies determined by the peak picking procedure of its FFT spectrum. And then the index can be calculated for the various frequency signals resulted from each filter.

In order to validate this procedure it is applied on the ambient vibration response of the tower before and after two extreme events: Nuri typhoon, and Taiwan Hualien earthquake.

In case of Nuri typhoon; the signals obtained by 16 sensors are filtered according to highest peak, then decomposed and the first IMF of each signal is recorded for both sets of signals before and after Nuri typhoon. Figure 6.10 shows different samples of these IMFs. Then the energy is calculated by Equation (6.4.1) for each IMF resulting two vectors of energy values to be

applied in Equation (6.4.3), thus one value of DI is calculated. The procedure is then repeated on the next set of signals filtered at the next frequency peaks.

The resulting DI vector after Nuri typhoon for the signals filtered upon the highest 6 peaks are as following:

$$DI = \{1.00 \quad 0.97 \quad 0.91 \quad 0.99 \quad 0.95 \quad 0.97\}$$

All the calculated indexes prove no damage in the tower structure inferred by the approaching unity values. This concluded result applies also on the assessment performed after Taiwan Hualien earthquake by the same method, in which DI values are: 0.98, 0.99, 1.00, 0.99, 1.00, and 0.97.

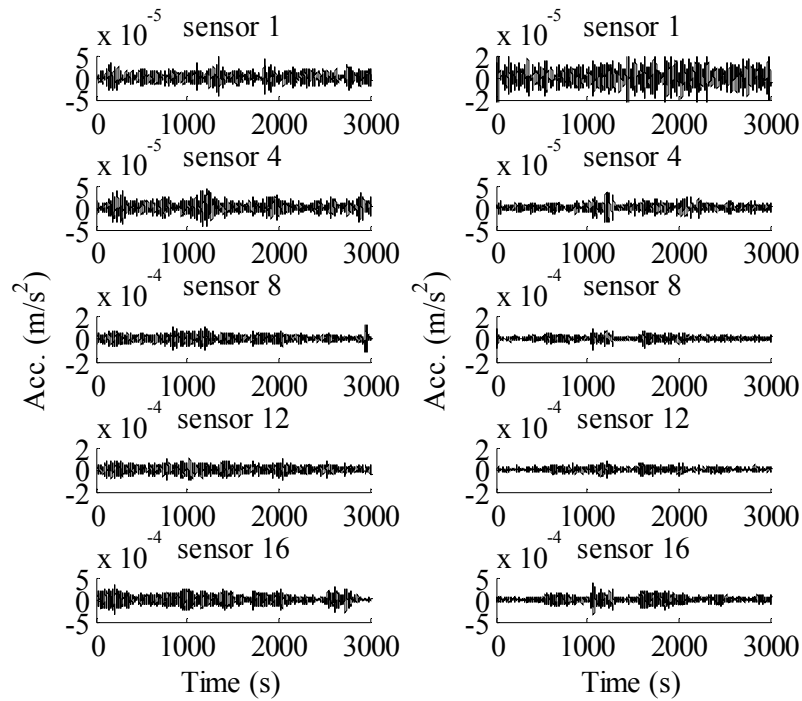


Figure 6.10. First IMF's of the signals measured before (left) and after (right) Nuri typhoon after being filtered.

6.5 Conclusions

In this chapter, three different approaches of damage assessment are studied and applied on the case study of this dissertation GTVT. The three approaches are: damage assessment by the instantaneous frequency and phase angle curves produced by HHT analysis, MAC, COMAC, and MCC coefficients considering mode shapes produced by HHT analysis, and damage index based on EMD approach and the energy of the IMFs.

The three approaches show a sufficient capability in assessing the structure of GTVT. They all confirmed the previously performed assessment by other methods in the past chapters. The first approach showed the ability to provide an online assessment during an extreme event. While in the second approach it was found that MAC, COMAC, and MCC obtained based on HHT analysis could be identified as time varying assessment factors. The third approach is validated and the results are verified to give a further investigation approach to obtain a damage index that considers the energy induced in the structure.

Nevertheless, the case of study in this dissertation proved not to have suffered any damage during the whole considered events, which gave the same results in every adopted approach for damage assessment, while it could be more reliable if these approaches have been evaluated on an experimental model that could be damaged for experimental purposes, and then the differences will be clear and the evaluation will be more realistic.

Conclusions

The research work of the thesis is part of a bigger campaign to monitor the tower of Guangzhou city held by the Polytechnic University of Hong Kong. The scope is monitoring the tower dynamical behavior in various weather conditions and under exposure to extreme events, and to analyze this response by the aid of several algorithms to reach for a full performance assessment in real time. The response data were obtained through the well-established SHM system that the tower is equipped with, so the data can then be applied to researches.

In this thesis the response of the tower under five typhoons and two earthquakes is studied, accordingly, the corresponding response data is collected to the benefit of this study. Signals measured during typhoons are analyzed by FDD method aiming at identifying the modal parameters of the structure, and correlating them with the wind properties for the several typhoons. The mode shapes of the tower extracted by this method were used later in the damage assessment process of tower, which is based on performing three coefficients that proved to have the ability to give a sign for a possible damage in the structure by its dynamical response measured before and after dynamic excitation.

The signals obtained during the considered extreme events are then analyzed again by the aid of another method i.e. improved HHT by filtering approach, and systematically, the modal parameters of the structure are obtained.

Finally, three different approaches of damage assessment based on HHT analysis are investigated and applied to assess the tower condition. The three approaches are: damage assessment by the instantaneous frequency and phase angle curves produced by HHT analysis, MAC, COMAC, and MCC

coefficients considering mode shapes produced by HHT analysis, and finally by a proposed damage index based on EMD approach and the energy of the produced IMFs.

Based on the work conducted in this research work the following remarks recommendations can be concluded:

- The five typhoons varied in the hourly mean wind speed as well as the main direction of blowing and duration, which gave the possibility to study the tower behavior under different types of typhoons and at different stages of the tower construction.
- The results proved that the fundamental frequencies of the tower were decreasing as the level of construction was increasing, while no sufficient change in the frequency was detected through different speeds of wind at the same stage of construction.
- The previous point could mean that the tower did not suffer any change in its properties during these typhoons, proved by the constant fundamental frequencies; which means no change occurred in the stiffness of the structure, however, the values of the frequency was slightly fluctuating around the real values due to the heavy rain accompanied by the typhoons which increased the mass of the tower.
- The damping ratios were found to slightly increase with the speed of the wind affecting the tower.
- Generally, the results of the conducted assessments by MAC, COMAC, and MCC coefficients based on FDD analysis for all the considered cases showed that the tower did not give any sign for a possible formation of damage.
- The more sensitive coefficient to modes inconsistency among the adopted is found to be MCC, as it considers all what is included in MAC in addition to its sensitivity to kinks formation.
- In particular, COMAC proved highest sensitivity among the others in case of ground motion exposure because it assesses each measuring point separately.

- Based on the last three points it is recommended in damage and deterioration detection in structures to choose the most sensitive index to the case of dynamic loading, and the more number of possible indexes of assessment are calculated is the better configuration of the tower condition to be given.
- The improved approach of HHT proved the ability to express sufficiently the dynamical behavior of the structure in both the time and frequency domain.
- The resulted fundamental frequencies presented by the improved HHT method are almost the same as that of FDD method.
- The improved HHT method possesses a strong power against noise; therefore, the first two vibration modes of GTVT, which were dominant during the typhoons, could be clearly presented in the HHT spectrum.
- When investigating the response to earthquakes, improved HHT method figured clearly the high energy imparted to higher modes of the tower which were dominant.
- In HHT spectra, it was relatively possible to detect the time at which the tower started to have a significant response to the ground motions; by tracking the point at which the energy started to have a sudden increase in the tower various vibration modes.
- It can be concluded also from the HHT spectra; that the dynamical behaviour of the tower did not alarm for any damage during the considered extreme events. This conclusion is proven by the almost constant frequency in the studied time period for each signal, in addition to the distribution energy intensity of each mode which remained within the narrowband without any energy shift to other bands in every obtained Hilbert spectrum, hence, no nonlinearity appeared in body of the structure i.e. no commencement of structural damage is detected.
- The three approaches presented in the last chapter show a sufficient capability in assessing the structure of GTVT, confirming the

previously performed assessment by other methods in the past chapters.

- The Instantaneous phase angle and frequency approach showed the ability to provide an online assessment for the tower during an extreme event.
- MAC, COMAC, and MCC obtained based on HHT analysis confirmed the results when obtained by FDD, giving as advantage, the possibility to be identified as time varying assessment factors.
- The proposed damage index based on the energy of the IMFs obtained by EMD also proved its reliability confirming the no-damage results giving a further investigation approach to obtain a damage index considering the energy induced in the structure.

Recommendations

The case of study in this dissertation proved not to have suffered any damage during the whole considered events, which gave the same results in every adopted approach for damage assessment, while it could be more reliable if these approaches have been evaluated on an experimental model that could be damaged in for experimental purposes, and then the differences between the two cases will be clear and the evaluation of the proposed damage assessment criteria will be more realistic.

The procedure for detecting the mode shapes of the structure based on HHT analysis along with the frequencies calculated based on the same method could be utilized in performing more damage coefficients that are based on modal analysis. Furthermore, an attempt to identify the considered coefficients as functions with time is highly recommended.

References

- A Benchmark Problem for the Structural Health Monitoring of High-Rise Slender Structures (2008),
<http://www.cse.polyu.edu.hk/benchmark/index.htm>.
- Allemang R. (2003). "The Modal Assurance Criterion Twenty Years of Use and Abuse", *Sound and Vibration*, 14-21.
- AlSaleh R., Casciati F., Fuggini C. (2009). "Detecting the torsional behavior of a tall building by GPS receivers", *Proceedings of the COMPDYN 2009, ECCOMAS Thematic Conference on Computational Methods in Structural Dynamics and Earthquake Engineering*, Rhodes, CD-ROM (article CD438).
- ARTEMIS Extractor Program (1999). *Structural Vibration Solution ApS.*, Release 3.2.
- Bao C. X., Hao H., Li Z. X., Zhu X. Q. (2009). "Time-varying system identification using a newly improved HHT algorithm", *Computers and Structure*, vol. 87, 1611–1623.
- Bernal D. and Gunes B. (2000). "An examination of instantaneous frequency as a damage detection tool", *Proceeding of the 14th Engineering Mechanics Conference*, Austin, TX, on CD.
- Brincker R., Ventura C., Andersen P. (2001). "Damping Estimation by Frequency Domain Decomposition", *International Society for Optical Engineering*, vol. 4359, 696-703.
- Brincker R., Zhang L., Anderson P. (2000). "Output-Only Modal Analysis by Frequency Domain Decomposition", *Proceeding of ISMA25*, vol. 2.
- Brincker R., Zhang L., Andersen P. (2001). "Modal identification of output-only systems using frequency domain decomposition", *Smart Materials and Structures*, vol. 10, 441-445.
- Brownjohn J., Pan T., Cheong H. (1998). "Dynamic response of Republic Plaza, Singapore", *The Structural Engineer*, vol. 76, 221–226.

- Casciati F. (2003). "An overview of structural health monitoring expertise within the European Union", *Structural health monitoring and intelligent infrastructure*, Balkema, Lisse, pp. 31–37.
- Casciati F., Alsaleh R., Fuggini C. (2009). "GPS-Based SHM of a tall building: torsional effects", *Proceedings of the 7th International Workshop on Structural Health Monitoring*, Stanford University, Stanford, 340-347.
- Casciati S. (2005). "Damage detection and localization in the space of the observed variables", *Ph.D. thesis*, Graduate School of Civil Engineering, University of Pavia, Pavia-Italy.
- Casciati S. (2010). "Response Surface Models to Detect and Localize Distributed Cracks in a Complex Continuum", *Journal of Engineering Mechanics*, vol. 136, no. 9, 1131–1142.
- Chen J. (2009). "Application of Empirical Mode Decomposition in Structural Health Monitoring: Some Experience". *Advances in Adaptive Data Analysis*, vol. 1, no. 4, 601–621.
- Chen J., Garba J. (1998). "On-orbit damage assessment for large space structures", *AIAA Journal*, vol. 26, no. 12, 1119-1126.
- Chen H., Yan Y., Jiang J. (2007). "Vibration-based damage detection in composite wingbox structures by HHT", *Mechanical Systems and Signal Processing*, vol. 21, 307–321.
- Chen J., Xua Y., Zhang R. (2004). "Modal parameter identification of Tsing Ma suspension bridge under Typhoon Victor: EMD-HT method", *Journal of Wind Engineering and Industrial Aerodynamics*, vol. 92, 805–827.
- Cheng J., Yu D., Tang J., Yang, Y. (2008). "Application of frequency family separation method based upon EMD and local Hilbert energy spectrum method to gear fault diagnosis" *Mechanism and Machine Theory*, vol. 43, no. 6, 712-723.
- Cheraghi N., Riley M., Taheri F. (2005). "A novel approach for detection of damage in adhesively bonded joints in plastic pipes based on vibration methods using piezoelectric sensors", *IEEE International Conference on Systems*, vol. 4, 3472–3478.

- China post, *Web Site*, <http://www.chinapost.com.tw/taiwan/national/nationalnews/2010/03/05/246938/64-quake.htm>
- Facts and Details, *Website*, <http://factsanddetails.com/china.php?itemid=398&catid=10&subcatid=64#02>
- Farrar C., Worden K. (2007). "An introduction to structural health monitoring", *Philosophy Transaction of the Royal Society A*, 365, 303–315.
- Guo Y., Ni Y., Zhou H. (2009). "Condition Assessment of Post-ship-collision Bridges Using HHT Analysis", *The Fifth International Workshop on Advanced Smart Materials and Smart Structures Technology*, Boston-USA.
- Hu N., Wang X., Fukunaga H., Yao Z., Zhang H., Wu Z. (2001). "Damage assessment of structure using modal test data", *International Journal of Solids and Structures*, vol. 38, 3111-3126.
- Huang N., Shen Z., Long S., Wu M., Shih H., Zheng Q., Yen N., Tung C., Liu H. (1998). "The Empirical Mode Decomposition and the Hilbert Spectrum for Nonlinear and Non-Stationary Time Series Analysis", *Proceedings: Mathematical, Physical and Engineering Sciences*, vol. 454, no. 1971, 903-995.
- Kerschen G., Vakakis A., Lee Y., McFarland D., Bergman L. (2008). "Toward a fundamental understanding of the Hilbert-Huang transform in nonlinear structural dynamics", *Journal of Vibration and Control*, vol. 14, no. 1-2, 77-105.
- Kijewski-Correa T., Kilpatrick J., Kareem A., Kwon D., Bashor R., Kochly M., Young B., Abdelrazaq A., Galsworthy J., Isyumov N., Morrish D., Sinn R., Baker W. (2006). "Validating wind-induced response of tall buildings: synopsis of the Chicago full-scale monitoring program", *Journal of Structural Engineering*, vol. 132, 1509–1523.
- Ko J., Ni Y. (2005). "Technology developments in structural health monitoring of large-scale bridges", *Engineering Structures*, vol. 27, no.12, 1715-1725
- Le T., Tamura Y. (2009). "Modal Identification of Ambient Vibration Structure using Frequency Domain Decomposition and Wavelet Transform", *The Seventh Asia-Pacific Conference on Wind Engineering*, Taipei-Taiwan.

- Lei Y., He Z., Zi Y. (2009). "Application of the EEMD method to rotor fault diagnosis of rotating machinery", *Mechanical Systems and Signal Processing*, vol. 23, 1327–1338.
- Li Q., Wu J. (2007). "Time-frequency analysis of typhoon effects on a 79-storey tall building", *Journal of Wind Engineering and Industrial Aerodynamics* 95, 1648–1666.
- Lin S., Yang J., Zhou L. (2005). "Damage identification of a benchmark building for structural health monitoring", *Smart Materials and Structures*, vol. 14, 162–S169.
- Liu B., Riemenschneider S., Xu Y. (2006). "Gearbox fault diagnosis using empirical mode decomposition and Hilbert spectrum", *Mechanical System and Signal Processing*, vol. 20, no. 3, 718–734.
- Matlab (2004). *The MathWork Inc.*, Version 7 (R14).
- Mendis P., Ngo T., Haritos N., Hira A., Samali B., Cheung J. (2007). "Wind Loading on Tall Buildings", *EJSE Special Issue: Loading on Structures*, 41–54.
- Ni Y. Q., Xia Y., Chen W. H., Lu Z. R., Liao W. Y., Ko J. M. (2009). "Monitoring of wind properties and dynamic responses of a supertall structure during typhoon periods", *4th International Conference on Structural Health Monitoring on Intelligent Infrastructure (SHMII-4)*, Zurich, Switzerland.
- Ni Y. Q., Xia Y., Liao W. Y., Ko J. M. (2009). "Technology innovation in developing the structural health monitoring system for Guangzhou New TV Tower", *Journal of Structural Control and Health Monitoring*, vol. 16, no. 1, 73–98.
- Ni Y. Q., Xia Y., Liao W. Y., Zhang P. (2008). "Development of a Structural Health Monitoring System for Guangzhou New TV Tower", *Advances in Science and Technology*, vol. 56, 414–419.
- Peng Z., Tse P., Chu F. (2005). "An improved Hilbert–Huang transform and its application in vibration signal analysis", *Journal of Sound and Vibration*, vol. 286, 187–205.

- Pines D. and Salvino L. (2002). "Health monitoring of one dimensional structures using empirical mode decomposition and the Hilbert-Huang transform", *Proceedings of the SPIE Smart Structures and Materials Symposium*, San Diego-USA, 127-143.
- Rezaei D., Taheri F. (2009). "Experimental validation of a novel structural damage detection method based on empirical mode decomposition", *Smart Material and Structures*, vol. 18, 1-14.
- Ricles J., Kosmatka J. (1992). "Damage detection in elastic structures using vibratory residual forces and weighted sensitivity", *AIAA Journal*, vol. 30, no. 9, 2310-2316
- Roitman N., Viero P. (1997). "Detection and location of damages in offshore platforms: An application of some methods using eigenvectors", *Proceedings of SPIE, the International Society for Optical Engineering*, vol. 3089, no. 2, 1124-1131.
- Salvino L. and Pines D. (2006), "Structural damage detection using empirical mode decomposition and HHT", *Journal of Sound and Vibration*, vol. 294, 97-124.
- Tan Y. (2010). "Wind Property and Wind Response Analysis of Guangzhou New TV Tower during Typhoons", *Master thesis*, Department of Civil and Structural Engineering at Hong Kong Polytechnic University.
- Wikipedia, *Website*, <http://en.wikipedia.org/wiki>.
- Wu T., Chung Y. (2009). "Misalignment diagnosis of rotating machinery through vibration analysis via the hybrid EEMD and EMD approach", *Smart Materials & Structures*, vol. 18, 1-13.
- Wu Z. H., Huang N. E. (2009). "Ensemble Empirical Mode Decomposition: A Noise- Assisted Data Analysis Method", *Advances in Adaptive Data Analysis*, vol.1, no.1, 1-41.
- Xia Y., Ni Y.Q., Ko J. M., Chen H. B. (2008). "ANCRiSST benchmark problem on structural health Monitoring of high-rise slender structures", *The 4th International Workshop on Advanced Smart Materials and Smart Structures Technologies*, Tokyo, Japan.

- Xia Y., Ni Y. Q., Ko J. M., Liao W. Y., Chen W. H. (2009). "ANCRiSST Benchmark Problem on Structural Health Monitoring of High-Rise Slender Structures – Phase I: Field Vibration Measurement".
- Xui Y., Chen S., Zhang R. (2003). "Modal Identification of Di Wang Building Under Typhoon York Using The Hilbert–Huang Transform Method", *The Structural Design of Tall and Special Buildings*, vol. 12, 21–47.
- Yang W. X. (2008). "Interpretation of mechanical signals using an improved Hilbert–Huang transform", *Mechanical Systems and Signal Processing*, vol. 22, 1061–1071.
- Yang Y., Lei (2000). "System identification of linear structures using Hilbert transform and empirical mode decomposition", *Proceedings of the 18th International Modal Analysis Conference*, Antonio TX-USA, vol. 1, 213–219.
- Yang J., Lei Y., Lin S., Huang, N. (2004), "Hilbert-Huang based approach for structural damage detection", *Journal of Engineering Mechanics - ASCE*, vol. 130, no.1, 85-95.
- Yang J., Lei Y., Pan S., Huang N. (2003). "System identification of linear structures based on Hilbert-Huang spectral analysis. Part I: normal modes". *Earthquake Engineering and Structural Dynamic*, vol. 32. 1443-1467.
- Yang B. Suh C. (2004). "Interpretation of crack-induced rotor non-linear response using instantaneous frequency", *Mechanical System and Signal Processing*, vol. 18, no. 3, 491–513.
- Zemmour A. (2006). "The Hilbert-Huang Transform for Damage Detection in Plate Structures", *MSc. Thesis*, Faculty of the Graduate School of the University of Maryland, College Park. Maryland-USA.

Appendix A

GTVT Response during Extreme Events

A.1 Introduction

The whole response to extreme events data of the GTVT which were considered throughout the research work of this dissertation is demonstrated in this Appendix.

Acceleration time histories recorded during the wind events; Kammuri, Nuri, Hagupit, Molave, and Koppu typhoons, are demonstrated in the following section by Figures A.1 – A.19, whereas, those recorded during the ground motion events; Southern Taiwan, and Taiwan Hualien earthquakes are demonstrated by Figures A.20 and A.21.

A.2 Response of GTVT to Typhoons

A.2.1 Typhoon Kammuri

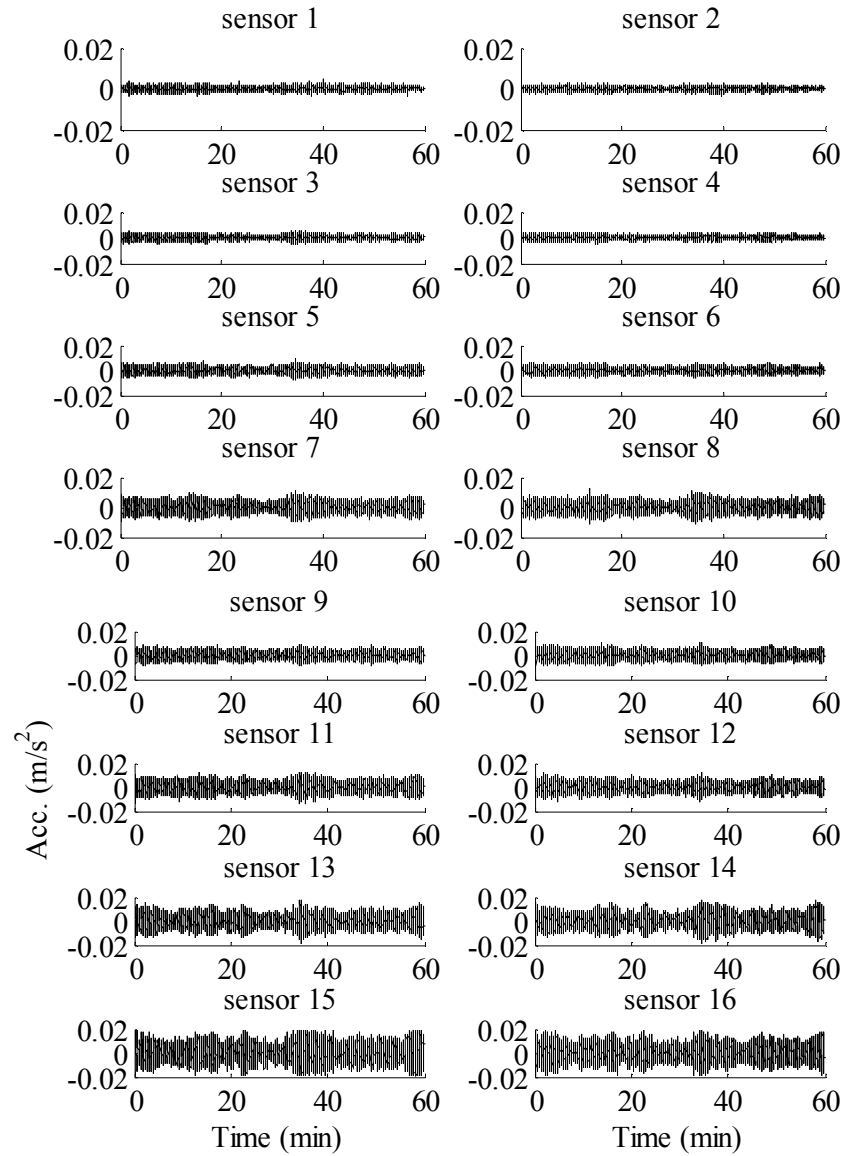


Figure A.1. Response measured on 6th/8/2008 from 17:32 to 18:32.

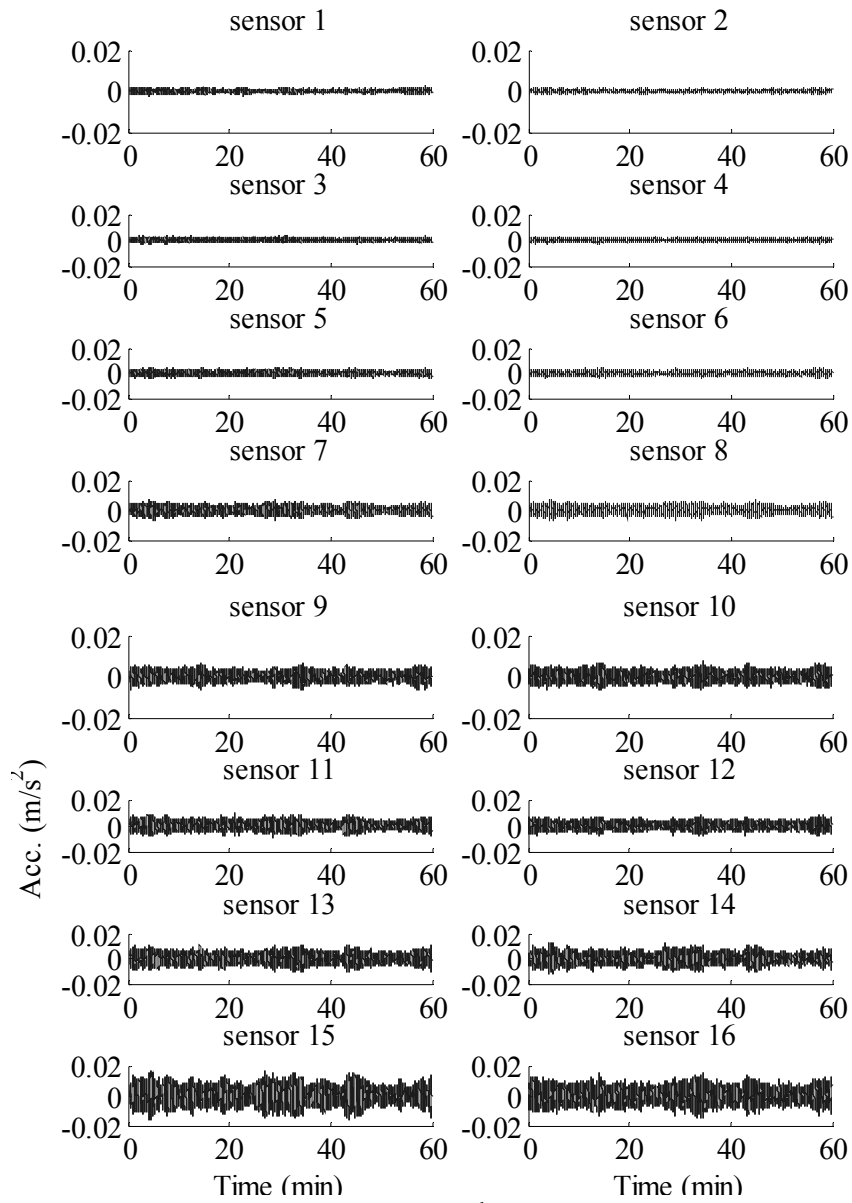


Figure A.2. Response measured on 6th/8/2008 from 19:32 to 20:32.

A.2.2 Typhoon Nuri

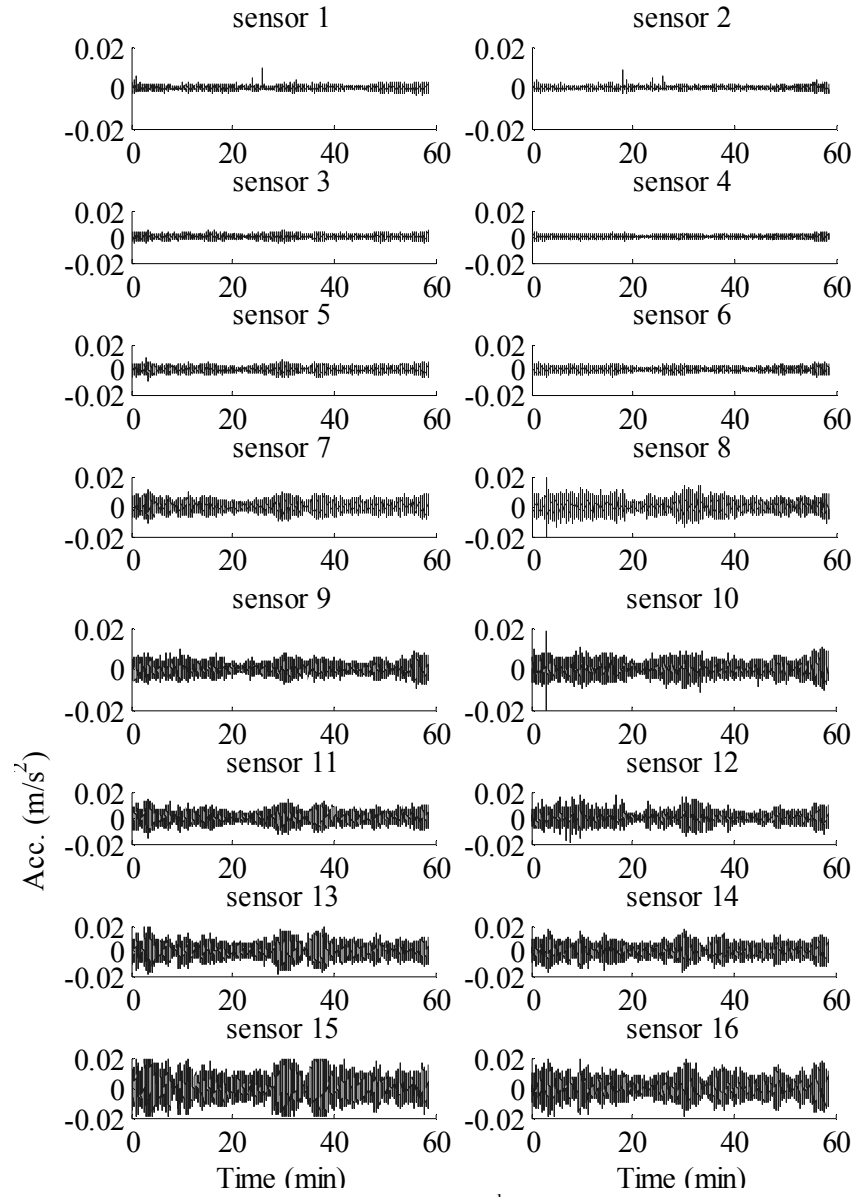


Figure A.3. Response measured on 22nd/8/2008 from 14:00 to 15:00.

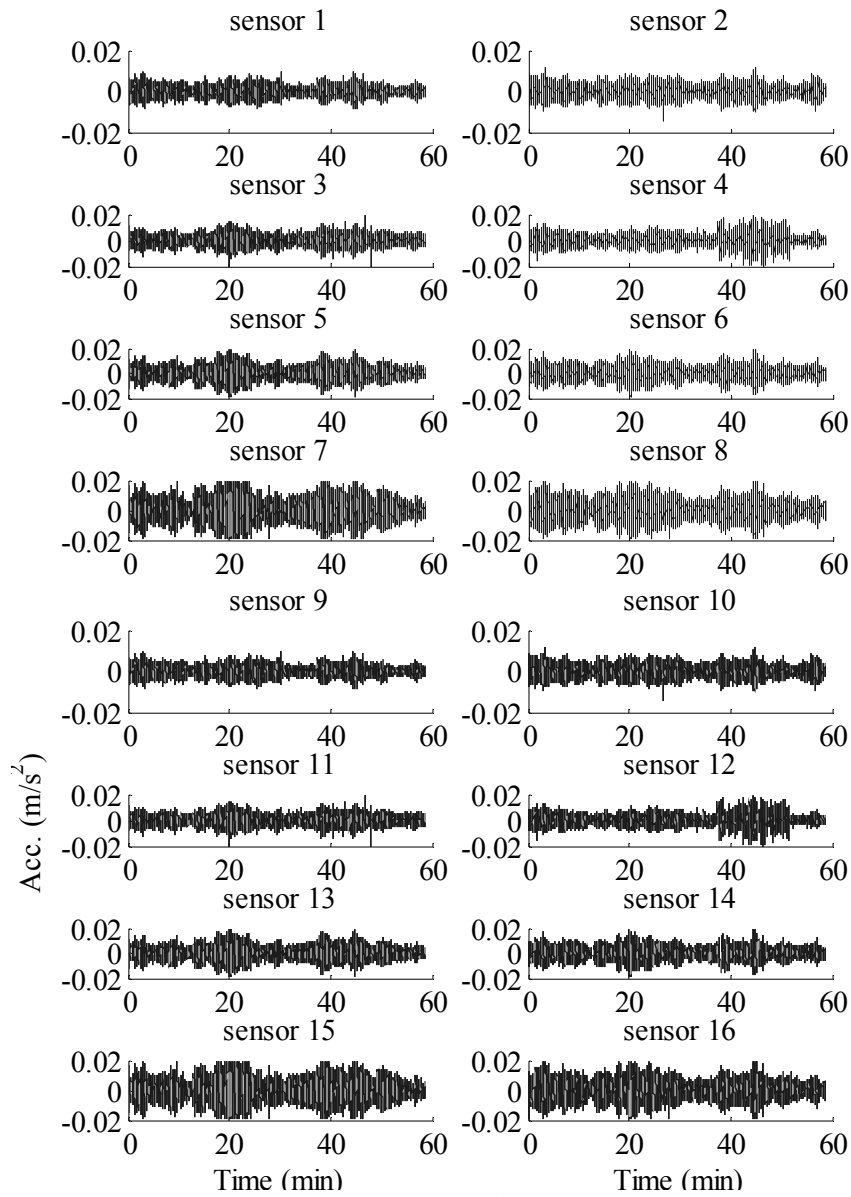


Figure A.4. Response measured on 22nd/8/2008 from 15:00 to 16:00.

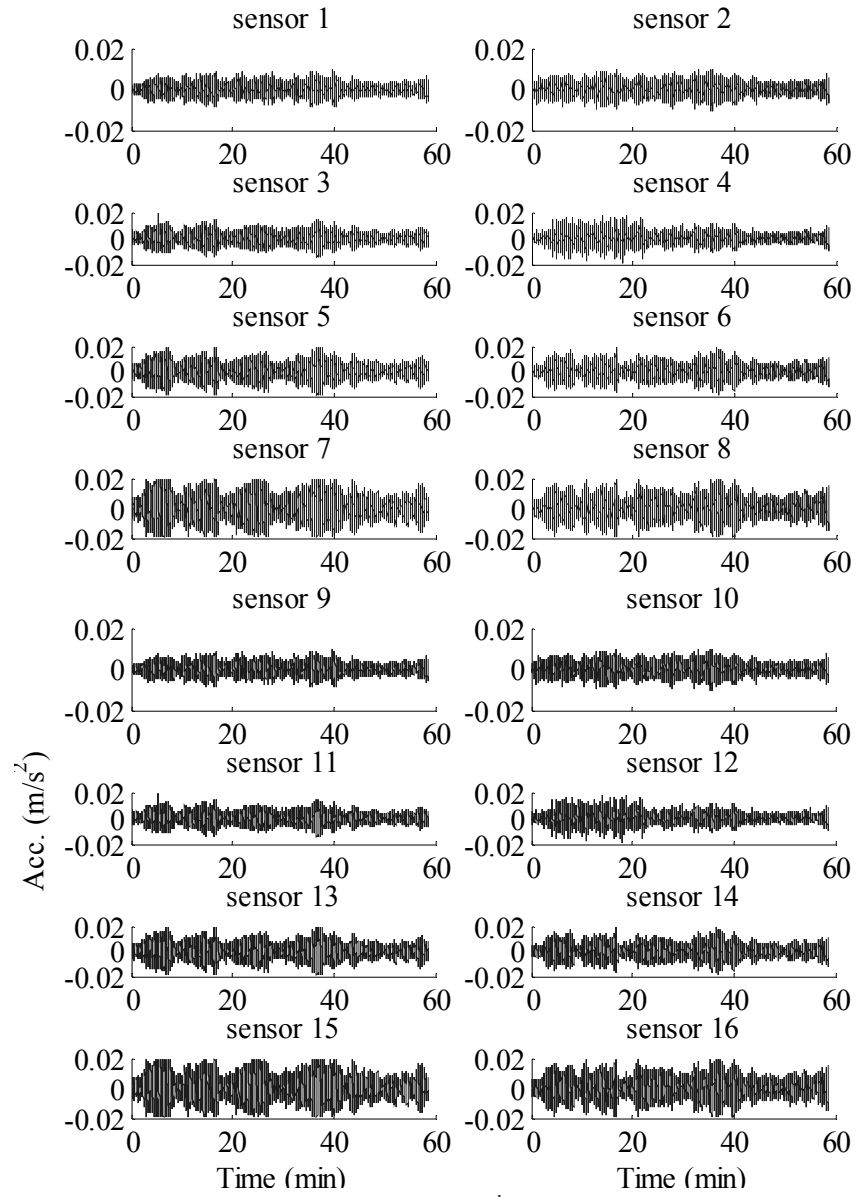


Figure A.5. Response measured on 22nd/8/2008 from 16:00 to 17:00.

A.2.3 Typhoon Hagupit

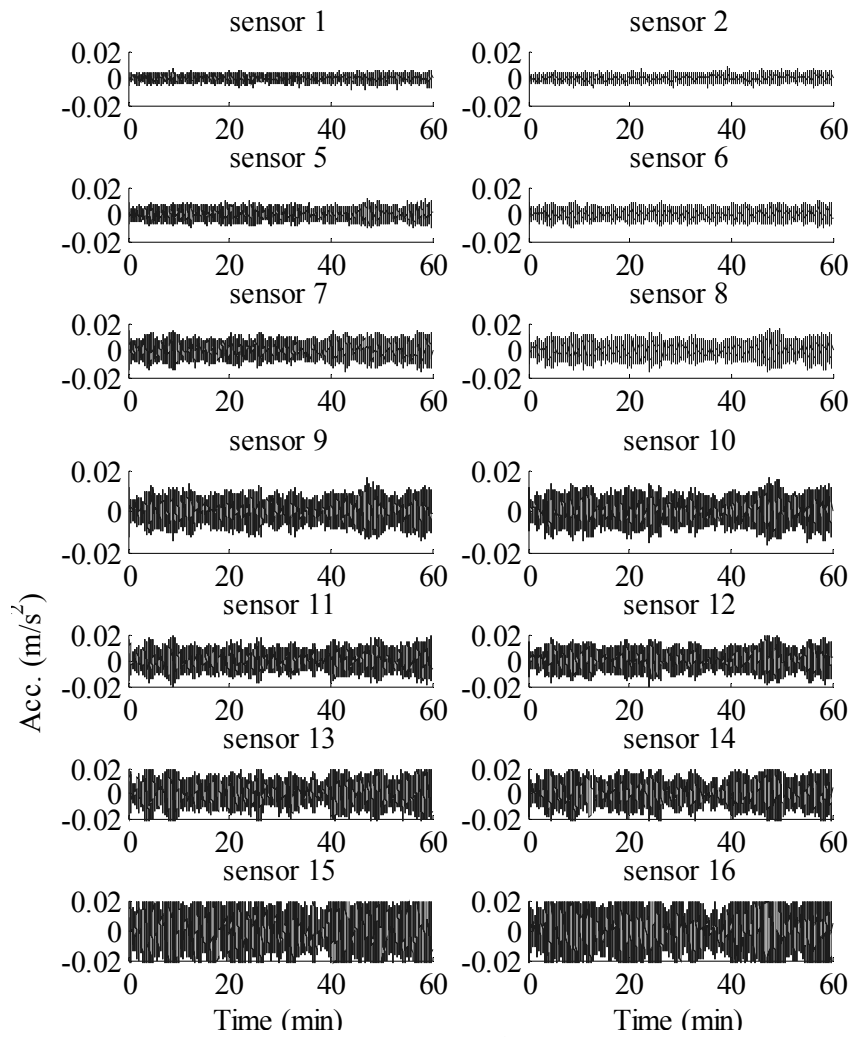
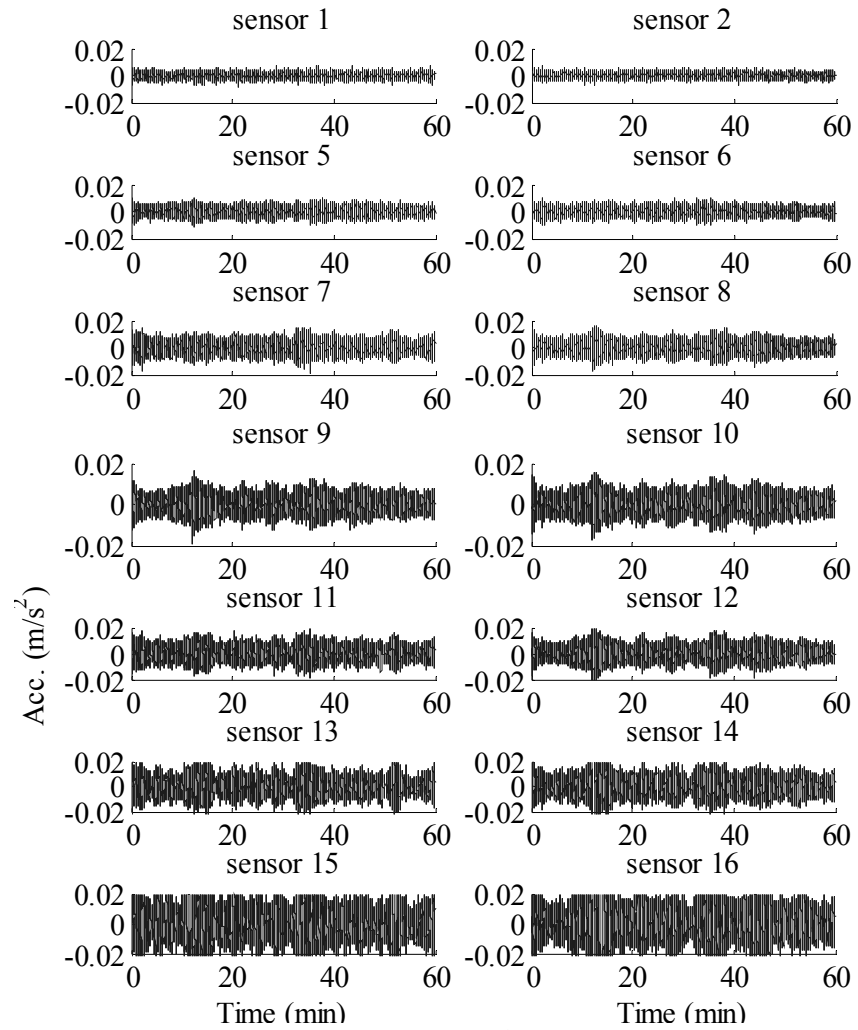


Figure A.6. Response measured on 24th/9/2008 from 3:00 to 4:00.

Figure A.7. Response measured on 24th/9/2008 from 4:00 to 5:00.

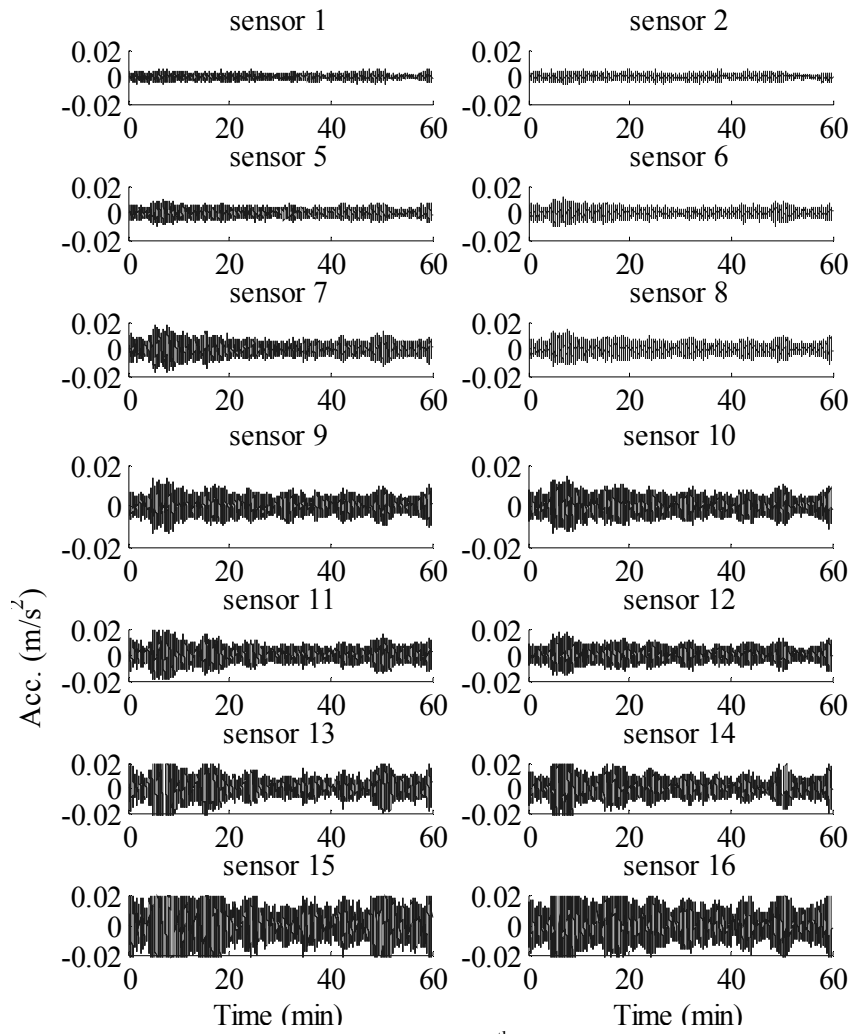


Figure A.8. Response measured on 24th/9/2008 from 5:00 to 6:00.

A.2.4 Typhoon Molave

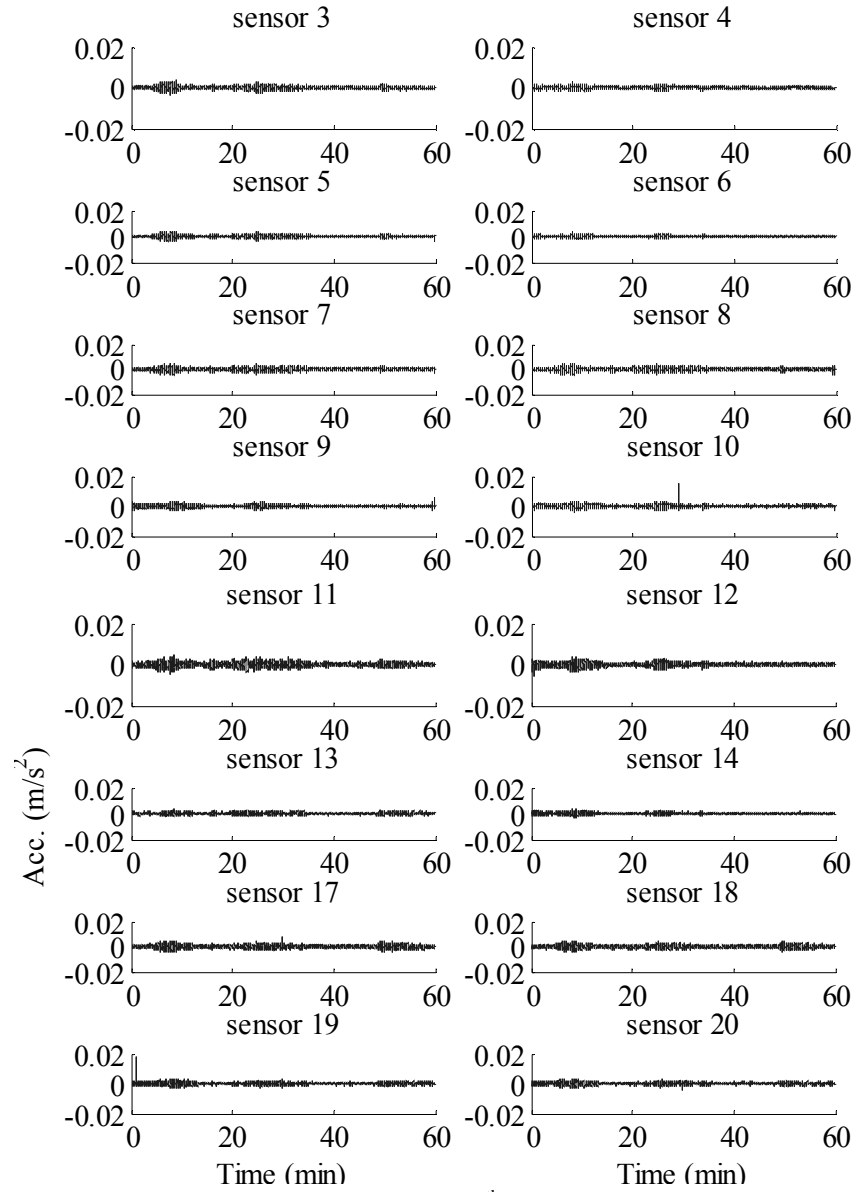


Figure A.9. Response measured on 18th/7/2009 from 17:32 to 18:32.

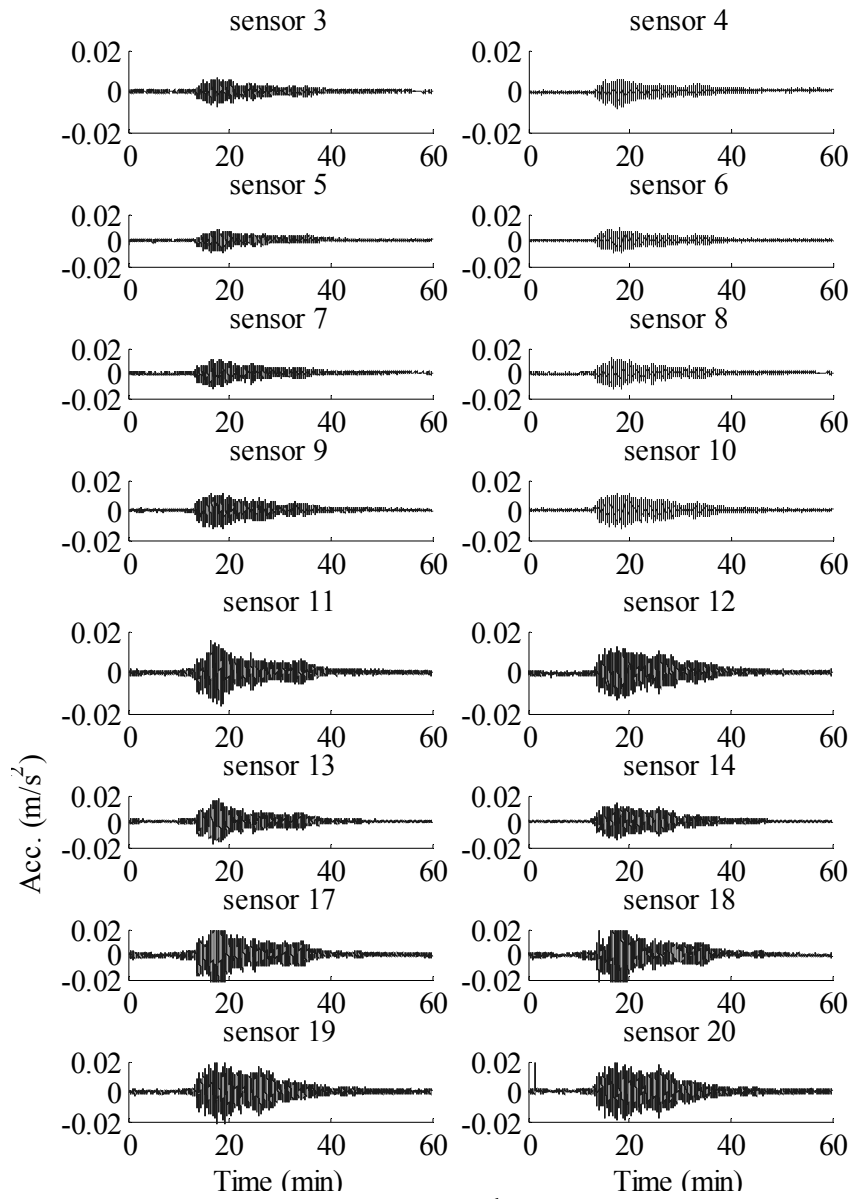
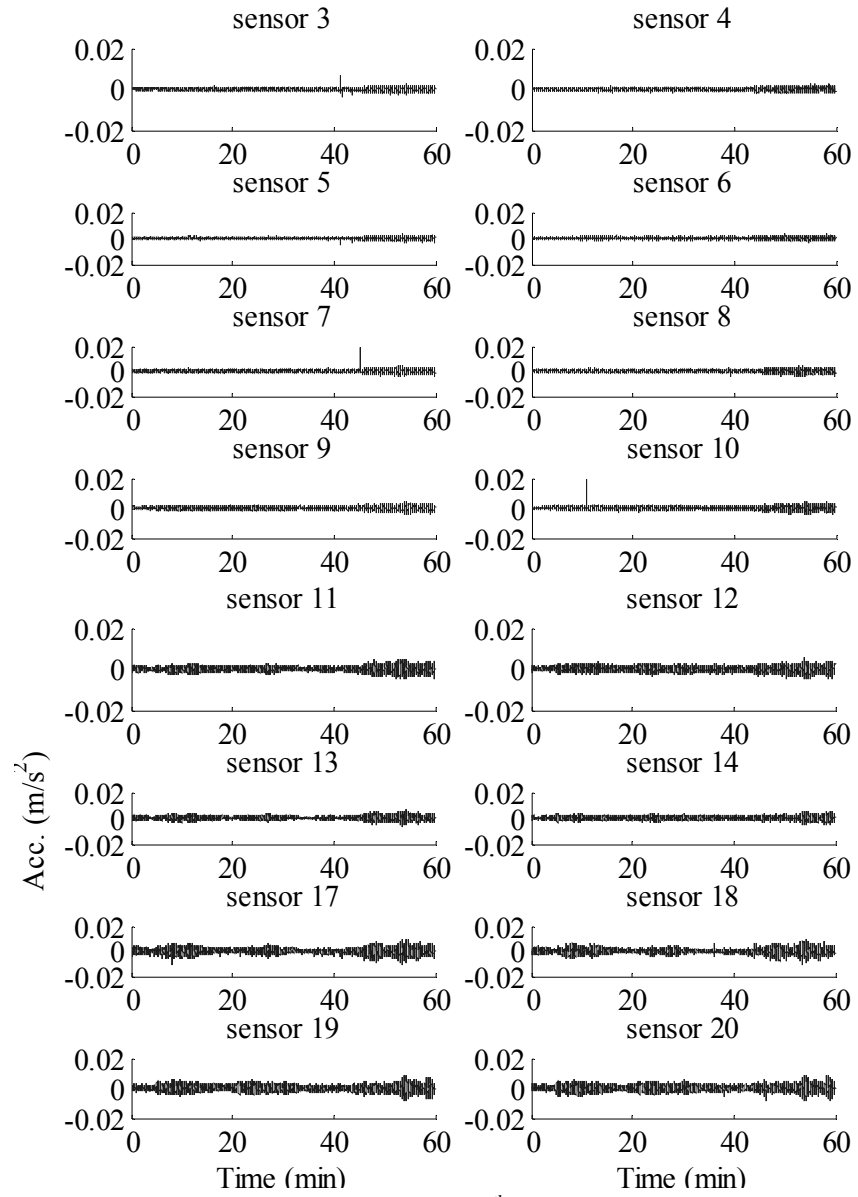


Figure A.10. Response measured on 18th/7/2009 from 18:32 to 19:32.

Figure A.11. Response measured on 18th/7/2009 from 19:32 to 20:32.

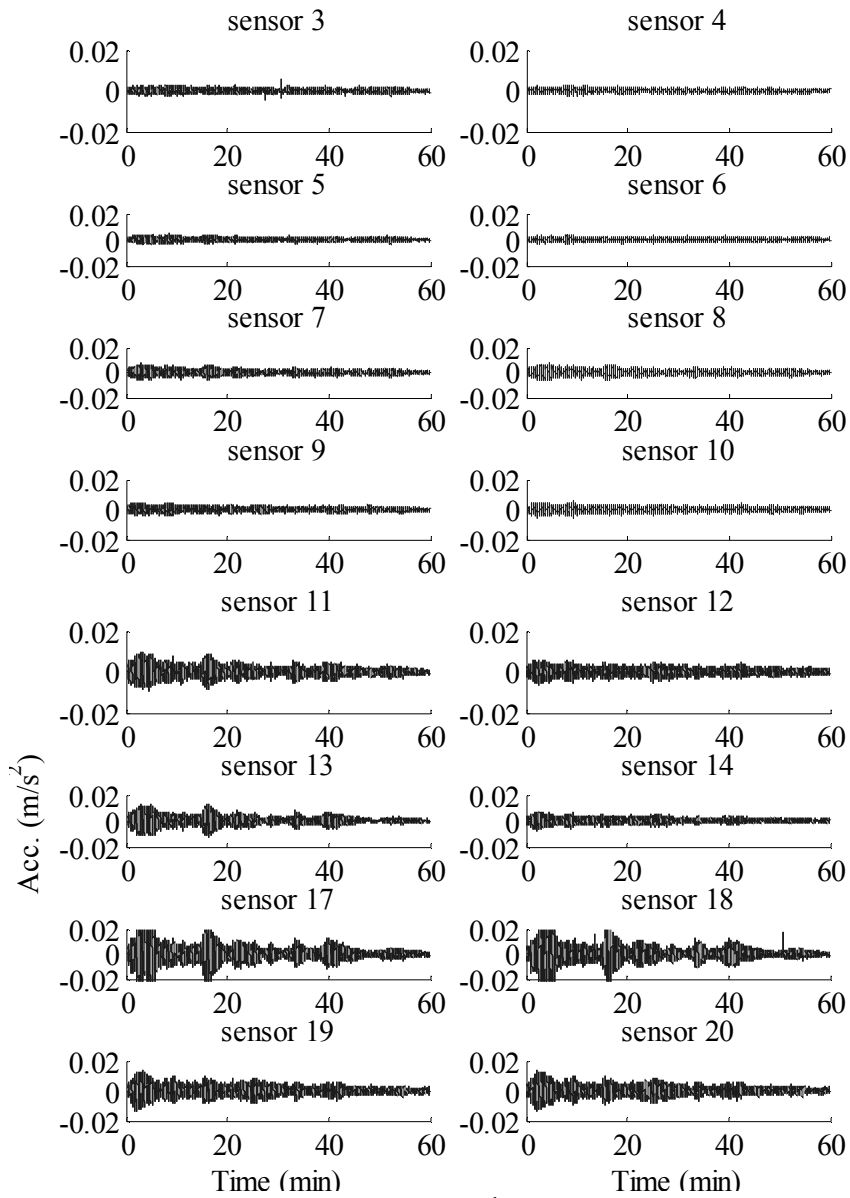
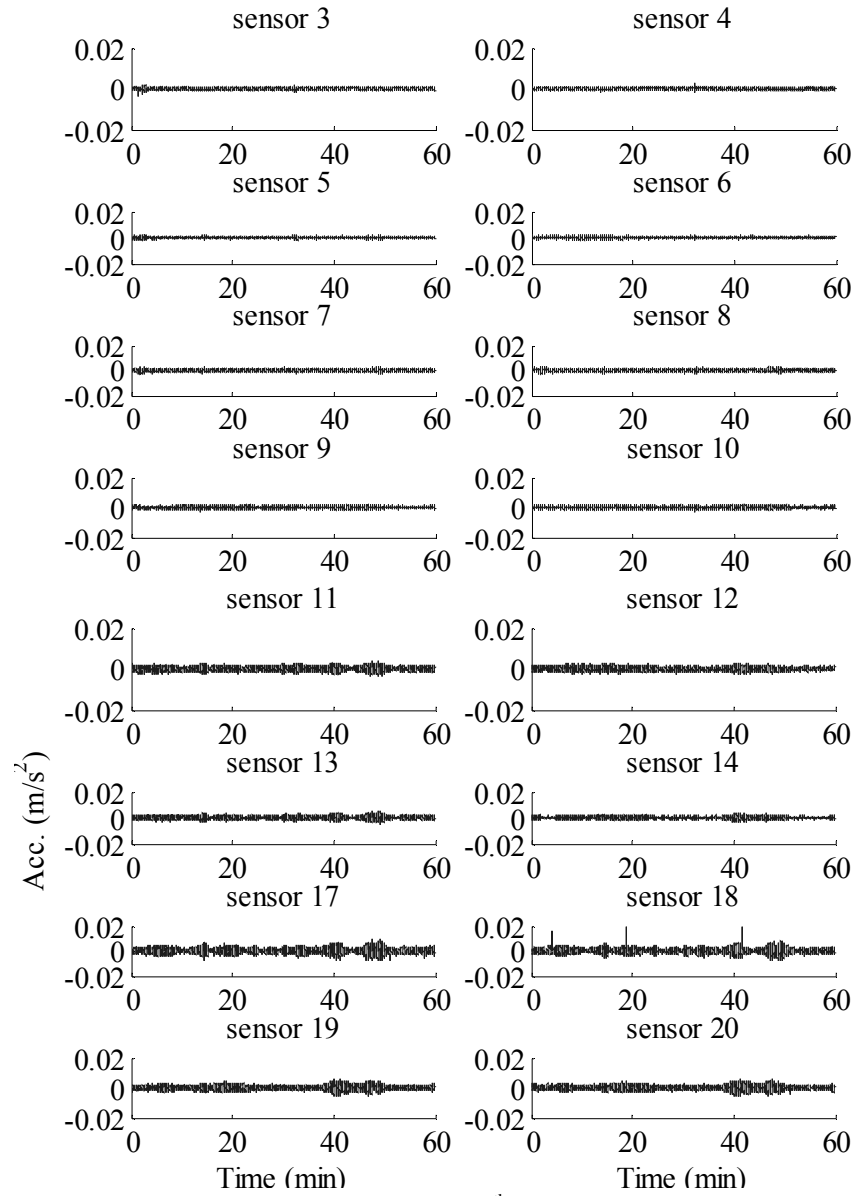


Figure A.12. Response measured on 18th/7/2009 from 20:32 to 21:32.

Figure A.13. Response measured on 18th/7/2009 from 21:32 to 22:32.

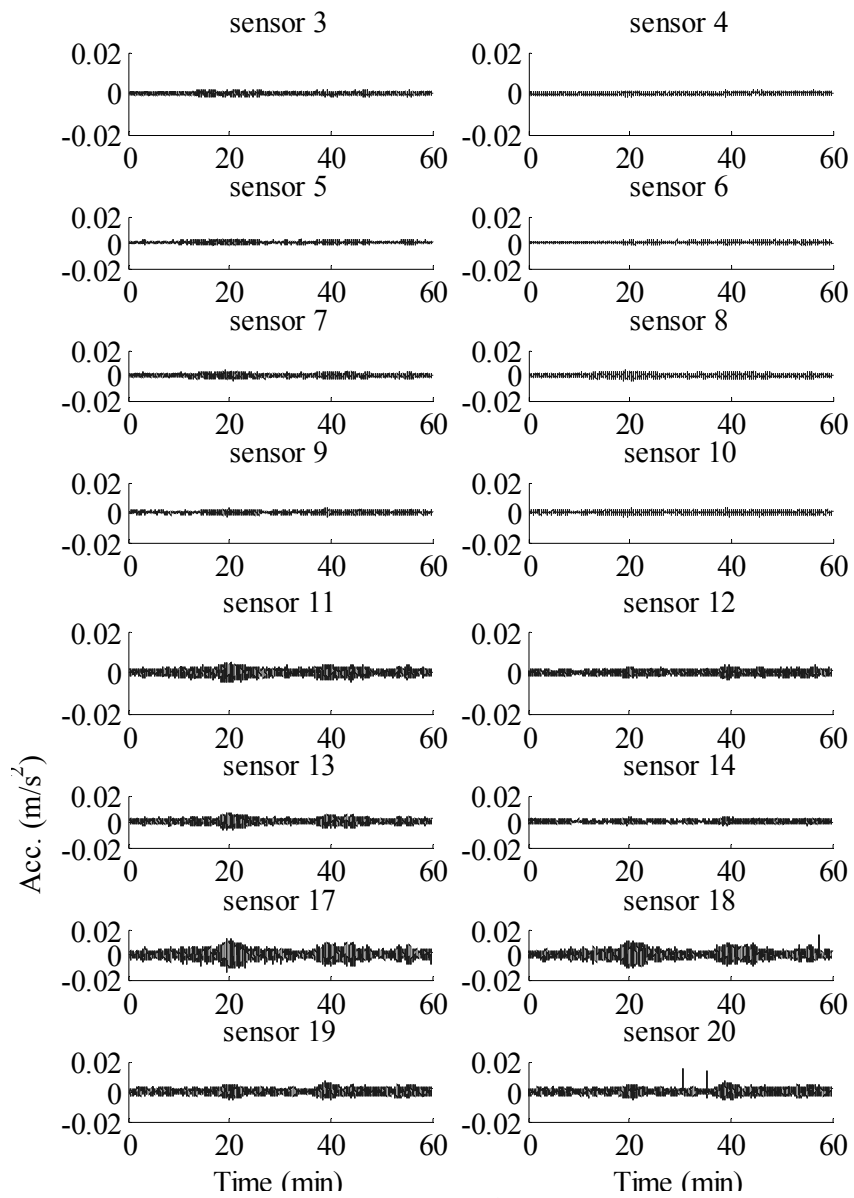
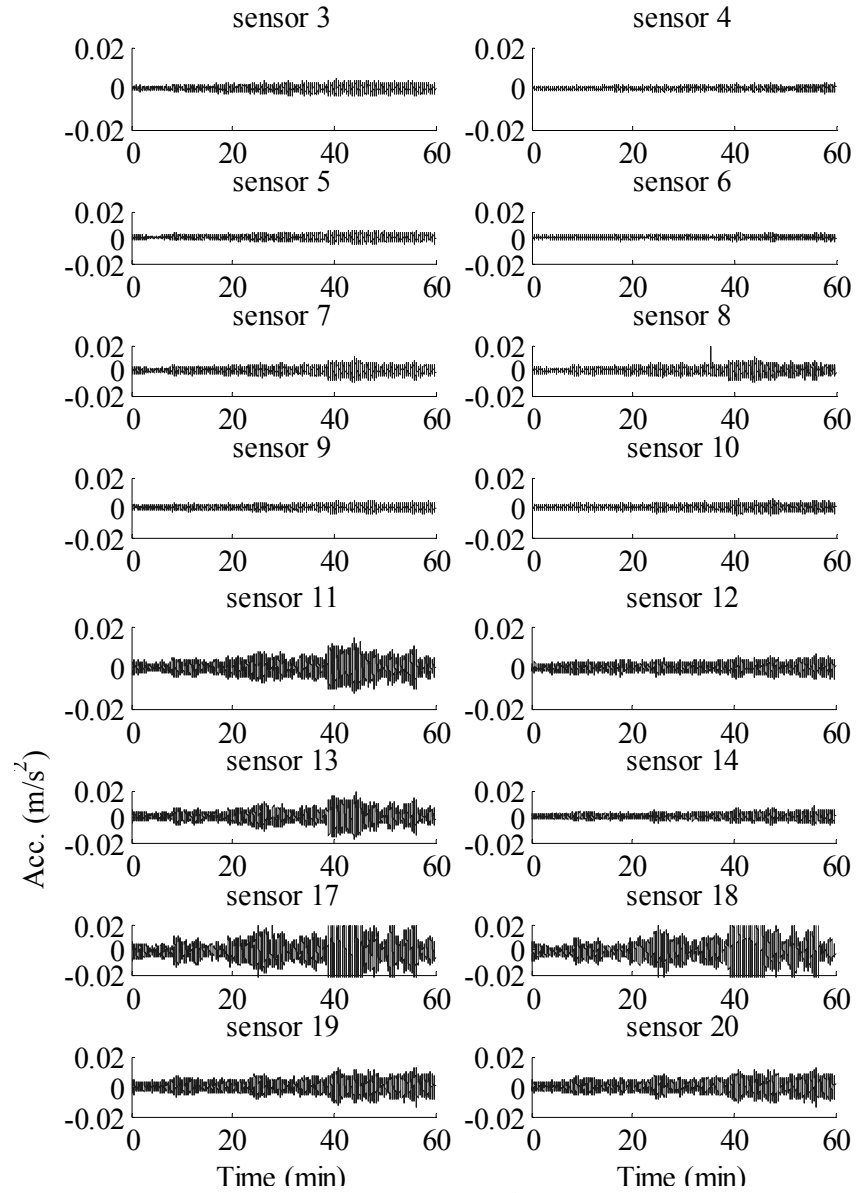


Figure A.14. Response measured on 18th/7/2009 from 22:32 to 23:32.

Figure A.15. Response measured on 19th/7/2009 from 0:32 to 1:32.

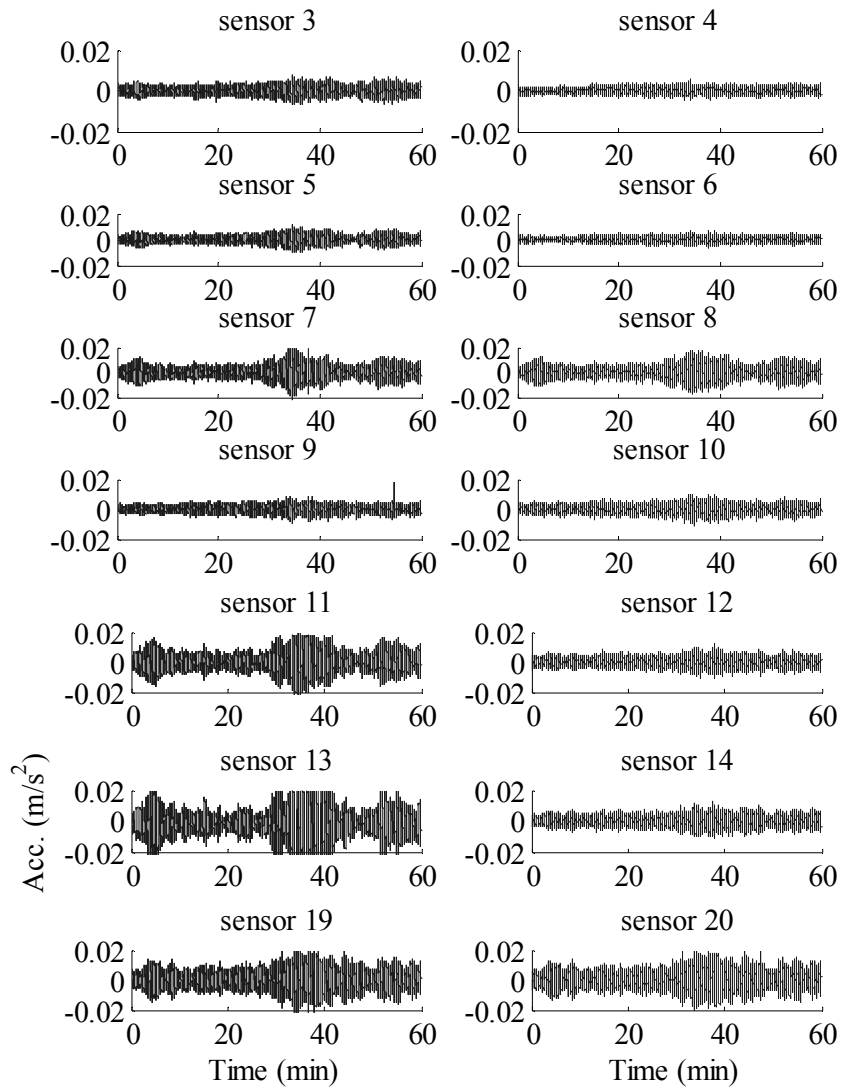


Figure A.16. Response measured on 19th/7/2009 from 1:32 to 2:32.

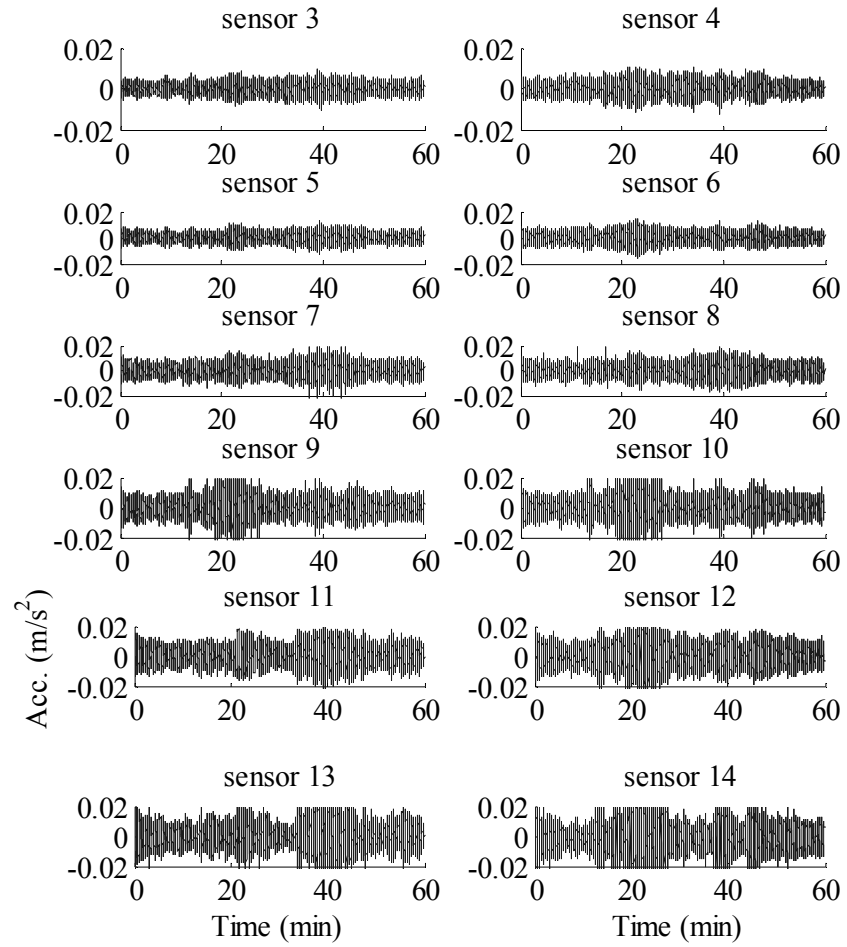


Figure A.17. Response measured on 19th/7/2009 from 5:32 to 6:32.

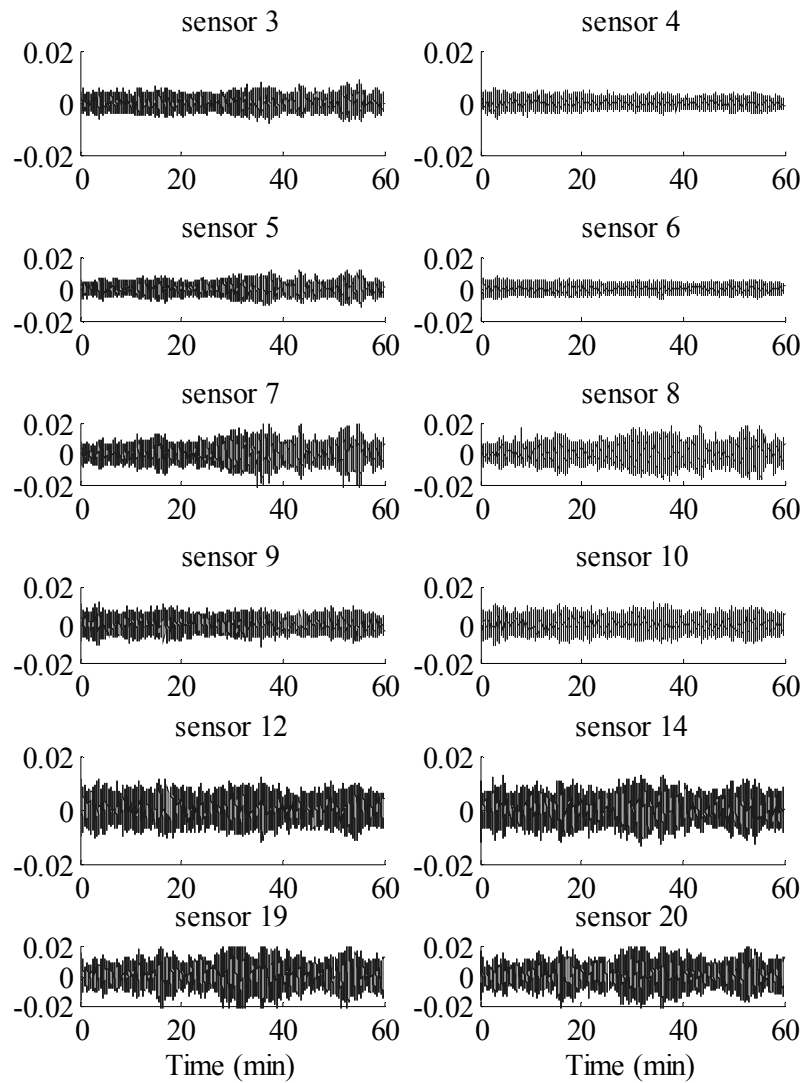


Figure A.18. Response measured on 19th/7/2009 from 6:32 to 7:32.

A.2.5 Typhoon Koppu

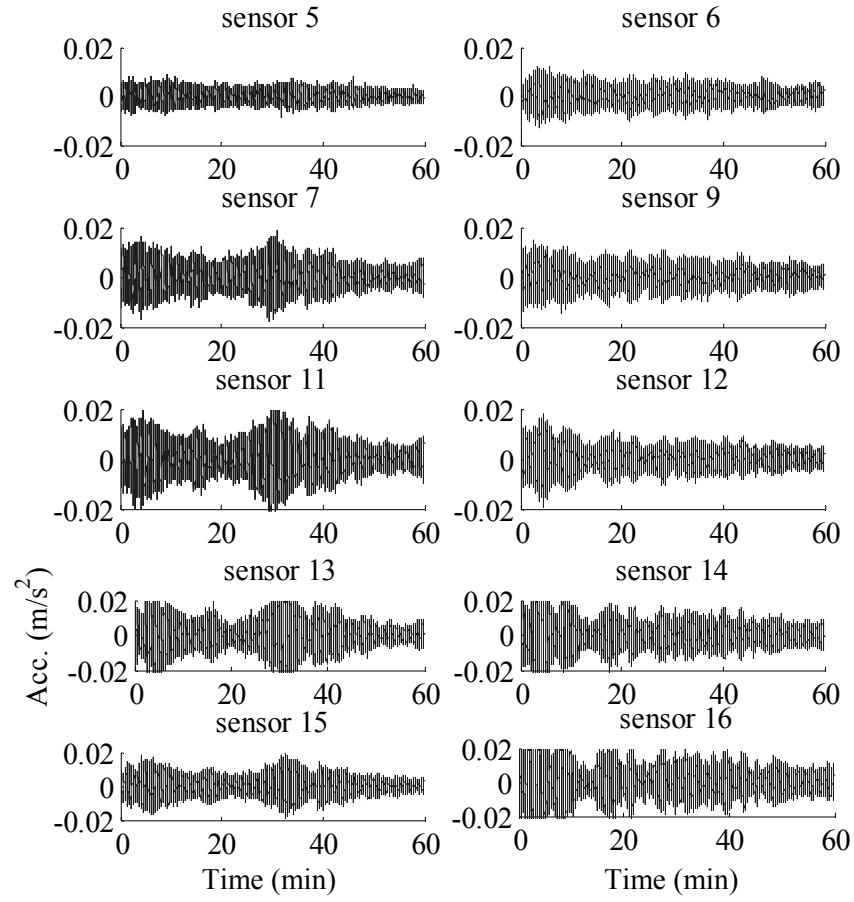


Figure A.19. Response measured on 15th/9/2009 from 6:00 to 7:00.

A.3 Response of GTVT to Earthquakes

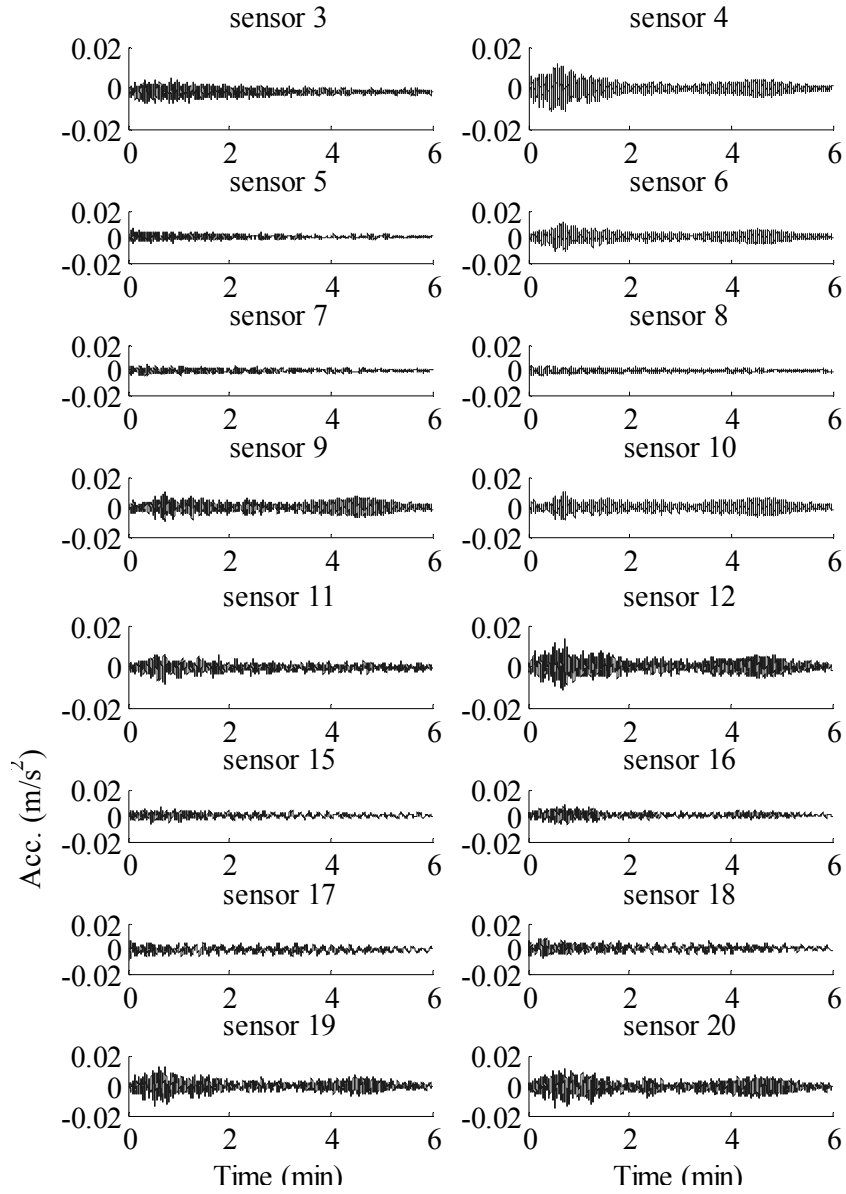


Figure A.20. Response measured during Southern Taiwan earthquake.

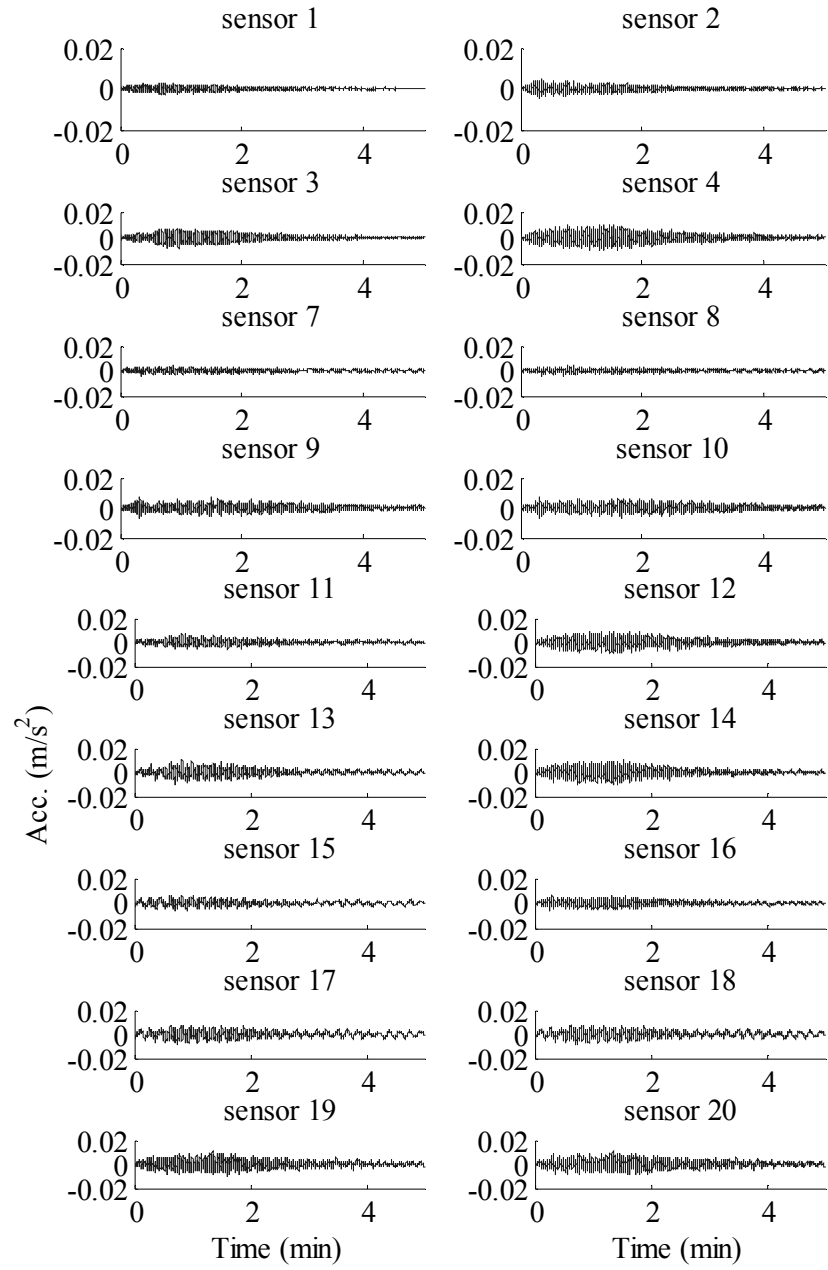


Figure A.21. Response measured during Taiwan Hualien earthquake.

Appendix B

Spectral Density of GTVT Response Signals during Extreme Events by FDD Method

B.1 Introduction

The Power spectral density diagrams of the response signals shown in Appendix A performed by FDD method are demonstrated in this Appendix

PSD's for signals recorded during the wind events; Kammuri, Nuri, Hagupit, Molave, and Koppu typhoons, are demonstrated in the following section by Figures B.1 –B.20, whereas, PSD's of those recorded during the ground motion events; Southern Taiwan, and Taiwan Hualien earthquakes are demonstrated by Figures B.21 and B.22.

All the figures included in this appendix are produced by the aid of ARTeMIS software.

B.2 PSD of GTVT Response to Typhoons

B.2.1 Typhoon Kammuri

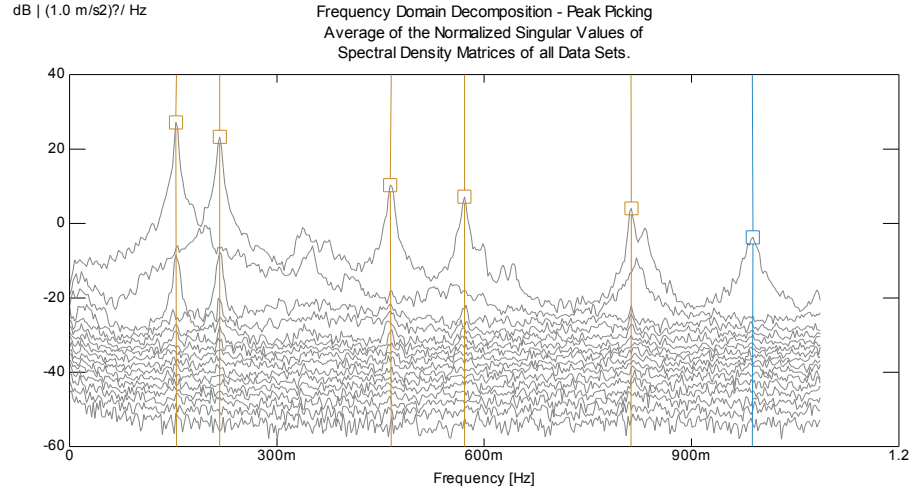


Figure B.1. PSD of signal obtained on 6th/8/2008 from 17:32 to 18:32.

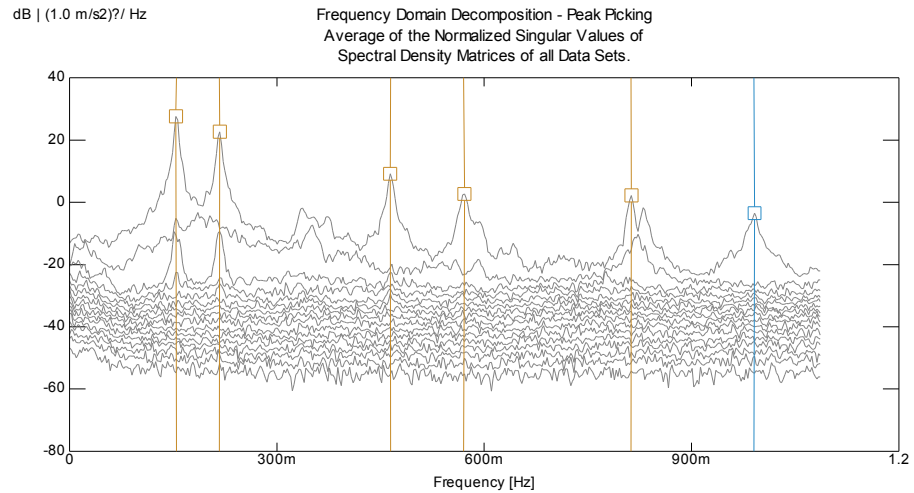
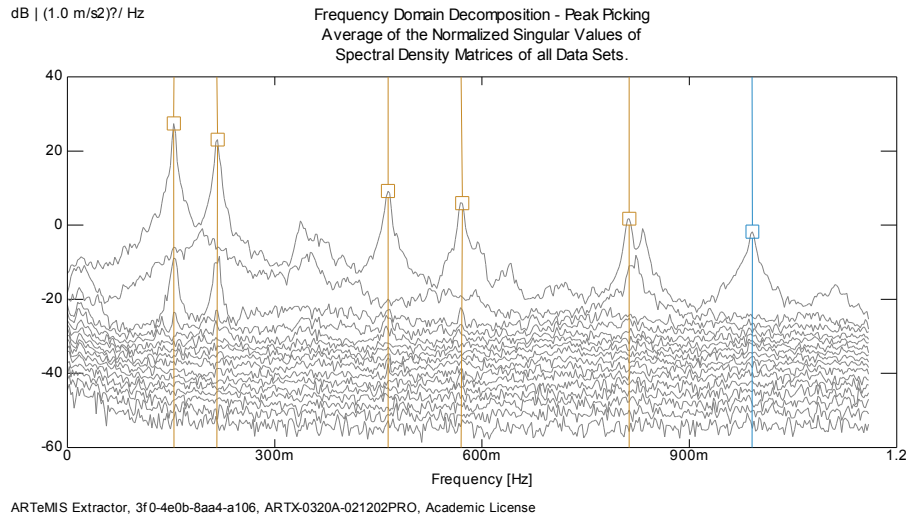
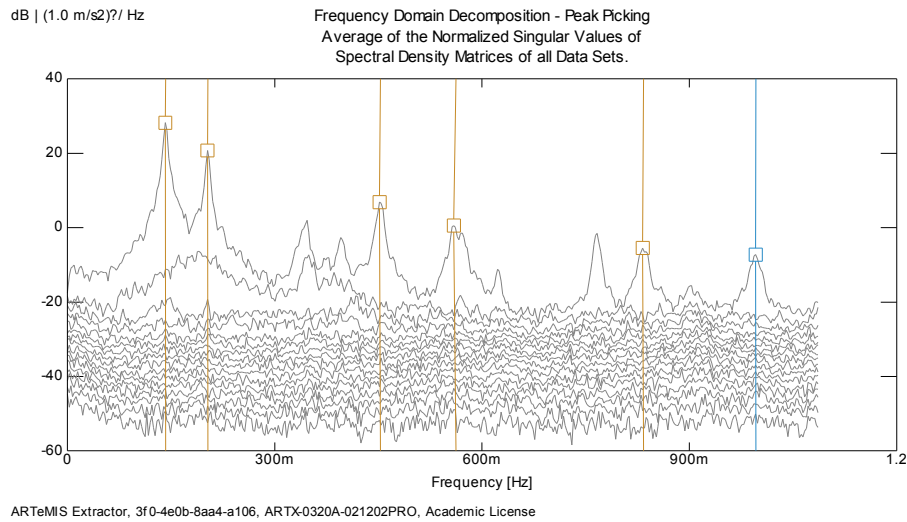


Figure B.2. PSD of signal obtained on 6th/8/2008 from 18:32 to 19:32.

Figure B.3. PSD of signal obtained on 6th/8/2008 from 19:32 to 20:32.

B.2.2 Typhoon Nuri

Figure B.4. PSD of signal obtained on 22nd/8/2008 from 14:00 to 15:00.

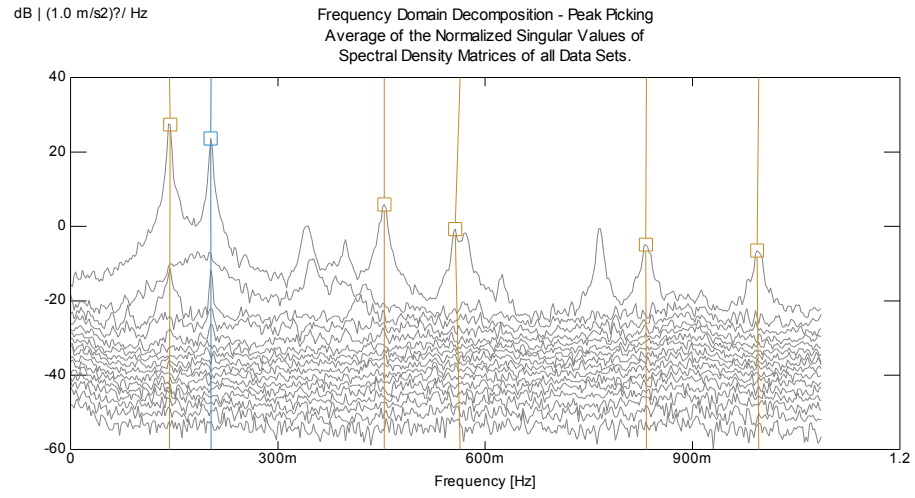


Figure B.5. PSD of signal obtained on 22nd/8/2008 from 15:00 to 16:00.

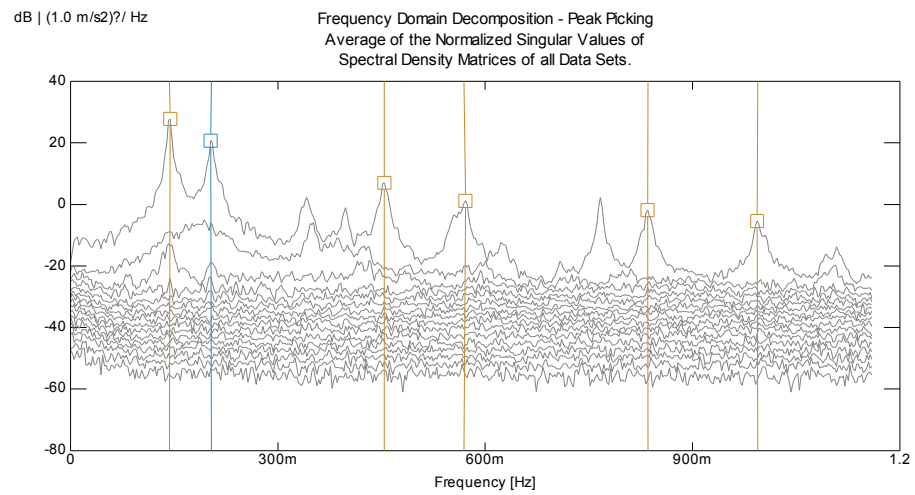
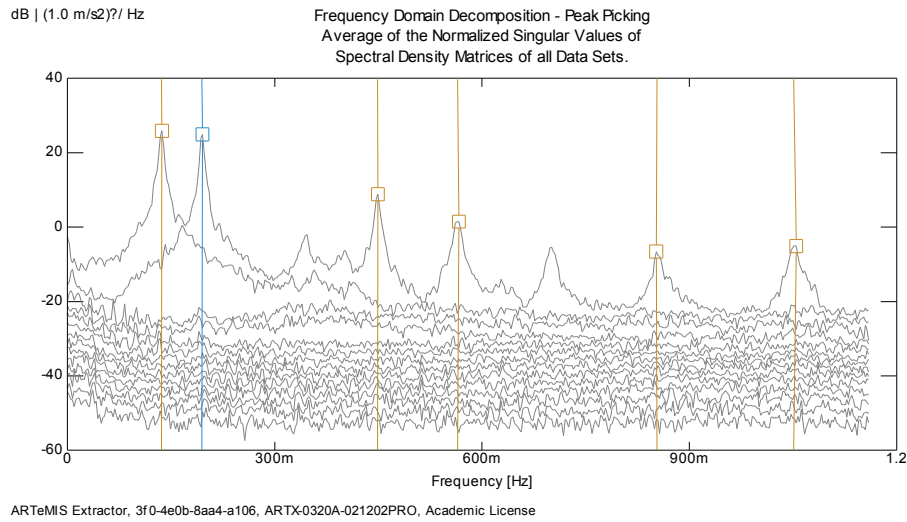
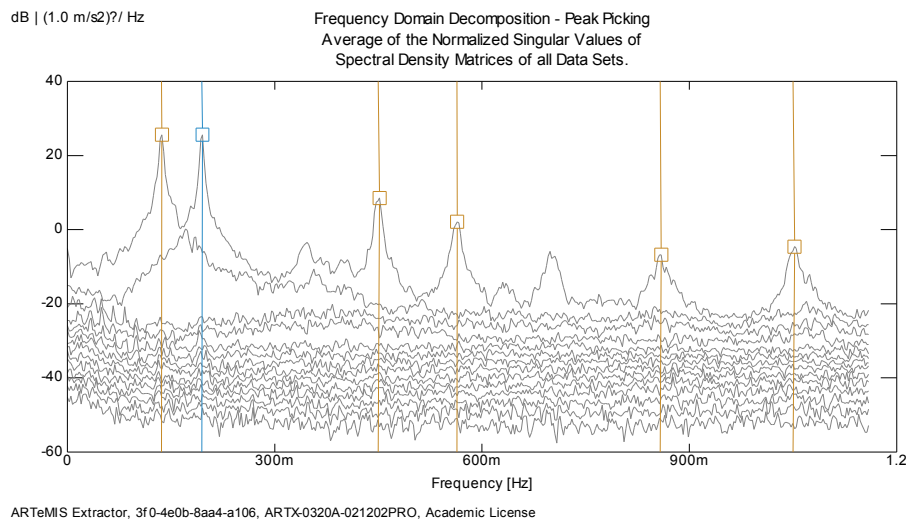


Figure B.6. PSD of signal obtained on 22nd/8/2008 from 16:00 to 17:00.

B.2.3 Typhoon Hagupit

Figure B.7. PSD of signal obtained on 24th/9/2008 from 3:00 to 4:00.Figure B.8. PSD of signal obtained on 24th/9/2008 from 4:00 to 5:00.

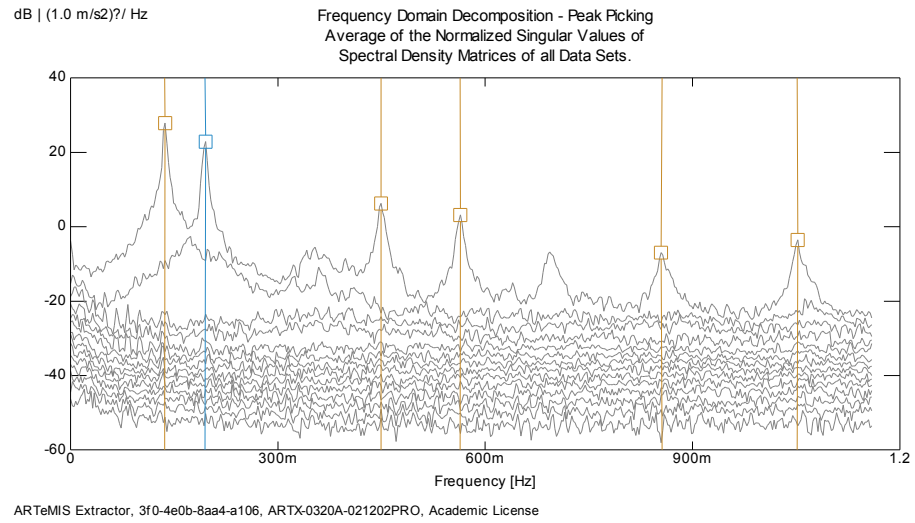


Figure B.9. PSD of signal obtained on 24th/9/2008 from 5:00 to 6:00.

B.2.4 Typhoon Molave

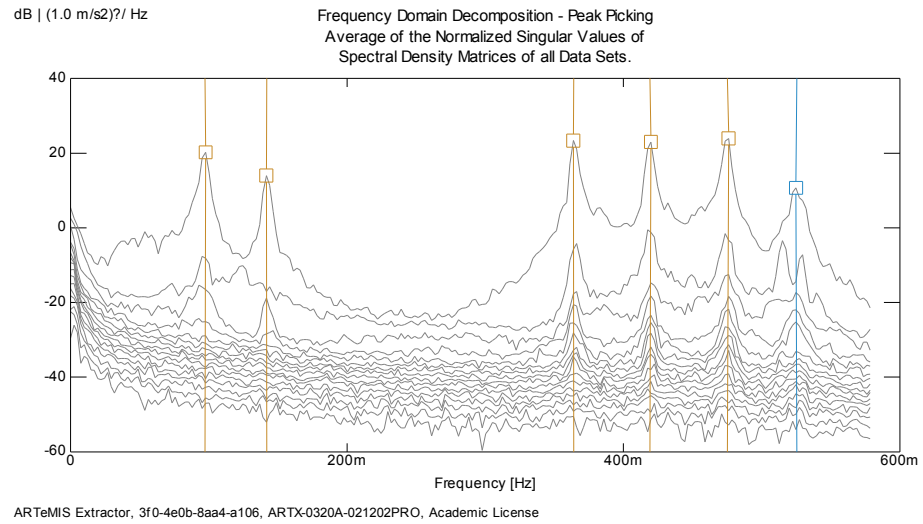
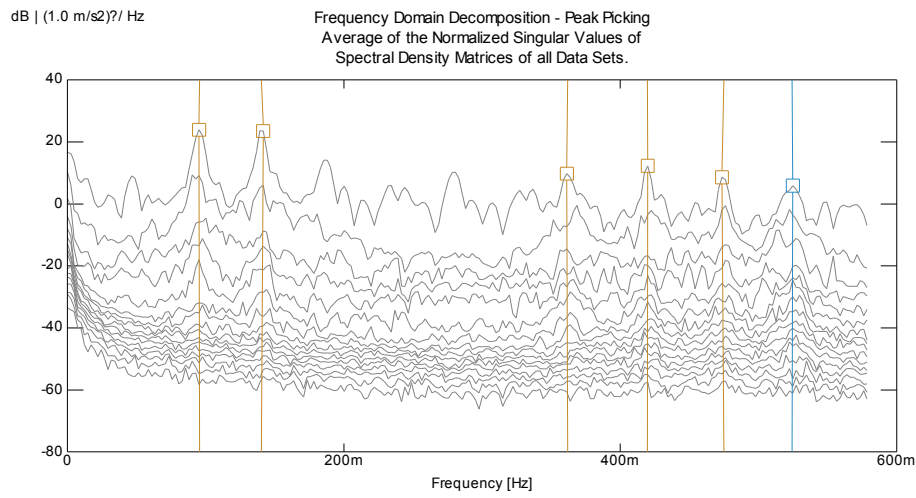
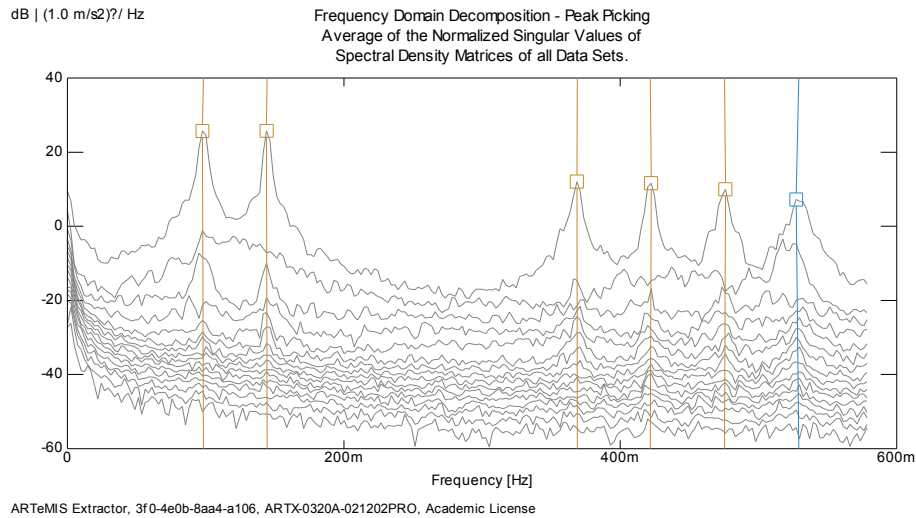


Figure B.10. PSD of signal obtained on 18th/7/2009 from 17:32 to 18:32.

Figure B.11. PSD of signal obtained on 18th/7/2009 from 18:32 to 19:32.Figure B.12. PSD of signal obtained on 18th/7/2009 from 19:32 to 20:32.

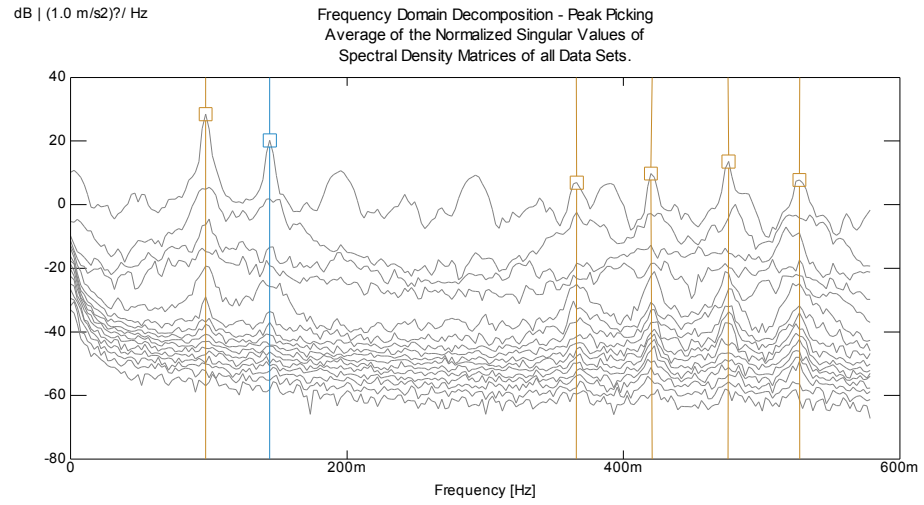


Figure B.13. PSD of signal obtained on 18th/7/2009 from 20:32 to 21:32.

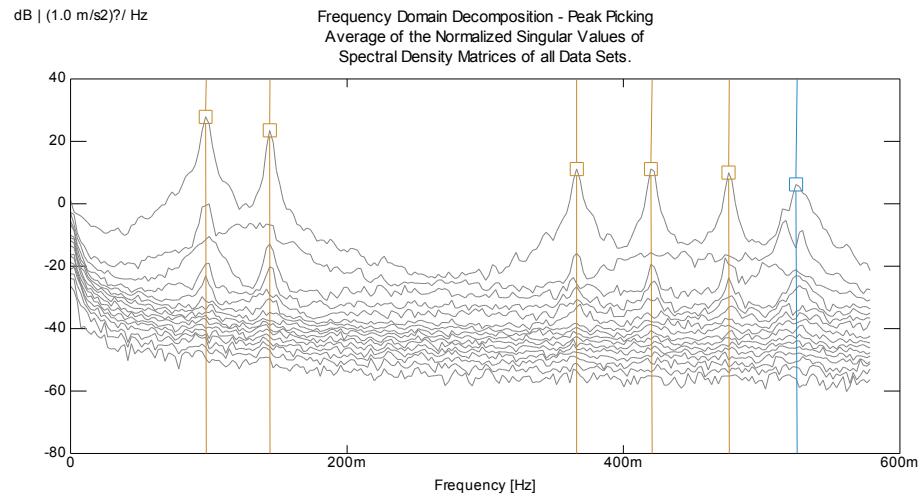
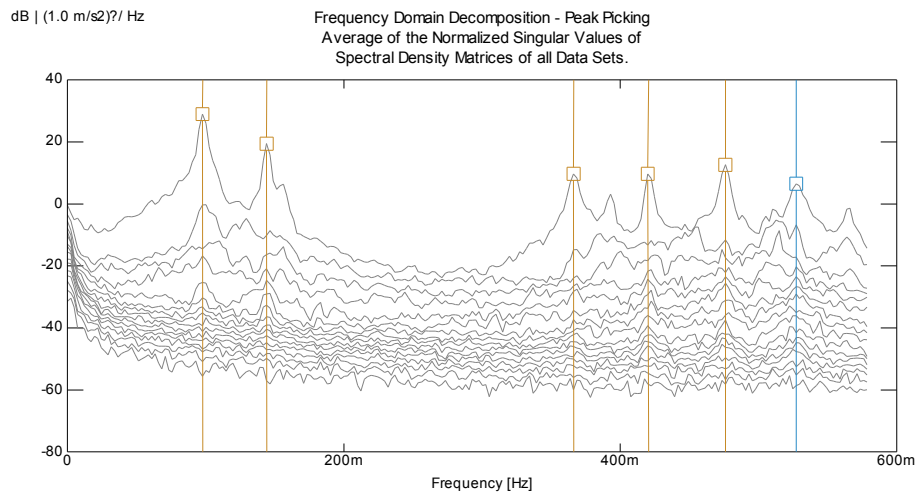
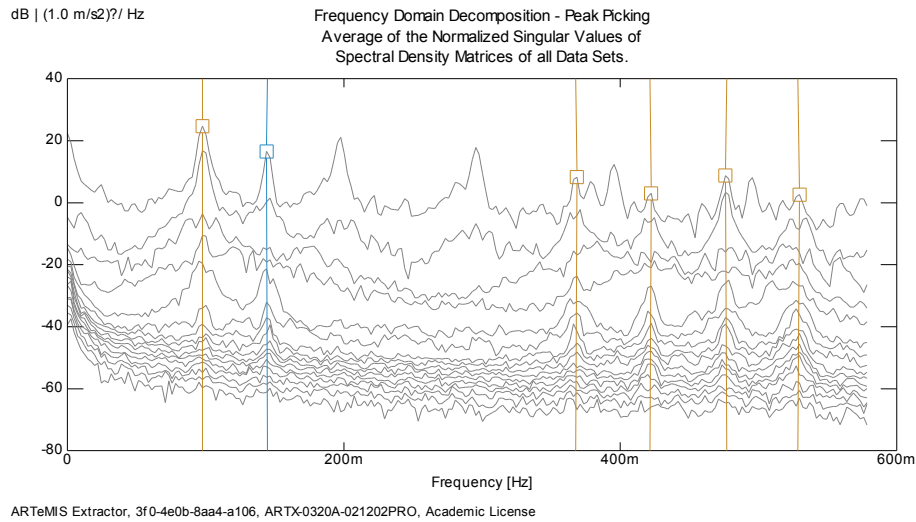
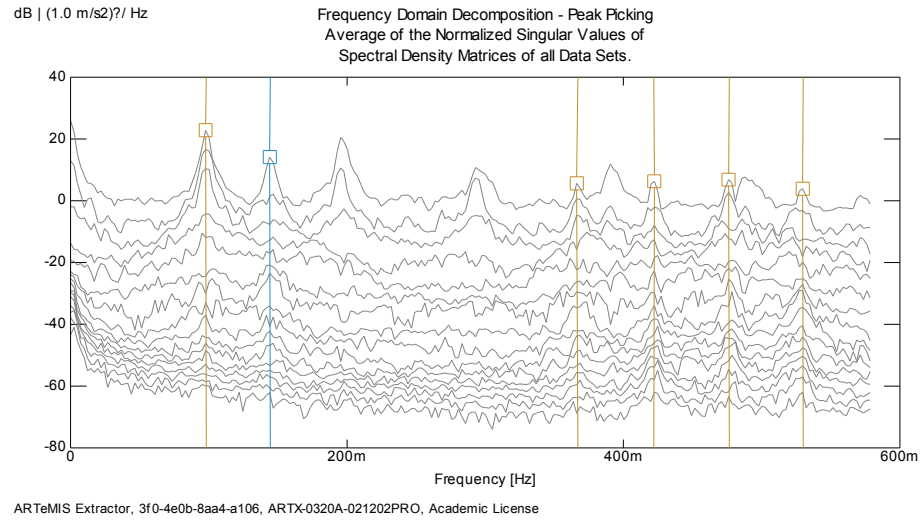
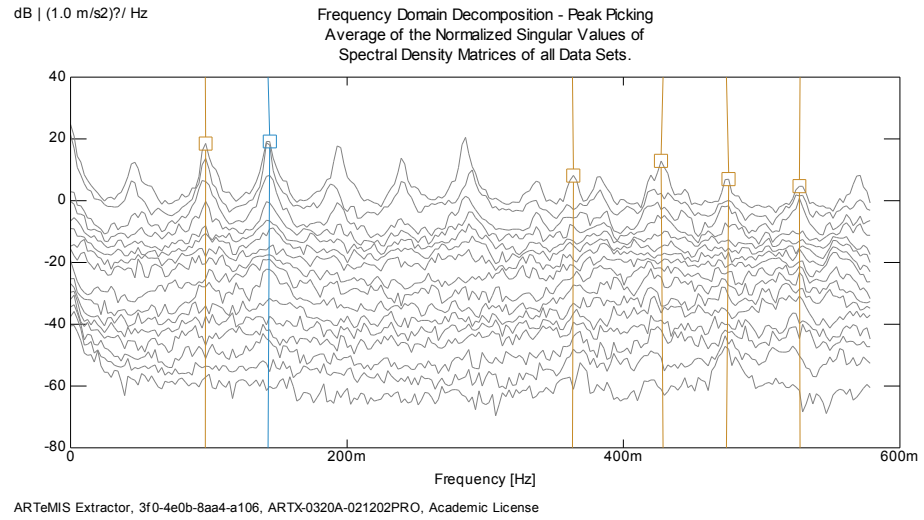
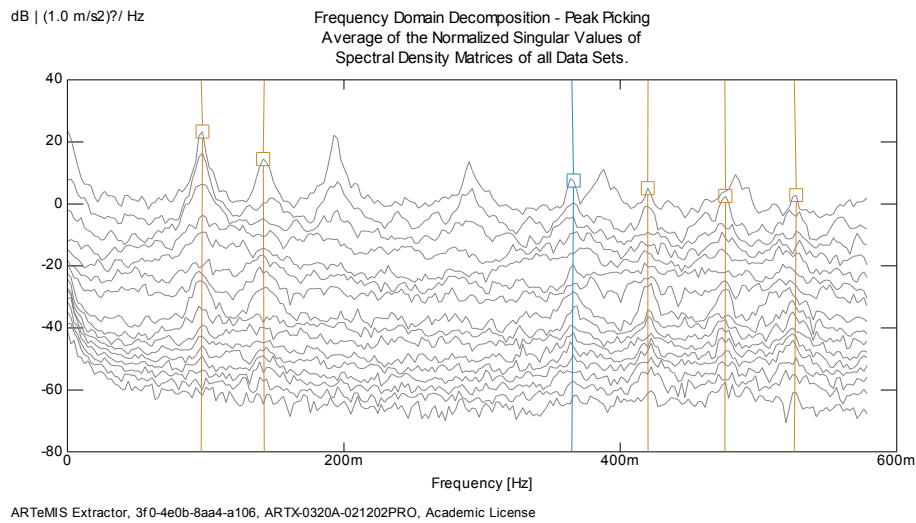


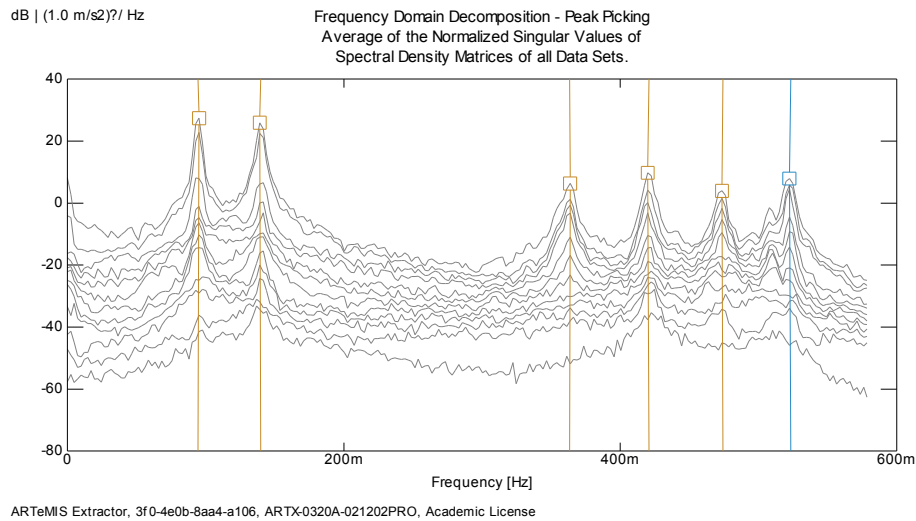
Figure B.14. PSD of signal obtained on 18th/7/2009 from 21:32 to 22:32.

Figure B.15. PSD of signal obtained on 18th/7/2009 from 22:32 to 23:32.Figure B.16. PSD of signal obtained on 19th/7/2009 from 0:32 to 1:32.

Figure B.17. PSD of signal obtained on 19th/7/2009 from 1:32 to 2:32.Figure B.18. PSD of signal obtained on 19th/7/2009 from 5:32 to 6:32.

Figure B.19. PSD of signal obtained on 19th/7/2009 from 6:32 to 7:32.

B.2.5 Typhoon Koppu

Figure B.20. PSD of signal obtained on 15th/9/2009 from 6:00 to 7:00.

B.3 PSD of GTVT Response to Earthquakes

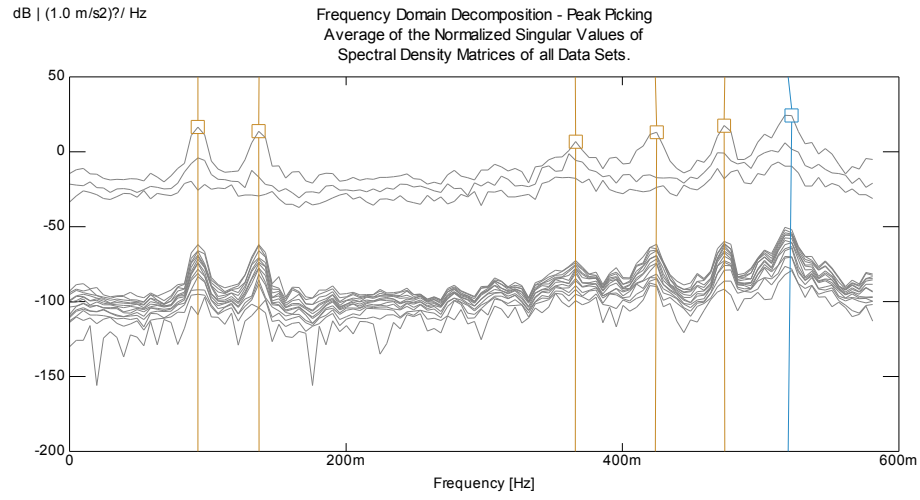


Figure B.21. PSD of signal obtained during Southern Taiwan earthquake.

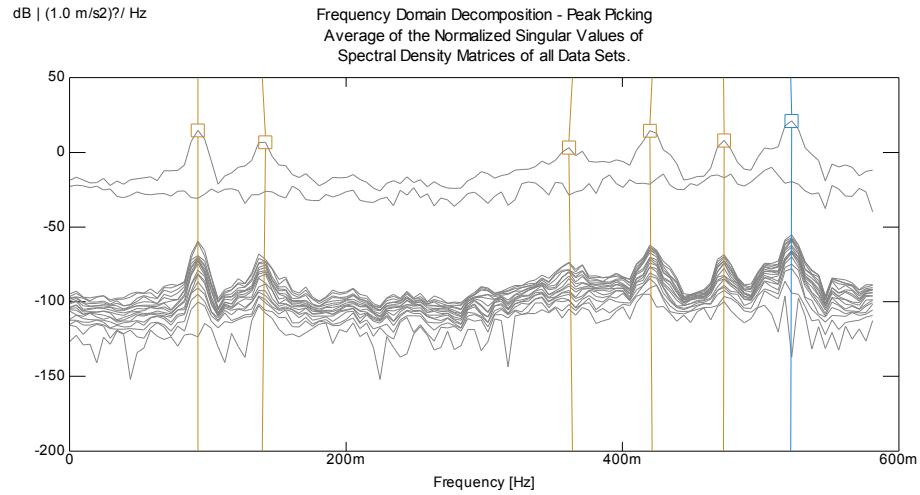


Figure B.22. PSD of signal obtained during Taiwan Hualien earthquake.

Appendix C

Hilbert-Huang Spectra of GTVT Response Signals during Extreme Events

C.1 Introduction

The Power spectral diagrams of chosen response signals performed by HHT method are demonstrated in this Appendix

In the second section Hilbert Huang (HH) spectrums for 15 minutes of the signals recorded during the wind events; Kammuri, Nuri, Hagupit, Molave, and Koppu typhoons, are demonstrated, while, HH spectrums of the available signal recorded during the ground motion events; Southern Taiwan, and Taiwan Hualien earthquakes are demonstrated in the third section.

C.2 HHT Spectra of GTVT Response Signals to Typhoons

C.2.1 Typhoon Kammuri

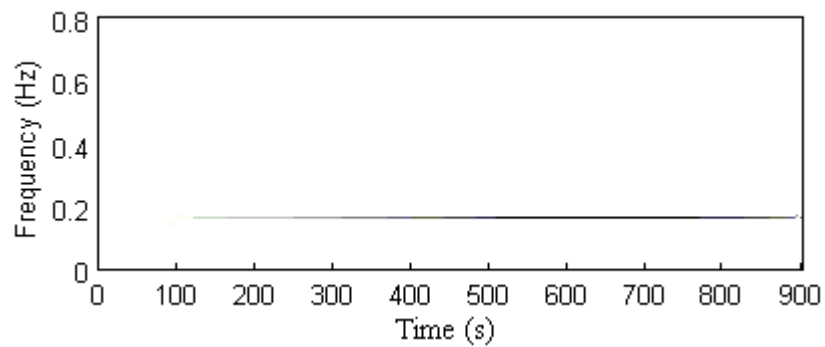


Figure C.1. HHT of signal obtained at sensor 1.

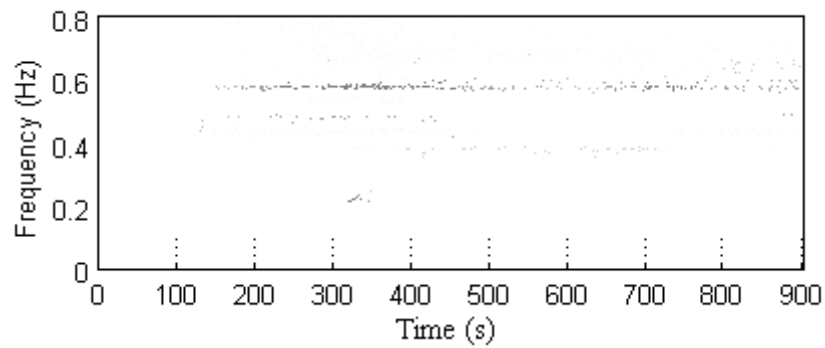


Figure C.2. HHT of signal obtained at sensor 2.

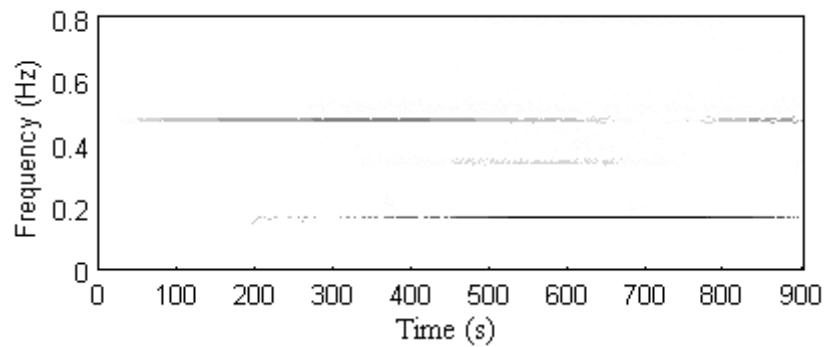


Figure C.3. HHT of signal obtained at sensor 3.

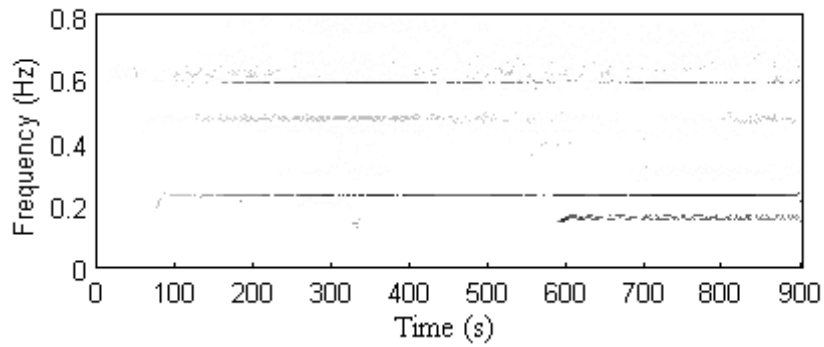


Figure C.4. HHT of signal obtained at sensor 4.

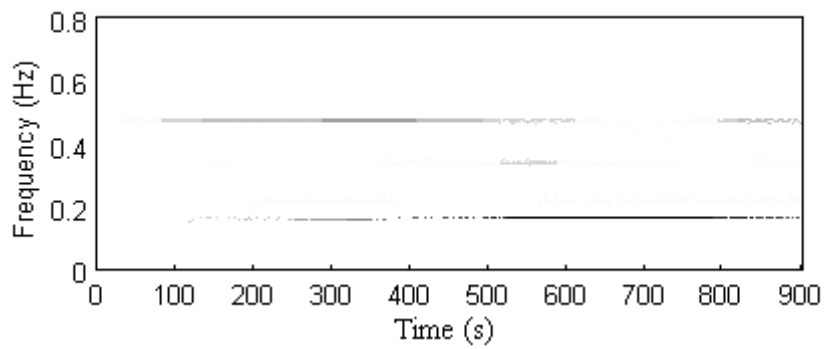


Figure C.5. HHT of signal obtained at sensor 5.

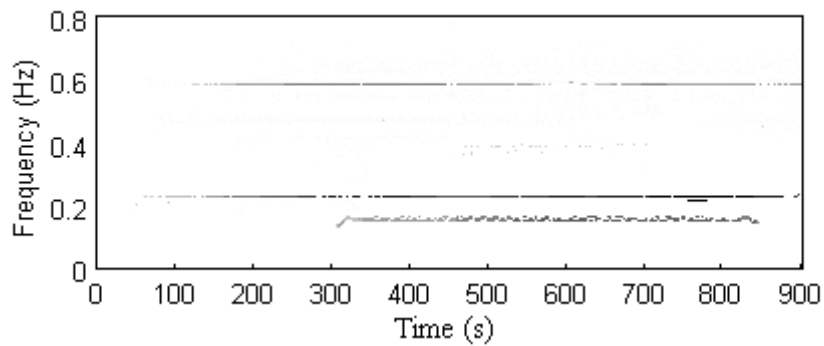


Figure C.6. HHT of signal obtained at sensor 6.

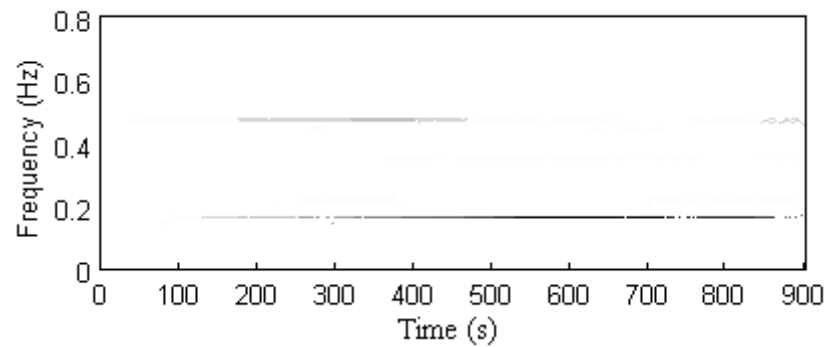


Figure C.7. HHT of signal obtained at sensor 7.

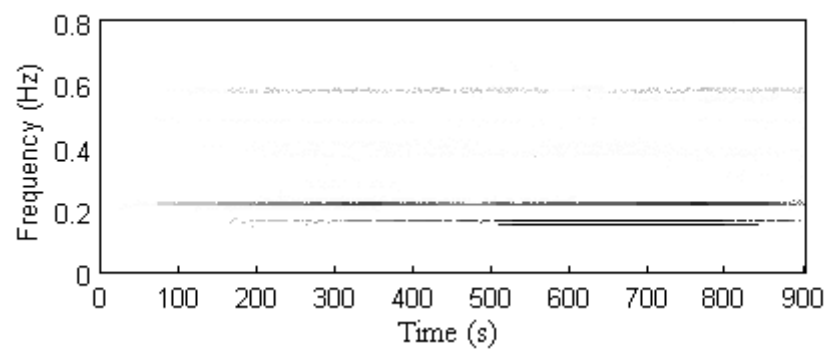


Figure C.8. HHT of signal obtained at sensor 8.

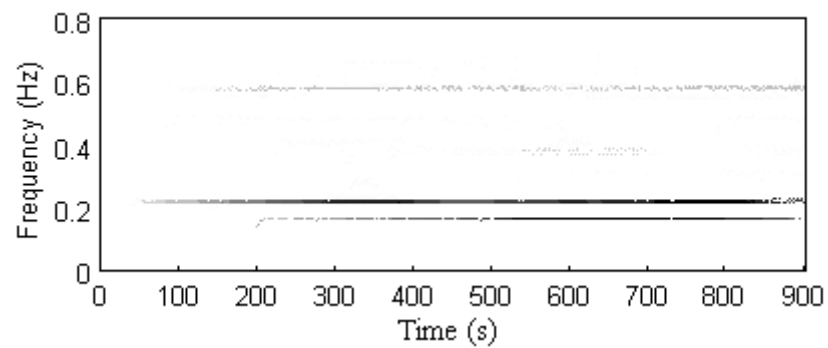


Figure C.9. HHT of signal obtained at sensor 9.

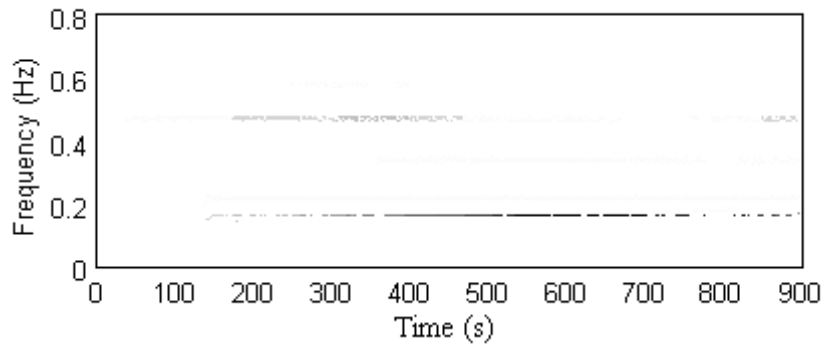


Figure C.10. HHT of signal obtained at sensor 10.

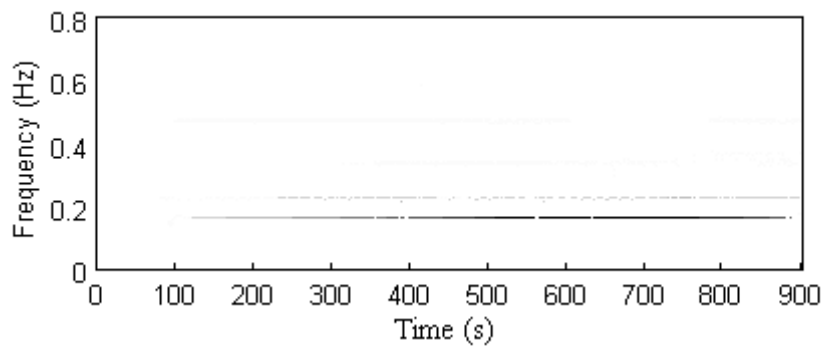


Figure C.11. HHT of signal obtained at sensor 11.

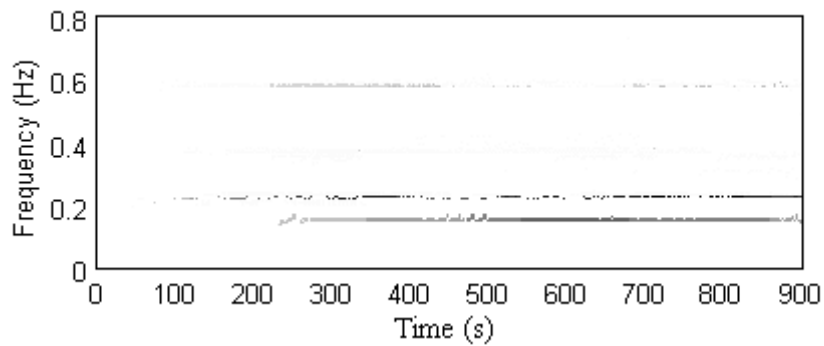


Figure C.12. HHT of signal obtained at sensor 12.

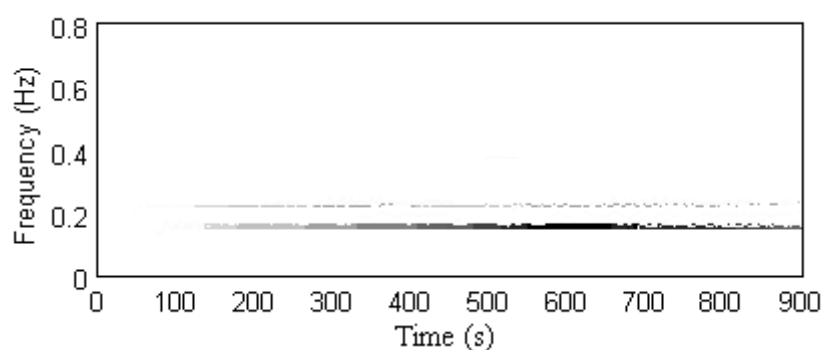


Figure C.13. HHT of signal obtained at sensor 13.

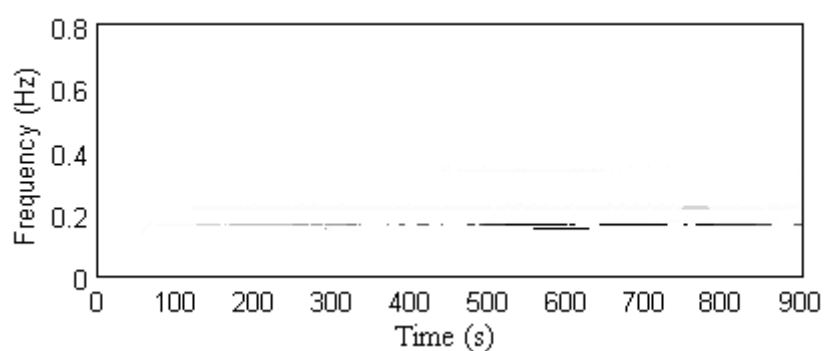


Figure C.14. HHT of signal obtained at sensor 14.

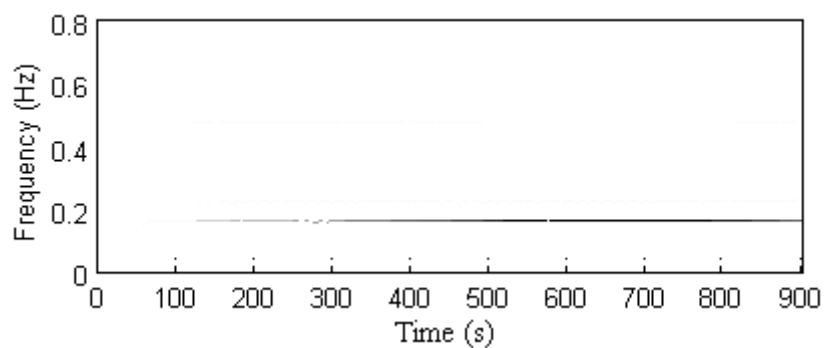


Figure C.15. HHT of signal obtained at sensor 15.

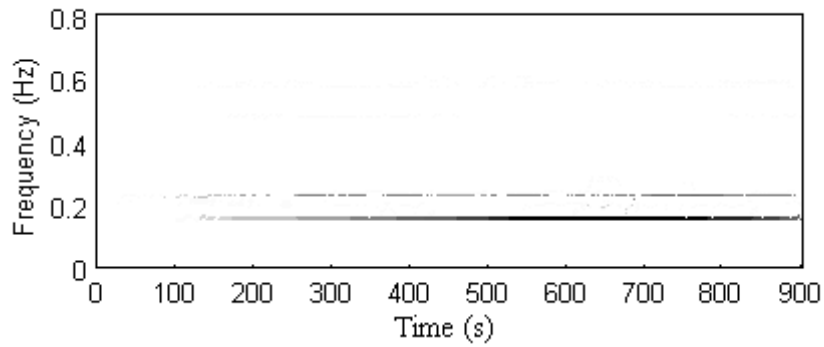


Figure C.16. HHT of signal obtained at sensor 16.

C.2.2 Typhoon Nuri

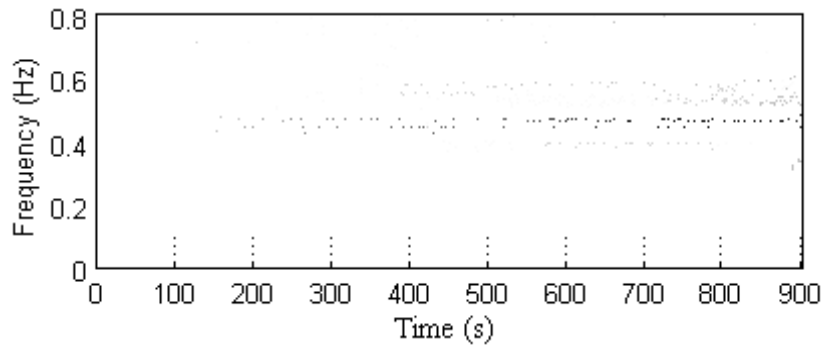


Figure C.17. HHT of signal obtained at sensor 1.

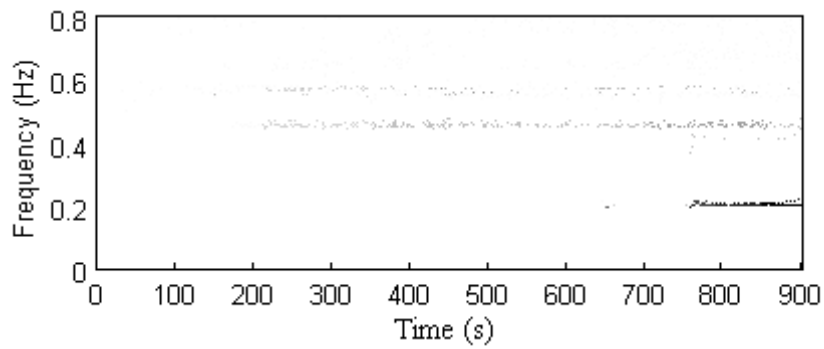


Figure C.18. HHT of signal obtained at sensor 2.

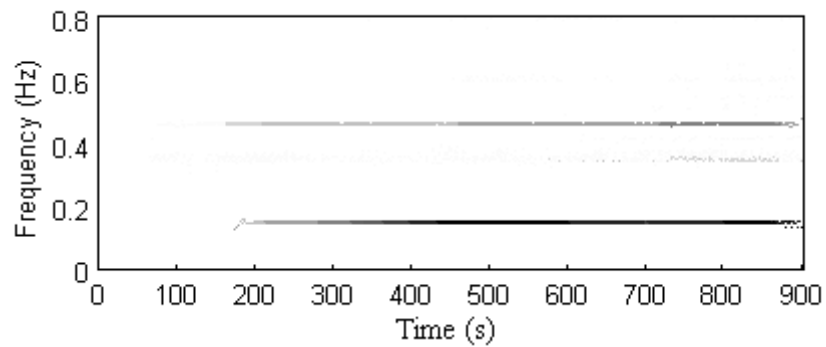


Figure C.19. HHT of signal obtained at sensor 3.

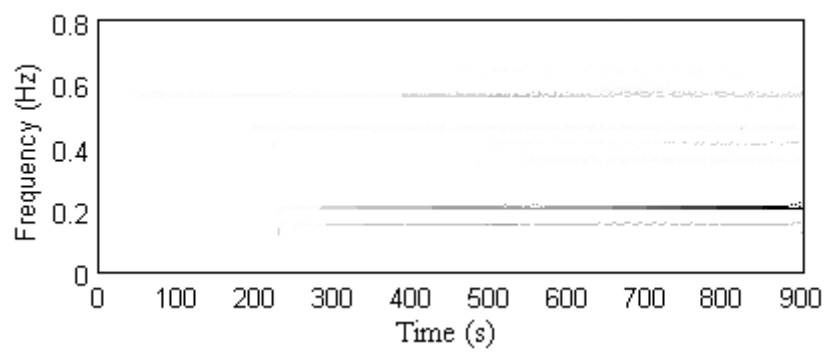


Figure C.20. HHT of signal obtained at sensor 4.

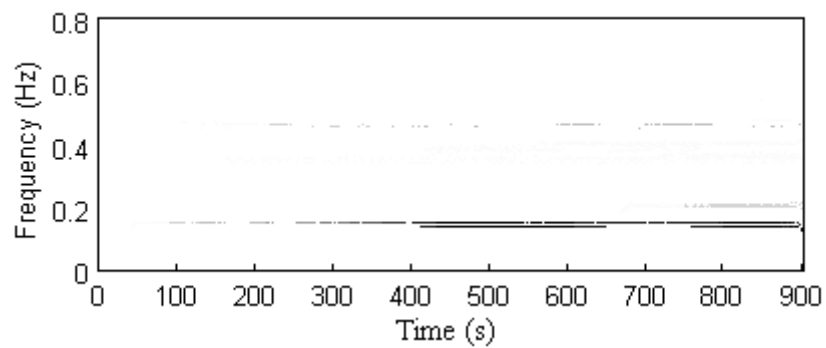


Figure C.21. HHT of signal obtained at sensor 5.

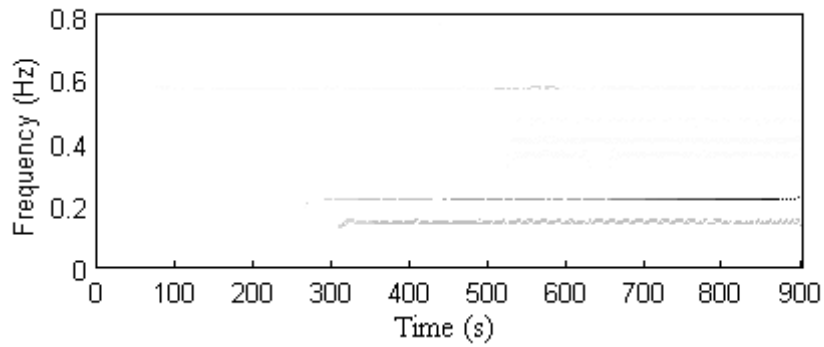


Figure C.22. HHT of signal obtained at sensor 6.

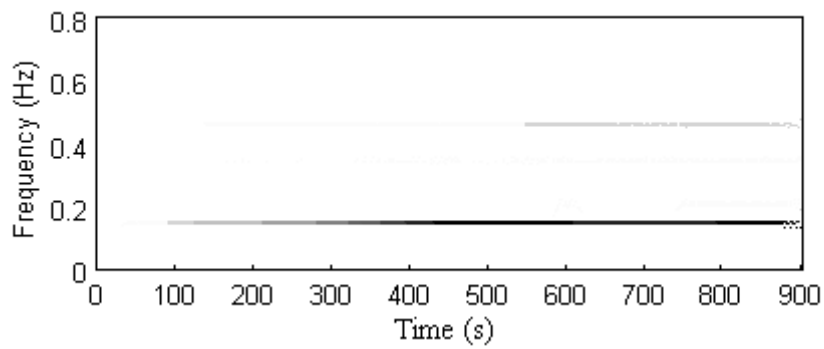


Figure C.23. HHT of signal obtained at sensor 7.

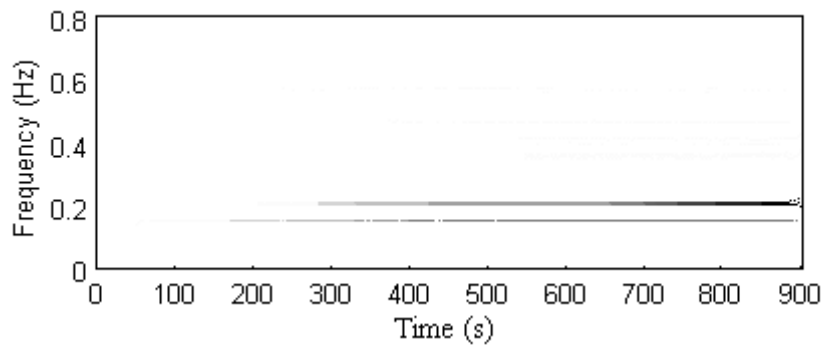


Figure C.24. HHT of signal obtained at sensor 8.

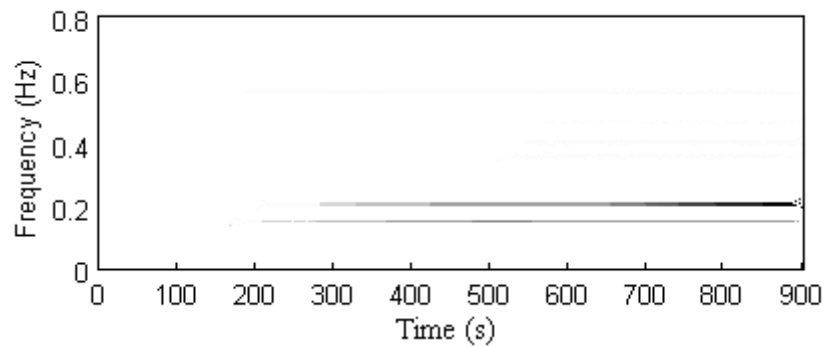


Figure C.25. HHT of signal obtained at sensor 9.

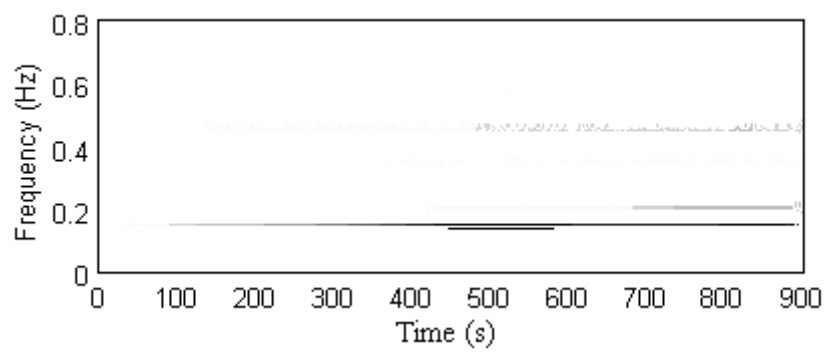


Figure C.26. HHT of signal obtained at sensor 10.

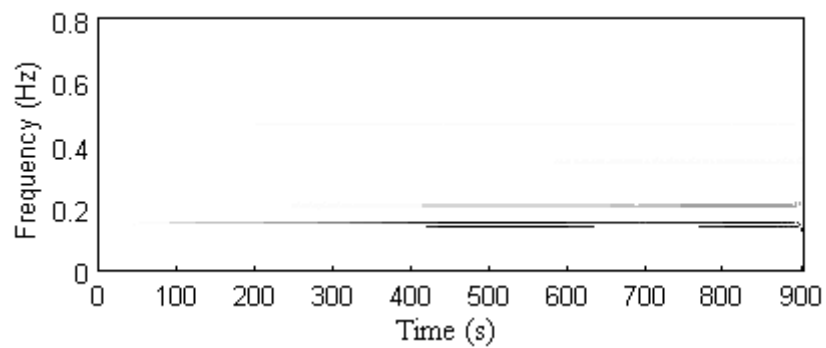


Figure C.27. HHT of signal obtained at sensor 11.

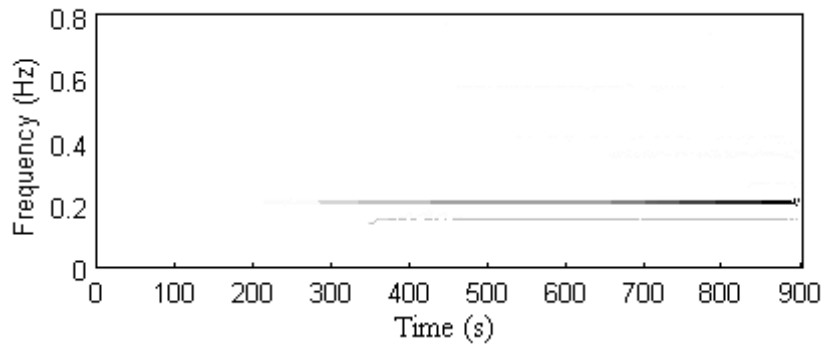


Figure C.28. HHT of signal obtained at sensor 12.

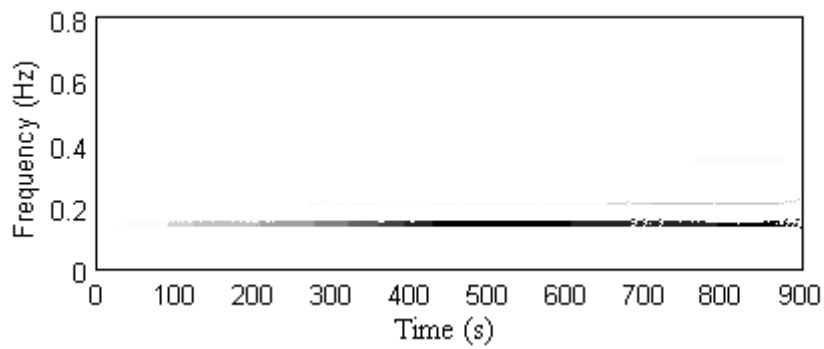


Figure C.29. HHT of signal obtained at sensor 13.

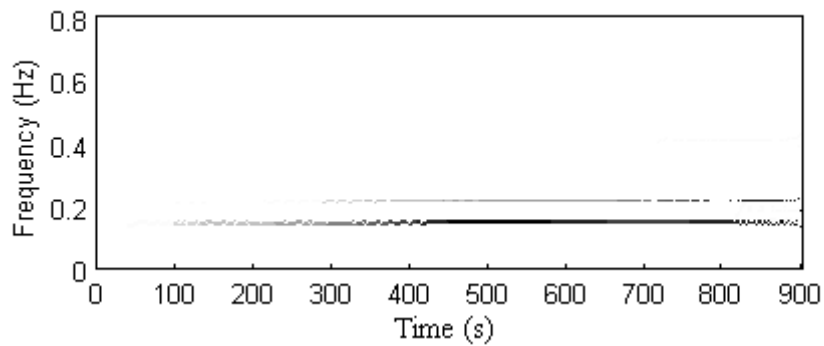


Figure C.30. HHT of signal obtained at sensor 14.

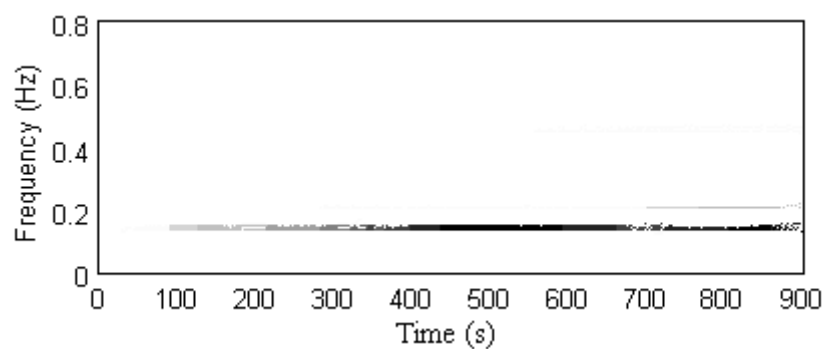


Figure C.31. HHT of signal obtained at sensor 15.

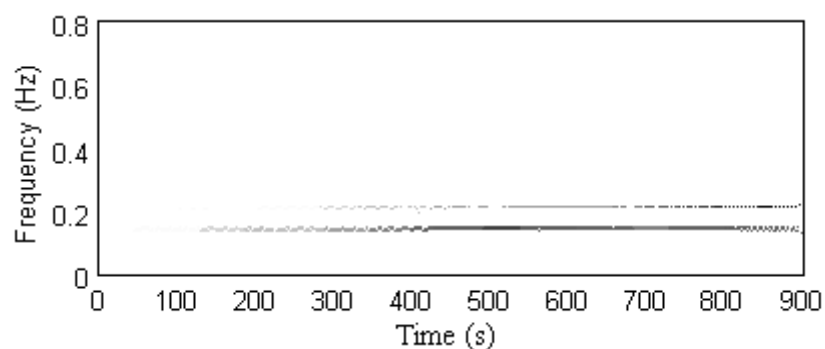


Figure C.32. HHT of signal obtained at sensor 16.

C.2.3 Typhoon Hagupit

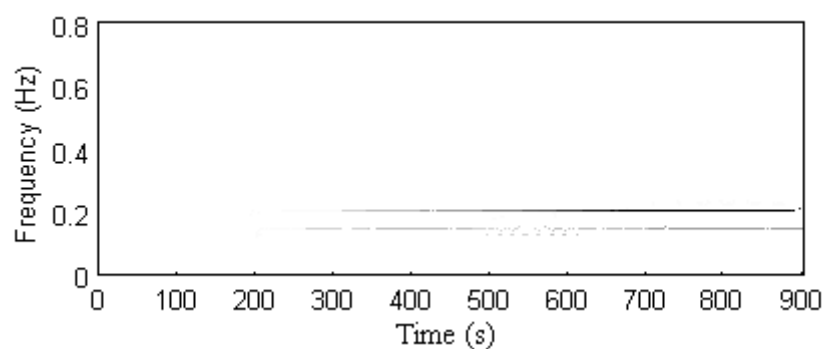


Figure C.33. HHT of signal obtained at sensor 1.

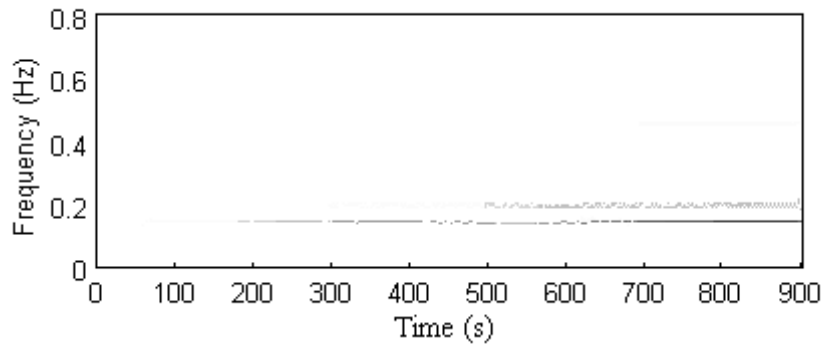


Figure C.34. HHT of signal obtained at sensor 2.

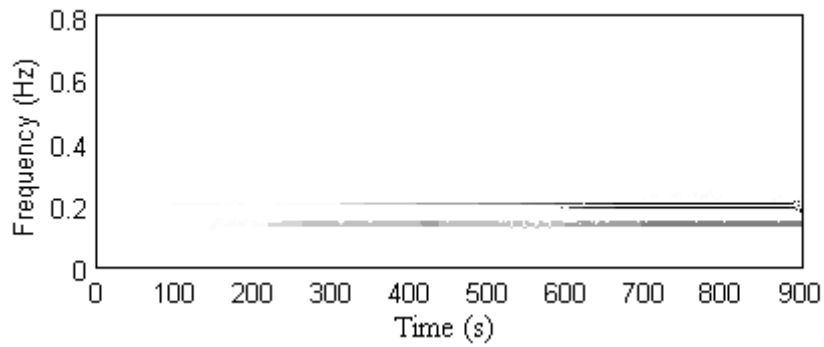


Figure C.35. HHT of signal obtained at sensor 5

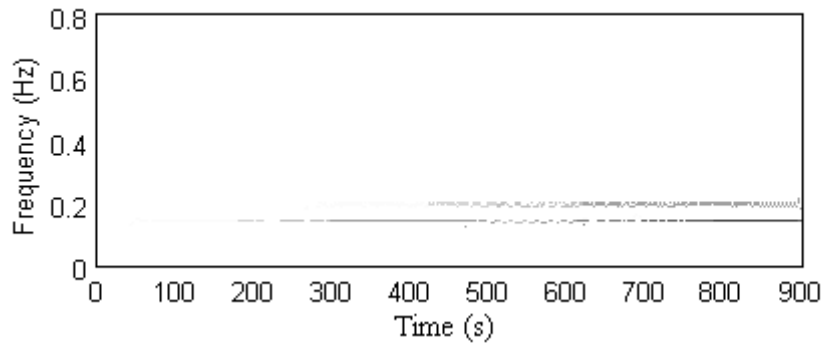


Figure C.36. HHT of signal obtained at sensor 6.

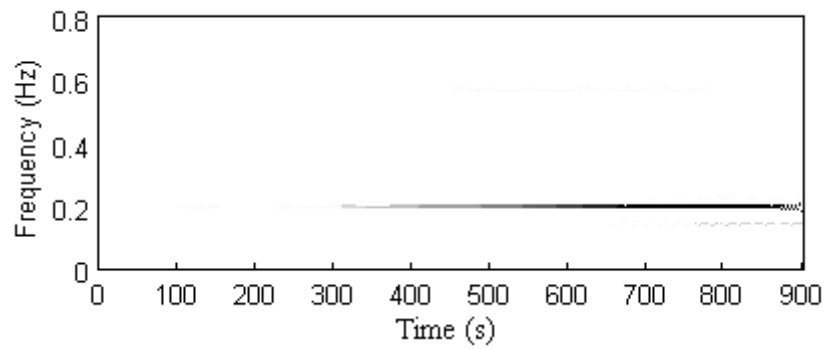


Figure C.37. HHT of signal obtained at sensor 7.

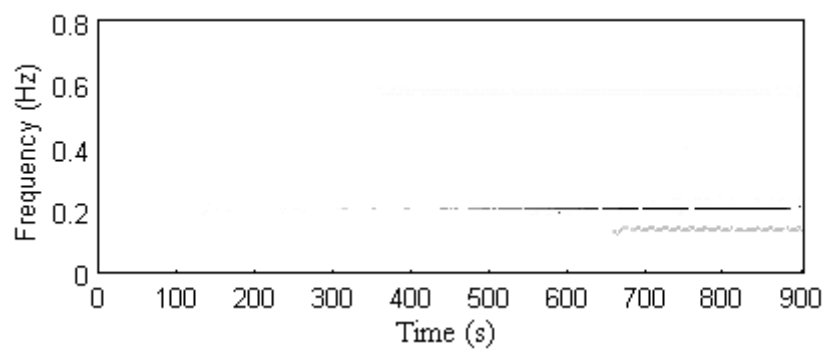


Figure C.38. HHT of signal obtained at sensor 8.

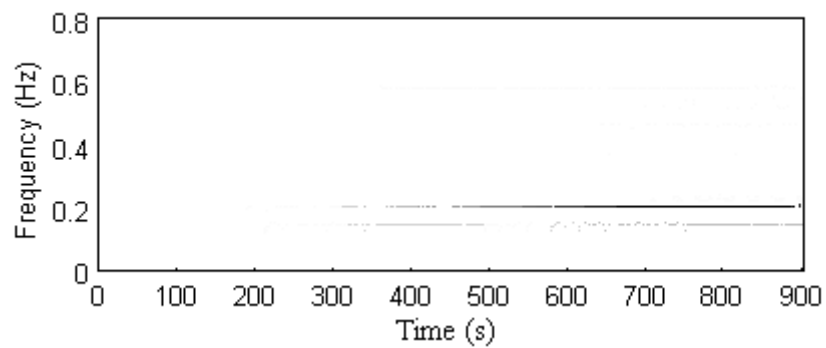


Figure C.39. HHT of signal obtained at sensor 9.

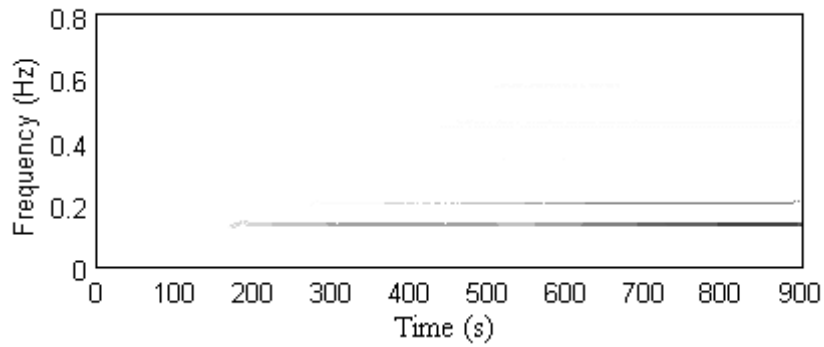


Figure C.40. HHT of signal obtained at sensor 10.

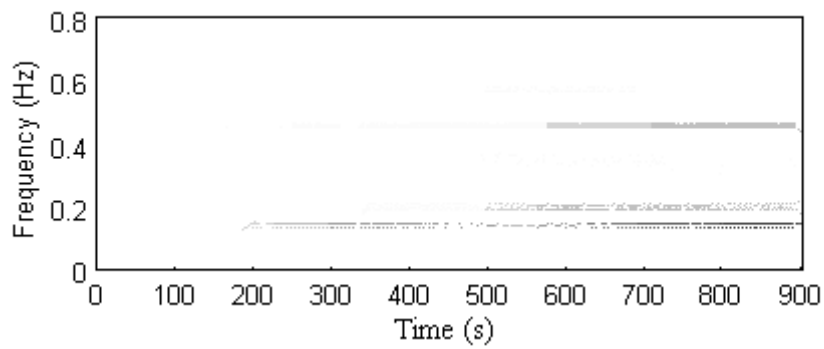


Figure C.41. HHT of signal obtained at sensor 11.

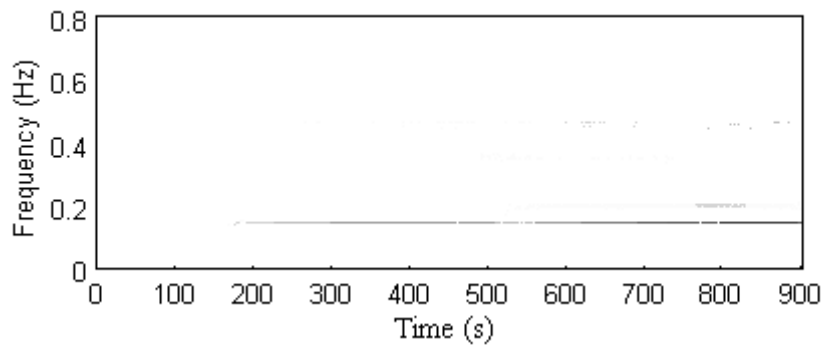


Figure C.42. HHT of signal obtained at sensor 12.

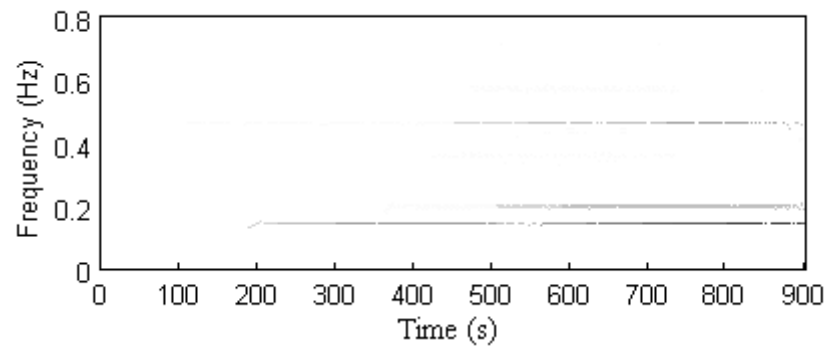


Figure C.43. HHT of signal obtained at sensor 13.

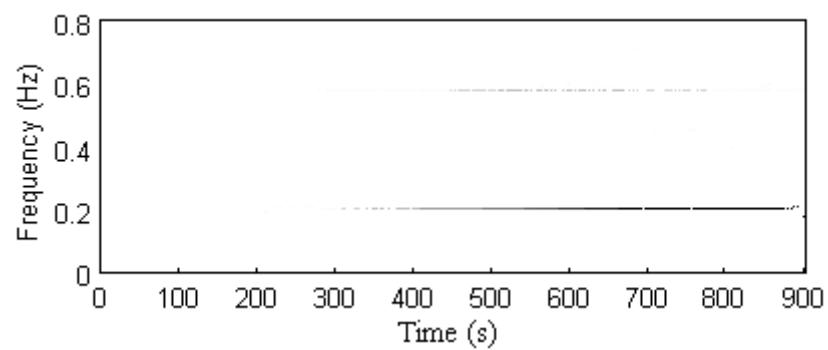


Figure C.44. HHT of signal obtained at sensor 14.

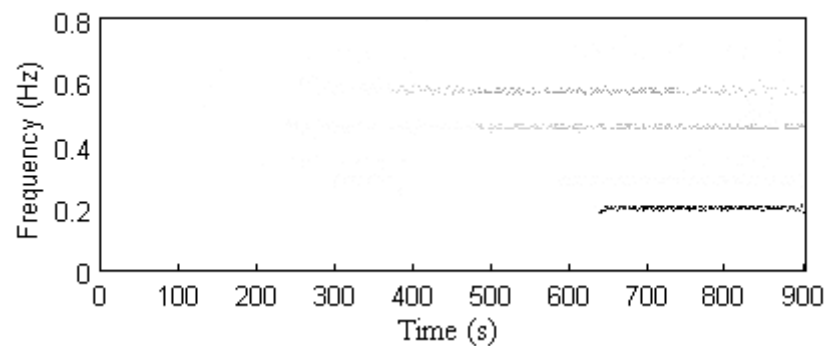


Figure C.45. HHT of signal obtained at sensor 15.

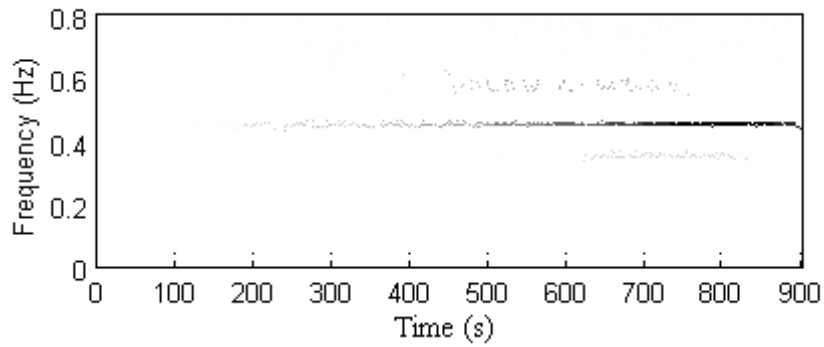


Figure C.46. HHT of signal obtained at sensor 16.

C.2.4 Typhoon Molave

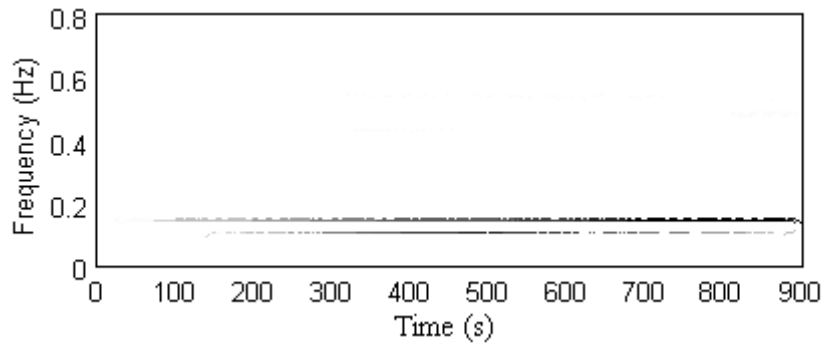


Figure C.47. HHT of signal obtained at sensor 3.

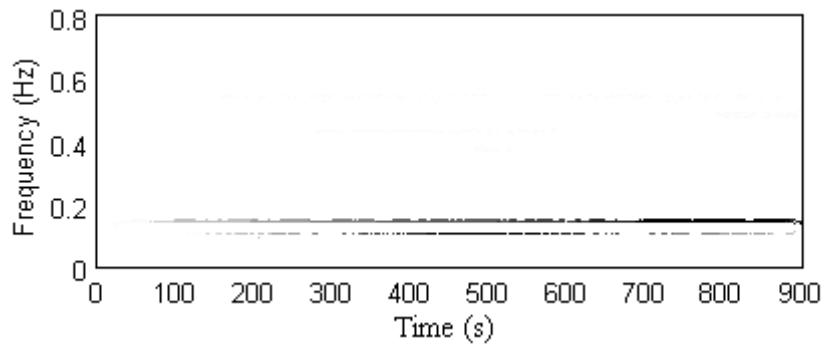


Figure C.48. HHT of signal obtained at sensor 4.

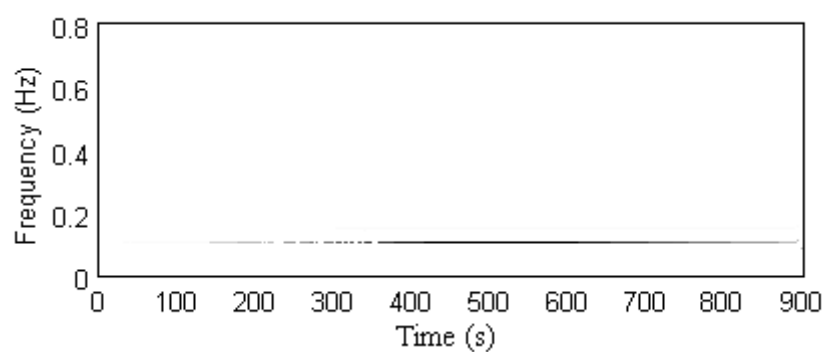


Figure C.49. HHT of signal obtained at sensor 5.

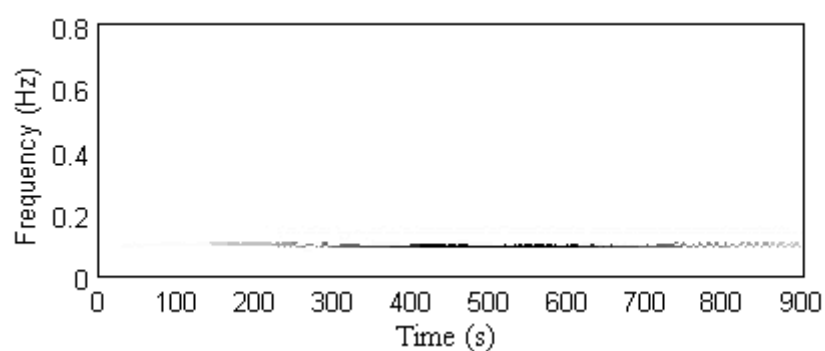


Figure C.50. HHT of signal obtained at sensor 6.

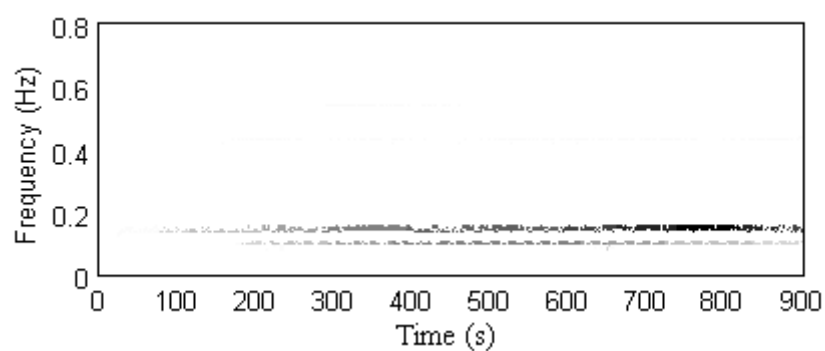


Figure C.51. HHT of signal obtained at sensor 7.

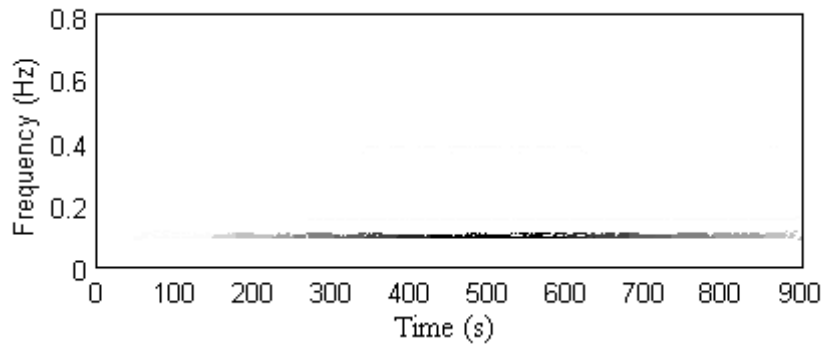


Figure C.52. HHT of signal obtained at sensor 8.

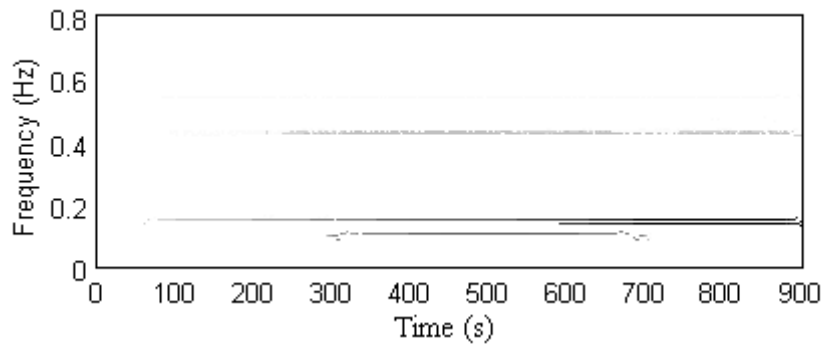


Figure C.53. HHT of signal obtained at sensor 9.

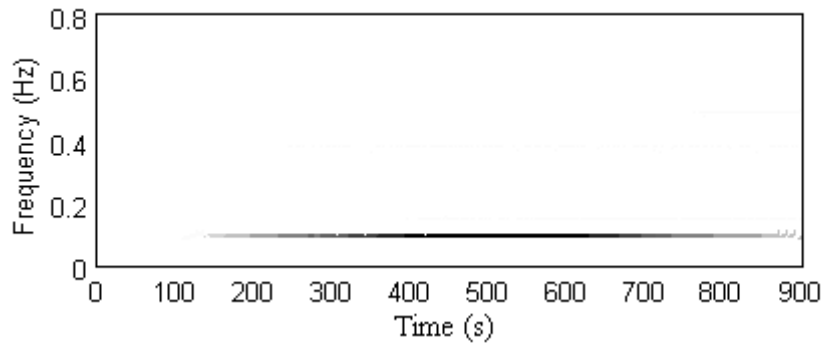


Figure C.54. HHT of signal obtained at sensor 10.

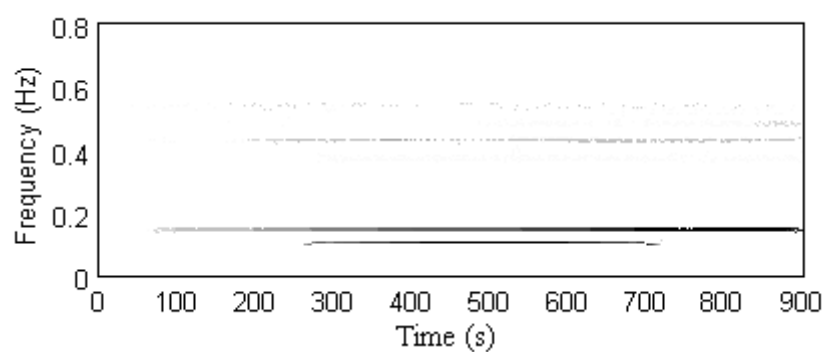


Figure C.55. HHT of signal obtained at sensor 11.

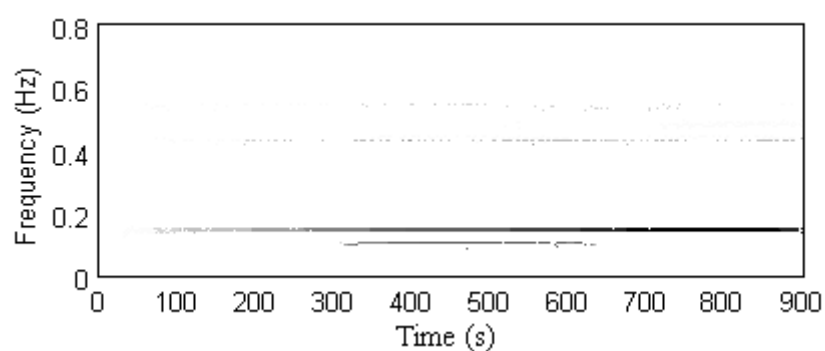


Figure C.56. HHT of signal obtained at sensor 12.

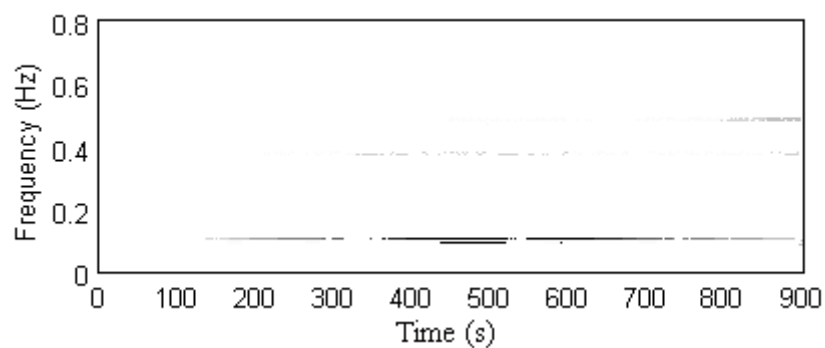


Figure C.57. HHT of signal obtained at sensor 13.

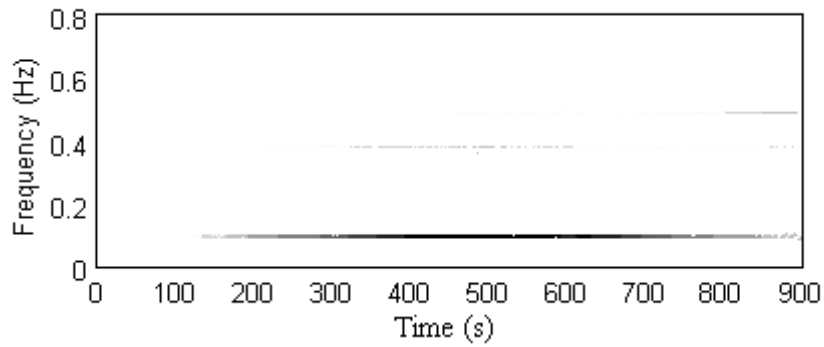


Figure C.58. HHT of signal obtained at sensor 14.

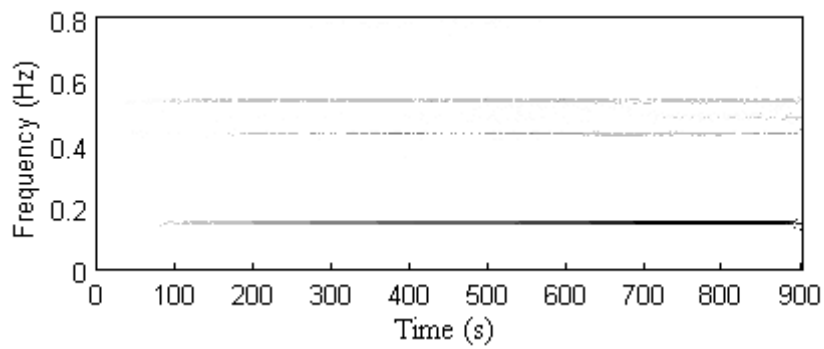


Figure C.59. HHT of signal obtained at sensor 17.

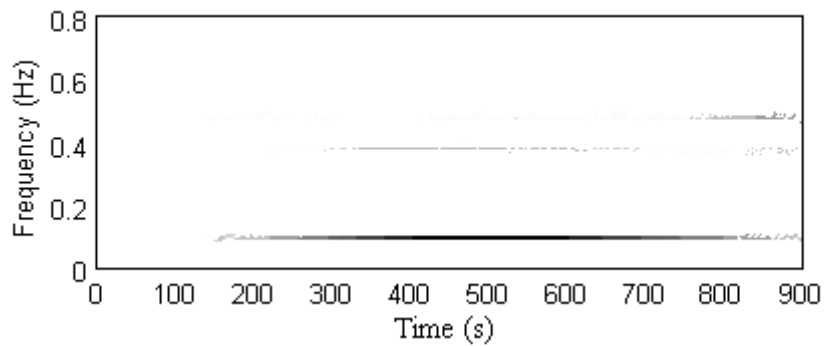


Figure C.60. HHT of signal obtained at sensor 18.

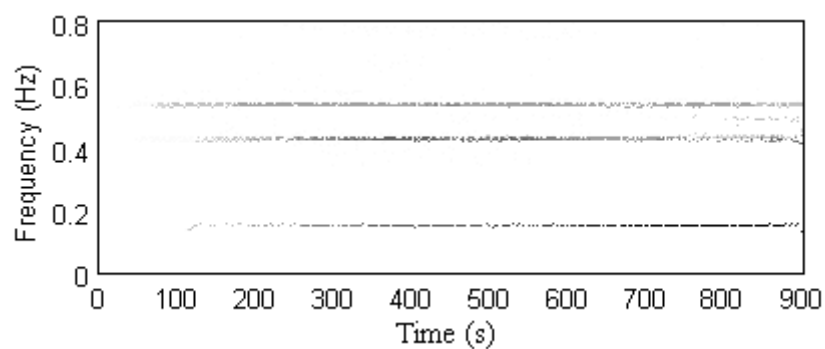


Figure C.61. HHT of signal obtained at sensor 19.

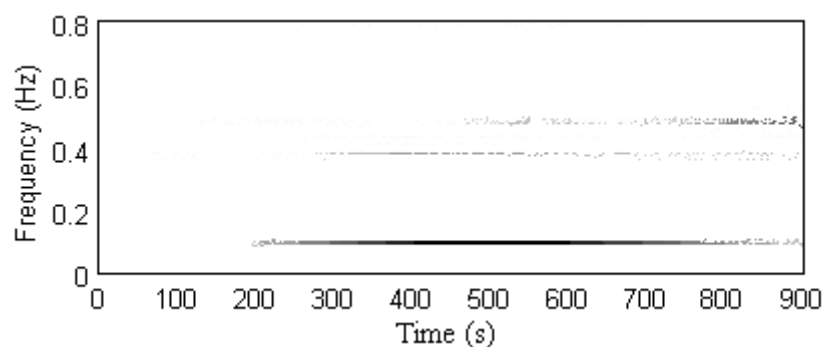


Figure C.62. HHT of signal obtained at sensor 20.

C.2.5 Typhoon Koppu

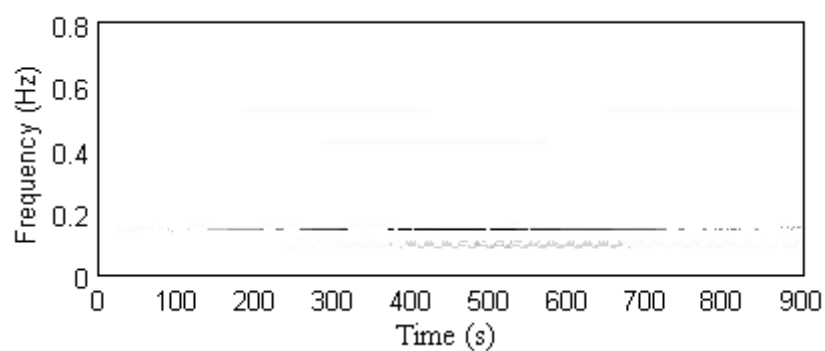


Figure C.63. HHT of signal obtained at sensor 5.

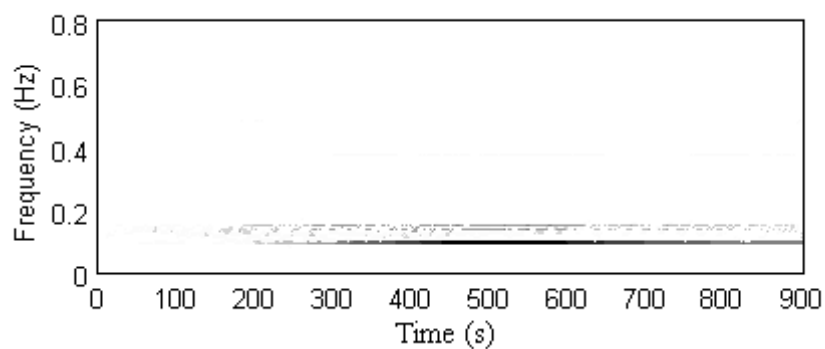


Figure C.64. HHT of signal obtained at sensor 6.

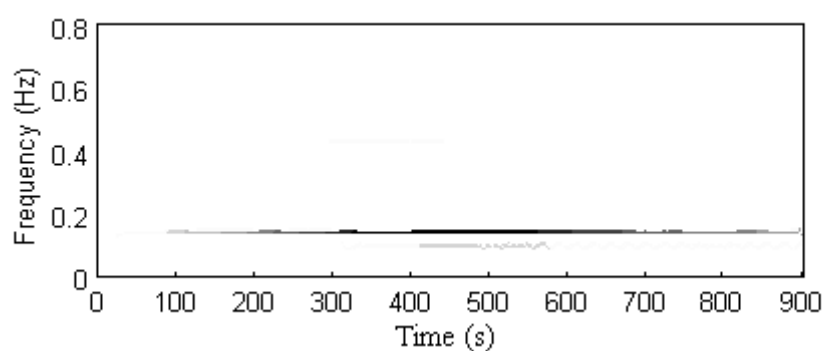


Figure C.65. HHT of signal obtained at sensor 7.

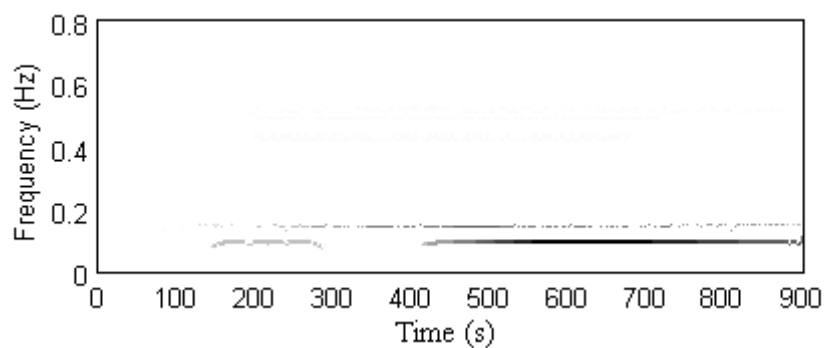


Figure C.66. HHT of signal obtained at sensor 9.

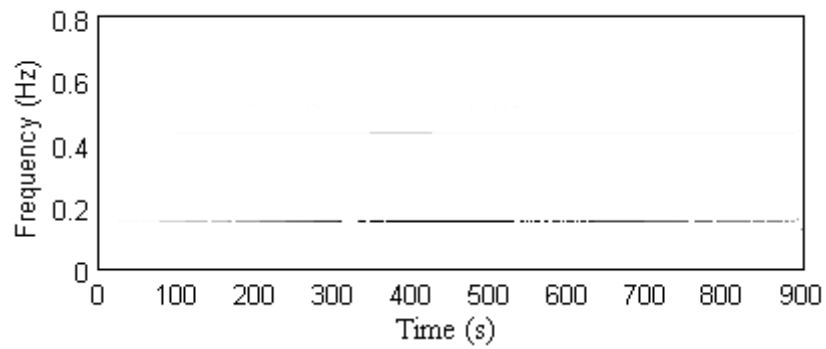


Figure C.67. HHT of signal obtained at sensor 11.

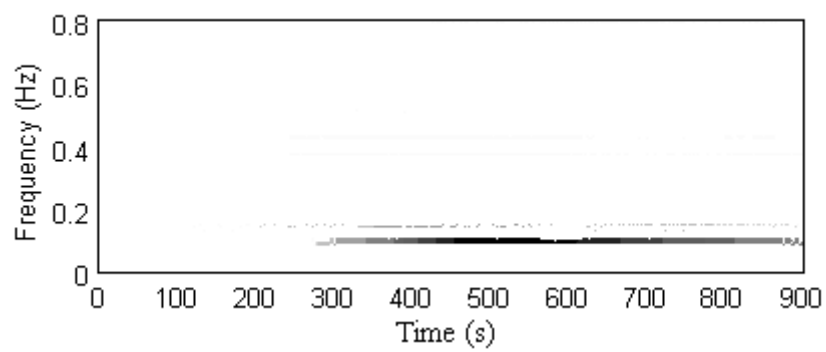


Figure C.68. HHT of signal obtained at sensor 12.

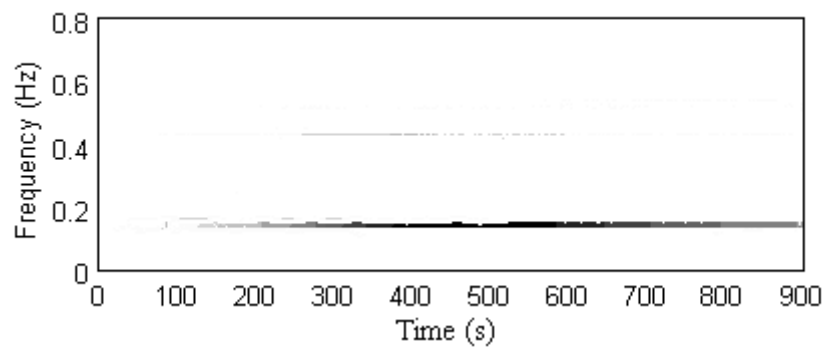


Figure C.69. HHT of signal obtained at sensor 13.

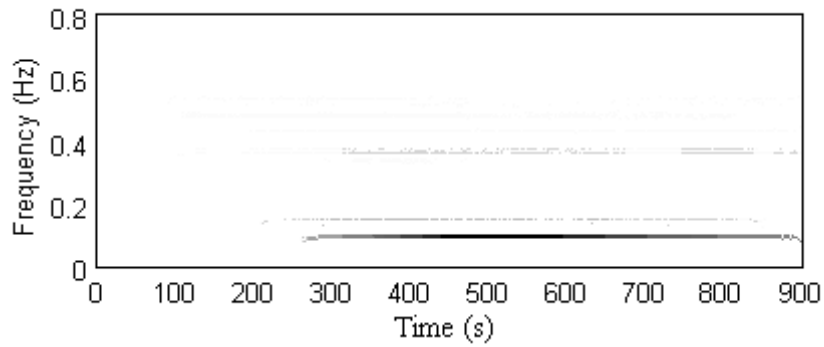


Figure C.70. HHT of signal obtained at sensor 14.

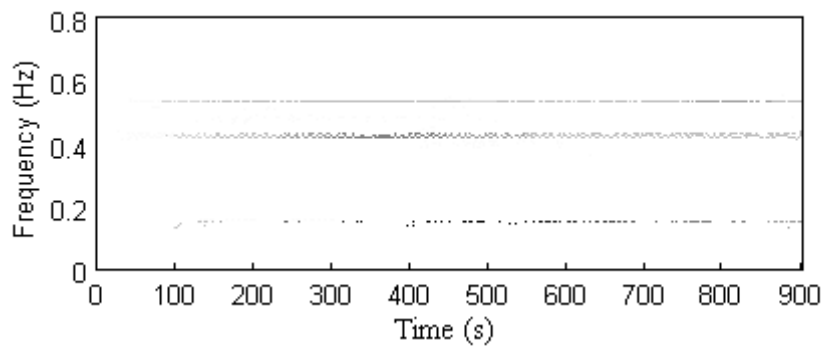


Figure C.71. HHT of signal obtained at sensor 15.

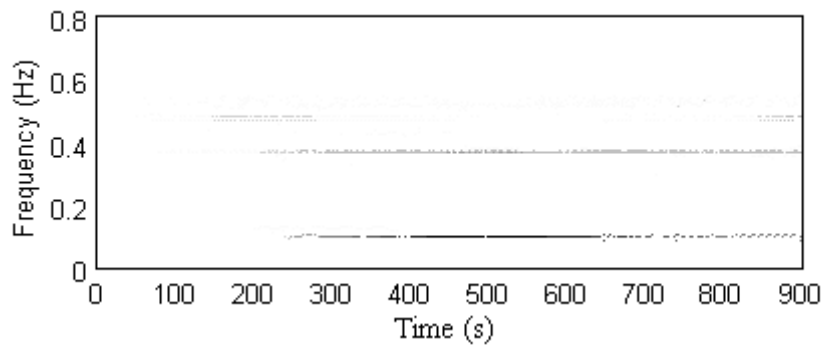


Figure C.72. HHT of signal obtained at sensor 16.

C.3 HHT Spectra of GTVT Response Signals to Earthquakes

C.3.1 Southern Taiwan earthquake

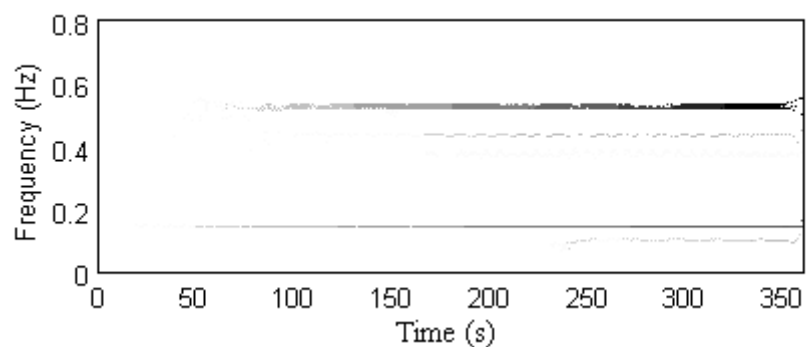


Figure C.73. HHT of signal obtained at sensor 3.

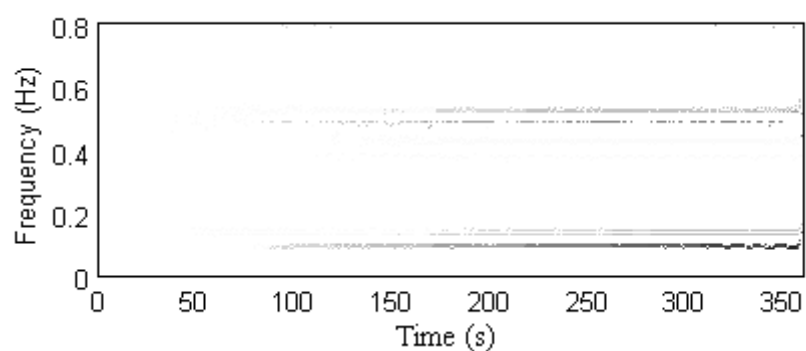


Figure C.74. HHT of signal obtained at sensor 4.

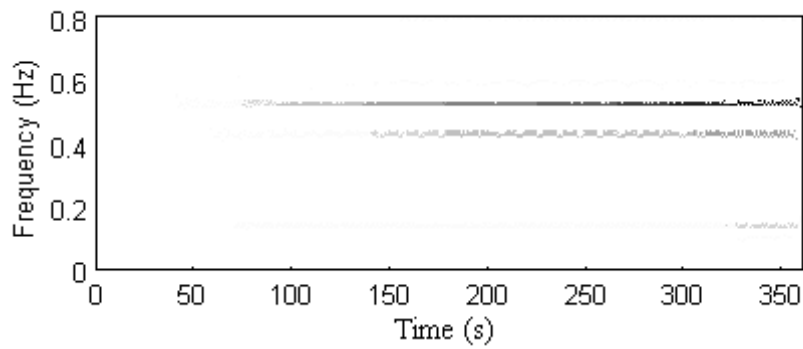


Figure C.75. HHT of signal obtained at sensor 5.

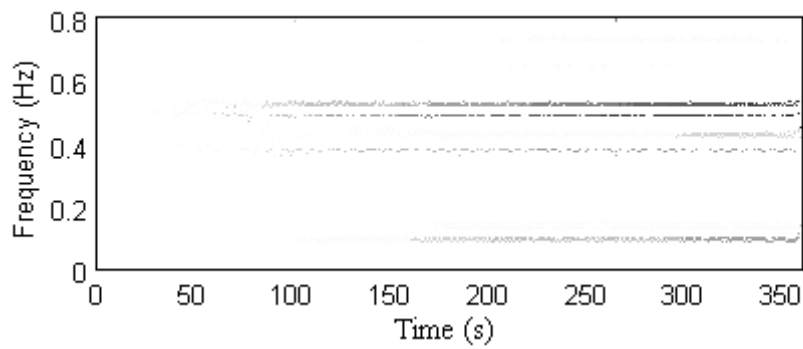


Figure C.76. HHT of signal obtained at sensor 6.

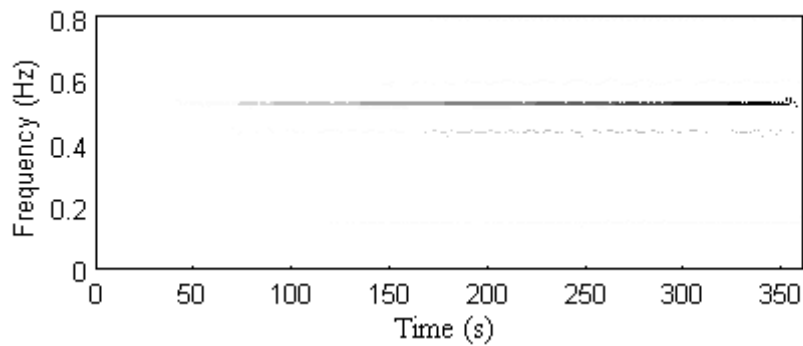


Figure C.77. HHT of signal obtained at sensor 7.

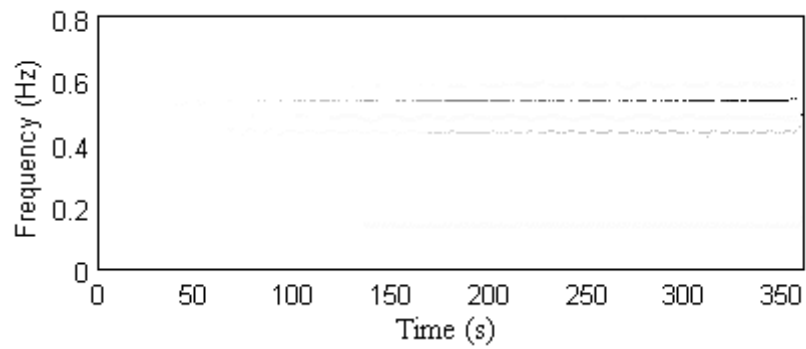


Figure C.78. HHT of signal obtained at sensor 8.

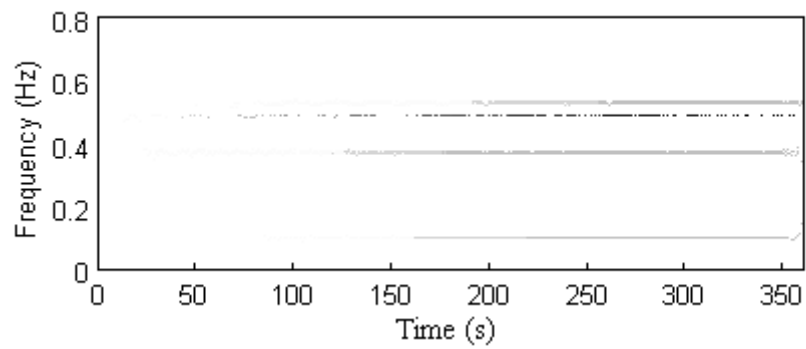


Figure C.79. HHT of signal obtained at sensor 9.

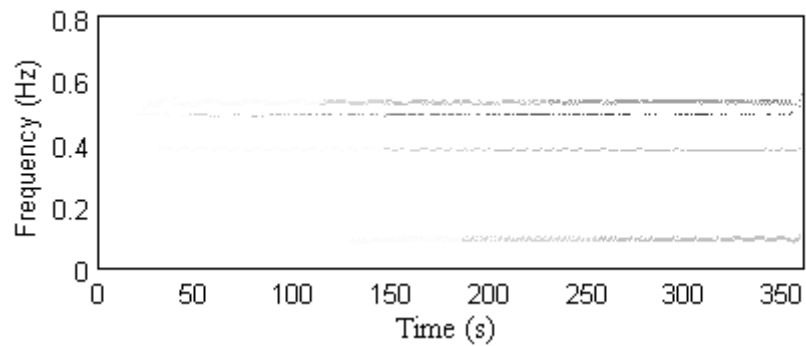


Figure C.80. HHT of signal obtained at sensor 10.

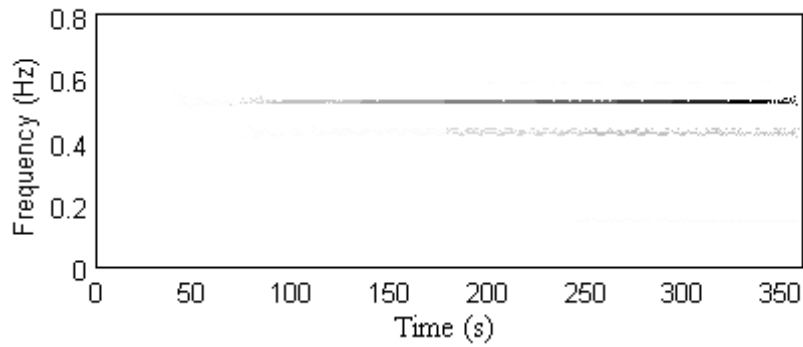


Figure C.81. HHT of signal obtained at sensor 11.

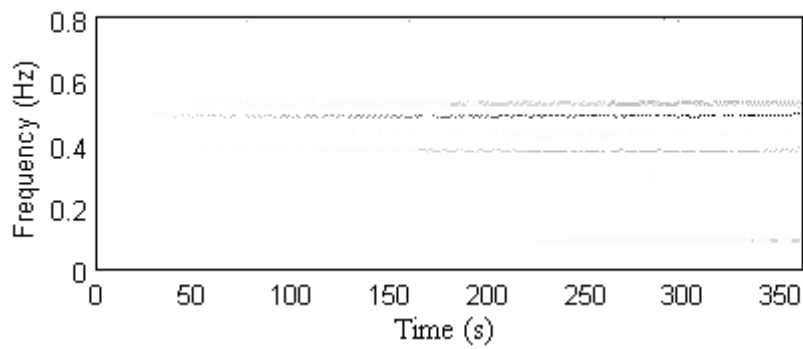


Figure C.82. HHT of signal obtained at sensor 12.

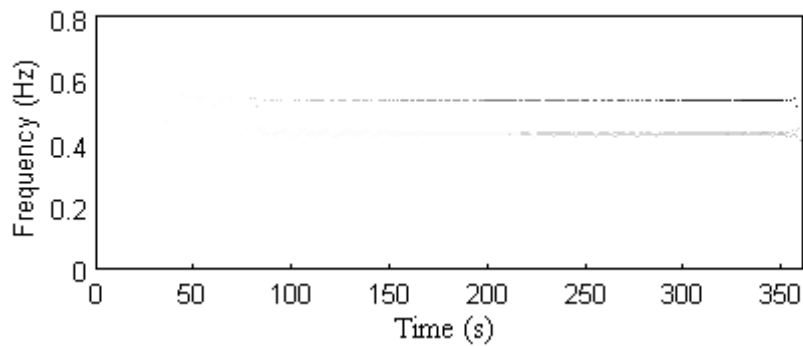


Figure C.83. HHT of signal obtained at sensor 15.

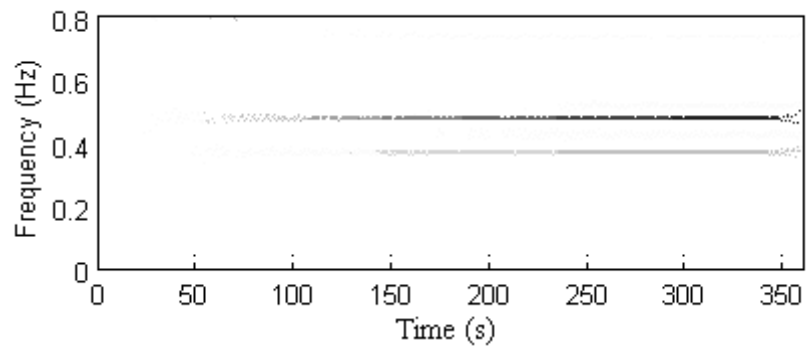


Figure C.84. HHT of signal obtained at sensor 16.

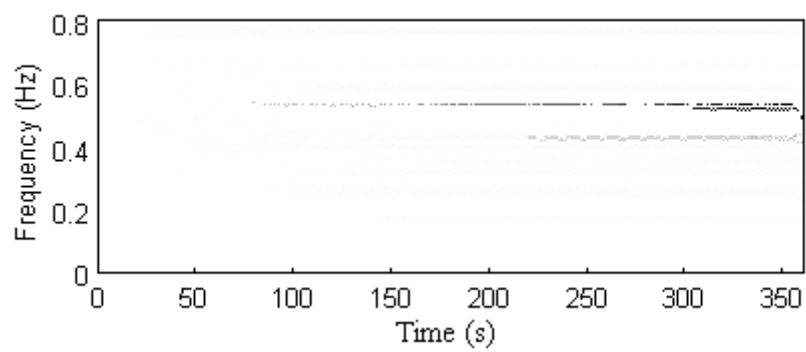


Figure C.85. HHT of signal obtained at sensor 17.

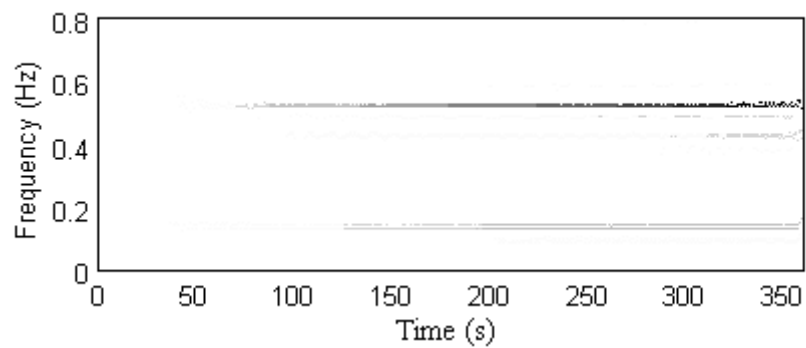


Figure C.86. HHT of signal obtained at sensor 18.

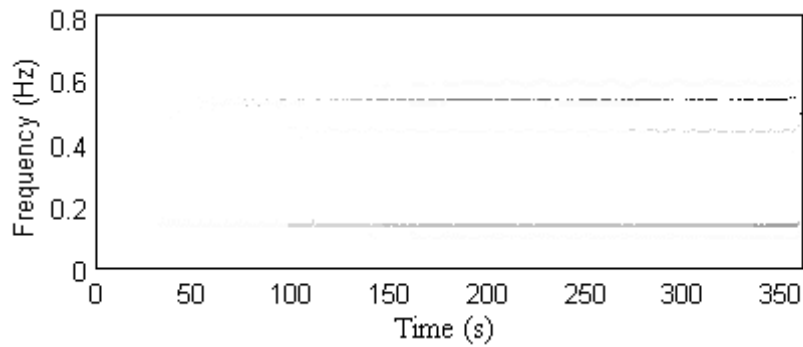


Figure C.87. HHT of signal obtained at sensor 19.

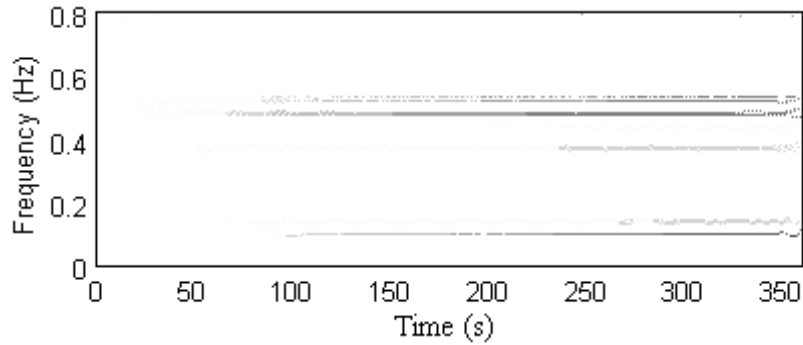


Figure C.88. HHT of signal obtained at sensor 20

C.3.2 Taiwan Hualien earthquake

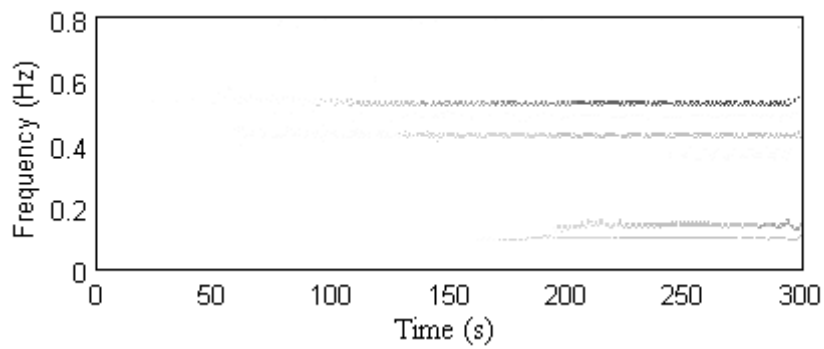


Figure C.89. HHT of signal obtained at sensor 1.

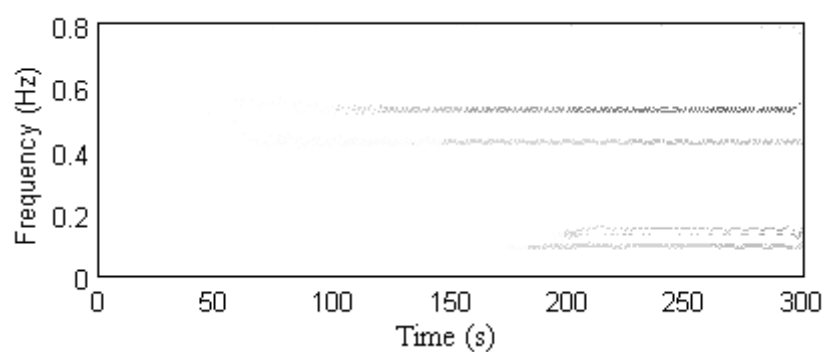


Figure C.90. HHT of signal obtained at sensor 2.

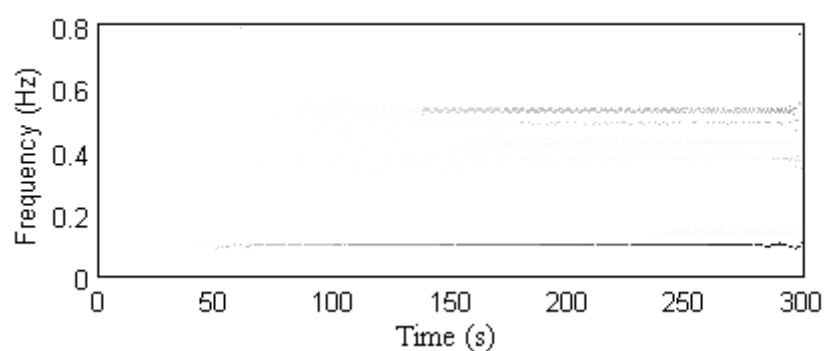


Figure C.91. HHT of signal obtained at sensor 3.

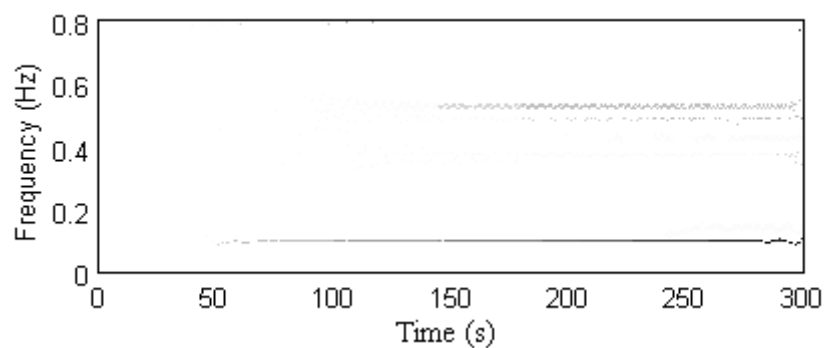


Figure C.92. HHT of signal obtained at sensor 4.

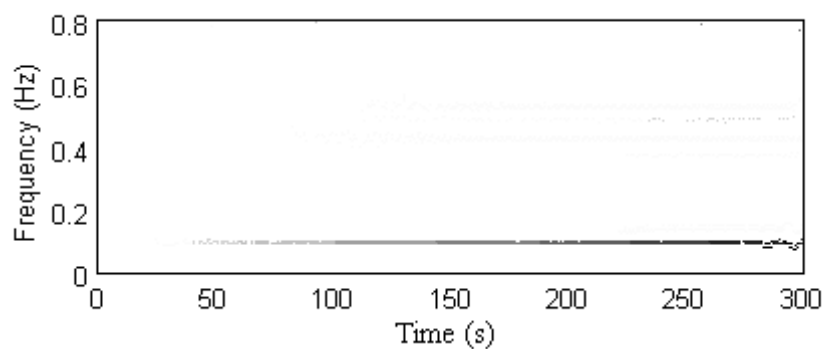


Figure C.93. HHT of signal obtained at sensor 7.

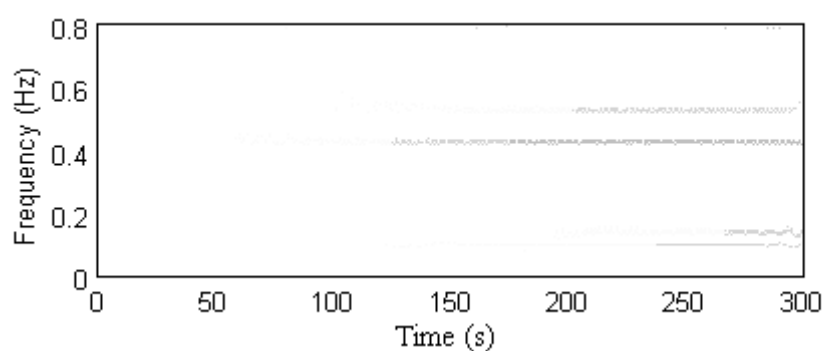


Figure C.94. HHT of signal obtained at sensor 8.

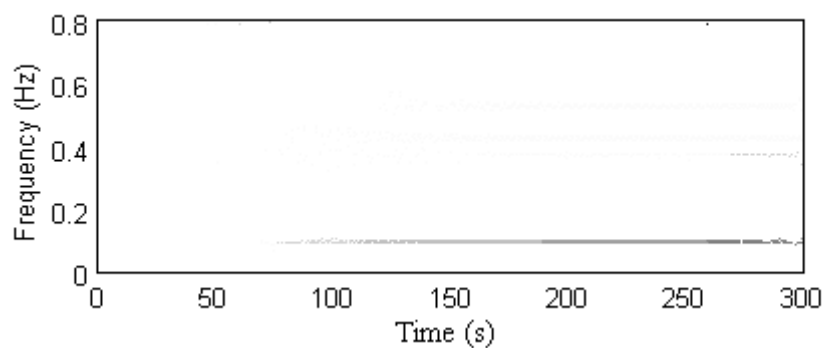


Figure C.95. HHT of signal obtained at sensor 9.

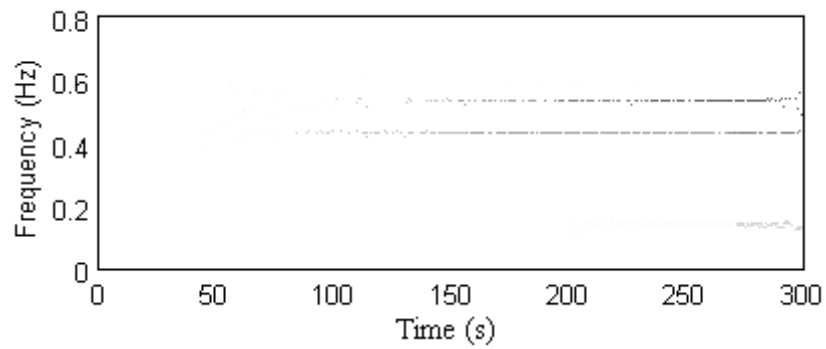


Figure C.96. HHT of signal obtained at sensor 10.

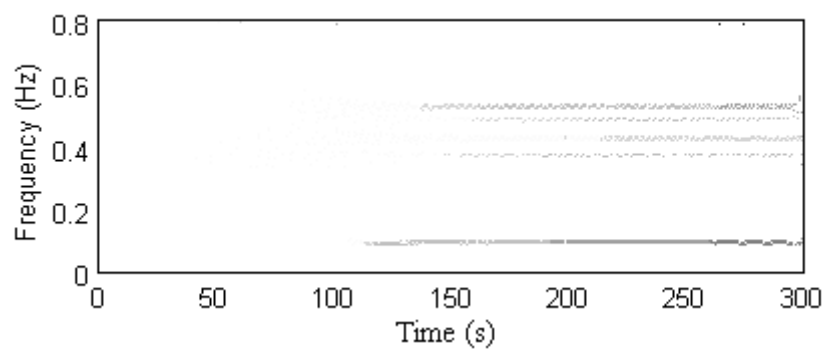


Figure C.97. HHT of signal obtained at sensor 11.

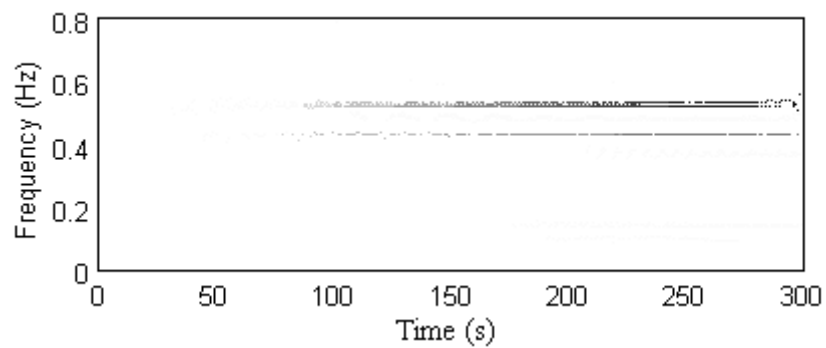


Figure C.98. HHT of signal obtained at sensor 12.

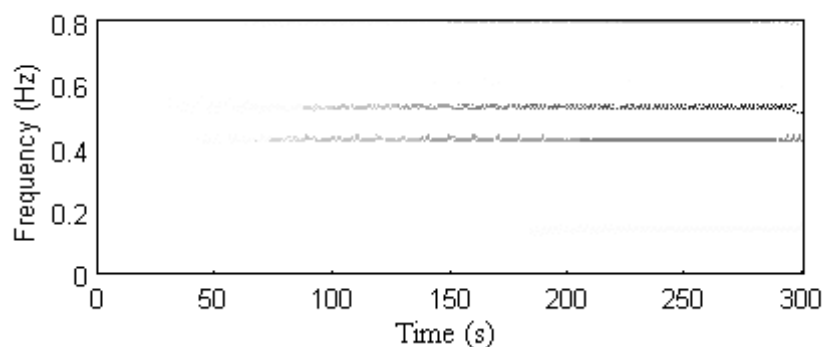


Figure C.99. HHT of signal obtained at sensor 13.

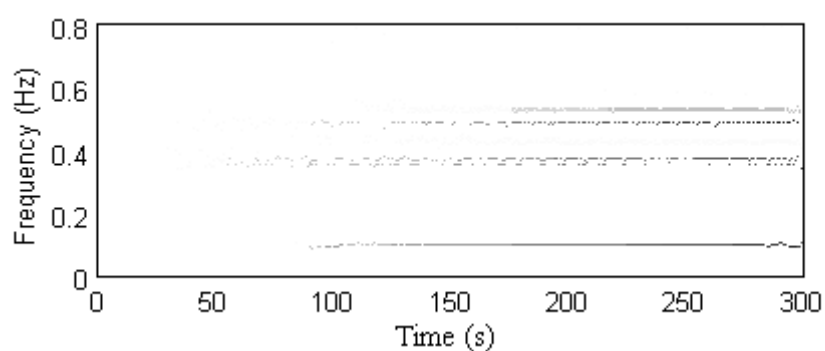


Figure C.100. HHT of signal obtained at sensor 14.

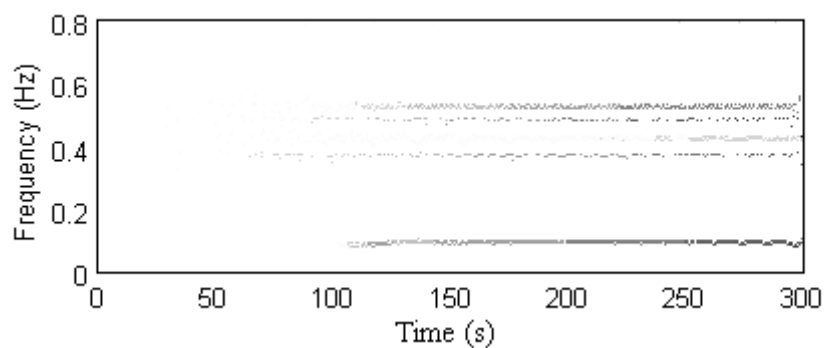


Figure C.101. HHT of signal obtained at sensor 15.

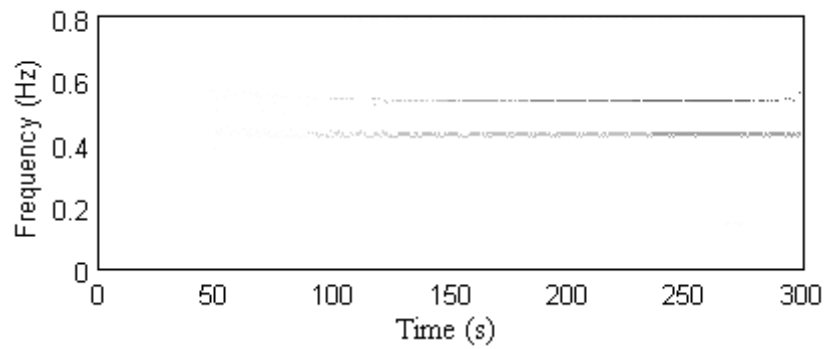


Figure C.102. HHT of signal obtained at sensor 16.

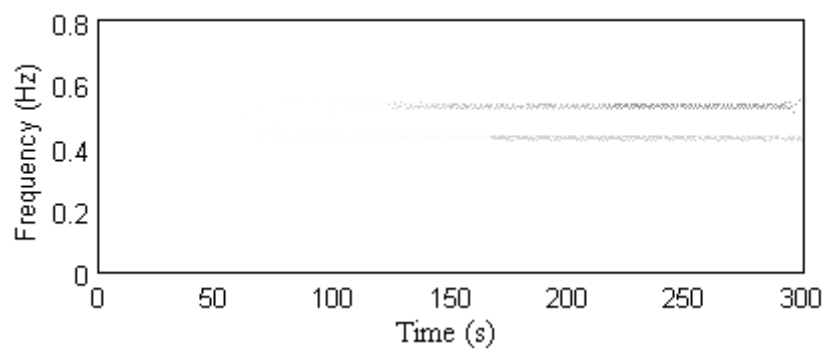


Figure C.103. HHT of signal obtained at sensor 17.

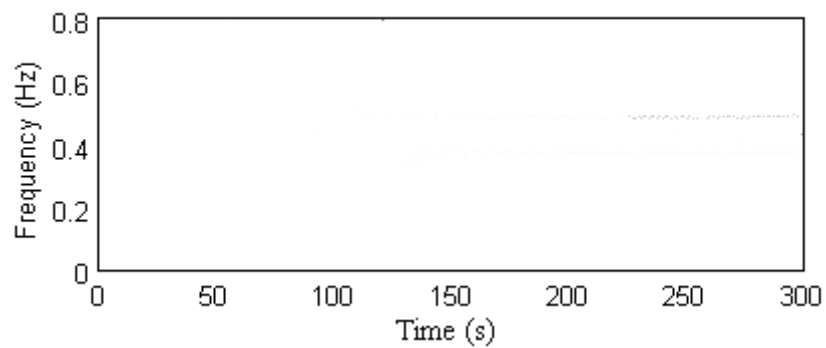


Figure C.104. HHT of signal obtained at sensor 18.

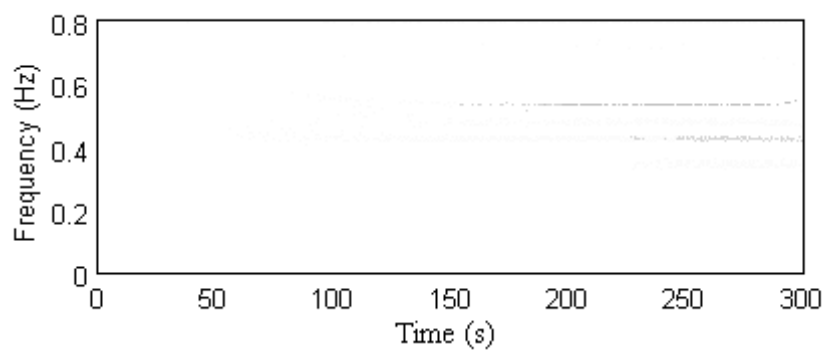


Figure C.105. HHT of signal obtained at sensor 19.